

# Exploring the Morphology, Chemistry, and Mechanics of Biogenic Silica in Diatoms

## ***Citation for published version (APA):***

Soleimani, M. (2022). *Exploring the Morphology, Chemistry, and Mechanics of Biogenic Silica in Diatoms*. [Phd Thesis 1 (Research TU/e / Graduation TU/e), Chemical Engineering and Chemistry]. Eindhoven University of Technology.

## ***Document status and date:***

Published: 21/04/2022

## ***Document Version:***

Publisher's PDF, also known as Version of Record (includes final page, issue and volume numbers)

## ***Please check the document version of this publication:***

- A submitted manuscript is the version of the article upon submission and before peer-review. There can be important differences between the submitted version and the official published version of record. People interested in the research are advised to contact the author for the final version of the publication, or visit the DOI to the publisher's website.
- The final author version and the galley proof are versions of the publication after peer review.
- The final published version features the final layout of the paper including the volume, issue and page numbers.

[Link to publication](#)

## ***General rights***

Copyright and moral rights for the publications made accessible in the public portal are retained by the authors and/or other copyright owners and it is a condition of accessing publications that users recognise and abide by the legal requirements associated with these rights.

- Users may download and print one copy of any publication from the public portal for the purpose of private study or research.
- You may not further distribute the material or use it for any profit-making activity or commercial gain
- You may freely distribute the URL identifying the publication in the public portal.

If the publication is distributed under the terms of Article 25fa of the Dutch Copyright Act, indicated by the "Taverne" license above, please follow below link for the End User Agreement:

[www.tue.nl/taverne](http://www.tue.nl/taverne)

## ***Take down policy***

If you believe that this document breaches copyright please contact us at:

[openaccess@tue.nl](mailto:openaccess@tue.nl)

providing details and we will investigate your claim.

# **Exploring the Morphology, Chemistry, and Mechanics of Biogenic Silica in Diatoms**

PROEFSCHRIFT

ter verkrijging van de graad van doctor aan de Technische Universiteit Eindhoven, op gezag van de rector magnificus prof.dr.ir. F.P.T. Baaijens, voor een commissie aangewezen door het College voor Promoties, in het openbaar te verdedigen op donderdag 21 April 2022 om 16:00 uur

door

**Mohammad Soleimani**

Geboren te Ilam, Iran

Dit proefschrift is goedgekeurd door de promotoren en de samenstelling van de promotiecommissie is als volgt:

Voorzitter: prof.dr. F. Gallucci

Promotor: prof.dr. R.A.T.M. van Benthem

Co-promotor: dr. H. Friedrich

Leden: prof.dr. S. Weiner (Weizmann Institute of Science)

prof.dr. E. Brunner (TU Dresden)

prof.dr.ir. P.D. Anderson

prof.dr.ir. E.J.M. Hensen

*Het onderzoek of ontwerp dat in dit thesis wordt beschreven is uitgevoerd in overeenstemming met de TU/e Gedragscode Wetenschapsbeoefening.*

*To my lovely wife and my beloved parents*



Mohammad Soleimani

Exploring the Morphology, Chemistry, and Mechanics of Biogenic Silica in Diatoms

Eindhoven University of Technology, 2022

This research was carried out under project number C16033a in the framework of the Partnership Program of the Materials innovation institute M2i ([www.m2i.nl](http://www.m2i.nl)) and the NWO Domain Science, which is part of the Netherlands Organization for Scientific Research.

A catalogue record is available from the Eindhoven University of Technology Library  
ISBN: 978-90-386-5483-6

Cover design by Mohammad Soleimani and Siyamak Parsa

## Summary

Biocomposite materials provide great insight into how nature has been able to optimize multiple functional properties by combining relatively simple components e.g., brittle materials with organic molecules. In this respect, biogenic silica as found in diatoms has been an inspiring topic for a variety of scientific disciplines to reveal its formation alongside its chemical and morphological properties. Diatoms are unicellular photosynthetic algae, which inhabit aquatic environments and are well-known due to the fascinating morphology of their highly ornamented biogenic silica structure, the frustule. It is established that the frustule provides some practical functions such as light-harvesting and mechanical protections for the living cell, while its physical and chemical properties can be altered by the surrounding conditions such as the presence of non-essential metal ions or salinity level. Concurrently, it is known that during the frustule formation, the incorporation of  $\text{Al}^{3+}$  into the newly formed frustule enhances its hydrolysis resistance. However, further effects of this non-essential metal ion on morphological, chemical, and mechanical properties of diatom frustules are rather unclear. Revealing these properties of diatom frustules at the relevant length scale in correlation with the growth medium and conditions (particularly in the presence of  $\text{Al}^{3+}$ ) is a challenging task to accomplish. However, concurrently it is interesting to learn which novel approaches can lead to the development of new insights and a new understanding of the properties of biogenic silica in diatoms. In order to determine the aforementioned properties of biogenic silica in diatoms, advanced electron microscopy techniques such as scanning and transmission electron microscopy, electron tomography, focused ion beam micromachining, and micromanipulators are employed in this thesis.

In Chapter 1, a general introduction including a brief background of biocomposite, biogenic silica and its properties in diatoms alongside the motivation of this thesis and the characterization techniques to achieve its goals are presented. In Chapter 2, biogenic silica formation in diatom *Craspedostauros sp.* in the presence of  $\text{Al}^{3+}$  is investigated. In this chapter, the frustule formation in this diatom *species* including changes to its overall morphology, silica thickness, and composition are monitored by various analytical techniques. In Chapter 3, the design and implementation of a flexible workflow for measuring the mechanical properties of diatom frustule constituents i.e., valves and girdle bands, is described. In this chapter, a versatile approach combining focused ion beam scanning electron microscopy and micromanipulators is presented to isolate, transfer, and determine the mechanical properties of frustule constituents of one of the smallest diatom species, the circo-centric diatom *Thalassiosira pseudonana* grown at different salinity levels. In Chapter 4, the effects of  $\text{Al}^{3+}$  on morphological, chemical, and mechanical properties of frustule of the diatom *Thalassiosira pseudonana* are explored. In this chapter, the developed workflow in Chapter 3 is employed in combination with electron tomography and finite element method simulations to determine the effect of  $\text{Al}^{3+}$  on Young's modulus of girdle bands and valves individually. In Chapter 5, as another proof of concept for the developed workflow, the mechanical properties of a different diatom (*Craspedostauros sp.*) are studied. In addition, in situ manipulation of the valves is conducted, enabling repositioning them in the best possible direction for in situ mechanical defor-

mation testing. Chapter 6 is set out to explore the applicability of focused ion beam micromachining and manipulators to determine the mechanical properties of synthetic silica (thin films). Here free-standing silica thin beams with the desired dimensions are fabricated and by in situ bending tests their Young's modulus are determined. In addition, the effects of gallium ion beam irradiation and relative humidity on the mechanical properties of as-fabricated silica beams are studied. Finally, in Chapter 7, a summary, directions for future research, and some concluding remarks are presented.

## List of Abbreviations

1D	one dimensional
2D	two dimensional
3D	three dimensional
AAS	atomic absorption spectroscopy
AFM	atomic force microscopy
CN	central nodule
C.sp.	<i>Craspedostauros</i> sp.
CPD	critical point dryer
EDS	energy dispersive x-ray spectroscopy
EM	electron microscopy
ET	electron tomography
FEG	field emission gun
FEM	finite element method
FIB	focused ion beam
FMS	force measurement system
Ga	gallium
LM	light microscopy
LCPA	long chain polyamine
MAS	magic angle spinning
NMR	nuclear magnetic resonance
PiFM	photo-induced force microscopy
PSU	practical salinity unit
RH	relative humidity
SDV	silica deposition vesicle
SEM	scanning electron microscopy
SIT	silicic acid transporter
TEM	transmission electron microscopy
TEOS	tetraethyl orthosilicate
TGA	Thermogravimetric analysis
T.p.	<i>Thalassiosira pseudonana</i>

# Contents

<b>Chapter 1 .....</b>	<b>1</b>
<b>Introduction.....</b>	<b>1</b>
1.1 General introduction.....	2
1.2 Characterization techniques to unveil the complex morphology of diatoms .....	10
1.3 Aim and outline of the thesis.....	14
1.4 References .....	16
<b>Chapter 2 .....</b>	<b>24</b>
<b>Modifying the thickness, pore size, and composition of diatom frustule in <i>Craspedostauros</i> sp. with Al<sup>3+</sup> ions.....</b>	<b>24</b>
2.1 Introduction .....	25
2.2 Materials and methods .....	26
2.3 Results .....	30
2.4 Discussion .....	37
2.5 Summary .....	39
2.6 References .....	40
2.7 Appendix .....	44
<b>Chapter 3 .....</b>	<b>53</b>
<b>In situ Manipulation and Micromechanical Characterization of Diatom Frustule Constituents Using Focused Ion Beam Scanning Electron Microscopy .....</b>	<b>53</b>
3.1 Introduction .....	54
3.2 Results and Discussion.....	55
3.3 Conclusions .....	64
3.4 Experimental Section .....	64
3.5 References .....	66
3.6 Appendix .....	70
<b>Chapter 4 .....</b>	<b>79</b>
<b>How Al<sup>3+</sup> ions in the growth medium affect the frustule Morphology, Chemistry, and Mechanical Properties of Diatom <i>Thalassiosira pseudonana</i>.....</b>	<b>79</b>
4.1 Introduction .....	80
4.2 Results .....	81
4.3 Discussion .....	89

4.4	Materials and Methods .....	91
4.5	Reference.....	94
4.6	Appendix .....	99
<b>Chapter 5</b> .....		<b>105</b>
<b>Investigating the Morphology and Mechanics of Biogenic Hierarchical Materials at and below Micrometer Scale</b> .....		<b>105</b>
5.1	Introduction .....	106
5.2	Results and discussion.....	107
5.3	Conclusions .....	112
5.4	Materials and Methods .....	112
5.5	References .....	114
5.6	Appendix Movies .....	117
<b>Chapter 6</b> .....		<b>118</b>
<b>In situ Fabrication, Manipulation, and Mechanical Characterization of Free-Standing Silica Thin Films Using Focused Ion Beam Scanning Electron Microscopy</b> .....		<b>118</b>
6.1	Introduction .....	119
6.2	Results and discussion.....	121
6.3	Conclusions .....	132
6.4	Experimental Section .....	132
6.5	Reference.....	134
6.6	Appendix .....	139
<b>Chapter 7</b> .....		<b>146</b>
7.1	Summary .....	146
7.2	Outlook.....	148
7.3	References .....	152
<b>List of publications</b> .....		<b>154</b>
<b>Curriculum vitae</b> .....		<b>156</b>
<b>Acknowledgements</b> .....		<b>157</b>



# Chapter 1

## Introduction



## 1.1 General introduction

Through the evolutionary process for millions of years, many living organisms have discovered a way of creating highly sophisticated mineralized biological materials (also referred to as biocomposites) for a variety of functions<sup>1,2</sup>. In general, biocomposites are formed by a combination of inorganic and biologically derived organic constituents via environmentally benign routes at ambient conditions. Biocomposites possess remarkable mechanical properties that are mainly unmatched by their synthetic counterparts<sup>3</sup>. In contrast to the relatively limited properties of the main individual components, such as brittle minerals and soft proteins, they manage to concurrently maintain low weight on the one hand side, and high stiffness, high strength, and toughness on the other; a combination of properties which is extremely challenging to achieve in manmade materials<sup>2,4,5</sup>. There is a growing body of literature that recognizes the importance of learning how living organisms produce these biocomposites in correlation with their ultimate functions<sup>6-8</sup>. Being able to take these lessons is key to realizing novel synthetic approaches towards high-performance materials using low temperatures, mild pressures, and in aqueous solution<sup>9</sup>. Understanding the way in which biocomposite materials are formed and how they function does not necessarily mean duplicating their exact structural-function properties: it may simply lead to obtaining valuable insights and key concepts from their existence which eventually can be adapted and used for synthetic materials.

Despite the abundance and morphological complexity of biocomposites, only about 60 minerals are employed by living organisms to form them, nearly half of these minerals contain calcium<sup>10</sup>. Calcium carbonate ( $\text{CaCO}_3$ ) is one of the predominant biominerals which exists in crystalline forms of calcite and aragonite alongside its amorphous phase. Mollusk shells, bird eggs, and coral, are well-known examples in which  $\text{CaCO}_3$  is utilized. Moreover, calcium phosphate in the form of hydroxyapatite which is the main mineral forming the biocomposite of bone and teeth is another type of calcium type mineral<sup>11</sup>. Among various biocomposites made of calcium, nacre (Figure 1.1) from seashells is a well-studied material that is made of aragonite tiles arranged together with a small amount (5 % volume) of organic constituents<sup>12</sup>. The overall arrangement in the nacre resembles a three-dimensional brick and mortar wall with hierarchical features that are found at different length scales. It has been established that even though 95 % of nacre is made of aragonite, its toughness is significantly higher than synthetic aragonite<sup>13</sup>. It has been suggested that its excellent mechanical performances, such as Young's modulus in the range of 60-70 GPa, depend on several parameters at different length scales, ranging from nano to micrometers<sup>3,7</sup>. This poses the questions: What are the engineering principles and secrets used in designing such strong biocomposites from relatively “weak” constituents in nacre? Do the organic building blocks play a role in the overall toughness and hardness of biocomposites? Can we achieve comparable mechanical properties by mimicking biocomposites? An excellent example of obtaining mechanical properties in synthetic minerals comparable with their biomineral counterpart is the effect of amino acids on hardness of calcite crystals<sup>14</sup>. It has been confirmed that the hardness of this mineral can easily be

tuned by the amount of amino acid enclosed within its crystal structure. This example demonstrates the important role of even small amounts of organic constituents on the final mechanical properties of minerals. However, further work is needed to investigate into how these constituents define the final optimized mechanical properties of biocomposite materials.

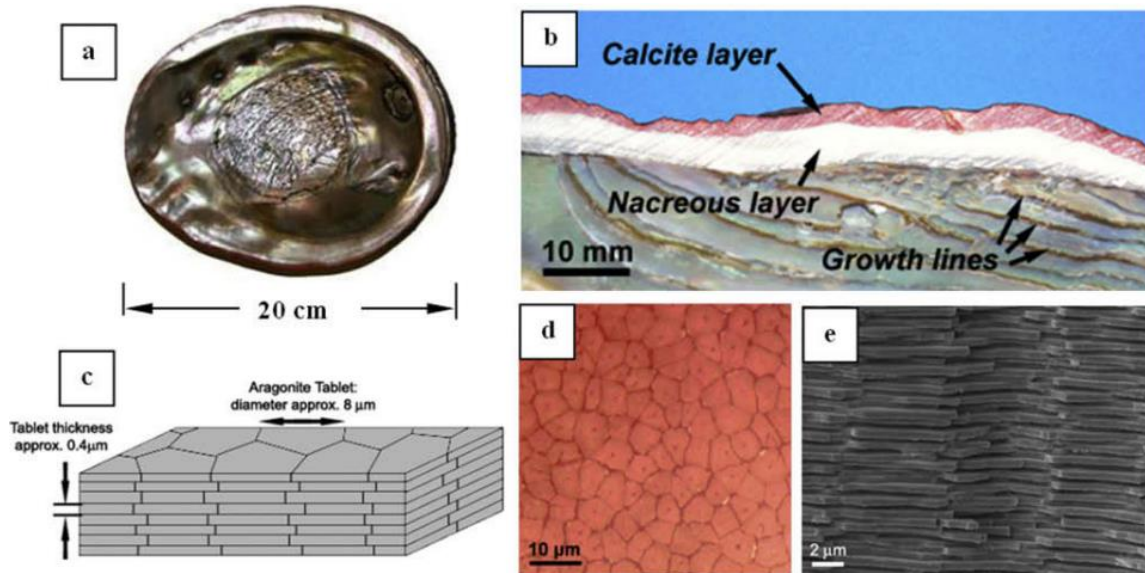


**Figure 1.1.** The multiscale structure of nacre (a) micrograph of inside of the shell; (b) cross section micrograph of a red abalone shell; (c) schematic illustration of the brick wall like microstructure; (d) micrograph of the tiling of the tablets; (e) SEM image of a cross-section of the tablets. Adapted with permission from ref<sup>7</sup>.

### 1.1.1 Different forms of silica

Besides calcium, silicon, which is the second most abundant element in the earth's crust, mainly in the form of silica ( $\text{SiO}_2$ ), is also an essential element for biocomposites produced by several living organisms<sup>15</sup>. Despite its chemical simplicity, silica in nature is found in numerous forms of crystalline and amorphous structures (Figure 1.2)<sup>16</sup>. Most of the natural crystalline silica, are made of three-dimensional frameworks of corner-sharing tetrahedra of  $\text{SiO}_4$ . Quartz as a well-known example of crystalline silica is present in nearly all major rock types and top soils and accounts for approximately 12 wt % of the earth's crust<sup>17</sup>. Crystalline silica are mainly thermodynamically stable under ambient conditions and possess high hardness, and high melting point likely due to the strong bond of Si-O and three-dimensional connectivity of the tetrahedra<sup>16</sup>. Notwithstanding the abundance and wide applicability of quartz as a raw material for numerous industrial applications, processing usually requires high temperature and pressure<sup>18,19</sup>. In the new global economy, energy consumption and its direct effect on climate change have become a central issue for the production of materials. Therefore, in the long term, finding solutions to minimize energy consumption for processing of such materials seems appealing. Furthermore, it has become clear in the past decades that long-time exposure of human lung tissue to micron-sized crystalline silica products causes severe respiratory diseases such as silicosis and cancer, which has triggered the search for a safer and more benign substitution for crystalline silica-based materials<sup>20</sup>.

Another form of silica is amorphous silica which is basically similar to its crystalline phases comprising  $\text{SiO}_4$  tetrahedra in a continuous but more random framework, i.e. without long range order. In other words, in amorphous silica, silicon and oxygen atoms are not organized in a fixed geometrical arrangement and thus do not produce a crystalline pattern observable by diffraction techniques<sup>21</sup>. Amorphous silica is employed in different industrial applications such as medicine, food, electronics, tires, and many others, and it is an essential part of many products<sup>22-26</sup>. In general, there are two types of manufacturing processes, referred to as thermal and wet methods, to produce amorphous synthetic silica. The thermal process often leads to fumed silicas and vitreous/fused silicas. On the other hand, the amorphous silicas which are produced based on wet process known as colloidal silica, silica gel and precipitated silica<sup>27</sup>. Obviously, the thermal process necessitates high temperature while wet procedures often require extreme pH to obtain desired products with tailored properties. Even though synthetic amorphous silica forms have been manufactured relatively cheap and uniform in a wide variety of structures and sizes, their morphology does not yet match the complexity and hierarchy of natural (biogenic) amorphous silica forms<sup>28-30</sup>. In addition, the manipulation of silica-based materials at the nanometer length scale for designing complex structures for specific applications is challenging since manipulation of all nanomaterials has been recognized as one of the great challenges of science for designing new materials with tailored properties<sup>31</sup>. Therefore, biogenic silica which often possesses highly ordered structures at different length scale can be of particular interest for state-of-the-art applications of micro/nanoscaled materials<sup>32,33</sup> as well as a potential candidate for industrial application of synthetic amorphous silica<sup>34</sup>.

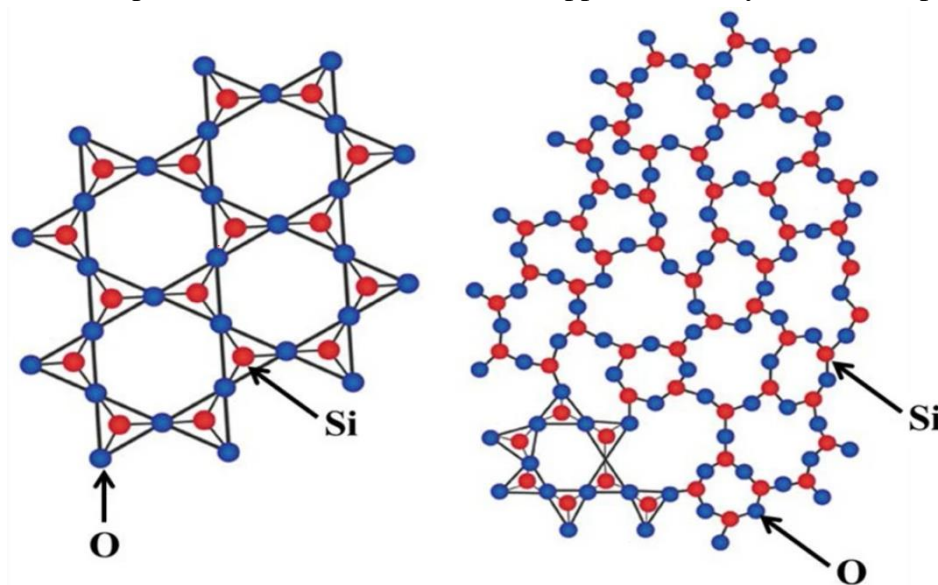


**Figure 1.2.** Structure of crystalline (left) and amorphous (right) silica. (Red spheres present silicon atoms and blue show oxygen atoms, respectively). Adapted with permission from ref<sup>35</sup>.

Biogenic silica often possess hierarchical morphologies obtaining by the condensation of silicic acid in ambient conditions and well controlled means within the living organisms. This process takes place through various biological pathways leading to the solidification of silicic acid and is known as biosilicification<sup>36</sup>. The process of silica formation is predominately present in sponges,

diatoms, radiolaria, and synurophytes (Figure 1.3)<sup>15,37</sup>. It is well known that silica is highly insoluble at neutral pH while its soluble form (silicic acid) is present in comparatively copious amounts in most aquatic environments and can easily be accumulated and condensed through polymerization by these organisms<sup>15</sup>. These living organisms have discovered unique ways to use the opportunities offered by silica chemistry to form their amorphous biogenic silica, concurrently adapting themselves to the limitations of silica chemistry e.g. rapid polycondensation at elevated concentration<sup>38</sup>. In contrast to crystalline forms of silica, no severe adverse effect of biogenic silica has been reported to date<sup>39</sup>. Therefore, characterizing biogenic silica at different levels of hierarchy and understating their formation mechanism may inspire the formation of bioinspired and biomimetic silica-based materials as well as exploiting them for developing economic and environmentally benign materials for industrial applications<sup>40-44</sup>. In this thesis, the diatom's frustule, which is one of the most well-known biogenic silica structures, is studied. Specifically, its morphological, chemical, and mechanical properties are investigated in correlation to its growth medium conditions.

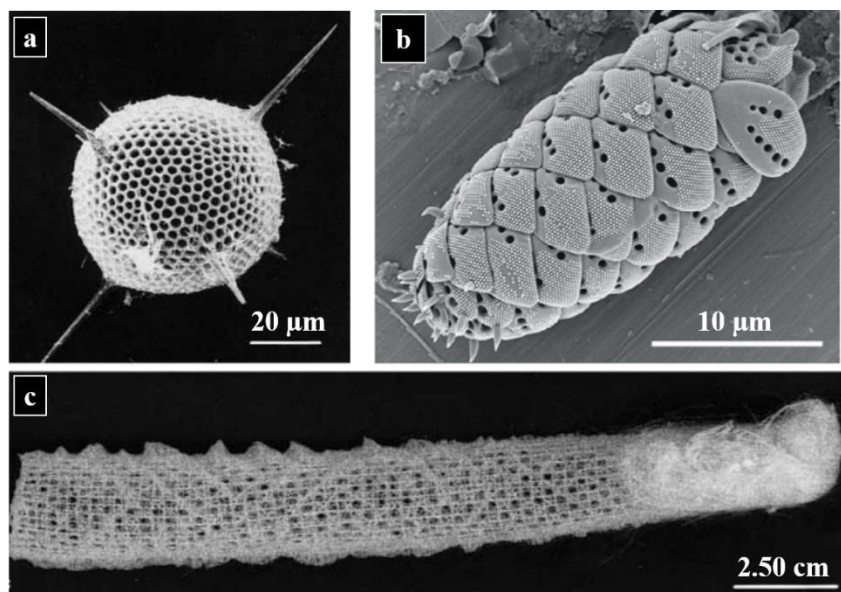


**Figure 1.3.** SEM images of different organisms comprise silica. (a) radiolaria (unknown species) (b) cell of *Mallomonas lichenensis* (c) sponge, (*Euplectella* Owens). Adapted with permission from refs<sup>45,15</sup>.

### 1.1.2 Diatoms and their frustule formation

Diatoms are unicellular photosynthetic algae that live in most aquatic environments with a large variety of shapes<sup>46</sup>. Diatoms are the dominant primary producers in the oceans and are estimated to be responsible for 40 % of the total marine primary food production<sup>47</sup>. To date, more than 10,000 diatom species have been identified. They possess wide variations in morphology, porosity, hierarchy, geometries and their sizes range from 2 to 2000 micrometers<sup>48</sup>. Diatoms are categorized into two types based on their symmetry: circo-centric diatoms which have rotational symmetry about their central axis, and pennate diatoms which are bilaterally symmetrical<sup>49</sup>. The most intricate aspect of diatoms is their cell wall, the frustule, which is a highly ornamented micro- and nanostructured silica (Figure 1.4a). The frustule is recognized as a composite of organic molecules



and hydrated amorphous silica which is constructed in a petri-dish like arrangement. It consists of two valves and several overlapping girdle bands<sup>50,51</sup>. The current understanding regarding the frustule formation is that silicon (Si), an essential element for cell division and growth, is taken up from the environment by the diatom cells in the form of orthosilicic acid ( $\text{Si}(\text{OH})_4$ ) by silicic acid transporter proteins (SITs)<sup>52,53</sup>. After Si uptake, the process of silica formation and morphogenesis of the frustule takes place in confined intracellular organelles with mildly acidic pH called the silica deposition vesicles (SDVs)<sup>54,55</sup>. The presence of various macromolecules within the frustule such as long chain polyamines (LCPA) and silaffines has led to the assumption that they are involved in the biosilification process of the frustule within the SDVs<sup>37,56-58</sup>. Nonetheless, the intracellular processes of transport of silicic acid that finally leads to deposition of silica within the SDVs are not fully understood<sup>59-61</sup>. Figure 1.4b shows the cell cycle in a diatom cell, where it begins at the frustule's maximum number of girdle bands. After cytokinesis, new silica is constructed within individual SDV for each daughter cell followed by additional silica deposition which accompanies the expansion of the SDV. Eventually, after valve formation within the cell, the newly formed silica structures are transported to the surface of each protoplast by SDV exocytosis followed by separation of the daughter cells. The girdle band formation and addition to the cell wall are species-specific. In some diatom species, the girdle bands are formed after valve formation before the daughter cell separation, and in others, girdle bands are added to the cell wall after the sibling cells' separation<sup>62,63</sup>. Even though it has been postulated that the process of frustule formation requires only 2 % of the total energy budget of the cell, the formation of these 3D intricate structures with high reproducibility suggests a genetically encoded procedure for possible practical functions<sup>64,65</sup>.

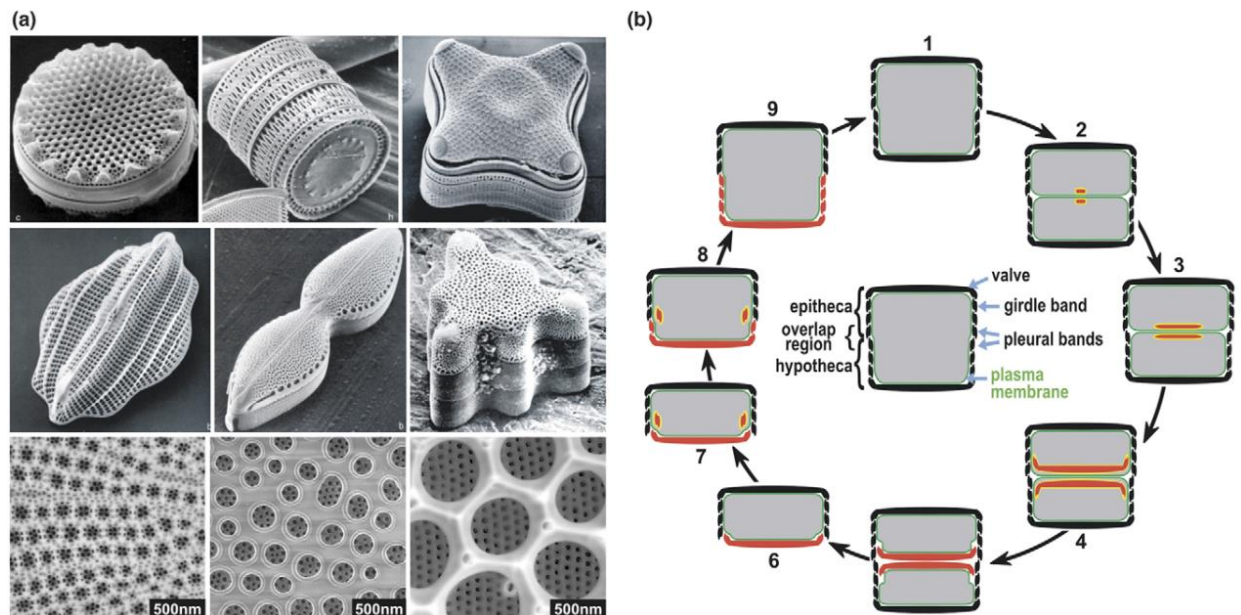


**Figure 1.4.** (a) SEM images of different diatom frustules (top and middle rows images represent overviews of intact diatom frustules of different species and images in bottom row show nanostructures of diatom frustules). (b) Schematic illustration of cell division and frustule formation within the diatom cell is shown. Adapted with permission from ref <sup>62</sup>.

### 1.1.3 Frustule functions and properties

Previously researchers have recognized several functions of diatom frustules. For instance, it has been hypothesized that the valves and girdle bands are involved in light manipulation and harvesting in diatoms, consequently contributing to the photosynthetic activities of the cell<sup>65,66</sup>. It is suggested that due to the different shapes, structures, and patterns of the frustules, each diatom species has unique optical properties<sup>67</sup>. Furthermore, filtering and controlling the flow of nutrients while preventing bacteria and viruses from penetrating into the cell are achieved by the nanoporous structures within the frustule<sup>68</sup>. In addition, the specific shape and morphology of frustules lead to decreasing the sinking speed of diatoms, providing a longer time for diatoms to stay near the water surface, resulting in a longer exposure to sunlight<sup>64</sup>. More importantly, due to its exceptional mechanical properties, frustules act as armor and protection against predators<sup>69</sup>. Zooming in on frustule thickness alone, there already seem to be contradicting requirements: while a thicker frustule can lead to superior protection, it can also cause the diatoms to sink faster as well as hinder the flow of nutrients between the surrounding environment and the diatom cells. It has been shown that increasing the silica contents of the frustule leads to a decrease in copepod grazing<sup>70</sup>. Thus, an optimized balance is critical between frustule morphology and composition in correlation with various environmental conditions to fulfill the aforementioned functions properly. In this balance, it is still not known to what extent the particular morphology of the frustules and their flexibility upon environmental variations are due to requirements for mechanical protection or other mentioned biological duties.

### 1.1.4 Flexibility of the frustule morphology and composition in correlation with environmental factors

Previous investigations have revealed that morphological parameters of diatom frustules vary in correlation with their growth medium conditions, likely due to the alteration in the intracellular silicification process<sup>65</sup>. For instance, increasing the salinity level in the growth medium results in pore size enlargement<sup>71</sup>. Also, temperature, light intensity/wavelength, and pH of the medium significantly alter the size, shape, and morphology of several diatom frustules<sup>72-74</sup>. Likewise, the presence of non-essential metal ions in the growth medium affects the frustule morphology and composition (Figure 1.5). This approach has been used for the modification of diatom frustules for technological applications<sup>75-77</sup>. For example, the morphology of ribs and costa of diatom *Nitzschia palea* is altered owing to the presence of cadmium (Cd) ions<sup>78</sup>. In addition, the co-feeding of diatom *Thalassiosira weissflogii* with titanium (Ti) precursors alongside Si induces photocatalytic activities in its frustule<sup>79</sup>. Likewise, germanium (Ge) incorporation into the frustule of *Craspedostauros sp.* (previously known as *Pinnularia sp.*) results in photoluminescence and electroluminescence properties<sup>80</sup>.

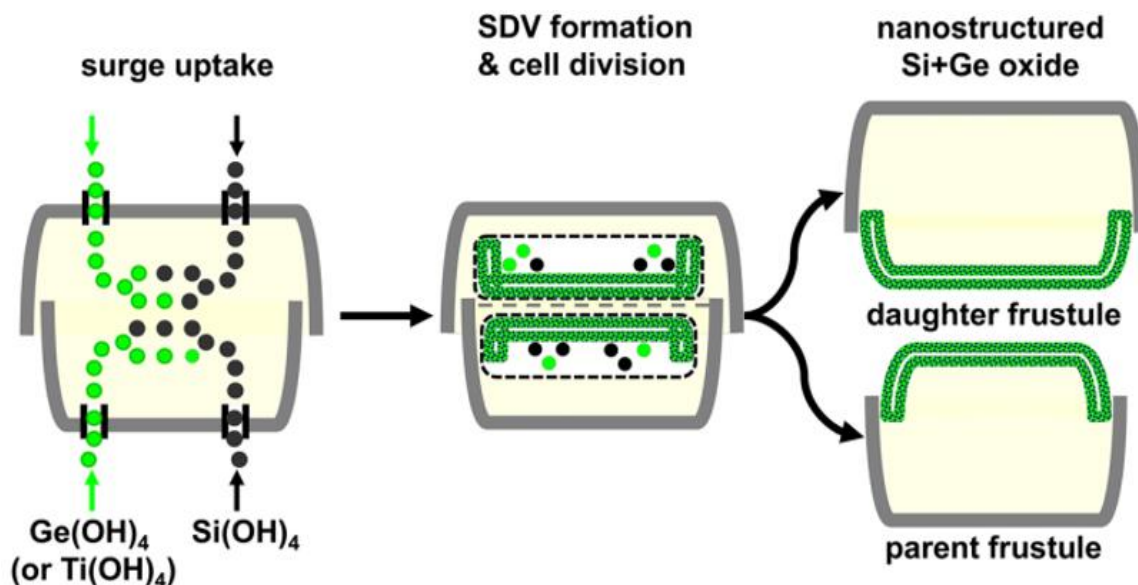


**Figure 1.5.** Schematic illustration of metal incorporation into diatom frustule during its formation within the SDV of a living diatom cell. Adapted with permission from ref<sup>75</sup>.

Besides the aforementioned metal ions, aluminum ( $\text{Al}^{3+}$ ) is another non-essential metal ion known to be taken up by diatom species inducing new properties in the frustules<sup>81,82</sup>. The internalization of  $\text{Al}^{3+}$  into several diatom cells has been confirmed in which  $\text{Al}^{3+}$  is distributed within the cell at different subcellular parts such as granules, debris, organelles, and proteins<sup>83,84</sup>. Also, extensive research has shown that  $\text{Al}^{3+}$  incorporation into the frustules of diatom species has noticeably enhanced hydrolysis/dissolution resistance<sup>85,86</sup>. Thus, it has been proposed that upon elimination of the organic casting around the frustule, incorporation of  $\text{Al}^{3+}$  is the key factor in hindering hydrolysis of the frustule. As a result of replacing one out of every 70 Si atoms with  $\text{Al}^{3+}$  in the diatom frustule, its solubility decreased by 25 %<sup>87,88</sup>. Additionally,  $\text{Al}^{3+}$  incorporation has resulted in enhanced acidity in the frustule of *Thalassiosira pseudonana*<sup>82</sup>. However, to the best of our knowledge, there has been no investigation on  $\text{Al}^{3+}$  incorporation and its impact on the morphological, chemical, and consequently the mechanical properties of diatom frustules. Accordingly, in this thesis it is investigated how, and to what extent, the presence of a certain concentration of  $\text{Al}^{3+}$  in the growth medium can modify the aforementioned properties of the frustule. The obtained insights here, can lead to improving and tuning the properties of industrially applied biogenic silica.

Alternatively, concepts known only in material science and technology of silica-based applications, can be discovered in biogenic silica of diatoms accordingly. For instance, it has been shown that the addition of aluminum compounds into silicate glasses significantly improves their chemical stability and mechanical properties<sup>89,90</sup>. These properties are tuned by the amount of  $\text{Al}^{3+}$  in the silicate network and its coordination environment. It has been found that the presence of  $\text{Al}^{3+}$  in its four coordinated state plays a strong role in enhancing the formation of  $\text{Q}^4$ , meanwhile hindering the  $\text{Q}^3$  formation in silicate glasses<sup>89</sup>. (Note: in  $^{29}\text{Si}$  NMR spectroscopy, Si atom and the four

oxygen atoms around it, are presented as  $Q^0$ ,  $Q^1$ ,  $Q^2$ ,  $Q^3$ ,  $Q^4$  where the numbers 0–4 indicate the number of ‘Si’ units attached by oxygens to another silicon atom) (Figure 1.6)<sup>38</sup>.

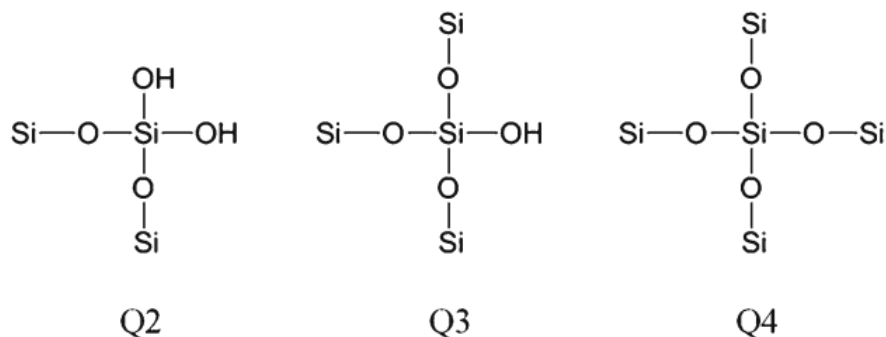


**Figure 1.6.** Scheme of silicon environments in  $Q^2$ ,  $Q^3$ , and  $Q^4$  where  $n$  represents the number of Si–O groups bonded to the central Si atom. Adapted with permission from ref<sup>91</sup>.

Another example of the role of  $\text{Al}^{3+}$  on the physical and chemical properties of silica-based materials is in silica coatings. These coatings are broadly used in industrial applications such as corrosion protection and anti-reflection layers<sup>92–94</sup>. The role of traces of three-valent metal ions like  $\text{Al}^{3+}$  which leave coordination gaps in the otherwise four valent silica network is known to be critical to many key properties in these applications such as mechanical and chemical stability<sup>95</sup>. However, the exact mechanisms by which these characteristics are affected remain equally elusive to their biological fate in diatom growth. Therefore, by investigating the properties of  $\text{Al}^{3+}$  incorporated biogenic silica within the diatom frustule, valuable insights in the field of alumino-silica formation may be obtained which ultimately can be applied/adapted for enhancing the properties of synthetic silica-based coatings.

### 1.1.5 Mechanical properties of the frustule

In recent years, the mechanical properties of diatom species have been investigated by experimental and numerical approaches. For instance, mechanical properties of diatoms *Coscinodiscus sp* and *Navicula pilliculosa* have been measured by AFM at different regions of their frustule<sup>96,97</sup>. It has been suggested that the Young's modulus and hardness vary even within the frustules from one location to another. Also conventional nanoindentation has been performed on large diatoms such as *Coscinodiscus concinnus* and *Synedra sp* to pinpoint the intrinsic mechanical properties such as Young's modulus and hardness of their frustules<sup>98,99</sup>. Furthermore, in situ mechanical testing, either on the whole diatom frustule or its fragments, has been performed inside a scanning electron microscope<sup>100,101</sup>. It is now well established from these studies that there is a direct correlation between the morphological properties and ultimate mechanical performance of the frustules. However, to date, there is only one study where the modification of the frustule morphology due to altered environmental conditions (in this case lack of iron in the growth medium) and its relationships with mechanical performance has been systemically studied<sup>102</sup>. Consequently, further research should be undertaken to investigate the relationship between various environmental factors such as salinity and presence of non-essential metal ions in the growth medium with morphological, chemical, and mechanical properties of diatom frustules.



Furthermore, the effect of chemical treatments on mechanical performance of frustule has been studied, indicating a direct effect of chemical composition on the mechanical properties of the frustules<sup>103</sup>. Currently, there is no universal treatment for sample preparation of diatom frustule, and in most of the reported methods, harsh chemicals have been employed which can alter the properties of frustules<sup>104</sup>. This indicates a need to utilize mild chemicals and conditions during cleaning diatom frustules in order not to compromise their chemical and structural integrity during the sample preparation for mechanical testings.

In addition to the experimental studies, several numerical investigations have been conducted by using finite element method (FEM) on different frustule models to obtain their mechanical properties. For almost all of these numerical studies, SEM images of the frustules have been employed as initial data to build the 3D models for the simulations<sup>105-107</sup>. Despite many advantages of these investigations which shed some new lights on the correlation between morphological and mechanical properties of the frustule, due to the simplified models and unknown dimensions of underlying micro and nanostructures of the frustules, revealing the intrinsic mechanical properties of the frustule and distribution of the stress over their structure is a challenging task to achieve. Therefore, a versatile procedure to obtain realistic three-dimensional (3D) models of the complicated geometry and morphology of different frustules is needed which is also investigated in this thesis.

### 1.2 Characterization techniques to unveil the complex morphology of diatoms

Light microscopy (LM) was the predominant technique for more than a century for studying diatoms, leading to their identification and classification based on their shapes and symmetries<sup>46</sup>. However, due to the limited resolution of LM, it could not reveal submicron details in the structure of diatom frustules. In the last few decades, several higher resolution imaging techniques have been extensively used to identify different diatom species and various properties of their internal and external structures. An example of the necessity of using high-resolution imaging techniques to identify the exact genus of diatom species was appreciated in chapter 2 of this thesis. A pennate marine diatom had been identified and used in various publications under the name of *Pinnularia sp.* for many years<sup>108-110</sup>. After the publication of our first paper containing several high-resolution SEM images of different micro- and nanostructures of frustule of this species, we were alerted by many taxonomists about the misidentification of this diatom species. Following the consultation with the commercial supplier of this species (UTEX Culture Collection of Algae) and diatom experts, the accurate name was revealed to be *Craspedostauros sp.*

In the following sections, several imaging techniques for diatom characterization are briefly described.

#### 1.2.1 Atomic Force Microscopy (AFM)

In a typical scanning probe microscope (SPM), an image is generated by mechanically moving a probe in a scanning manner, point by point and line by line, over the surface of an object and recording the interaction between the probe and surface. Equivalently, AFM provides an image of

the specimen's surface based on the force interaction between a sharp tip ( $<10$  nm) at the end of a cantilever and the sample at very short distances (0.2-10 nm) between them. An AFM instrument is comprised of several important items such as a sharp tip, a sensing system to detect the cantilever's deflection, a feedback system to control and monitor the deflection, a mechanical scanning system to scan the surface, and a display system to translate the obtained data into an image<sup>111</sup>. AFM analysis of biological samples, including diatoms, have several advantages such as relatively easy sample preparation, providing a three-dimensional surface topology of the specimen, high-resolution imaging of the nanostructured features, being able to image and characterize living diatom cells in their growth medium condition in real-time, and determining the mechanical properties of the diatom frustules<sup>112</sup>. To date, AFM investigations have been widely conducted either on live cells or treated-diatom frustules. For instance, AFM analysis on diatom biosilica nanostructure, have been carried out on different frustules of pennate diatoms where it was conclusively confirmed that this biosilica was composed of a conglomerate of different colloidal silica spherical particles with coarse roughness<sup>113</sup>. Also, living cells of diatom species have been investigated in their natural conditions, providing a flexible platform for monitoring living diatom species<sup>114,115</sup>. Furthermore, extracellular polysaccharides fibrils excreted by diatom species into their surrounding medium or attached to their cell walls have been investigated by AFM analysis<sup>116,117</sup>. However, alongside the aforementioned beneficial aspects of AFM, several limitations hamper its universal applicability. For instance, since the XY scan range of AFM is approximately 100  $\mu\text{m}$  and in Z axis is about 10  $\mu\text{m}$ , imaging and analysis of large diatom frustules is not possible<sup>112</sup>. Besides, similar to particulate micro and nano-objects, the positioning and landing of the AFM cantilever for small diatoms is challenging.

### 1.2.2 Transmission Electron Microscopy (TEM)

The basic principles of TEM are comparable to LM whereas an electron beam is used instead of light to transmit through the specimen and generate a magnified image. Due to the shorter wavelength of electrons compared to light (100,000 times shorter), TEM provides significantly higher resolution images, containing valuable information about morphology, composition, and crystallization of a given sample. Typically, in a TEM instrument, a beam of electrons is generated by the electron gun. The electron gun also accelerates the electrons towards the sample giving them adequate energy to pass through the specimen by accelerating voltages from 80 to 300 kV (the accelerating voltage can be adjusted based on the sample). The accelerated electrons are focused into a beam of controlled diameter and convergence angle by condenser lenses prior to their interaction with the specimen. After traveling through the sample, transmitted electrons are passing through the objective lens to either generate a focused diffraction pattern or a magnified first image. Then, the obtained diffraction patterns or images are further magnified by projector lenses prior to recording<sup>118</sup>. Based on this operation procedure, TEM is able to reveal fine details of any specimen including external and internal structures of diatom frustule at (sub-) nanometer resolution. Also, obtaining 3D structures of a complex geometry such as diatom frustule for FEM simulation, can be achieved by electron tomography (ET). In the ET technique, a beam of electrons is

transmitted through the specimen at different incremental degrees around the center of the sample. Following acquisition of multiple images at different angles, a 3D image of the samples is obtained<sup>119</sup>. To date there has been no detailed investigation on ET and diatom frustule. To the best of our knowledge, most of the previous TEM analysis on diatom species have been mainly conducted on the frustules morphological characteristics<sup>120-122</sup>. Also, TEM has been used to identify the features of the biological internal ultra-structures such as the nucleus, microtubules, chloroplasts, the Golgi apparatus, and cytoplasmic vesicles<sup>123,124</sup>. Furthermore, different stages leading to frustule formation and morphogenesis within the SDVs have been studied by TEM as well<sup>125,126</sup>. However, TEM has several limitations for the characterization of both internal and external structures of diatoms too: it requires an electron transparent sample, has a small field of view, is difficult to operate, and is known for possible damage to beam sensitive specimen.

### 1.2.3 Scanning Electron Microscopy (SEM)

SEM is a well-established technique and one of the most popular imaging tools used in a wide variety of scientific and technological disciplines such as biology, chemistry, material science, physics, electronics, etc. SEM combines numerous advantages over TEM such as having a large field of view and depth of focus, relatively ease of operation, a larger sample chamber, being compatible with various environments, and easily adaptable for different samples with size range from millimeter to a few nanometers<sup>127</sup>. The essential principle of SEM is to scan the surface of the specimen with a focused beam of (high-energy) electrons in order to generate an image. The interaction between the incident electron beam and the sample results in emissions of secondary electrons (SE), back scattering of incident electrons (BSE), energy dispersive x-ray spectroscopy and (EDS/EDX) that all combined contain valuable information about the size, composition, crystallography, and shape of a given sample<sup>128</sup>. As shown in Figure 1.7a conventional SEM comprises distinct items such as an electron source, apertures, various lenses, coils, detectors, etc. which each play an important role in obtaining an image with a resolution of a few nanometers. Commonly inside the SEM chamber and column, high vacuum conditions are required to prevent the scattering of incident electrons by gas molecules, to protect the electron gun from degradation, and more importantly to enable acquisition of high-resolution images of the specimen<sup>129</sup>. Thus, SEM has been employed as one of the key tools to character micro and nanostructures of diatom frustules. For instance, taxonomy and identification of many diatom species have been performed by SEM images of their external surfaces<sup>130,131</sup>. Also, SEM-EDS elemental analysis has revealed the chemical composing of different diatom frustules<sup>132,133</sup>. However, SEM has several drawbacks. Specifically, due to a lack of control over the orientation of deposited frustules, the limitation in observation of cross-sections of the sample, as well as the internal structures of diatom, applicability of this technique to characterize many aspects of the diatom frustule and its internal nanostructures is restricted. Additionally, similar to other biological samples, understanding the biogenic silica formation in diatoms necessitates elucidation of the underlying cellular and molecular biology processes within the cell, which is not directly possible by SEM imaging of the surface of the

frustule. However, fortunately, a conventional SEM instruments can easily be upgraded by integration with numerous accessories, particularly a combination of Focused Ion Beam (FIB) and micromanipulators<sup>134-137</sup>, which alleviates most of the aforementioned restrictions to characterize various properties of diatom frustules and also the internal structures of cells.

### 1.2.4 Focused Ion Beam Scanning Electron Microscopy (FIB-SEM)

The integration of a FIB into a conventional SEM (also known as a dual-beam system) not only provides an unprecedented opportunity for in situ micro/nanofabrication and modification of any small objects with high spatial accuracy within the SEM but also enables to obtain 3D information from the internal structure of the specimen (Figure 1.7b)<sup>138,139</sup>. Due to its capability to conduct localized milling and deposition of various conductor and insulator materials, FIB-SEM has been used in the semiconductor industry, biology, materials science, and other scientific disciplines for several decades. The localized FIB deposition is based on chemical vapor deposition (CVD) by using a direct writing technique. Instead, FIB etching/ milling is based on scattering of the atoms of material of interest by bombarding them with accelerated heavy ions. The ion source in FIB is often a material with low vapor pressure and low melting point. Gallium (Ga) with its low melting point ( $< 30\text{ }^{\circ}\text{C}$ ) has been one of the promising ion sources for FIB milling over the last few decades. Typically, the Ga ion source is made of a reservoir which is connected to a very sharp tungsten needle. By heating the source, Ga liquid is formed which flows toward the tip of the tungsten needle. Then, via a strong electric field, a point source of less than 5 nm in diameter is formed and Ga ions are extracted from the tip. The obtained ions are accelerated in an electric field of up to 30 kV towards the sample. Following the collision of  $\text{Ga}^+$  ions with the target materials, the solid atoms of the samples are sputtered out, enabling FIB milling for a variety of experiments such as fabrication of micro and nanoscale objects, lamella preparation for TEM investigations, serial slice and view, and also chemical analysis of the specimen<sup>140-142</sup>. This technique has also been employed to investigate the properties of diatom frustules and internal organelles of several diatom species in great details. Specifically, the initial silica formation within the cell, the presence or confinement for silica formation, measuring the concentration of the silica pool within different regions of the cell, and the connection between different organelles of a cell have all been observed by FIB slice and view process<sup>143,144</sup>.

### 1.2.5 Micromanipulation

Besides the integration of FIB with SEM which provides real-time imaging and concurrently fabrication of miniaturized objects, micro/nanomanipulation systems can be integrated inside the SEM chamber as well (Figure 1.7c). This combination realizes a platform for simultaneous imaging, fabrication, and direct manipulation of the micro and nanoscale specimen<sup>145</sup>. An analogy to this platform would be giving an SEM a pair of hands by mounting the micromanipulators within its chamber, so as to facilitate a variety of experiments and characterization procedures. Micromanipulation, which is also known as a complementary technique for top-down and bottom-up approaches, enables flexible movement in three axes and accurate positioning of submicron objects for nano device and nanostructures manufacturing<sup>134</sup>. However, one of the most important aspects

of integration of a micromanipulator within an SEM instrument is the capability of performing a variety of mechanical and electrical characterizations of micro and nanoscale samples. This combination enables real-time monitoring of the mechanical behavior of any miniaturized specimen with high force-displacement resolution<sup>146</sup>. For instance, in situ mechanical testing such as bending, indentation, and compression tests via micromanipulators inside a SEM has been one of the attractive approaches for observing the deformation behaviors of 1D & 2D materials, as well as more complex micro, and nano structures<sup>147,148</sup>. Nonetheless, this technique has not been well-explored for characterizing the mechanical properties of the diatom frustule, neither for in situ fabrication, manipulation and mechanical testing of synthetic silica based materials. In this thesis, FIB-SEM and micromanipulators have extensively been employed to develop new flexible workflows for the manipulation and characterization of the biogenic and synthetic silicas.

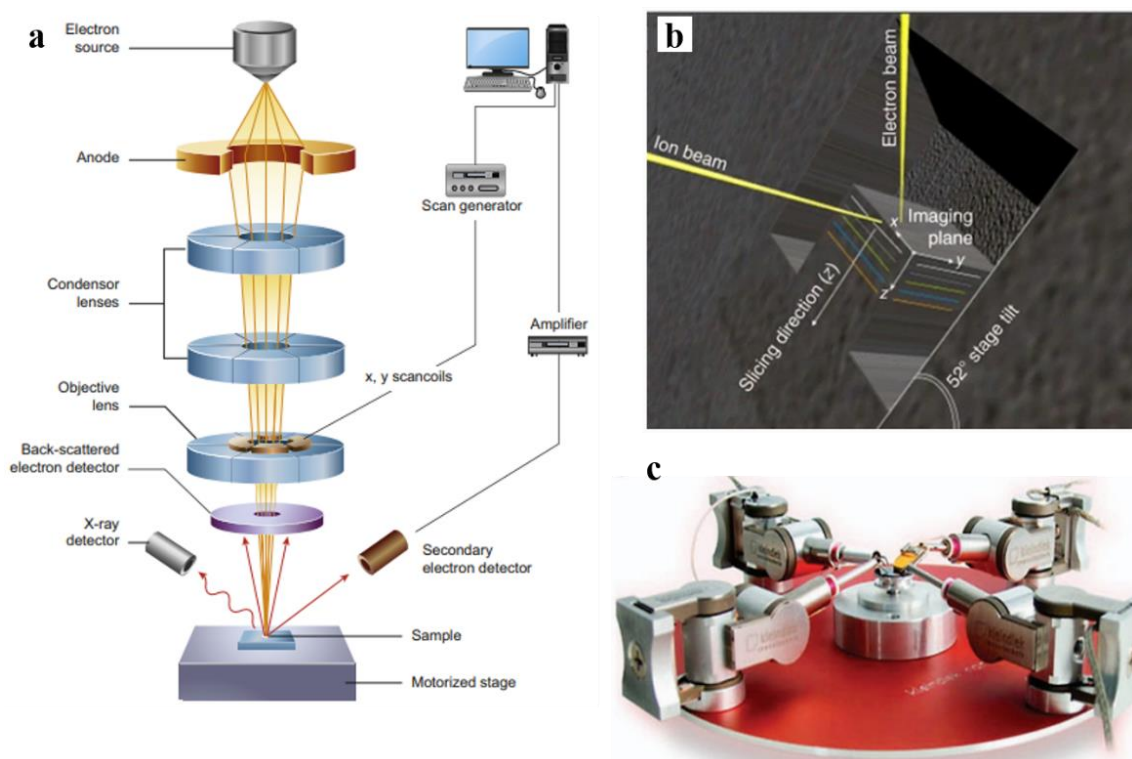


**Figure 1.7.** (a) Schematic illustration of various components of SEM microscope. Adapted with permission from ref<sup>149</sup>; (b) scheme of slice and view process by FIB-SEM. Adapted with permission from ref<sup>150</sup>; (c) a micrographs of four micromanipulators mounted on an SEM stage. Adapted with permission from ref<sup>134</sup>.

### 1.3 Aim and outline of the thesis

Revealing the properties of diatom frustules in correlation with their growth medium and conditions is a challenging task to accomplish. However, concurrently it is intriguing to learn which novel approaches can lead to the development of new insights and a new understanding of the properties of biogenic silica that ultimately can be adapted and used for a wide range of synthetic materials and applications. Here, there are four primary aims that we attempt to achieve: First, to investigate the effect of  $\text{Al}^{3+}$  on the morphological and chemical properties of the diatom frustule.

Second, to develop novel approaches for in situ mechanical testing of diatom frustules without altering their chemical/morphological characteristics, while using realistic models obtained by ET for FEM simulations to determine their intrinsic mechanical properties. Third, to unravel the effect of  $\text{Al}^{3+}$  as well as salinity levels in the growth medium on the mechanical properties of diatom frustules by exploiting the developed workflows. Fourth, to develop a versatile approach to determine the mechanical properties of silica thin film as a model example of synthetic silica. Ultimately this approach can be used to investigate the effect of  $\text{Al}^{3+}$  on the mechanical properties of these man-made materials as well. Accordingly, this thesis attempts to achieve these objectives in five experimental chapters which are briefly described in the paragraphs below.

**Chapter 2** explores the ways in which diatom *Craspedostauros sp.* builds its biogenic silica structures while  $\text{Al}^{3+}$  is present in its growth medium. In this chapter, the frustule formation in this diatom species including changes to its overall morphology, silica thickness, and composition, in the presence of  $\text{Al}^{3+}$  is investigated. Various analytical techniques such as  $^{27}\text{Al}$  solid-state NMR, atomic absorption spectroscopy (AAS), TEM, SEM, FIB and EDS are employed to demonstrate the incorporation of  $\text{Al}^{3+}$  into the frustule and subsequently its impact on morphology, thickness, and internal structure.

**Chapter 3** describes the design and implementation of a flexible workflow for measuring the mechanical properties of diatom frustule constituents individually. In this chapter, a versatile approach combining FIB-SEM and micromanipulators is presented to isolate, transfer, and determine the mechanical properties of frustule constituents of one of the smallest diatom species, the circumcentric diatom *Thalassiosira pseudonana*. More specifically, girdle bands and valves are separated by FIB milling and manipulation. Then, in situ mechanical studies on isolated girdle bands and valves are conducted to determine their mechanical properties. Furthermore, the effect of salinity level in the growth medium on mechanical properties of girdle bands and valves are studied.

In **Chapter 4**, in order to determine the effect of  $\text{Al}^{3+}$  on mechanical properties of frustule of diatom *Thalassiosira pseudonana*, the established technique in chapter 3 is employed. Moreover, via ET the complex geometry of the valve and subsequently its 3D model is obtained which is used in FEM simulations to determine the Young's modulus. Furthermore, the  $\text{Al}^{3+}$  distribution and its coordination environment in the frustule, alongside its impact on silica condensation, and morphological variations of the frustule are investigated by a combination of spectroscopic and electron microscopic techniques.

In **Chapter 5**, as another proof of concept for the developed workflow, the mechanical properties of a different diatom species, the pennate *Craspedostauros sp.*, are studied on a factor of 5 larger length scale. In this chapter, we present a streamlined approach in which by a combination of in situ mechanical testing inside SEM with 3D model obtained from STEM-ET alongside FEM simulation, the Young's modulus of the frustule of the diatom *Craspedostauros sp.* at the micrometer

scale is derived. In addition, in situ manipulation of the valves is conducted, enabling to reposition them in the best possible direction for in situ mechanical deformation testing.

**Chapter 6** is set out to explore the applicability of the combination of FIB-SEM and micromanipulation to determine the mechanical properties of synthetic silica (thin films). Here, by combination of FIB-SEM and micromanipulators we fabricate free-standing silica thin beam with the desired dimensions. In situ bending tests on as-fabricated silica beams with different widths leads to obtaining their Young's modulus.

In **Chapter 7** a summary, directions for future research, and some concluding remarks are presented.

## 1.4 References

- 1 Weiner, S. & Addadi, L. Design strategies in mineralized biological materials. *Journal of Materials Chemistry* **7**, 689-702 (1997).
- 2 Luz, G. M. & Mano, J. F. Mineralized structures in nature: examples and inspirations for the design of new composite materials and biomaterials. *Composites Science and Technology* **70**, 1777-1788 (2010).
- 3 Ji, B. & Gao, H. Mechanical properties of nanostructure of biological materials. *Journal of the Mechanics and Physics of Solids* **52**, 1963-1990 (2004).
- 4 Arakaki, A., Shimizu, K., Oda, M., Sakamoto, T., Nishimura, T. & Kato, T. Biomineralization-inspired synthesis of functional organic/inorganic hybrid materials: organic molecular control of self-organization of hybrids. *Organic & Biomolecular Chemistry* **13**, 974-989 (2015).
- 5 Libonati, F. & Buehler, M. J. Advanced structural materials by bioinspiration. *Advanced Engineering Materials* **19**, 1600787 (2017).
- 6 Ghazlan, A., Ngo, T., Tan, P., Xie, Y. M., Tran, P. & Donough, M. Inspiration from Nature's body armours—a review of biological and bioinspired composites. *Composites Part B: Engineering* **205**, 108513 (2021).
- 7 Espinosa, H. D., Rim, J. E., Barthelat, F. & Buehler, M. J. Merger of structure and material in nacre and bone—Perspectives on de novo biomimetic materials. *Progress in Materials Science* **54**, 1059-1100 (2009).
- 8 Meyers, M. A., Chen, P.-Y., Lin, A. Y.-M. & Seki, Y. Biological materials: structure and mechanical properties. *Progress in Materials Science* **53**, 1-206 (2008).
- 9 Zhou, H., Fan, T. & Zhang, D. Biotemplated materials for sustainable energy and environment: current status and challenges. *ChemSusChem* **4**, 1344-1387 (2011).
- 10 Addadi, L. & Weiner, S. Control and design principles in biological mineralization. *Angewandte Chemie International Edition in English* **31**, 153-169 (1992).
- 11 Chen, P.-Y., Lin, A., Lin, Y.-S., Seki, Y., Stokes, A., Peyras, J., Olevsky, E., Meyers, M. A. & McKittrick, J. Structure and mechanical properties of selected biological materials. *Journal of the mechanical behavior of biomedical materials* **1**, 208-226 (2008).
- 12 Bruet, B. J. F., Qi, H. J., Boyce, M. C., Panas, R., Tai, K., Frick, L. & Ortiz, C. Nanoscale Morphology and Indentation of Individual Nacre Tablets from the Gastropod Mollusc *Trochus Niloticus*. *Journal of Materials Research* **20**, 2400-2419 (2005).
- 13 Barthelat, F., Li, C.-M., Comi, C. & Espinosa, H. D. Mechanical properties of nacre constituents and their impact on mechanical performance. *Journal of Materials Research* **21**, 1977-1986 (2006).
- 14 Kim, Y.-Y., Carloni, J. D., Demarchi, B., Sparks, D., Reid, D. G., Kunitake, M. E., Tang, C. C., Duer, M. J., Freeman, C. L. & Pokroy, B. Tuning hardness in calcite by incorporation of amino acids. *Nature Materials* **15**, 903-910 (2016).

- 15 Perry, C. C. & Keeling-Tucker, T. Biosilicification: the role of the organic matrix in structure control. *JBIC Journal of Biological Inorganic Chemistry* **5**, 537-550 (2000).
- 16 Flörke, O. W., Graetsch, H. A., Brunk, F., Benda, L., Paschen, S., Bergna, H. E., Roberts, W. O., Welsh, W. A., Libanati, C. & Ettlinger, M. Silica. *Ullmann's Encyclopedia of Industrial Chemistry* (2000).
- 17 Gunter, M. E. Quartz—The Most Abundant Mineral Species in the Earth's Crust and a Human Carcinogen? *Journal of Geoscience Education* **47**, 341-349 (1999).
- 18 Vatalis, K. I., Charalambides, G. & Benetis, N. P. Market of high purity quartz innovative applications. *Procedia Economics and Finance* **24**, 734-742 (2015).
- 19 Beall, G. H. Industrial applications of silica. *Silica*, 469-506 (2018).
- 20 Esswein, E. J., Breitenstein, M., Snawder, J., Kiefer, M. & Sieber, W. K. Occupational exposures to respirable crystalline silica during hydraulic fracturing. *Journal of Occupational and Environmental Hygiene* **10**, 347-356 (2013).
- 21 Waddell, W. H. Silica, amorphous. *Kirk-Othmer Encyclopedia of Chemical Technology* (2000).
- 22 Vallet-Regí, M. & Balas, F. Silica materials for medical applications. *The Open Biomedical Engineering Journal* **2**, 1 (2008).
- 23 Barthel, H., Rösch, L. & Weis, J. Fumed silica-production, properties, and applications. *Organosilicon Chemistry Set: From Molecules to Materials*, 761-778 (2005).
- 24 Bernardos Bau, A. & Kourimska, L. Applications of mesoporous silica materials in food: a review. *Czech Journal of Food Sciences* **31**, 99-107 (2013).
- 25 ten Brinke, J. W. Silica reinforced tyre rubbers: mechanistic aspects of the role of coupling agents. (2002).
- 26 Laskowski, Ł., Laskowska, M., Vila, N., Schabikowski, M. & Walcarius, A. Mesoporous silica-based materials for electronics-oriented applications. *Molecules* **24**, 2395 (2019).
- 27 McLaughlin, J. K., Chow, W. H. & Levy, L. S. Amorphous silica: a review of health effects from inhalation exposure with particular reference to cancer. *Journal of Toxicology and Environmental Health, Part A Current Issues* **50**, 553-566 (1997).
- 28 Yang, X.-Y., Chen, L.-H., Li, Y., Rooke, J. C., Sanchez, C. & Su, B.-L. Hierarchically porous materials: synthesis strategies and structure design. *Chemical Society Reviews* **46**, 481-558 (2017).
- 29 Sumper, M. & Brunner, E. Learning from diatoms: nature's tools for the production of nanostructured silica. *Advanced Functional Materials* **16**, 17-26 (2006).
- 30 Vogel, N., Retsch, M., Fustin, C.-A., Del Campo, A. & Jonas, U. Advances in colloidal assembly: the design of structure and hierarchy in two and three dimensions. *Chemical Reviews* **115**, 6265-6311 (2015).
- 31 Fleming, G. R. & Ratner, M. A. Grand challenges in basic energy sciences. *Phys. Today* **61**, 28 (2008).
- 32 Zhang, Y. X. & Sun, X. W. in *Diatom Nanotechnology* 175-200 (2017).
- 33 Rea, I., Dardano, P., Ferrara, M. A. & de Stefano, L. in *Diatom Nanotechnology* 111-125 (2017).
- 34 Fanderlik, I. *Silica glass and its application*. (Elsevier, 2013).
- 35 Prabha, S., Durgalakshmi, D., Rajendran, S. & Lichtfouse, E. Plant-derived silica nanoparticles and composites for biosensors, bioimaging, drug delivery and supercapacitors: a review. *Environmental Chemistry Letters* **19**, 1667-1691 (2021).
- 36 Fernandes, F. M., Coradin, T. & Aimé, C. Self-assembly in biosilicification and biotemplated silica materials. *Nanomaterials* **4**, 792-812 (2014).
- 37 Sumper, M. & Kröger, N. Silica formation in diatoms: the function of long-chain polyamines and silaffins. *Journal of Materials Chemistry* **14**, 2059-2065 (2004).
- 38 Belton, D. J., Deschaume, O. & Perry, C. C. An overview of the fundamentals of the chemistry of silica with relevance to biosilicification and technological advances. *The FEBS journal* **279**, 1710-1720 (2012).



- 39 Rabovsky, J. Biogenic amorphous silica. *Scandinavian Journal of Work, Environment & Health*, 108-110 (1995).
- 40 Noll, F., Sumper, M. & Hampp, N. Nanostructure of diatom silica surfaces and of biomimetic analogues. *Nano Letters* **2**, 91-95 (2002).
- 41 Yang, W., Lopez, P. J. & Rosengarten, G. Diatoms: self assembled silica nanostructures, and templates for bio/chemical sensors and biomimetic membranes. *Analyst* **136**, 42-53 (2011).
- 42 Ragni, R., Cicco, S. R., Vona, D. & Farinola, G. M. Multiple routes to smart nanostructured materials from diatom microalgae: a chemical perspective. *Advanced Materials* **30**, 1704289 (2018).
- 43 Losic, D., Mitchell, J. G. & Voelcker, N. H. Diatomaceous lessons in nanotechnology and advanced materials. *Advanced Materials* **21**, 2947-2958 (2009).
- 44 Bose, R., Saha, R., Chattopadhyay, S. & Pal, R. Utilization of nanoporous biosilica of diatoms as a potential source material for fabrication of nanoelectronic device and their characterization. *Journal of Applied Phycology* **32**, 3041-3049 (2020).
- 45 Siver, P. A. in *Freshwater Algae of North America (Second Edition)* (eds John D. Wehr, Robert G. Sheath, & J. Patrick Kociolek) 607-651 (Academic Press, 2015).
- 46 Seckbach, J. & Kociolek, P. *The diatom world*. Vol. 19 (Springer Science & Business Media, 2011).
- 47 Tréguer, P., Bowler, C., Moriceau, B., Dutkiewicz, S., Gehlen, M., Aumont, O., Bittner, L., Dugdale, R., Finkel, Z. & Iudicone, D. Influence of diatom diversity on the ocean biological carbon pump. *Nature Geoscience* **11**, 27-37 (2018).
- 48 Wang, Y., Cai, J., Jiang, Y., Jiang, X. & Zhang, D. Preparation of biosilica structures from frustules of diatoms and their applications: current state and perspectives. *Applied Microbiology and Biotechnology* **97**, 453-460 (2013).
- 49 Round, F. E. C. R. M. M. D. G. *The Diatoms : biology & morphology of the genera*. (Cambridge University Press, 1990).
- 50 Hildebrand, M. Diatoms, biomineralization processes, and genomics. *Chemical Reviews* **108**, 4855-4874 (2008).
- 51 Zhang, D., Wang, Y., Cai, J., Pan, J., Jiang, X. & Jiang, Y. Bio-manufacturing technology based on diatom micro- and nanostructure. *Chinese Science Bulletin* **57**, 3836-3849 (2012).
- 52 Hildebrand, M. Silicic acid transport and its control during cell wall silicification in diatoms. *Biomineralization from biology to biotechnology and medical application*, 171-188 (2000).
- 53 Grachev, M., Sherbakova, T., Masyukova, Y. & Likhoshway, Y. A potential zinc-binding motif in silicic acid transport proteins of diatoms. *Diatom Research* **20**, 409-411 (2005).
- 54 Vrieling, E. G., Gieskes, W. & Beelen, T. P. Silicon deposition in diatoms: control by the pH inside the silicon deposition vesicle. *Journal of Phycology* **35**, 548-559 (1999).
- 55 Heintze, C., Formanek, P., Pohl, D., Hauptstein, J., Rellinghaus, B. & Kröger, N. An intimate view into the silica deposition vesicles of diatoms. *BMC Materials* **2**, 1-15 (2020).
- 56 Kröger, N., Lorenz, S., Brunner, E. & Sumper, M. Self-assembly of highly phosphorylated silaffins and their function in biosilica morphogenesis. *Science* **298**, 584-586 (2002).
- 57 Kröger, N., Deutzmann, R., Bergsdorf, C. & Sumper, M. Species-specific polyamines from diatoms control silica morphology. *Proceedings of the National Academy of Sciences* **97**, 14133-14138 (2000).
- 58 Poulsen, N., Sumper, M. & Kröger, N. Biosilica formation in diatoms: characterization of native silaffin-2 and its role in silica morphogenesis. *Proceedings of the National Academy of Sciences* **100**, 12075-12080 (2003).
- 59 Mayzel, B., Aram, L., Varsano, N., Wolf, S. G. & Gal, A. Structural evidence for extracellular silica formation by diatoms. *Nature communications* **12**, 1-8 (2021).
- 60 Brunner, E., Gröger, C., Lutz, K., Richthammer, P., Spinde, K. & Sumper, M. Analytical studies of silica biomineralization: towards an understanding of silica processing by diatoms. *Applied Microbiology and Biotechnology* **84**, 607-616 (2009).

- 61 Scheffel, A., Poulsen, N., Shian, S. & Kröger, N. Nanopatterned protein microrings from a diatom that direct silica morphogenesis. *Proceedings of the National Academy of Sciences* **108**, 3175-3180 (2011).
- 62 Kröger, N. Prescribing diatom morphology: toward genetic engineering of biological nanomaterials. *Current Opinion in Chemical Biology* **11**, 662-669 (2007).
- 63 Kröger, N. & Poulsen, N. Diatoms—from cell wall biogenesis to nanotechnology. *Annual Review of Genetics* **42**, 83-107 (2008).
- 64 Raven, J. & Waite, A. The evolution of silicification in diatoms: inescapable sinking and sinking as escape? *New phytologist* **162**, 45-61 (2004).
- 65 Ellegaard, M., Lenau, T., Lundholm, N., Maibohm, C., Friis, S. M. M., Rottwitt, K. & Su, Y. The fascinating diatom frustule—can it play a role for attenuation of UV radiation? *Journal of Applied Phycology* **28**, 3295-3306 (2016).
- 66 Goessling, J. W., Su, Y., Maibohm, C., Ellegaard, M. & Kühl, M. Differences in the optical properties of valve and girdle band in a centric diatom. *Journal of the Royal Society Interface Focus* **9**, 20180031 (2019).
- 67 Mishler, J., Blake, P., Alverson, A. J., Roper, D. K. & Herzog, J. B. in *Nanobiosystems: Processing, Characterization, and Applications VII*. 91710P (International Society for Optics and Photonics).
- 68 Hale, M. S. & Mitchell, J. G. Functional morphology of diatom frustule microstructures: hydrodynamic control of Brownian particle diffusion and advection. *Aquatic Microbial Ecology* **24**, 287-295 (2001).
- 69 Hamm, C. E., Merkel, R., Springer, O., Jurkojc, P., Maier, C., Pechtel, K. & Smetacek, V. Architecture and material properties of diatom shells provide effective mechanical protection. *Nature* **421**, 841-843 (2003).
- 70 Pančić, M., Torres, R. R., Almeda, R. & Kiørboe, T. Silicified cell walls as a defensive trait in diatoms. *Proceedings of the Royal Society B* **286**, 20190184 (2019).
- 71 Vrieling, E. G., Sun, Q., Tian, M., Kooyman, P. J., Gieskes, W. W., van Santen, R. A. & Sommerdijk, N. A. Salinity-dependent diatom biosilicification implies an important role of external ionic strength. *Proceedings of the National Academy of Sciences* **104**, 10441-10446 (2007).
- 72 Jung, S. W., Youn, S. J., Shin, H. H., Yun, S. M., Ki, J.-S. & Lee, J. H. Effect of temperature on changes in size and morphology of the marine diatom, *Ditylum brightwellii* (West) Grunow (Bacillariophyceae). *Estuarine, Coastal and Shelf Science* **135**, 128-136 (2013).
- 73 Hervé, V., Derr, J., Douady, S., Quinet, M., Moisan, L. & Lopez, P. J. Multiparametric analyses reveal the pH-dependence of silicon biomineralization in diatoms. *PloS one* **7**, e46722 (2012).
- 74 Hoogstraten, A., Timmermans, K. R. & de Baar, H. J. Morphological and Physiological Effect in *Proscia Alata* (BACILLARIOPHYCEAE) Grown Under Different Light and CO<sub>2</sub> Conditions of the Modern Southern Ocean 1 *Journal of Phycology* **48**, 559-568 (2012).
- 75 Brzozowska, W., Sprynskyy, M., Wojtczak, I., Dąbek, P., Witkowski, A. & Buszewski, B. “Outsourcing” diatoms in fabrication of metal-doped 3D biosilica. *Materials* **13**, 2576 (2020).
- 76 Rogato, A. & De Tommasi, E. Physical, Chemical, and Genetic Techniques for Diatom Frustule Modification: Applications in Nanotechnology. *Applied Sciences* **10**, 8738 (2020).
- 77 Rorrer, G. in *Diatom Nanotechnology* 79-110 (Royal Society of Chemistry, 2017).
- 78 Heredia, A., Figueira, E., Rodrigues, C. T., Rodríguez-Galván, A., Basiuk, V. A., Vrieling, E. G. & Almeida, S. F. Cd<sup>2+</sup> affects the growth, hierarchical structure and peptide composition of the biosilica of the freshwater diatom *Nitzschia palea* (Kützinger) W. Smith. *Phycological Research* **60**, 229-240 (2012).
- 79 Lang, Y., del Monte, F., Rodriguez, B. J., Dockery, P., Finn, D. P. & Pandit, A. Integration of TiO<sub>2</sub> into the diatom *Thalassiosira weissflogii* during frustule synthesis. *Scientific Reports* **3**, 1-11 (2013).

- 80 Jeffries, C., Solanki, R., Rangineni, Y., Wang, W., Chang, C. h. & Rorrer, G. L. Electroluminescence and photoluminescence from nanostructured diatom frustules containing metabolically inserted germanium. *Advanced Materials* **20**, 2633-2637 (2008).
- 81 Machill, S., Köhler, L., Ueberlein, S., Hedrich, R., Kunaschk, M., Paasch, S., Schulze, R. & Brunner, E. Analytical studies on the incorporation of aluminium in the cell walls of the marine diatom *Stephanopyxis turris*. *BioMetals* **26**, 141-150 (2013).
- 82 Köhler, L., Machill, S., Werner, A., Selzer, C., Kaskel, S. & Brunner, E. Are diatoms “green” aluminosilicate synthesis microreactors for future catalyst production? *Molecules* **22**, 2232 (2017).
- 83 Liu, Q., Zhou, L., Liu, F., Fortin, C., Tan, Y., Huang, L. & Campbell, P. G. Uptake and subcellular distribution of aluminum in a marine diatom. *Ecotoxicology and Environmental Safety* **169**, 85-92 (2019).
- 84 Crémazy, A., Levy, J. L., Campbell, P. G. & Fortin, C. Uptake and subcellular partitioning of trivalent metals in a green alga: comparison between Al and Sc. *Biometals* **26**, 989-1001 (2013).
- 85 Liu, D., Yuan, P., Tian, Q., Liu, H., Deng, L., Song, Y., Zhou, J., Losic, D., Zhou, J. & Song, H. Lake sedimentary biogenic silica from diatoms constitutes a significant global sink for aluminium. *Nature Communications* **10**, 1-7 (2019).
- 86 Koning, E., Gehlen, M., Flank, A.-M., Calas, G. & Epping, E. Rapid post-mortem incorporation of aluminum in diatom frustules: Evidence from chemical and structural analyses. *Marine Chemistry* **106**, 208-222 (2007).
- 87 Van Cappellen, P., Dixit, S. & van Beusekom, J. Biogenic silica dissolution in the oceans: Reconciling experimental and field-based dissolution rates. *Global Biogeochemical Cycles* **16**, 23-21-23-10 (2002).
- 88 Dixit, S., Van Cappellen, P. & van Bennekom, A. J. Processes controlling solubility of biogenic silica and pore water build-up of silicic acid in marine sediments. *Marine Chemistry* **73**, 333-352 (2001).
- 89 Xiang, Y., Du, J., Smedskjaer, M. M. & Mauro, J. C. Structure and properties of sodium aluminosilicate glasses from molecular dynamics simulations. *The Journal of Chemical Physics* **139**, 044507 (2013).
- 90 Bansal, N. P. & Doremus, R. H. *Handbook of glass properties*. (Elsevier, 2013).
- 91 La Vars, S. M., Johnston, M. R., Hayles, J., Gascooke, J. R., Brown, M. H., Leterme, S. C. & Ellis, A. V. <sup>29</sup>Si {1 H} CP-MAS NMR comparison and ATR-FTIR spectroscopic analysis of the diatoms *Chaetoceros muelleri* and *Thalassiosira pseudonana* grown at different salinities. *Analytical and Bioanalytical Chemistry* **405**, 3359-3365 (2013).
- 92 Prado, R., Beobide, G., Marcaide, A., Goikoetxea, J. & Aranzabe, A. Development of multifunctional sol-gel coatings: Anti-reflection coatings with enhanced self-cleaning capacity. *Solar Energy Materials and Solar Cells* **94**, 1081-1088 (2010).
- 93 Ciriminna, R., Fidalgo, A., Palmisano, G., Ilharco, L. M. & Pagliaro, M. Silica-Based Sol-Gel Coatings: A Critical Perspective from a Practical Viewpoint. *Biobased and Environmental Benign Coatings*, 149-159 (2016).
- 94 Gąsiorek, J., Szczurek, A., Babiarczuk, B., Kaleta, J., Jones, W. & Krzak, J. Functionalizable sol-gel silica coatings for corrosion mitigation. *Materials* **11**, 197 (2018).
- 95 Chen, C.-H., Li, S.-Y., Chiang, A. S., Wu, A. T. & Sun, Y. Scratch-resistant zeolite anti-reflective coating on glass for solar applications. *Solar energy materials and solar cells* **95**, 1694-1700 (2011).
- 96 Almqvist, N., Delamo, Y., Smith, B., Thomson, N., Bartholdson, Å., Lal, R., Brzezinski, M. & Hansma, P. Micromechanical and structural properties of a pennate diatom investigated by atomic force microscopy. *Journal of Microscopy* **202**, 518-532 (2001).
- 97 Losic, D., Short, K., Mitchell, J. G., Lal, R. & Voelcker, N. H. AFM nanoindentations of diatom biosilica surfaces. *Langmuir* **23**, 5014-5021 (2007).

- 98 Subhash, G., Yao, S., Bellinger, B. & Gretz, M. Investigation of mechanical properties of diatom frustules using nanoindentation. *Journal of Nanoscience and Nanotechnology* **5**, 50-56 (2005).
- 99 Moreno, M. D., Ma, K., Schoenung, J. & Dávila, L. P. An integrated approach for probing the structure and mechanical properties of diatoms: Toward engineered nanotemplates. *Acta biomaterialia* **25**, 313-324 (2015).
- 100 Aitken, Z. H., Luo, S., Reynolds, S. N., Thaulow, C. & Greer, J. R. Microstructure provides insights into evolutionary design and resilience of *Coscinodiscus* sp. frustule. *Proceedings of the National Academy of Sciences* **113**, 2017-2022 (2016).
- 101 Topal, E., Rajendran, H., Zgłobicka, I., Gluch, J., Liao, Z., Clausner, A., Kurzydłowski, K. J. & Zschech, E. Numerical and experimental study of the mechanical response of diatom frustules. *Nanomaterials* **10**, 959 (2020).
- 102 Wilken, S., Hoffmann, B., Hersch, N., Kirchgessner, N., Dieluweit, S., Rubner, W., Hoffmann, L. J., Merkel, R. & Peeken, I. Diatom frustules show increased mechanical strength and altered valve morphology under iron limitation. *Limnology and Oceanography* **56**, 1399-1410 (2011).
- 103 Romann, J., Chauton, M. S., Hanetho, S. M., Vebner, M., Heldal, M., Thaulow, C., Vadstein, O., Tranell, G. & Einarsrud, M.-A. Diatom frustules as a biomaterial: effects of chemical treatment on organic material removal and mechanical properties in cleaned frustules from two *Coscinodiscus* species. *Journal of Porous Materials* **23**, 905-910 (2016).
- 104 Saad, E. M., Pickering, R. A., Shoji, K., Hossain, M. I., Glover, T. G., Krause, J. W. & Tang, Y. Effect of cleaning methods on the dissolution of diatom frustules. *Marine Chemistry* **224**, 103826 (2020).
- 105 Gutiérrez, A., Gordon, R. & Dávila, L. P. Deformation modes and structural response of diatom frustules. *J. Mater. Sci. Eng. Adv. Technol* **15**, 105-134 (2017).
- 106 Gutiérrez, A., Guney, M. G., Fedder, G. K. & Dávila, L. P. The role of hierarchical design and morphology in the mechanical response of diatom-inspired structures via simulation. *Biomaterials Science* **6**, 146-153 (2018).
- 107 Lu, J., Sun, C. & Wang, Q. J. Mechanical simulation of a diatom frustule structure. *Journal of Bionic Engineering* **12**, 98-108 (2015).
- 108 Jeffryes, C., Gutu, T., Jiao, J. & Rorrer, G. L. Metabolic insertion of nanostructured TiO<sub>2</sub> into the patterned biosilica of the diatom *Pinnularia* sp. by a two-stage bioreactor cultivation process. *ACS Nano* **2**, 2103-2112 (2008).
- 109 Kraai, J. A., Wang, A. X. & Rorrer, G. L. Photonic Crystal Enhanced SERS Detection of Analytes Separated by Ultrathin Layer Chromatography Using a Diatom Frustule Monolayer. *Advanced Materials Interfaces* **7**, 2000191 (2020).
- 110 Chauton, M. S., Skolem, L. M., Olsen, L. M., Vullum, P. E., Walmsley, J. & Vadstein, O. Titanium uptake and incorporation into silica nanostructures by the diatom *Pinnularia* sp.(Bacillariophyceae). *Journal of Applied Phycology* **27**, 777-786 (2015).
- 111 Rugar, D. & Hansma, P. Atomic force microscopy. *Physics today* **43**, 23-30 (1990).
- 112 Luís, A. T., Hlúbiková, D., Vaché, V., Choquet, P., Hoffmann, L. & Ector, L. Atomic force microscopy (AFM) application to diatom study: review and perspectives. *Journal of Applied Phycology* **29**, 2989-3001 (2017).
- 113 Crawford, S. A., Higgins, M. J., Mulvaney, P. & Wetherbee, R. Nanostructure of the diatom frustule as revealed by atomic force and scanning electron microscopy. *Journal of Phycology* **37**, 543-554 (2001).
- 114 Higgins, M. J., Sader, J. E., Mulvaney, P. & Wetherbee, R. Probing the surface of living diatoms with atomic force microscopy: the nanostructure and nanomechanical properties of the mucilage layer 1. *Journal of Phycology* **39**, 722-734 (2003).
- 115 Gebeshuber, I. C., Kindt, J., Thompson, J., Del Amo, Y., Stachelberger, H., Brzezinski, M., Stucky, G., Morse, D. & Hansma, P. Atomic force microscopy study of living diatoms in ambient conditions. *Journal of Microscopy* **212**, 292-299 (2003).

- 116 Chen, L., Weng, D., Du, C., Wang, J. & Cao, S. Contribution of frustules and mucilage trails to the mobility of diatom *Navicula* sp. *Scientific Reports* **9**, 1-12 (2019).
- 117 Higgins, M. J., Crawford, S. A., Mulvaney, P. & Wetherbee, R. Characterization of the adhesive mucilages secreted by live diatom cells using atomic force microscopy. *Protist* **153**, 25-38 (2002).
- 118 Kohl, H. & Reimer, L. Transmission Electron Microscopy. *Springer Series in Optical Sciences* **36** (2008).
- 119 Friedrich, H., De Jongh, P. E., Verkleij, A. J. & De Jong, K. P. Electron tomography for heterogeneous catalysts and related nanostructured materials. *Chemical reviews* **109**, 1613-1629 (2009).
- 120 Horvát, S., Fathima, A., Görlich, S., Schlierf, M., Modes, C. D. & Kröger, N. Computational analysis of the effects of nitrogen source and *sin1* knockout on biosilica morphology in the model diatom *Thalassiosira pseudonana*. *Discover Materials* **1**, 1-10 (2021).
- 121 Gutu, T., Gale, D. K., Jeffries, C., Wang, W., Chang, C.-h., Rorrer, G. L. & Jiao, J. Electron microscopy and optical characterization of cadmium sulphide nanocrystals deposited on the patterned surface of diatom biosilica. *Journal of Nanomaterials* **Article number 9**, 1–7 (2009).
- 122 Ragni, R., Cicco, S., Vona, D., Leone, G. & Farinola, G. M. Biosilica from diatoms microalgae: smart materials from bio-medicine to photonics. *Journal of Materials Research* **32**, 279-291 (2017).
- 123 Zglobicka, I., Gluch, J., Liao, Z., Werner, S., Guttmann, P., Li, Q., Bazarnik, P., Plocinski, T., Witkowski, A. & Kurzydowski, K. J. Insight into diatom frustule structures using various imaging techniques. *Scientific Reports* **11**, 1-10 (2021).
- 124 Bedoshvili, E., Likhoshvay, Y. V. & Grachev, M. Ultrastructure of diatom *Synedra acus* subsp. *radians* as revealed by transmission electron microscopy after mild silica dissolution. *Biology Bulletin* **34**, 303-306 (2007).
- 125 Schmid, A.-M. M. & Schulz, D. Wall morphogenesis in diatoms: deposition of silica by cytoplasmic vesicles. *Protoplasma* **100**, 267-288 (1979).
- 126 Li, C.-W. & Volcani, B. Studies on the biochemistry and fine structure of silica shell formation in diatoms. *Protoplasma* **124**, 10-29 (1985).
- 127 Zhou, W., Apkarian, R., Wang, Z. L. & Joy, D. in *Scanning microscopy for nanotechnology* 1-40 (Springer, 2006).
- 128 Goldstein, J. I., Newbury, D. E., Michael, J. R., Ritchie, N. W., Scott, J. H. J. & Joy, D. C. *Scanning electron microscopy and X-ray microanalysis*. (Springer, 2017).
- 129 Inkson, B. J. in *Materials Characterization Using Nondestructive Evaluation (NDE) Methods* (eds Gerhard Hübschen, Iris Altpeter, Ralf Tschuncky, & Hans-Georg Herrmann) 17-43 (Woodhead Publishing, 2016).
- 130 Morales, E. A., Siver, P. A. & Trainor, F. R. Identification of diatoms (Bacillariophyceae) during ecological assessments: comparison between light microscopy and scanning electron microscopy techniques. *Proceedings of the academy of natural sciences of Philadelphia* **151**, 95-103 (2001).
- 131 Kesici, K., Tüney, İ., ZEREN, D., GÜDEN, M. & Sukatar, A. Morphological and molecular identification of pennate diatoms isolated from Urla, İzmir, coast of the Aegean Sea. *Turkish Journal of Biology* **37**, 530-537 (2013).
- 132 Lang, Y., Del Monte, F., Collins, L., Rodriguez, B. J., Thompson, K., Dockery, P., Finn, D. P. & Pandit, A. Functionalization of the living diatom *Thalassiosira weissflogii* with thiol moieties. *Nature Communications* **4**, 1-6 (2013).
- 133 Walsh, P. J., Clarke, S. A., Julius, M. & Messersmith, P. B. Exploratory testing of diatom silica to map the role of material attributes on cell fate. *Scientific reports* **7**, 1-13 (2017).
- 134 Shi, C., Luu, D. K., Yang, Q., Liu, J., Chen, J., Ru, C., Xie, S., Luo, J., Ge, J. & Sun, Y. Recent advances in nanorobotic manipulation inside scanning electron microscopes. *Microsystems & Nanoengineering* **2**, 1-16 (2016).
- 135 Mick, U., Eichhorn, V., Wortmann, T., Diederichs, C. & Fatikow, S. in *2010 IEEE International Conference on Robotics and Automation*. 4088-4093 (IEEE).

- 136 Spehner, D., Steyer, A. M., Bertinetti, L., Orlov, I., Benoit, L., Pernet-Gallay, K., Schertel, A. & Schultz, P. Cryo-FIB-SEM as a promising tool for localizing proteins in 3D. *Journal of Structural Biology* **211**, 107528 (2020).
- 137 Li, P., Chen, S., Dai, H., Yang, Z., Chen, Z., Wang, Y., Chen, Y., Peng, W., Shan, W. & Duan, H. Recent advances in focused ion beam nanofabrication for nanostructures and devices: fundamentals and applications. *Nanoscale* **13**, 1529-1565 (2021).
- 138 Zhou, X., Li, T., Cui, Y., Fu, Y., Liu, Y. & Zhu, L. In situ focused ion beam scanning electron microscope study of microstructural evolution of single tin particle anode for Li-ion batteries. *ACS Applied Materials & Interfaces* **11**, 1733-1738 (2019).
- 139 Kant, K. & Losic, D. in *FIB Nanostructures* 1-22 (Springer, 2013).
- 140 Wirth, R. Focused Ion Beam (FIB) combined with SEM and TEM: Advanced analytical tools for studies of chemical composition, microstructure and crystal structure in geomaterials on a nanometre scale. *Chemical Geology* **261**, 217-229 (2009).
- 141 Phaneuf, M. Applications of focused ion beam microscopy to materials science specimens. *Micron* **30**, 277-288 (1999).
- 142 Narayan, K. & Subramaniam, S. Focused ion beams in biology. *Nature Methods* **12**, 1021-1031 (2015).
- 143 Kumar, S., Rechav, K., Kaplan-Ashiri, I. & Gal, A. Imaging and quantifying homeostatic levels of intracellular silicon in diatoms. *Science Advances* **6**, eaaz7554 (2020).
- 144 Hildebrand, M., Kim, S., Shi, D., Scott, K. & Subramaniam, S. 3D imaging of diatoms with ion-abrasion scanning electron microscopy. *Journal of Structural Biology* **166**, 316-328 (2009).
- 145 Zhang, Q., Li, H., Gan, L., Ma, Y., Golberg, D. & Zhai, T. In situ fabrication and investigation of nanostructures and nanodevices with a microscope. *Chemical Society Reviews* **45**, 2694-2713 (2016).
- 146 Lu, Y., Shen, Y., Liu, X., Ahmad, M. R. B. & Chen, Y. Article ID 8016571 (Hindawi, 2017).
- 147 Antoniou, N., Rykaczewski, K. & Uchic, M. D. In situ FIB-SEM characterization and manipulation methods. *MRS Bulletin* **39**, 347-352 (2014).
- 148 Jiang, C., Lu, H., Zhang, H., Shen, Y. & Lu, Y. Recent advances on in situ SEM mechanical and electrical characterization of low-dimensional nanomaterials. *Scanning* **2017**, Article ID 1985149 (2017).
- 149 Inkson, B. in *Materials characterization using nondestructive evaluation (NDE) methods* 17-43 (Elsevier, 2016).
- 150 Holzer, L., Indutnyi, F., Gasser, P., Münch, B. & Wegmann, M. Three-dimensional analysis of porous BaTiO<sub>3</sub> ceramics using FIB nanotomography. *Journal of Microscopy* **216**, 84-95 (2004).

# Chapter 2

## Modifying the thickness, pore size, and composition of diatom frustule in *Craspedostauros sp.* with $\text{Al}^{3+}$ ions

### Abstract

Diatoms are unicellular photosynthetic algae that produce a silica exoskeleton (frustule) which exposes a highly ordered nano to micro scale morphology. In recent years there has been a growing interest in modifying diatom frustules for technological applications. This is achieved by adding non-essential metals to the growth medium of diatoms which in turn modifies morphology, composition, and resulting properties of the frustule. Here, we investigate the frustule formation in diatom *Craspedostauros sp.*<sup>1</sup>, including changes to overall morphology, silica thickness, and composition, in the presence of  $\text{Al}^{3+}$  ions at different concentrations. Our results show that in the presence of  $\text{Al}^{3+}$  the total silica uptake from the growth medium increases, although a decrease in the growth rate is observed. This leads to a higher inorganic content per diatom resulting in a decreased pore diameter and a thicker frustule as evidenced by electron microscopy. Furthermore,  $^{27}\text{Al}$  solid-state NMR, FIB-SEM, and EDS results confirm that  $\text{Al}^{3+}$  becomes incorporated into the frustule during the silicification process, thus, improving hydrolysis resistance. This approach may be extended to a broad range of elements and diatom species towards the scalable production of silica materials with tunable hierarchical morphology and chemical composition.

### The results presented in this chapter are based on:

Soleimani, M., Rutten, L., Maddala, S. P., Wu, H., Eren, E. D., Mezari, B., Schreur-Piet, I., Friedrich, H. & van Benthem, R. A. *Modifying the thickness, pore size, and composition of diatom frustule in *Craspedostauros sp.* with  $\text{Al}^{3+}$  ions*. Scientific Reports **10**, 19498 (2020).

---

<sup>1</sup>Previously this diatom was identified as *Pinnularia sp* by the commercial supplier (UTEX Culture Collection of Algae). But, after our publication, we were alerted by taxonomists about the misidentification of this diatom species and the accurate name was revealed to be *Craspedostauros sp.* Accordingly, we have used the accurate terminology throughout this thesis.

## 2.1 Introduction

Unicellular photosynthetic algae commonly known as diatoms are ubiquitous throughout most aquatic environments<sup>1</sup>. As such diatoms have evolved to tolerate or adapt to a broad range of environmental conditions including the presence of non-essential metals ions, some of which are toxic<sup>2,3</sup>. The most characteristic feature of diatoms are their biogenic silica cell walls termed the frustule comprising two valves (epitheca and hypotheca) and a number of girdle bands<sup>4</sup>. The frustule, which has a species-specific morphology including micro and nanopatterns, is reproduced during the cell division cycle<sup>5</sup>. For frustule formation in each cycle, water-soluble monosilicic acid, a silica precursor, is taken up from the environment into the diatom cell by silicic acid transporter proteins (SITs)<sup>6,7</sup>. Eventually, the frustule is constructed in a confined intracellular organelle with mildly acidic pH called the silica deposition vesicle (SDV)<sup>8</sup>. The presence of some specific macromolecules such as silaffines and long-chain polyamines in the frustule has led to the assumption that they are involved in silica formation<sup>9,10</sup>. However, the intracellular processes which ultimately lead to frustule formation are remarkably altered in response to changing environmental conditions<sup>11</sup>.

Besides salinity, light intensity/wavelength, pH and temperature<sup>12-17</sup>, also the presence of non-essential metals<sup>18</sup> is influencing the chemistry and morphology of frustule formation. Diatoms can take up some of these elements into the silica, thus, modifying the frustule properties<sup>19</sup>. For instance, the presence of germanium in the growth medium of *Craspedostauros sp.* has led to an alteration in the pore array morphology and induced photoluminescence and electroluminescence properties<sup>20</sup>. Similarly, cadmium uptake by *Nitzschia palea* not only has modified the morphology of the costa and pores of the valves but also altered the embedded organic constituent<sup>21</sup>. Furthermore, the addition of titanium, zirconium, tin, and germanium to the growth medium resulted in variations in frustule morphology of *Synedra Acus* adversely affecting on the mechanical strength of the valves<sup>22</sup>. Lastly, incorporation of titanium by *Thalassiosira weissflogii* has resulted in photocatalytic activity of the frustule material<sup>23</sup>.

Another technologically important element is aluminum (Al) that can be taken up and incorporated into the frustule of diatom modifying its properties<sup>24</sup>. Incorporation of Al into the *Thalassiosira pseudonana* with a silicon to aluminum (Si:Al) ratio of 50:1 has resulted in catalytic activity<sup>25</sup>. Most notably, Al incorporation into frustules of several diatom species has shown a significantly enhanced hydrolysis resistance compared to their Al-free types<sup>26,27</sup>. To date, the internalization of Al into the diatom cells has been investigated from a biological perspective in which Al is distributed within the cell at different subcellular compounds such as granules, debris, organelles, and proteins<sup>28,29</sup>. From the material science perspective exploring the effect of inorganic constituents like Al on the frustule pore size or thickness and the parameters controlling silicification are important too. In recent years, there has been an increasing interest in employing diatom frustules for technological applications such as catalysts, in optic, for drug delivery, and for separation applications<sup>30-35</sup>. The morphological features of the nanopatterned structures are crucial for some of



these applications. However, these technologically interesting effects of Al on frustule formation including morphology, thickness and composition have never been studied.

In this chapter, the effects of  $\text{Al}^{3+}$  on the biogenic silica formation in raphid pennate marine diatom *Craspedostauros sp.* (*C.sp.*) were studied. Besides cell density and total silicic acid uptake in dependence of  $\text{Al}^{3+}$  concentration in the growth medium, especially morphological changes, thickness variations and composition were studied by a combination of imaging and spectroscopy techniques. This investigation has unveiled that not only *C.sp.* responded to the presence of  $\text{Al}^{3+}$  via decreasing the growth rate and increasing Si uptake, but also there was an interdependence between the  $\text{Al}^{3+}$  concentration and nanoporosity as well as the thickness of the valve. Unraveling the correlation between  $\text{Al}^{3+}$  ion concentration and morphological features is a crucial step towards manipulating the nanopatterned structures in diatoms for technological applications.

## 2.2 Materials and methods

### 2.2.1 Diatom culture

*C.sp.* (UTEX B679) was received from the UTEX Culture Collection of Algae and cultivated in artificial seawater medium supplemented with f/2 medium (ASW-f/2). The chemical composition of the medium is provided in the Appendix Table A2.1. The cell cultures were synchronized using the following procedure, cells of *C.sp.* were grown inside a climate cabinet (Flohr, Netherlands) at 23°C, a cycle of 14 h day/10 h night, and light intensity of 3000 Lux. Small aliquot (1ml) (depending on the required volume of the final culture) of a stock culture was added to a flask culture which contained ASW-f/2 medium. After seven days cells were gently harvested via centrifugation at 2.4 rpm and incubated in silicon free medium (contained aforementioned ASW-f/2 components except for silicon) for at least 24 hours to have a synchronized starter culture.

### 2.2.2 $\text{Al}^{3+}$ addition experiments

Different aluminum concentrations were employed in the form of dissolved aluminum chloride in artificial seawater to achieve  $\text{Al}^{3+}$  concentrations of 0.2  $\mu\text{M}$ , 1  $\mu\text{M}$ , and 2  $\mu\text{M}$  which resemble the upper level of concentrations found in the seawater. This naturally occurring upper concentration of  $\text{Al}^{3+}$  is found in the tropical Angola Basin and the inlet of the Amazon river and is the concentration found in coastal regions<sup>27,36,37</sup>. A control culture was grown without  $\text{Al}^{3+}$  addition. Four batches of *C.sp.* cultures were prepared as follows, 20 mL of ASW-f/2 and desired  $\text{Al}^{3+}$  concentration in a 75 mL culture flask was inoculated with 0.5 mL of the synchronized starter culture. Culture flasks were shaken manually every single day to assure proper mixing of the medium. Throughout this chapter, the terms ‘C<sub>0</sub>, C<sub>1</sub>, C<sub>2</sub>, and C<sub>3</sub>’ will refer to diatom cultures with 0, 0.2, 1, and 2  $\mu\text{M}$   $\text{Al}^{3+}$  ion concentration, respectively.

### 2.2.3 Cell density measurement, Si and $\text{Al}^{3+}$ uptake, and silica content

Cell density measurements were performed using an Automated Cell Counter for three biological replicates. The growth rate within the exponential phase was calculated using the following equation  $\mu = [\ln(N_f) - \ln(N_i)]/t$ , where  $N_f$  and  $N_i$  are final and initial cell numbers respectively, and

t is test period in day<sup>38</sup>. Silicon (Si) and Aluminium (Al) uptake was measured using an atomic absorption spectrometer (Shimadzu AA7000, Japan) equipped with a GFA 7000 pyrolytic coated furnace tube, an autosampler, and a D2 background correction lamp. The wavelengths employed for Al and Si measurements were 309.5 nm and 251.8 nm, respectively. To measure the concentrations at the different interval times in the growth medium, diatom cells were filtered out by centrifugation. At each time point, 500  $\mu$ L of the medium was extracted and filtered with an Amicon Ultra-0.5 centrifuge filter (5 min, 14500 rpm). 100  $\mu$ L of the filtrate was diluted 100 times with Milli-Q and subsequently used for the measurements. To prevent silica contamination no glass ware was used throughout the whole process. By combining the results of cell density and Si uptake we could estimate the silica content per diatom cell. Therefore, the silica content per cell was calculated via dividing the amount of consumed Si in the growth medium by the number of cells that have been grown until day 4 which corresponds to the maximum cell density in the four cultures. Statistical significance was measured using a two-tailed t-test.

#### 2.2.4 Sample preparation for electron microscopy

Samples for electron microscopy were prepared in the following manner. First, brown diatom pellets were isolated from the suspended cultures at 14,500 rpm via centrifugation (Minispin Centrifuge, Eppendorf, Germany). The centrifuges pellets were suspended in Milli Q water and centrifuged. The process was repeated 5 times in order to ensure complete removal of the salts, unreacted silicic acid and obtain a brown pellet. After harvesting the living cells by centrifugation and prior to the morphological characterizations by imaging techniques, the organic casing around the frustules and internal organic compounds within the cells should be removed. Thus, several chemical treatments were introduced to obtain rather clean frustules. For instance, a combination of Hydrogen peroxide ( $\text{H}_2\text{O}_2$ ) and Hydrochloric acid (HCl) was used to clean the frustule of diatoms<sup>39,40</sup>. It is now demonstrated that this harsh treatment can significantly change the composition of the frustule and its mechanical performance<sup>41</sup>. Furthermore, Nitric acid ( $\text{HNO}_3$ ) and Sulfuric acid ( $\text{H}_2\text{SO}_4$ ) were employed to extract the internal and external organic compounds of several diatom frustules<sup>42-44</sup>. Although, the acid treatments are noticeably efficient and clean frustules can be obtained in a short period of time, they can significantly enhance the solubility rate of the frustules<sup>45</sup> as well as alter the chemical composition of frustules, particularly observed in the case of nitric acid<sup>46</sup>. In addition, nitric acid is known to selectively remove the incorporated Al from silica-based materials (zeolites)<sup>47</sup>. Alongside these methods, a so-called soft procedure for removing organic constituents of diatom frustule involves extraction using Ethylenediaminetetraacetic acid (EDTA) and Sodium dodecyl sulfate (SDS) were used by many research groups<sup>41,48-50</sup>. Despite the fact that this method has shown its capability to clean the frustules, it may impact the composition of the extracted frustule due to the enhancement of the solubility of silica in the presence of EDTA<sup>51</sup>. Together with this drawback of EDTA-SDS treatment, a few alterations caused by this method were observed during our experiments as well. For example, based on our experiments on fumed silica, it was demonstrated that this treatment can shift the Si-O-Si asymmetric vibration peak in IR spectroscopy to lower wavenumber, possibly due to changing the silica crosslinking (Appendix Figure

A2.1). More importantly,  $^{27}\text{Al}$  solid-state NMR spectroscopy was conducted on diatom *Thalassiosira pseudonana* (T.p.) grown in the presence of  $\text{Al}^{3+}$  before and after EDTA-SDS treatment. As shown in Figure A2.2, before the treatment, Al is mainly present in the form of six coordinated and only a small portion of it is four coordinated. However, after three times washing with EDTA-SDS at 90 °C there is a significant change in Al species in this sample. As can be seen in the graph, post treatment, the relative ratio of 4-coordinate Al to six coordinate Al varied substantially. It is therefore likely that such treatment alters the coordination environment of Al within the frustules which could result in changes in the silica condensation and the mechanical properties of the frustule. Therefore, since the main objective of cleaning procedures is to obtain clean frustules for morphological characterizations by microscopy techniques, an alternative method (without taking the risk of the above mentioned alterations) based on ethanol extraction was employed in this thesis. The intracellular components were extracted using ethanol in order to minimize the impact of extraction on chemistry and morphology of the frustule. The brown pellets were dispersed in absolute ethanol and centrifuged at 14,500 rpm to split girdle bands and valves from each other and to remove the organic constituents. This procedure was repeated at least 10 times to obtain an off white pellet at the bottom of the centrifuge tube. In order to ensure the complete isolation of valves from girdle bands, a suspension of the pellet was sonicated in a bath sonicator (Bransonic ultrasonic cleaner, model 1510E-DTH, 42 kHz, USA) for 5 minutes.

### **2.2.5 Scanning electron microscopy imaging and Energy-Dispersive x-ray Spectroscopy measurement**

For SEM imaging, a tiny amount of the white pellet was dispersed in ethanol and 50  $\mu\text{l}$  of the suspension was dropped onto a silicon wafer that was fixed to a standard SEM stub followed by drying in air. The material was then sputter-coated with gold using Turbo sputter coater Emitech K585X Dual (UK) with a thickness about 10 nm. For EDS line scan and elemental mapping, 10  $\mu\text{l}$  of the above suspension was pipetted onto a standard 200 mesh copper TEM grid covered by a 10 nm continuous carbon film. TEM grids were placed in an in-house made sample holder suitable for a SEM stage. SEM-EDS line scan and mapping were performed using SEM Quanta 3D FEG (Thermo Fisher Scientific, USA), at an acceleration voltage of 3 and 10 kV. EDS spot measurements were performed at an accelerating voltage of 10 kV using Phenom proX SEM (Thermo Fisher Scientific, USA). The mean diameters of areolae, and small pores were calculated via in house MATLAB scripts as shown in the appendix Figure A2.3&A2.4. In addition, length and width of the valves and morphological features such as transapical rib, cross extension, distance between neighboring areolae within an array ( $D_a$ ) and distance between two areolae of two parallel arrays ( $D_p$ ) were measured using Gatan Digital Micrograph for at least 15 valves pre culture. The area of the valve was determined as an ellipse.

### **2.2.6 Thickness measurements and the volume of the frustule**

TEM images were acquired on a Tecnai T20 G2 (Thermo Fisher Scientific, USA) operated at 200 kV and equipped with a LaB<sub>6</sub> filament and a 4k CETA CCD camera. All the diatoms were imaged

at the same magnification of 800 $\times$  with a typical dose  $< 0.5 \text{ e}^- \cdot \text{nm}^{-2} \cdot \text{s}^{-1}$ . Thickness mapping of diatoms was carried out with an in house MATLAB script which is detailed in the appendix (Appendix Table A2.2 and Appendix Figure A2.5). All scripts were developed in MATLAB version 2018b, <https://nl.mathworks.com/products/matlab.html>. Furthermore, the details of the calculated frustule volume are presented in the appendix (Appendix Figure A2.6). Statistical significance was measured using a two-tailed t-test.

### 2.2.7 FIB-SEM and internal view of *C.sp.*

In order to get some insights into how *C.sp.* responds to the presence of  $\text{Al}^{3+}$  ions, internal structures of the cell were exposed via focused ion beam scanning electron microscopy (FIB-SEM). Thus, *C.sp.* cells were harvested by centrifugation and fixed with 2.0 % paraformaldehyde and 1 % glutaraldehyde for 2 hours at room temperature. The fixed cells were gently rinsed two times with 0.1M sodium cacodylate buffer (pH 7.2) and postfixed for 1 hour at room temperature with 0.5 % (w/v)  $\text{OsO}_4$ . Then stained in 0.1 % uranyl acetate for three hours. After the staining cells were rinsed four times with Milli-Q water. The dehydration of the fixed cells was performed in an upgraded sequence of ethanol. Ultimately, Epon 812 was used to embed the cells. FIB tomography was typically conducted utilizing the aforementioned SEM. Throughout the FIB process, a beam of focused ions ( $\text{Ga}^+$ ) removes 100 nm thick slice from the surface of the embedded *C.sp.* cell at a current of 1 nA and acceleration voltage of 30 kV. Subsequently, an image of the freshly revealed surface was taken at an accelerating voltage of 5 kV by Back-Scattered Electron detector (BSE). This process was repeated slice by slice throughout the entire embedded cell (Appendix Figure A2.7 shows an overview of the process). Avizo (9.5, Thermo Fisher Scientific, USA) software was used for alignment, segmentation and rendering of the internal features of *C.sp.*

### 2.2.8 NMR spectroscopy and TGA

$^{27}\text{Al}$  solid state NMR spectra on diatoms was recorded using a Bruker DMX500 Avance spectrometer (Germany) operating at  $^{27}\text{Al}$  resonance frequency of 130.3 MHz. The measurement was performed at 25 kHz rotor spinning rate using a triple resonance 2.5 mm MAS NMR probe head. A one-pulse sequence was used with an  $18^\circ$  pulse of 1  $\mu\text{s}$  duration and an interscan delay of 0.5 sec.  $^{27}\text{Al}$  chemical shift was calibrated using saturated Aluminium nitrate solution. TGA measurements were performed using Q500 TGA (TA instruments, Germany). Diatom pellets (2 to 4 mg) were loaded on to platinum pans and heated from 30  $^\circ\text{C}$  to 1000  $^\circ\text{C}$  in air. The temperature was ramped up at 20  $^\circ\text{C}/\text{min}$  while maintaining a gas flow rate of 60 mL/min.

### 2.2.9 Frustule dissolution experiment

In order to monitor the effect of  $\text{Al}^{3+}$  on the solubility of *C.sp.* frustules, dissolution experiments on  $\text{C}_0$  and  $\text{C}_3$  were carried out. After harvesting and washing the cells with demineralized water, the pellets were transferred into 40 ml demineralized water at 90  $^\circ\text{C}$  for 6 days. For measuring the Si concentration samples were taken daily. The sample preparation for Si concentration measurement via atomic absorption spectroscopy was the same as above.

## 2.3 Results

### 2.3.1 Morphological parameters

*C.sp.* is a raphid pennate marine diatom that has an imperfect rectangle prism shape. As shown in Figure 2.1a, two valves (the epitheca and hypotheca) are connected by a series of overlapping girdle bands. Each valve comprises a thick siliceous structure in the middle known as central nodule combining with raphe rib which elongates throughout the valve resulting in a cross-shaped structure (Figure 2.1b). In contrast to the valve, girdle bands are less elaborated and compose of different porous and nonporous areas (Figure 2.1c). Within the porous area of the valve, parallel adjacent transapical ribs are connected by neighboring cross extensions to form several arrays of the areolae which are about 200 nm in diameter. The cross extensions bridging two areolae within an array and transapical ribs separating two rows of areolae. Small pores are located within the areolae which have diameter in the range of 60-80 nm (Figure 2.1d).

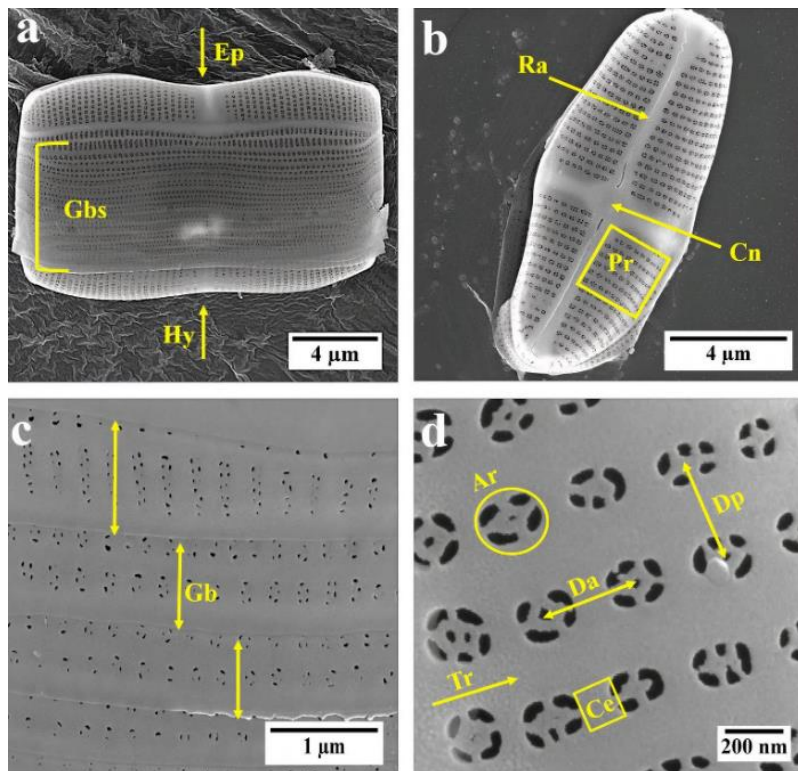


**Figure 2.1** (a) SEM images of isolated mature frustule of *C.sp.*; Gbs= girdle bands; Ep= Epitheca (bigger valve); Hy= Hypotheca (smaller valve); (b) isolated valve; Ra= raphe; Cn= central nodule; Pr= porous area; (c) individual girdle band (Gb); (d) porous area, Tr= transapical rib; Ar= areola Ce= cross extension; Da= distance between neighboring areolae within an array; Dp= distance between two areolae of two parallel arrays.

### 2.3.2 Morphological changes of *C.sp.* with increasing $\text{Al}^{3+}$ concentration

First it was determined whether morphological characteristics of the valve were modified by the presence of  $\text{Al}^{3+}$ . Figure 2.2a-d exhibit SEM images of valves grown at different  $\text{Al}^{3+}$  concentrations. By measuring the length, width, and area of valves it could be shown (Figure 2.2e) that the overall size of valves were unaltered due to the presence of  $\text{Al}^{3+}$ .

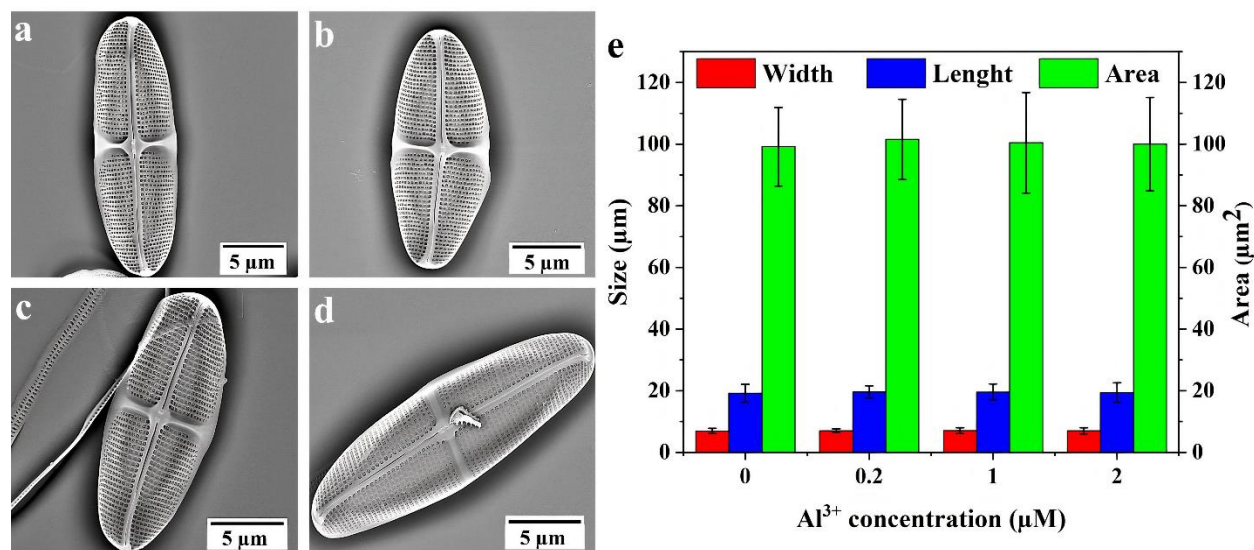


**Figure 2.2** SEM images of the interior surface of the valves of *C.sp.*; (a)  $C_0$ ; (b)  $C_1$ ; (c)  $C_2$ ; (d)  $C_3$ ; (e) measured length, width and area of valves as a function of  $\text{Al}^{3+}$  concentration obtained from  $n=15$  valves per culture. Error bars indicate standard deviation.

Nevertheless, a more detailed analysis elucidating the effect of  $\text{Al}^{3+}$  on the valve architecture at the nano and micro scale indicated subtle differences. Figure 2.3a-f present high magnification SEM images and a detailed analysis of the porous area. While the overall geometry of the pore arrays remained unchanged with increasing  $\text{Al}^{3+}$  concentration, i.e., the width of the cross extension (Ce), the width of transapical ribs (Tr), the average distance of the neighboring areolae within a pore array (Da) and the distance between two areolae of two parallel arrays (Dp) stayed constant; what stands out is that the diameter of small pores differs greatly between cultures. There was a close correlation between the reduction of the diameter of small pores and the increase in  $\text{Al}^{3+}$  ion concentration in the growth medium. The mean diameters of the small pores of the valve of  $C_0$ ,  $C_1$ ,  $C_2$ , and  $C_3$  were  $70 \pm 9$ ,  $61 \pm 10$ ,  $40 \pm 5$ , and  $35 \pm 4$  nm, respectively. Appendix Table A2.4 shows the statistical data of the image analyses.

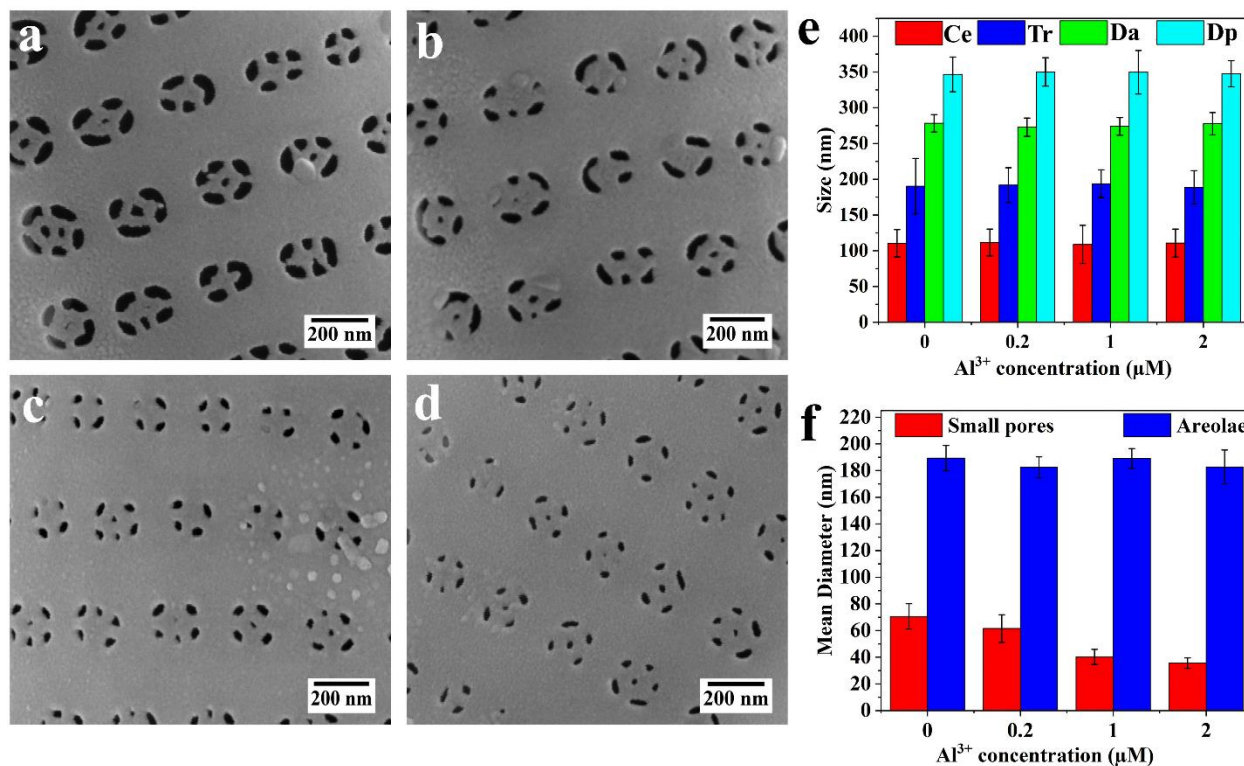


**Figure 2.3** (a-d) SEM images of porous area of valves of *C.sp.* grown in the cultures with different  $\text{Al}^{3+}$  concentrations (a)  $C_0$ ; (b)  $C_1$ ; (c)  $C_2$ ; (d)  $C_3$ ; (e, f) Bar graphs of measured architectural parameters of *C.sp.* ( $n=15$  valves per culture) as given in Fig1; (e) Width measurement of transapical rib and cross extension, distance between neighboring areolae within a pore array and distance between two areolae of two parallel arrays; (f) mean diameter of small pores and areolae. Error bars indicate standard deviation.

### 2.3.3 Macroscopic Al distribution and atomic coordination environment

Besides subtle morphological changes, incorporation of  $\text{Al}^{3+}$  into the frustule may occur. In order to identify the presence of Al in the frustule and how it is coordinated, EDS spot scan, line scan and elemental mapping and  $^{27}\text{Al}$  solid state NMR of the frustule of *C.sp.* of  $C_3$  were performed. This sample was chosen for its high concentration of  $\text{Al}^{3+}$  which can be detected via SEM-EDS and NMR. Also, SEM-EDS spot measurements and mapping of  $C_0$ ,  $C_1$ , and  $C_2$  were conducted to pinpoint the presence and distribution of Si, O, and Al in the valves and girdle bands. Due to the lack or very low concentration of Al in  $C_0$  and  $C_1$  EDS did not reveal the presence of Al (Figure 2.4a,b and Appendix Figure A2.8). In contrast, mapping of the isolated valves and girdle bands of  $C_2$  and  $C_3$  confirmed the presence of Al alongside Si and O (Figure 2.4c,d). As shown in Figure 2.4d there was a homogenous distribution of Al in valve and girdle bands of  $C_3$ . However,  $C_2$  did not show a homogenous distribution of Al, which could be due to the low concentration of Al in the sample ( $\sim 100\text{Si}:1\text{Al}$ ). EDS spot analysis of  $C_3$  revealed the presence of Si, O, Al, C, Mg, Na, and N. In order to semi quantitatively compare the Si:Al ratios at the submicron level of  $C_3$ , EDS line scans of the porous area and girdle bands were conducted for 50 spots (Appendix Figure A2.8). The mean ratio of Si:Al was approximately 45:1 for both selected features which is comparable to the fed Si:Al ratio of this sample. Solid state  $^{27}\text{Al}$  NMR measurement was performed to



obtain information about the coordination state of aluminum in the frustule (Figure 2.4e). The sample showed two well resolved but broadened peaks located at 50 ppm and 6.5 ppm corresponding to four and six coordinated aluminum species<sup>24</sup>. The broad peaks indicate that the chemical environment of aluminum exhibits great structural variability. The presence of Al in the silica matrix has been shown to increase the acidity of synthetic amorphous silica<sup>52</sup>.

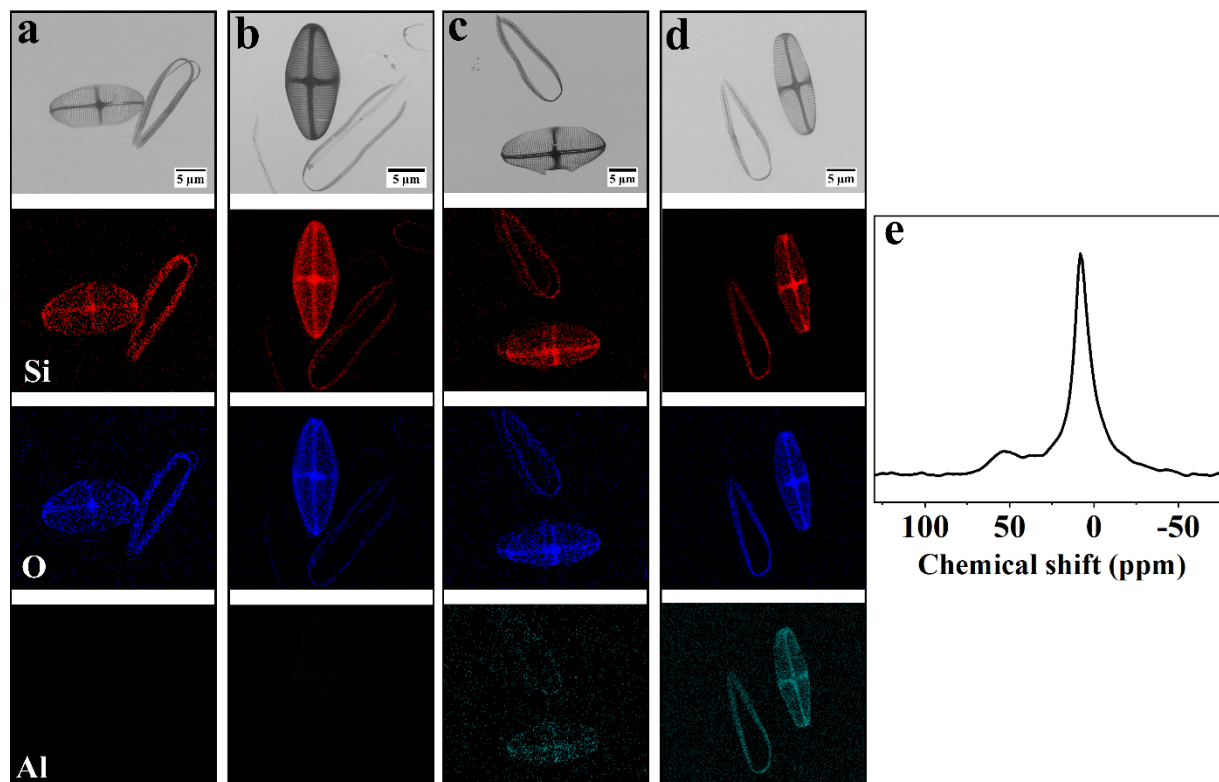


**Figure 2.4** SEM images and EDS elemental maps of isolated valves and girdle bands of (a) C<sub>0</sub>; (b) C<sub>1</sub>; (c) C<sub>2</sub>; (d) C<sub>3</sub>; red=Si; blue=O; green=Al; (e) <sup>27</sup>Al solid state NMR of C<sub>3</sub>.

### 2.3.4 The effect of Al<sup>3+</sup> on silicon uptake, cell density and total inorganic content

To assess whether and how Al<sup>3+</sup> influences the biosilicification process which ultimately leads to a homogeneous distribution of Al and only altering the pore size, Si and Al<sup>3+</sup> uptake, growth rate and inorganic/silica content of cell cultures were determined. The Si uptake vs. cell density measurements of the cultures of *C.sp.* with different Al<sup>3+</sup> concentrations are shown in Figure 2.5a. The figure shows that the cell density gradually increased in all four cultures until day 4 where they reached the maximum cell density. What is striking in this figure, is that the growth rate of the cells decreased by increasing the Al<sup>3+</sup> concentration in the growth medium also shown in Table 1. Interestingly, Si uptake determined from atomic adsorption spectroscopy showed that the amount of silicon taken up remained unchanged (Figure 2.5a). For instance, on day 5, the amount of consumed Si from C<sub>0</sub> to C<sub>3</sub> were 96.3±0.2, 96.9±0.1, 97.0±0.5, and 96.9±0.1 μM, respectively. This implies that increasing the Al<sup>3+</sup> concentration resulted in diatoms taking up larger quantities of Si per cell. The silica content per cell was estimated by dividing the amount of consumed Si in the



growth medium by the number of grown cells, as shown in Table 1. The average silica content of diatom cells for the cultures from C<sub>0</sub> to C<sub>3</sub> were 244±7, 298±11, 390±15, and 395±13 fmol/cell, respectively. This equals an increase of about 60 % in silica content in the presence of 2 µM Al<sup>3+</sup> ions. Comparing Al<sup>3+</sup> and Si uptake for C<sub>3</sub> showed the same progression for the first 48 hours (Appendix Figure A2.9). However, gradually Al<sup>3+</sup> uptake slowed down compared to Si uptake during the cultivation period which could be due to differences in uptake mechanism<sup>53</sup>. To rule out the possibility of Si precipitation/adsorption onto the surface of the cultures flask, a control experiment was carried out for C<sub>3</sub> without *C.sp.* cells (Appendix Figure A2.10). In addition, in order to verify whether the increased uptake resulted in an increase in the inorganic content, TGA measurements were performed on untreated diatoms by heating them in air from 30 to 1000 °C (Figure 2.5b)<sup>54</sup>. The initial 3 to 7 % weight loss observed below 200 °C was assigned to adsorbed water molecules<sup>55</sup>. All samples show a steep weight loss between 200 to 550 °C, corresponding to the loss due to the presence of biomolecules such as lipids, proteins, and silanols<sup>56,57</sup>. The samples containing aluminium show an additional weight loss step between 550 and 700 °C. No further weight loss was observed above 700 °C. As shown in Figure 2.5b the final inorganic content of the diatoms grown in the absence of aluminium (C<sub>0</sub>) was 29 %, whereas the presence of aluminium resulted in an increased inorganic content, namely 47 % in total for C<sub>3</sub>. This means that there is an approximately 60 % relative increase in inorganic content from C<sub>0</sub> to C<sub>3</sub>, in close agreement with the results from atomic absorption spectroscopy.

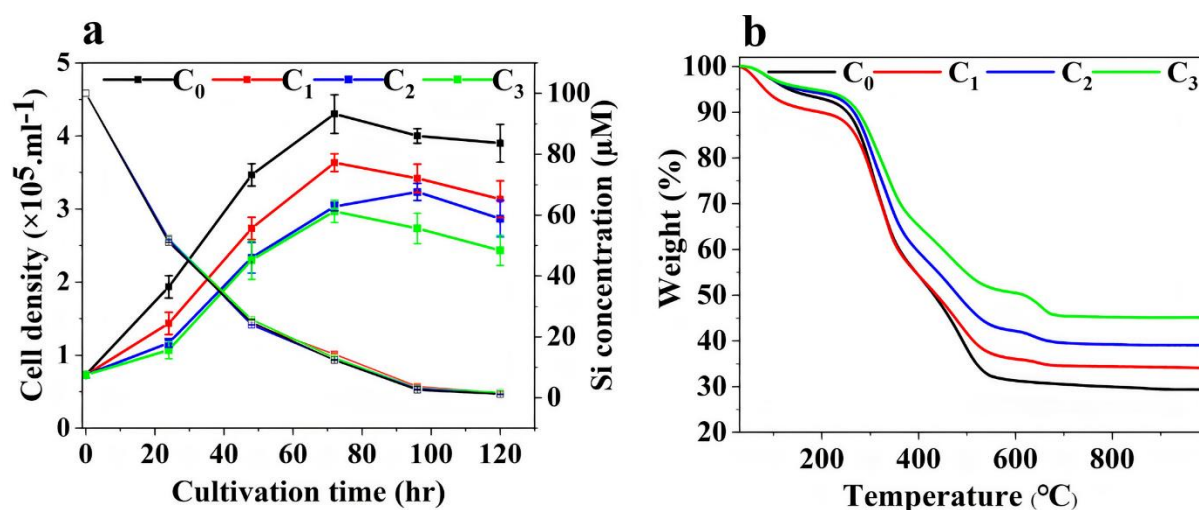


**Figure 2.5** (a) Cell density measurements of *C.sp.* at different Al<sup>3+</sup> concentrations as a function of cultivation time and Atomic absorption spectroscopy of decreasing silicon concentration in the different culture media as a function of cultivation time. Error bars indicate standard deviation for three culture replicates. On day 4<sup>th</sup>  $p \leq 0.05$ . (b) Thermogravimetric analysis (TGA) in air, of *C.sp.* frustule material grown at different Al<sup>3+</sup> concentrations.

**Table.2.1** Growth rate and calculated silica content of *C.sp.* grown in the presence of various  $\text{Al}^{3+}$  concentration. Average  $\pm$  standard deviation calculated from three culture replicates is given.

Culture number	Growth rate ( $\text{d}^{-1}$ )	Silica content ( $\text{fmol.cell}^{-1}$ )
$\text{C}_0$	$0.6 \pm 0.05$	$244 \pm 7$
$\text{C}_1$	$0.5 \pm 0.06$	$298 \pm 11$
$\text{C}_2$	$0.4 \pm 0.04$	$390 \pm 15$
$\text{C}_3$	$0.37 \pm 0.03$	$395 \pm 13$

### 2.3.5 The effect of $\text{Al}^{3+}$ on valve thickness

As the observed subtle changes in overall morphology cannot account for the 60 % increase in inorganic content, further characterization was performed to ascertain how *C.sp.* responds to this increased mineral uptake. To this end the thickness of the valves was measured from TEM images specifically focusing on thickness variations of the raphe, porous area, and the overall valve in the presence of  $\text{Al}^{3+}$ . TEM image analysis was carried out using an in-house MATLAB script which is presented in detail in the appendix section 2.7.3 including Table A2.2 and Figure A2.3. Figure 2.6a and b present the thickness maps of the whole valve and porous area of *C.sp.* grown at different  $\text{Al}^{3+}$  concentrations. This analysis clearly shows that the thickness of the valves increases with increasing  $\text{Al}^{3+}$  concentration (Figure 2.6c). From  $\text{C}_0$  to  $\text{C}_3$  the thickness of raphe increased from  $153 \pm 12$  to  $188 \pm 10$  nm. The thickness of porous area (excluding the areolae) for  $\text{C}_0$ ,  $\text{C}_1$ ,  $\text{C}_2$ , and  $\text{C}_3$  were  $49 \pm 7$ ,  $59 \pm 6$ ,  $71 \pm 5$ , and  $82 \pm 8$  nm, respectively. Increasing the  $\text{Al}^{3+}$  concentration to 2  $\mu\text{M}$  resulted in an increase of valve thickness about 40 nm (Figure 2.6c). The increased thickness at nearly identical overall dimensions leading to an increase in the volume of silica making up the frustule as shown in appendix Table A2.3. According to the SEM images, the total volume of the *C.sp.* was approximately  $1140 \pm 10.2 \mu\text{m}^3$ . The internal volumes and volumes of the frustule for the four cultures are depicted in appendix Table A3. There was approximately a 60 % increase in the volume of silica making up the frustule by 2  $\mu\text{M}$   $\text{Al}^{3+}$  addition. These results confirmed that  $\text{Al}^{3+}$  addition led to Si uptake enhancement which ultimately increased the thickness and reduced the pore size.

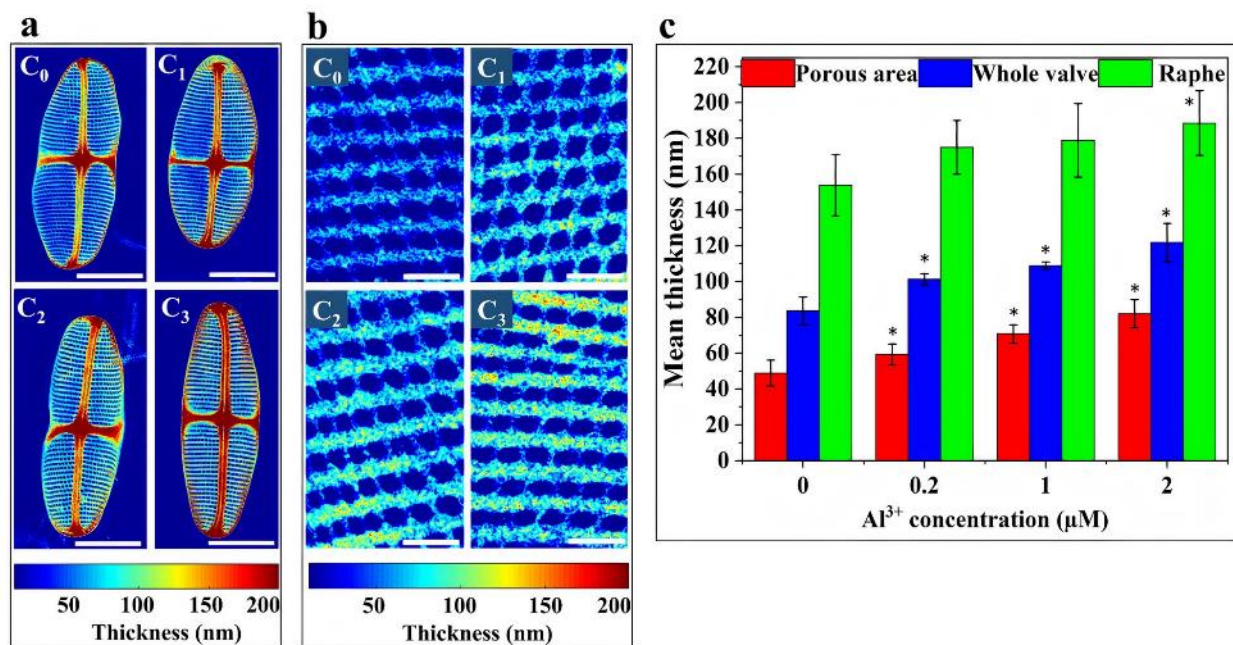


**Figure 2.6** (a) TEM thickness maps of *C.sp.* valves grown at different  $\text{Al}^{3+}$  concentrations (scale bar= 5  $\mu\text{m}$ ); (b) thickness maps of porous areas (scale bar=500 nm); (c) bar graphs of thickness measurements of porous area, raphe and whole valve (s). Error bars indicate standard deviation. \* indicates  $p \leq 0.05$ .

### 2.3.6 The effect of $\text{Al}^{3+}$ on the internal structure of *C.sp.*

In order to understand how *C.sp.* responds to  $\text{Al}^{3+}$ , the internal structure of intact *C.sp.* was investigated using FIB-SEM tomography. By sequentially FIB sectioning and SEM imaging, 200 cross-sections of an entire diatom were imaged. SEM images of internal structures of  $\text{C}_3$  revealed the presence of high contrast particles in BSE mode within the cells (Figure 2.7a-c). These particles were found in different regions of the cells. Figure 2.7a shows the internal structure of a parent cell in which two daughter cells are about to separate from each other. Chloroplasts (Chr) and newly formed valves (Df) are annotated in Figure 2.7a. As shown in Figure 2.7b,c most of the particles are found in the middle of the parent cell with some of them being close to the region where the silica deposition vesicle (SDV) is usually located<sup>57</sup>. EDS-mapping was performed on one of the cross-sections during the milling process to analyze the elemental composition. As shown in Figure 2.7d, Phosphorous, Aluminium, Oxygen, and Silicon are the main elements found in the particles. A 3D rendering of the internal structure of a *C.sp.* cell highlighting the distribution of particles is shown in Figure 2.7 e-g. The high contrast particles are located at the different parts of the cell having a mean diameter and volume of  $570 \pm 300$  nm and  $0.22 \pm 0.17 \mu\text{m}^3$ , respectively. In contrast to  $\text{C}_3$ , no high contrast particles were observed within the internal structure of  $\text{C}_0$  (Appendix Figure A2.11).

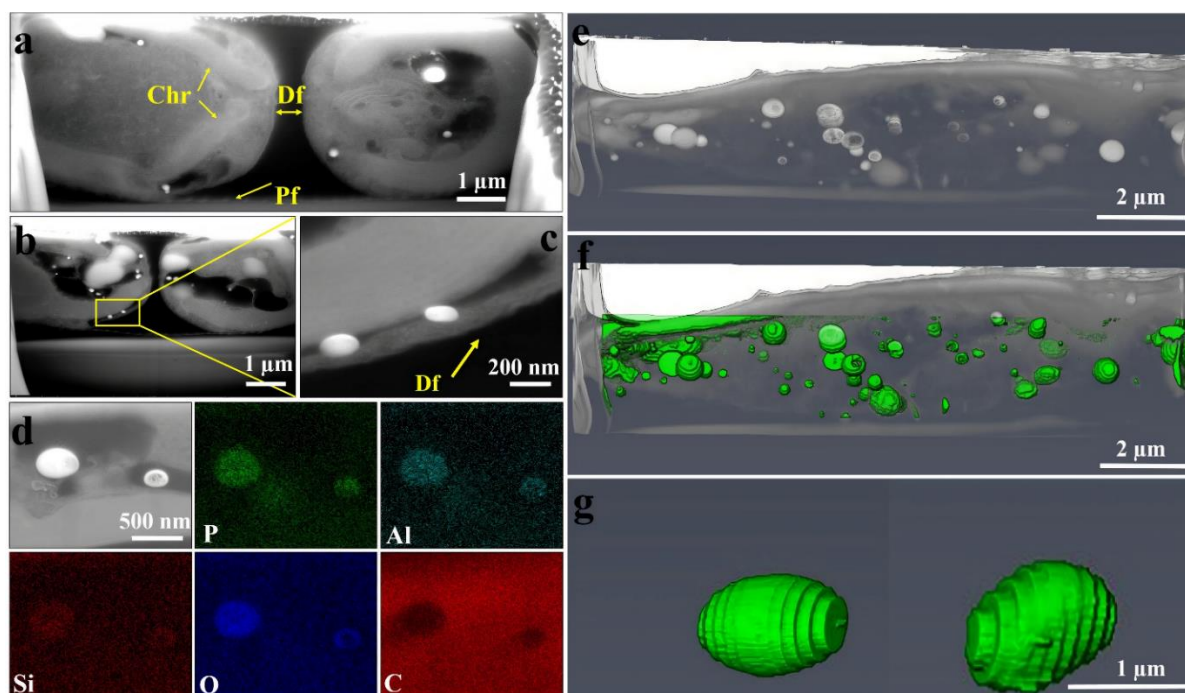


**Figure 2.7** SEM images of FIB cross-sections of *C.sp.* cell grown in  $2\ \mu\text{M}\ \text{Al}^{3+}$ . (a) Df= daughter frustules which are being formed within the cell, Pf= parental frustule, Chr= Chloroplasts; (b) presence of the particles at the different parts of the cell; (c) two particles are close to the region where the silica deposition vesicle (SDV) is located. (d) SEM image and EDS maps of the particles within the cell; (e-g) 3D rendering of the high contrast particles inside the cell.

### 2.3.7 The effect of $\text{Al}^{3+}$ on silica hydrolysis

The most studied effect of  $\text{Al}^{3+}$  on diatom frustules is the reduction of the silica hydrolysis or dissolution rate<sup>26</sup>. Here, atomic absorption spectroscopy was employed to monitor the effect of  $\text{Al}^{3+}$  on the dissolution of *C.sp.* frustules in demineralized water. The released Si concentration of  $\text{C}_0$  and  $\text{C}_3$  as a function of time is provided in Appendix Figure A2.12. The results show that after 24 hours the Si concentration of  $\text{C}_0$  reached  $80 \pm 6\ \mu\text{M}$ . Interestingly, no increase in Si concentration was detected after this point. In contrast, for  $\text{C}_3$  only  $3 \pm 0.9\ \mu\text{M}$  Si was detected after 24 hours. The Figure shows that there has been a gradual increase in the Si concentration until day 6 where it reached  $26 \pm 4\ \mu\text{M}$ . These findings provide further support for the hypothesis that Al incorporated frustules are remarkably hydrolysis resistant compared to their Al free types. It has been suggested that incorporation of  $\text{Al}^{3+}$  within the silica network leads to the formation of aluminosilicate anions which increases the negative charge of the structure. Thus, hydroxyl ions that catalyze the dissolution of amorphous silica, are repelled and the dissolution rate decreases subsequently<sup>27</sup>.

## 2.4 Discussion

The results of this investigation demonstrate that  $\text{Al}^{3+}$  addition decreased *C.sp.* growth rates significantly while the width, length and area of the valves were not altered (Figure 2.2 and 2.5a). This decrease in growth rate did not result in a concomitant decrease in Si uptake, indicating an

increased intracellular Si concentration in the presence of  $\text{Al}^{3+}$ . This increased silica uptake resulted in higher silica volume in the frustule (Table. A2.2) leading to an increased frustule thickness (Figure 2.6). Hence, the inorganic content of *C.sp.* grown in the presence of  $2\ \mu\text{M}\ \text{Al}^{3+}$  as found by TGA appeared to be approximately 60 % higher. The role of mineral particles inside the cell, most likely being metal-polyphosphate granules, has been suggested to be a tolerance mechanism for many organisms including diatoms to detoxify Al and other hard cations<sup>28,58</sup>. Therefore, the formation of the particles within the cell in the presence of  $\text{Al}^{3+}$  which contained a high amount of P, O, Si and Al (Figure 2.7) could be a tolerance strategy for *C.sp.* to cope with  $\text{Al}^{3+}$ . In accordance with the previous investigations, present findings have demonstrated that  $\text{Al}^{3+}$  can modify the frustule properties. For instance, the increase of the silica content of *Asterionella Ralfsii* var. *americana* with  $\text{Al}^{3+}$  addition is comparable to our results even though the reported valve size reduction was not observed in *C.sp.*<sup>59</sup>. Particularly the dissolution experiments, demonstrating a remarkable effect of  $\text{Al}^{3+}$  on the solubility of the frustule, are consistent with the previous investigations<sup>60</sup>.

Notwithstanding the 60 % increase in the silica/inorganic content in the presence of  $\text{Al}^{3+}$ , *C.sp.* could completely regulate the frustule formation without changing the overall morphology. The reduced diameter of small pores, in contrast to the unmodified areolae, cross-extensions, and transapical ribs, imply that merely the delicate fine-structures of the valve were influenced by  $\text{Al}^{3+}$ , as it has been observed for Ge and Ti incorporation into *C.sp.*<sup>20,61</sup> as well. In addition, we have shown here that even  $0.2\ \mu\text{M}\ \text{Al}^{3+}$  ( $\sim 500\text{Si}:1\text{Al}$ ) remarkably impacted the thickness of the valves. It can thus be suggested that a higher Si uptake in the presence of  $\text{Al}^{3+}$  led to the accumulation of a higher amount of Si inside the SDV which resulted in a thicker valve with smaller pores. It is worth referring that the process of valve formation for raphid pennate diatoms such as *C.sp.* undergoes a sequence of distinct stages for various morphological features such as central nodule, raphe, cross extension, and transapical ribs<sup>62</sup>. Therefore, a possible explanation for the homogenous distribution of Al and Si in EDS mapping and enhancing the thickness of porous area and raphe is that  $\text{Al}^{3+}$  is involved throughout the different stages of the valve formation. Also, the results of  $\text{Al}^{3+}$  uptake, FIB-SEM, and  $^{27}\text{Al}$  solid state NMR support the assumption that  $\text{Al}^{3+}$  is internalized and associated with the silicification process in *C.sp.*



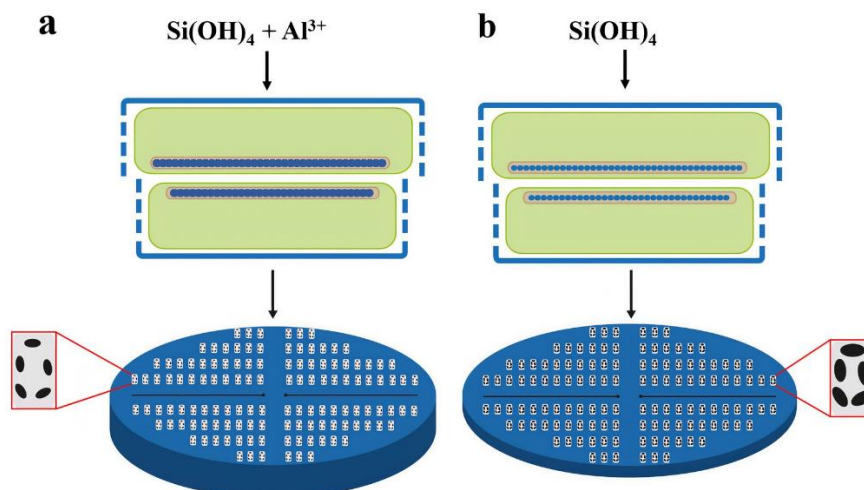


**Figure 2.8** Feeding diatom cells with and without  $\text{Al}^{3+}$  solution. (a) Diatom cell takes up  $\text{Al}^{3+}$  and  $\text{Si(OH)}_4$  during the cell cycle division resulting in a higher silica content inside the SDV (dark blue color) and a new thick valve with smaller pores. (b) Absence of  $\text{Al}^{3+}$  in the growth medium leads to a thin valve with relatively larger pores.

Previous studies have demonstrated that through chemical treatments such as acid etching or surface coating, the pore size and thickness of the frustule can be modified<sup>3</sup>. For instance, atomic layer deposition has been used to form an ultrathin film of  $\text{TiO}_2$  on the surface of the frustule of *Coscinodiscus sp.* and *Thalassiosira eccentrica* to modify the pore size and the thickness<sup>63</sup>. Besides, etching of the frustule of *Coscinodiscus sp.* with HF solution was performed to enlarge the pore size<sup>64</sup>. The main drawbacks of these methods are the involvement of extra steps after harvesting of the frustule and the use of high-risk chemicals. In contrast, modification of the frustule was effected with small amounts of metal salts during the cell growth of *C.sp.* in the present study. By changing the  $\text{Al}^{3+}$  concentration in the growth medium we could control the thickness and pore size of the frustule at the nanoscale (Figure 2.8). The current study shows that employing naturally occurring concentrations of a nonessential element in the growth medium leads to the formation of diatom frustules with a tunable morphology (thickness and pore size) and composition.

## 2.5 Summary

Here we showed that diatom *C.sp.* responded to the presence of  $\text{Al}^{3+}$  by decreasing the growth rate, formation of particles inside the cell, and increasing the intracellular silica content which resulted in thicker valves with smaller pores. The pore size, thickness, and dissolution rate of the valves of *C.sp.* can be tuned by  $\text{Al}^{3+}$  concentration in the growth medium. In addition, uptake and incorporation of  $\text{Al}^{3+}$  into the frustule resulted in its homogenous distribution at submicron level. While the underlying mechanisms is not clear, similar approaches and different species might be used to synthesize materials with complex and well defined morphological, and potentially chemical and mechanical properties in the future.

## 2.6 References

- 1 Wang, Y., Cai, J., Jiang, Y., Jiang, X. & Zhang, D. Preparation of biosilica structures from frustules of diatoms and their applications: current state and perspectives. *Applied Microbiology and Biotechnology* **97**, 453-460 (2013).
- 2 Yung, M. M., Kwok, K. W., Djurišić, A. B., Giesy, J. P. & Leung, K. M. Influences of temperature and salinity on physicochemical properties and toxicity of zinc oxide nanoparticles to the marine diatom *Thalassiosira pseudonana*. *Scientific Reports* **7**, 1-9 (2017).
- 3 Su, Y., Lundholm, N. & Ellegaard, M. Effects of abiotic factors on the nanostructure of diatom frustules—ranges and variability. *Applied Microbiology and Biotechnology* **102**, 5889-5899 (2018).
- 4 Hildebrand, M. Diatoms, biomineralization processes, and genomics. *Chemical Reviews* **108**, 4855-4874 (2008).
- 5 Zurzolo, C. & Bowler, C. Exploring bioinorganic pattern formation in diatoms. A story of polarized trafficking. *Plant Physiology* **127**, 1339-1345 (2001).
- 6 Hildebrand, M. in *Biomineralization from Biology to Biotechnology and Medical Application* 171-188 (Wiley, 2000).
- 7 Grachev, M., Sherbakova, T., Masyukova, Y. & Likhoshway, Y. A potential zinc-binding motif in silicic acid transport proteins of diatoms. *Diatom Research* **20**, 409-411 (2005).
- 8 Vrieling, E. G., Gieskes, W. & Beelen, T. P. Silicon deposition in diatoms: control by the pH inside the silicon deposition vesicle. *Journal of Phycology* **35**, 548-559 (1999).
- 9 Sumper, M. & Kröger, N. Silica formation in diatoms: the function of long-chain polyamines and silaffins. *Journal of Materials Chemistry* **14**, 2059-2065 (2004).
- 10 Kröger, N., Lorenz, S., Brunner, E. & Sumper, M. Self-assembly of highly phosphorylated silaffins and their function in biosilica morphogenesis. *Science* **298**, 584-586 (2002).
- 11 Falasco, E., Bona, F., Badino, G., Hoffmann, L. & Ector, L. Diatom teratological forms and environmental alterations: a review. *Hydrobiologia* **623**, 1-35 (2009).
- 12 Vrieling, E. G., Sun, Q., Tian, M., Kooyman, P. J., Gieskes, W. W., van Santen, R. A. & Sommerdijk, N. A. Salinity-dependent diatom biosilicification implies an important role of external ionic strength. *Proceedings of the National Academy of Sciences* **104**, 10441-10446 (2007).
- 13 Trobajo, R., Rovira, L., Mann, D. G. & Cox, E. J. Effects of salinity on growth and on valve morphology of five estuarine diatoms. *Phycological Research* **59**, 83-90 (2011).
- 14 Jung, S. W., Youn, S. J., Shin, H. H., Yun, S. M., Ki, J.-S. & Lee, J. H. Effect of temperature on changes in size and morphology of the marine diatom, *Ditylum brightwellii* (West) Grunow (Bacillariophyceae). *Estuarine, Coastal and Shelf Science* **135**, 128-136 (2013).
- 15 Javaheri, N., Dries, R., Burson, A., Stal, L., Sloot, P. & Kaandorp, J. Temperature affects the silicate morphology in a diatom. *Scientific Reports* **5**, 1-9 (2015).
- 16 Hervé, V., Derr, J., Douady, S., Quinet, M., Moisan, L. & Lopez, P. J. Multiparametric analyses reveal the pH-dependence of silicon biomineralization in diatoms. *PloS one* **7**, e46722 (2012).
- 17 Hoogstraten, A., Timmermans, K. R. & de Baar, H. J. Morphological and physiological effects in *Proboscia Atlata* (Bacillariophyceae) grown under different light and CO<sub>2</sub> conditions of the modern southern ocean *Journal of Phycology* **48**, 559-568 (2012).
- 18 Falasco, E., Bona, F., Ginepro, M., Hlúbiková, D., Hoffmann, L. & Ector, L. Morphological abnormalities of diatom silica walls in relation to heavy metal contamination and artificial growth conditions. *Water sa* **35**, 595-606 (2009).
- 19 Rorrer, G. in *Diatom Nanotechnology* 79-110 (Royal Society of Chemistry, 2017).
- 20 Jeffries, C., Solanki, R., Rangineni, Y., Wang, W., Chang, C. h. & Rorrer, G. L. Electroluminescence and photoluminescence from nanostructured diatom frustules containing metabolically inserted germanium. *Advanced Materials* **20**, 2633-2637 (2008).
- 21 Heredia, A., Figueira, E., Rodrigues, C. T., Rodríguez-Galván, A., Basiuk, V. A., Vrieling, E. G. & Almeida, S. F. Cd<sup>2+</sup> affects the growth, hierarchical structure and peptide composition of the

- biosilica of the freshwater diatom *Nitzschia palea* (Kützinger) W. Smith. *Phycological Research* **60**, 229-240 (2012).
- 22 Basharina, T. N., Danilovtseva, E. N., Zelinskiy, S. N., Klimenkov, I. V., Likhoshway, Y. V. & Annenkov, V. V. The effect of titanium, zirconium and tin on the growth of diatom *Synedra acus* and morphology of its silica valves. *Silicon* **4**, 239-249 (2012).
- 23 Lang, Y., Del Monte, F., Rodriguez, B. J., Dockery, P., Finn, D. P. & Pandit, A. Integration of TiO<sub>2</sub> into the diatom *Thalassiosira weissflogii* during frustule synthesis. *Scientific Reports* **3**, 3205 (2013).
- 24 Machill, S., Köhler, L., Ueberlein, S., Hedrich, R., Kunaschk, M., Paasch, S., Schulze, R. & Brunner, E. Analytical studies on the incorporation of aluminium in the cell walls of the marine diatom *Stephanopyxis turris*. *BioMetals* **26**, 141-150 (2013).
- 25 Köhler, L., Machill, S., Werner, A., Selzer, C., Kaskel, S. & Brunner, E. Are diatoms “green” aluminosilicate synthesis microreactors for future catalyst production? *Molecules* **22**, 2232 (2017).
- 26 Liu, D., Yuan, P., Tian, Q., Liu, H., Deng, L., Song, Y., Zhou, J., Losic, D., Zhou, J. & Song, H. Lake sedimentary biogenic silica from diatoms constitutes a significant global sink for aluminium. *Nature Communications* **10**, 1-7 (2019).
- 27 Koning, E., Gehlen, M., Flank, A.-M., Calas, G. & Epping, E. Rapid post-mortem incorporation of aluminum in diatom frustules: Evidence from chemical and structural analyses. *Marine Chemistry* **106**, 208-222 (2007).
- 28 Liu, Q., Zhou, L., Liu, F., Fortin, C., Tan, Y., Huang, L. & Campbell, P. G. Uptake and subcellular distribution of aluminum in a marine diatom. *Ecotoxicology and Environmental Safety* **169**, 85-92 (2019).
- 29 Crémazy, A., Levy, J. L., Campbell, P. G. & Fortin, C. Uptake and subcellular partitioning of trivalent metals in a green alga: comparison between Al and Sc. *Biometals* **26**, 989-1001 (2013).
- 30 Aw, M. S., Simovic, S., Addai-Mensah, J. & Losic, D. Silica microcapsules from diatoms as new carrier for delivery of therapeutics. *Nanomedicine* **6**, 1159-1173 (2011).
- 31 Aw, M. S., Simovic, S., Yu, Y., Addai-Mensah, J. & Losic, D. Porous silica microshells from diatoms as biocarrier for drug delivery applications. *Powder Technology* **223**, 52-58 (2012).
- 32 Losic, D., Rosengarten, G., Mitchell, J. G. & Voelcker, N. H. Pore architecture of diatom frustules: potential nanostructured membranes for molecular and particle separations. *Journal of Nanoscience and Nanotechnology* **6**, 982-989 (2006).
- 33 Yu, Y., Addai-Mensah, J. & Losic, D. Functionalized diatom silica microparticles for removal of mercury ions. *Science and Technology of Advanced Materials* **13**, 015008 (2012).
- 34 Fischer, C., Adam, M., Mueller, A. C., Sperling, E., Wustmann, M., van Pée, K.-H., Kaskel, S. & Brunner, E. Gold nanoparticle-decorated diatom biosilica: A favorable catalyst for the oxidation of d-glucose. *ACS Omega* **1**, 1253-1261 (2016).
- 35 De Stefano, L., Rotiroti, L., De Stefano, M., Lamberti, A., Lettieri, S., Setaro, A. & Maddalena, P. Marine diatoms as optical biosensors. *Biosensors and Bioelectronics* **24**, 1580-1584 (2009).
- 36 Zhou, L., Tan, Y., Huang, L. & Wang, W.-X. Enhanced utilization of organic phosphorus in a marine diatom *Thalassiosira weissflogii*: A possible mechanism for aluminum effect under P limitation. *Journal of Experimental Marine Biology and Ecology* **478**, 77-85 (2016).
- 37 Dixit, S., Van Cappellen, P. & van Bennekom, A. J. Processes controlling solubility of biogenic silica and pore water build-up of silicic acid in marine sediments. *Marine Chemistry* **73**, 333-352 (2001).
- 38 Papry, R. I., Ishii, K., Al Mamun, M. A., Miah, S., Naito, K., Mashio, A. S., Maki, T. & Hasegawa, H. Arsenic biotransformation potential of six marine diatom species: effect of temperature and salinity. *Scientific Reports* **9**, 1-16 (2019).
- 39 Aitken, Z. H., Luo, S., Reynolds, S. N., Thaulow, C. & Greer, J. R. Microstructure provides insights into evolutionary design and resilience of *Coscinodiscus* sp. frustule. *Proceedings of the National Academy of Sciences* **113**, 2017-2022 (2016).



- 40 Jeffries, C., Gutu, T., Jiao, J. & Rorrer, G. L. Two-stage photobioreactor process for the metabolic insertion of nanostructured germanium into the silica microstructure of the diatom *Pinnularia* sp. *Materials Science and Engineering: C* **28**, 107-118 (2008).
- 41 Romann, J., Chauton, M. S., Hanetho, S. M., Vebner, M., Heldal, M., Thaulow, C., Vadstein, O., Tranell, G. & Einarsrud, M.-A. Diatom frustules as a biomaterial: effects of chemical treatment on organic material removal and mechanical properties in cleaned frustules from two *Coscinodiscus* species. *Journal of Porous Materials* **23**, 905-910 (2016).
- 42 Vrieling, E. G., Beelen, T. P., Sun, Q., Hazelaar, S., van Santen, R. A. & Gieskes, W. W. Ultrasmall, small, and wide angle X-ray scattering analysis of diatom biosilica: interspecific differences in fractal properties. *Journal of Materials Chemistry* **14**, 1970-1975 (2004).
- 43 Boyle, J. A., Pickett-Heaps, J. D. & Czarnecki, D. B. Valve morphogenesis in the pennate diatom *Achnanthes coarctata*. *Journal of phycology* **20**, 563-573 (1984).
- 44 Nagy, S. S. in *The diatom world* 1-18 (Springer, 2011).
- 45 Saad, E. M., Pickering, R. A., Shoji, K., Hossain, M. I., Glover, T. G., Krause, J. W. & Tang, Y. Effect of cleaning methods on the dissolution of diatom frustules. *Marine Chemistry* **224**, 103826 (2020).
- 46 Heredia, A., van der Strate, H. J., Delgadillo, I., Basiuk, V. A. & Vrieling, E. G. Analysis of organo-silica interactions during valve formation in synchronously growing cells of the diatom *Navicula pelliculosa*. *ChemBioChem* **9**, 573-584 (2008).
- 47 Roberge, D. M., Hausmann, H. & Hölderich, W. F. Dealumination of zeolite beta by acid leaching: a new insight with two-dimensional multi-quantum and cross polarization <sup>27</sup>Al MAS NMR. *Physical Chemistry Chemical Physics* **4**, 3128-3135 (2002).
- 48 Chauton, M. S., Skolem, L., Olsen, L. M., Vullum, P. E., Walmsley, J. & Vadstein, O. Titanium uptake and incorporation into silica nanostructures by the diatom *Pinnularia* sp.(Bacillariophyceae). *Journal of applied phycology* **27**, 777-786 (2015).
- 49 Kumari, E., Görlich, S., Poulsen, N. & Kröger, N. Genetically programmed regioselective immobilization of enzymes in biosilica microparticles. *Advanced Functional Materials* **30**, 2000442 (2020).
- 50 Brunner, E., Gröger, C., Lutz, K., Richthammer, P., Spinde, K. & Sumper, M. Analytical studies of silica biomineralization: towards an understanding of silica processing by diatoms. *Applied Microbiology and Biotechnology* **84**, 607-616 (2009).
- 51 Demadis, K. D. & Mavredaki, E. Green additives to enhance silica dissolution during water treatment. *Environmental Chemistry Letters* **3**, 127-131 (2005).
- 52 Locus, R., Verboekend, D., Zhong, R., Houthoofd, K., Jaumann, T., Oswald, S., Giebel, L., Baron, G. & Sels, B. F. Enhanced acidity and accessibility in Al-MCM-41 through aluminum activation. *Chemistry of Materials* **28**, 7731-7743 (2016).
- 53 Thamtrakoln, K. & Hildebrand, M. Silicon uptake in diatoms revisited: a model for saturable and nonsaturable uptake kinetics and the role of silicon transporters. *Plant Physiology* **146**, 1397-1407 (2008).
- 54 Wang, J., Zhou, Q., Song, D., Qi, B., Zhang, Y., Shao, Y. & Shao, Z. Chitosan-silica composite aerogels: preparation, characterization and Congo red adsorption. *Journal of Sol-Gel Science and Technology* **76**, 501-509 (2015).
- 55 Belmabkhout, Y., Serna-Guerrero, R. & Sayari, A. Adsorption of CO<sub>2</sub>-containing gas mixtures over amine-bearing pore-expanded MCM-41 silica: application for gas purification. *Industrial & Engineering Chemistry Research* **49**, 359-365 (2010).
- 56 Kadam, D. M., Thunga, M., Wang, S., Kessler, M. R., Grewell, D., Lamsal, B. & Yu, C. Preparation and characterization of whey protein isolate films reinforced with porous silica coated titania nanoparticles. *Journal of Food Engineering* **117**, 133-140 (2013).
- 57 Bedoshvili, E., Likhoshway, Y. V. & Grachev, M. Ultrastructure of diatom *Synedra acus* subsp. *radians* as revealed by transmission electron microscopy after mild silica dissolution. *Biology Bulletin* **34**, 303-306 (2007).

- 58 Pettersson, A., Kunst, L., Bergman, B. & Roomans, G. M. Accumulation of aluminium by *Anabaena cylindrica* into polyphosphate granules and cell walls: an X-ray energy-dispersive microanalysis study. *Microbiology* **131**, 2545-2548 (1985).
- 59 Gensemer, R. W. Role of aluminium and growth rate in changes in cell size and silica content of silica-limited populations of *Asterionella Palfsii* var *Americana* (Bacillariophyceae). *Journal of Phycology* **26**, 250-258 (1990).
- 60 Van Cappellen, P., Dixit, S. & van Beusekom, J. Biogenic silica dissolution in the oceans: Reconciling experimental and field-based dissolution rates. *Global Biogeochemical Cycles* **16**, 23-21-23-10 (2002).
- 61 Chauton, M. S., Skolem, L. M., Olsen, L. M., Vullum, P. E., Walmsley, J. & Vadstein, O. Titanium uptake and incorporation into silica nanostructures by the diatom *Pinnularia* sp.(Bacillariophyceae). *Journal of Applied Phycology* **27**, 777-786 (2015).
- 62 Hildebrand, M. Biological processing of nanostructured silica in diatoms. *Progress in Organic Coatings* **47**, 256-266 (2003).
- 63 Losic, D., Triani, G., Evans, P. J., Atanacio, A., Mitchell, J. G. & Voelcker, N. H. Controlled pore structure modification of diatoms by atomic layer deposition of TiO<sub>2</sub>. *Journal of Materials Chemistry* **16**, 4029-4034 (2006).
- 64 Zhang, D., Wang, Y., Zhang, W., Pan, J. & Cai, J. Enlargement of diatom frustules pores by hydrofluoric acid etching at room temperature. *Journal of Materials Science* **46**, 5665-5671 (2011).

## 2.7 Appendix

### 2.7.1 The effect of EDTA-SDS treatment on the chemistry of frustule

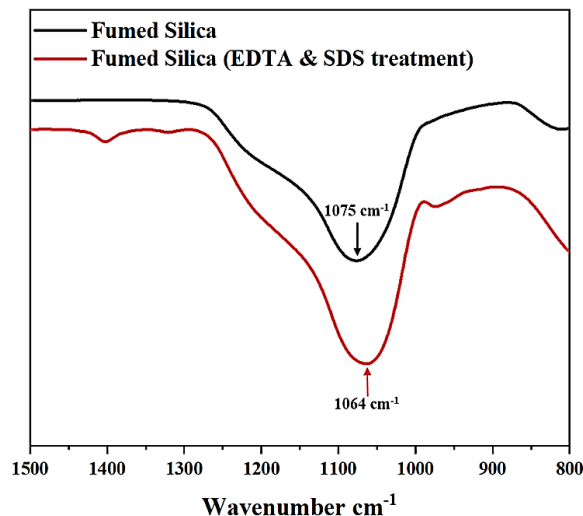


**Figure A2.1** IR spectra of fumed silica before and after EDTA and SDS treatment.

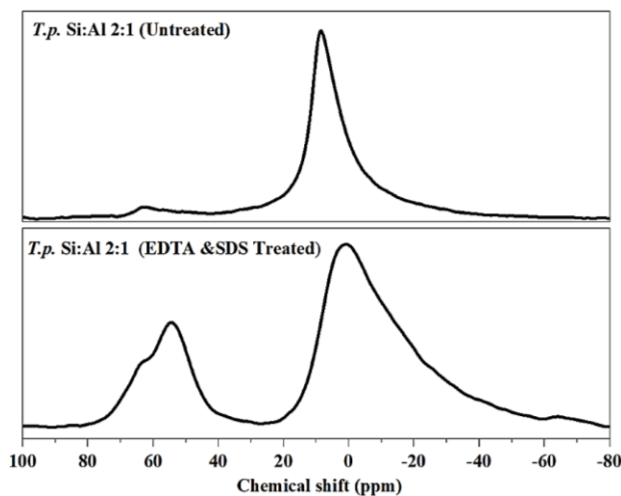


**Figure A2.2.**  $^{27}\text{Al}$  solid-state NMR of diatom *Thalassiosira pseudonana* (T.p.) grown in the presence of  $\text{Al}^{3+}$  with fed Si:Al ratio of 2:1.

### 2.7.2 Mean diameter of areolae and small pores measurements

The mean diameter of areola was measured for 15 valves per culture in SEM micrographs using an in house MATLAB script<sup>1</sup>. Appendix Figure A2.3 exhibits the selected axes for each areola. The average of the two-axes was used to determine areola diameter and error bars represent the standard deviations. Also, the mean diameter of small pore was determined via an in-house MATLAB script. Figure A2.4 shows the procedure for determining the mean diameter of small pore via the Matlab program.

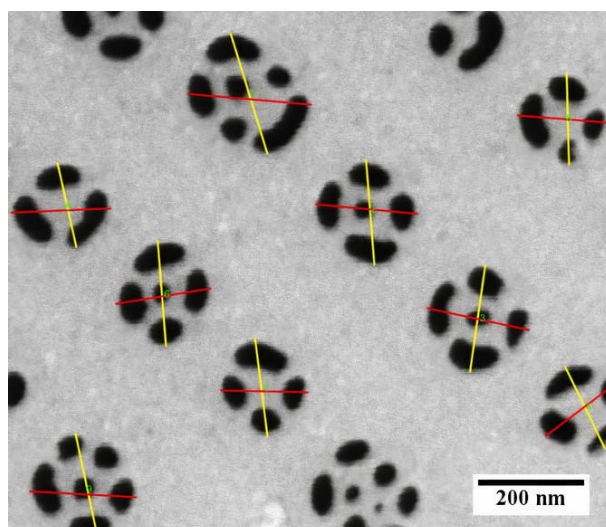


*Figure A2.3. Selected axes for measuring the diameter of the areolae.*

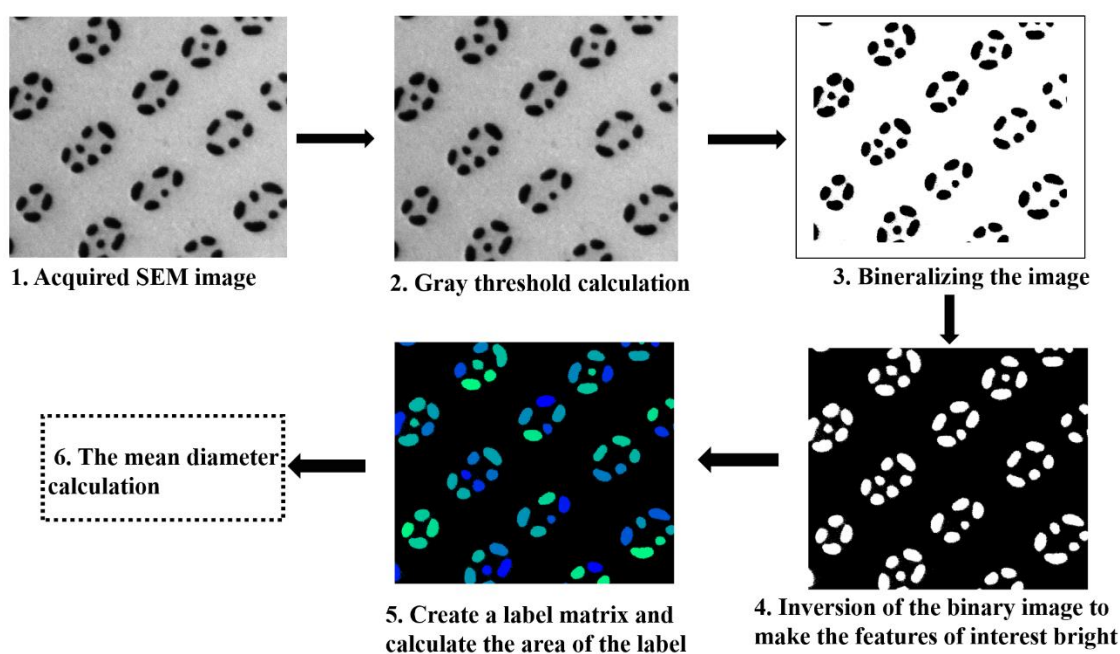


*Figure A2.4. Image analysis process for measuring the mean diameters of small pores.*

### 2.7.3 Thickness mapping

The thickness of the valves was measured from TEM images in the following manner: The contrast in the TEM images can be approximated by mass-thickness contrast considerations. Diatoms frustules, are amorphous materials, loaded on the continuous carbon grid and were imaged at a low magnification (800 $\times$ ). To map the thickness of a single diatom, one flat field (FFD) TEM image

only containing the unscattered incident electron flux  $I_0$  and one TEM image containing the electron flux  $I_t$  transmitted through the sample were acquired. The thickness of diatoms  $t_D$  can be estimated (Equation (1)) based on Lambert-Beer Law:

$$\frac{I_t}{I_0} = \exp\left(-\left(\frac{t_C}{\Lambda_C} + \frac{t_D}{\Lambda_D}\right)\right) \quad (1)$$

Where  $t_C$  is the thickness of the continuous carbon film in the TEM grid, and  $\Lambda_C$  and  $\Lambda_D$  are the elastic mean free path (EMFP,  $\Lambda$ ) of the carbon and the diatom, respectively. EMFP calculations are based on Reimer's book<sup>2</sup>. All the thickness analysis and EMFP calculations were performed using in-house MATLAB scripts<sup>3,4</sup>. Important parameters used in the calculations were shown in Table A2. Mapping the local thickness of the diatom was carried out using in-house MATLAB scripts. The detailed image analysis procedures are shown in Figure A2.5.

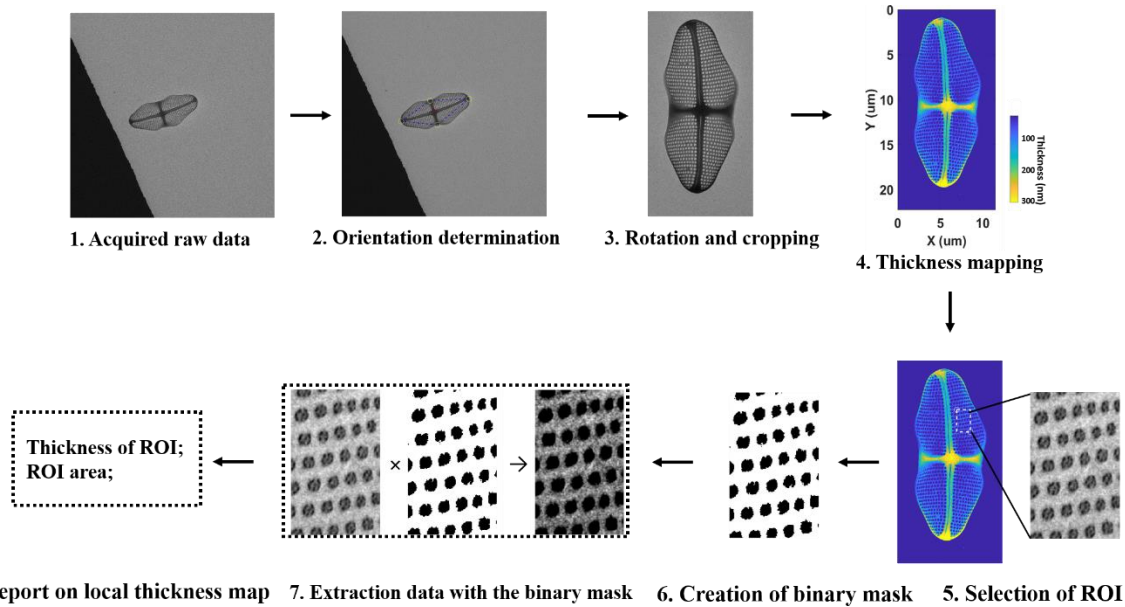


**Figure A2.5.** Image-processing procedures for single diatom and local area thickness mapping.

#### 2.7.4 Internal volume of *C.sp.* and the frustule volume

The volume of the entire *C.sp.* was calculated using a simple assumption that *C.sp.* is a rectangular prism.  $V = L \times W \times H$ . Where  $V$ ,  $L$ ,  $W$ , and  $H$  are volume, length, width and height of the whole *C.sp.* (Figure A2.6). Since, the length and width of the valves of the four cultures were comparable (SEM images) we used an average of *C.sp.* dimensions for determining the entire volume. The internal volume was calculated by subtracting the thickness of the frustule from the dimensions of the whole *C.sp.* Therefore, the volume of silica making up the frustule for each culture is the difference between the total volume and internal volume (Table A3). It is worth noting that for this calculation, the thickness of the porous area was used as the thickness of the whole frustule.

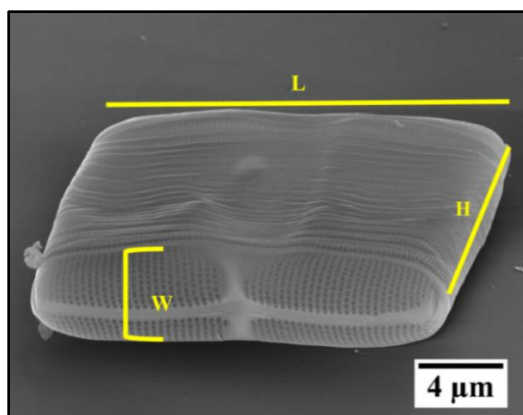


**Figure A2.6.** Overall structure of an intact *C.sp.* cell. Length, width, and height are shown.

### 2.7.5 FIB-SEM process of the embedded *C.sp.* cell

The embedded *C.sp.* cell was positioned at Eucentric height (10 mm) and tilted to 52° with the intention that the electron beam and the ion beam are focused at the coincidence point. Before the Serial Slice and View (SSV), a protective layer of platinum with dimensions of  $20 \times 10 \times 1 \mu\text{m}$  was deposited on the surface of *C.sp.* using ion beam deposition at 30 keV and an ion beam current (IBC) of 0.3 nA. In order to remove material in front of the embedded cell, bulk milling was performed with dimensions  $40 \times 20 \times 10 \mu\text{m}$  (IBC = 15 nA). Side trenches of  $10 \times 20 \times 5 \mu\text{m}$  were created using an IBC of 7 nA. The fiducial marker was made with  $z \geq 1 \mu\text{m}$  (IBC = 3 nA). Next the electron beam was focused on the cleaned block face and automated SSV operation was initiated using a milling IBC of 1 nA and a slice thickness of either 50 nm or 100 nm. Images of new revealed surface were taken in BSE mode.

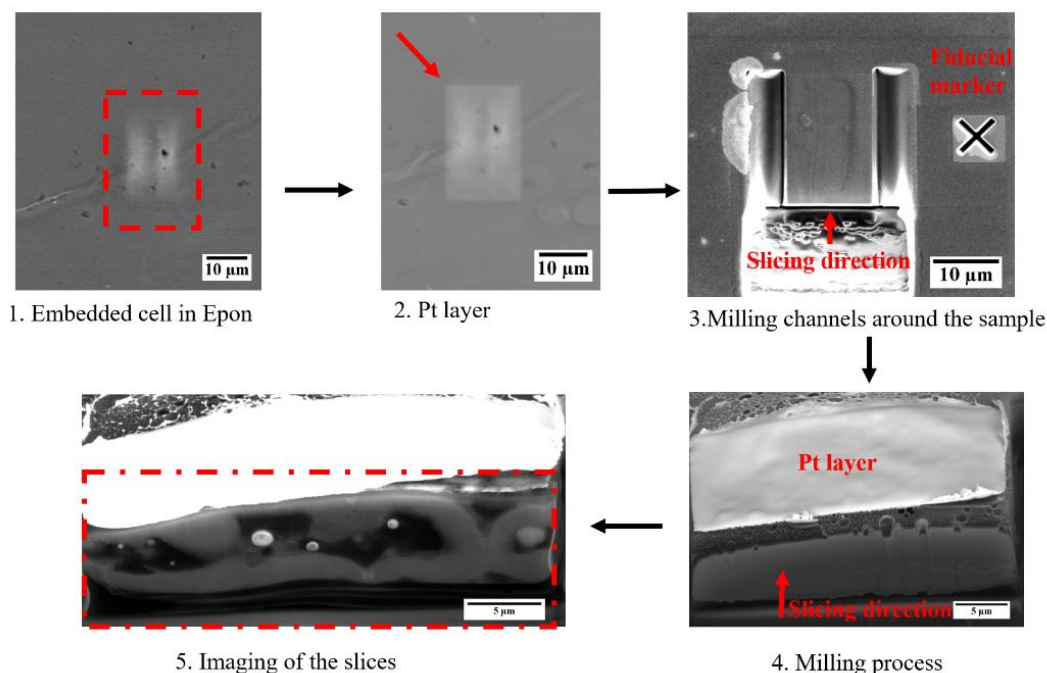


**Figure A2.7.** FIB-SEM process steps.

## 2.7.6 SEM-EDS spot and line scans measurements

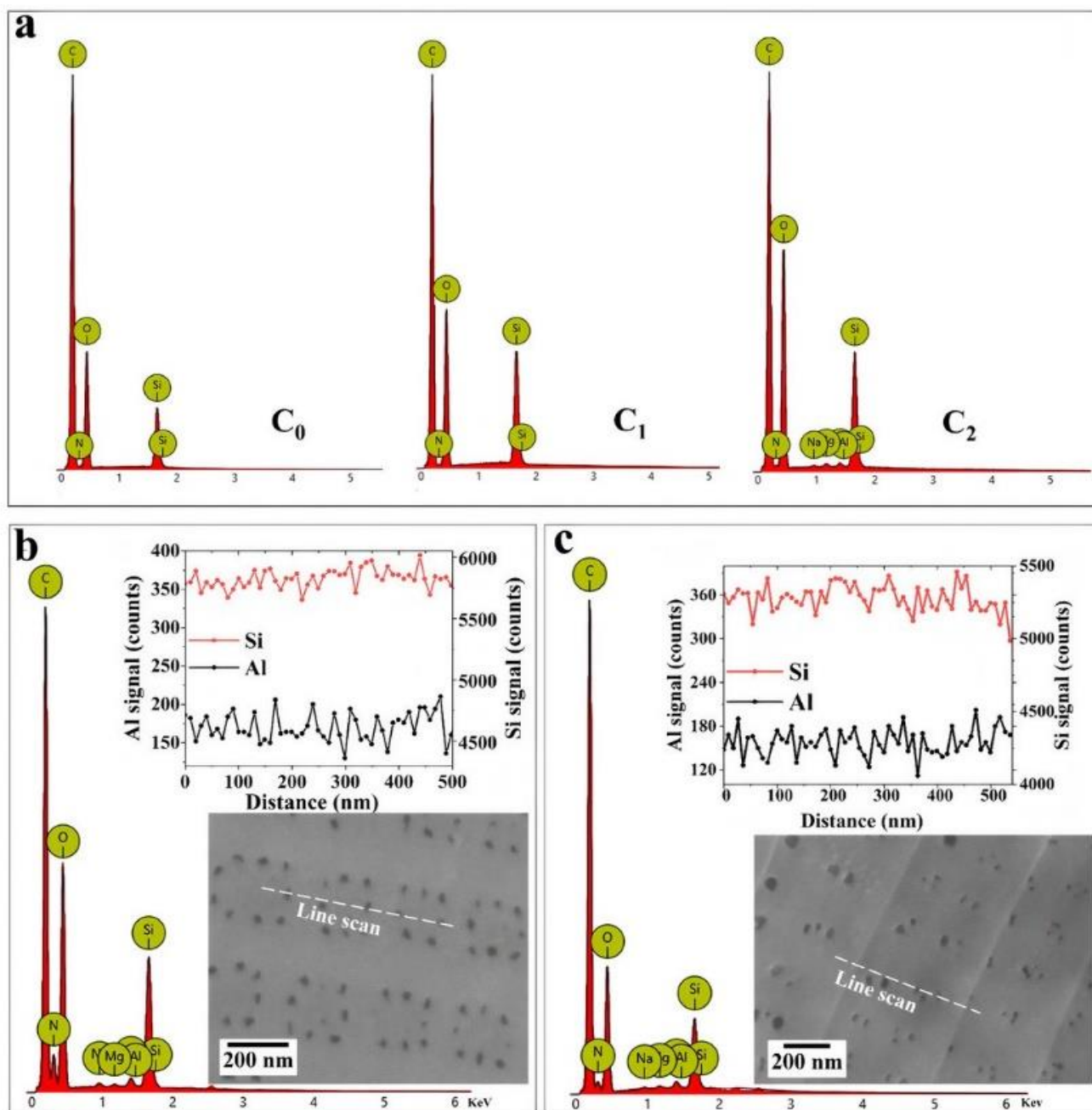


**Figure A2.8.** (a) SEM-EDS spot measurements of  $C_0$ - $C_2$ ; (b) Spot and line scan of porous area of  $C_3$ ; (c) Spot and line scan of girdle bands of  $C_3$ .



### 2.7.7 Si and Al<sup>3+</sup> uptake comparison

As shown in Figure A2.9, Si and Al<sup>3+</sup> were taken up during the cultivation time. the concentration of both elements decreased as a function of time. During the first 48 hours, the relative amounts of consumed Si and Al<sup>3+</sup> were comparable. However, after this point, a the rate of uptake differed.

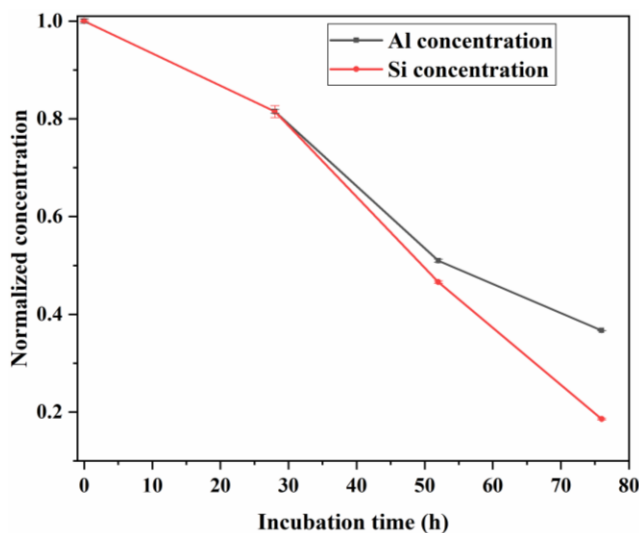


**Figure A2.9.** Si and Al<sup>3+</sup> uptake comparison of *C<sub>3</sub>* as a function of time

### 2.7.8 Control experiment: Variation of Si concentration in diatom free culture

Artificial seawater supplemented with f/2 medium (ASW-f/2) and 2  $\mu\text{M}$  Al<sup>3+</sup> was incubated in a culture flask in the absence of *C.sp.* cells. Every day, a sample was taken, and Si concentration was determined via atomic absorption spectrometer. As shown in the Figure A2.10 there was no reduction of Si concentration during the cultivation period.

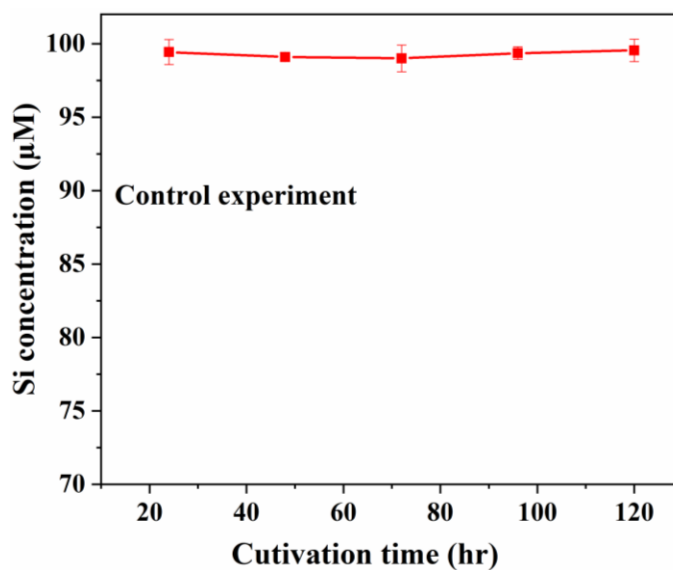


**Figure A2.10.** Control experiment without *C.sp.* cells.



### 2.7.9 Investigation of the internal structures of $C_0$ using FIB-SEM

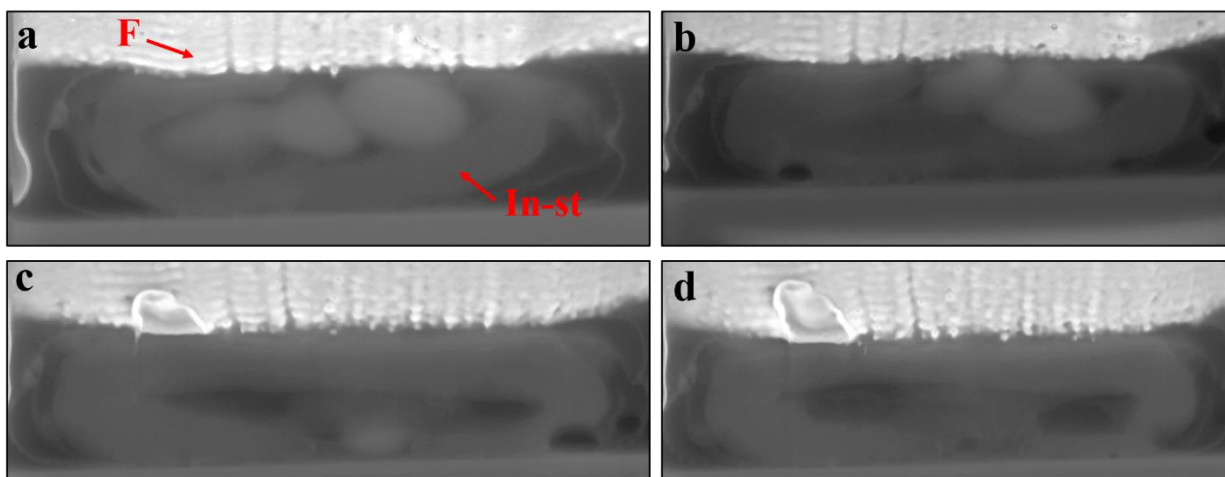


**Figure A2.11.** (a-d) depict the internal structures of  $C_0$  during the slice and view process.  $F$ = frustule,  $In-st$ = internal structures.

### 2.7.10 The effect of $Al^{3+}$ on silica hydrolysis

Diatoms ( $C_0$  &  $C_3$ ) were stored in demineralized water at 90 °C for 6 day. The Si concentration was determined via atomic absorption spectrometry.

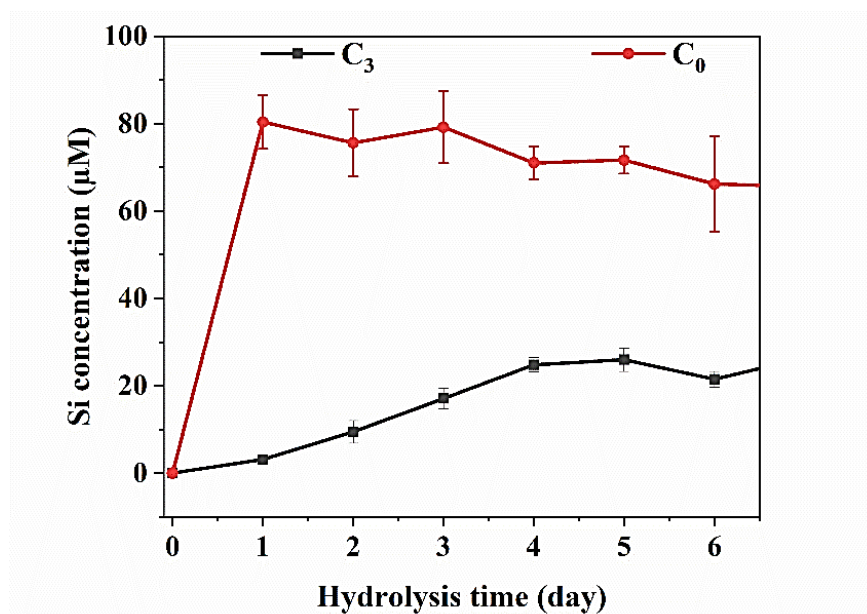


**Figure A2.12.** Si concentration as a function of time for  $C_0$  and  $C_3$ . Error bars represent standard deviation.

**Appendix Table A2.1.** Chemical composition of artificial seawater supplemented with f/2 medium.

Chemical	Final concentration
NaCl	356 mM
Na <sub>2</sub> SO <sub>4</sub>	25 mM
CaCl <sub>2</sub> .2H <sub>2</sub> O	8 mM
KCl	8 mM
H <sub>3</sub> BO <sub>3</sub>	404 $\mu$ M
KBr	714 $\mu$ M
NaF	71 $\mu$ M
NaHCO <sub>3</sub>	1.2 mM
MgCl <sub>2</sub> .7H <sub>2</sub> O	47 mM
Na <sub>2</sub> SiO <sub>3</sub> .9H <sub>2</sub> O	106 $\mu$ M
NaH <sub>2</sub> PO <sub>4</sub> .H <sub>2</sub> O	36 $\mu$ M
NaNO <sub>3</sub>	880 $\mu$ M
Fe(NH <sub>4</sub> ) <sub>2</sub> (SO <sub>4</sub> ) <sub>2</sub> . 6H <sub>2</sub> O	11.7 $\mu$ M
Na <sub>2</sub> MoO <sub>4</sub> .2H <sub>2</sub> O	35.9 nM
ZnSO <sub>4</sub> .7H <sub>2</sub> O	80 nM
CuCl <sub>2</sub>	40 nM
CoSO <sub>4</sub> . 7H <sub>2</sub> O	50 nM
MnSO <sub>4</sub> .4H <sub>2</sub> O	0.9 $\mu$ M
Na <sub>2</sub> EDTA.2H <sub>2</sub> O	11.7 $\mu$ M
Biotin vitamin	1 ml of a 2 mg/ml solution
vitamin B <sub>12</sub>	1 ml of a 4 mg/ml solution
Thiamine vitamin	1 ml of a 100 mg/ml solution

**Appendix Table A2.2.** Parameters used in EMFP ( $\Lambda$ ) calculations.

Materials	M <sub>w</sub> , g/mol	$\rho$ , g/cm <sup>3</sup>	$\Lambda$ , nm
SiO <sub>2</sub> (amorphous)	60.08	2.00	214.78
Carbon film	12.00	2.10	282.54

**Appendix Table A2.3.** Internal volume of *C.sp.* cell and the volume of silica making up the frustule (frustule volume). Average  $\pm$  Standard Deviations (n=5).

Culture number	Internal volume ( $\mu$ m <sup>3</sup> )	Frustule volume ( $\mu$ m <sup>3</sup> )
C <sub>0</sub>	1121.7 $\pm$ 2.3	19.2 $\pm$ 3.7
C <sub>1</sub>	1119.6 $\pm$ 3.4	21.4 $\pm$ 1.5
C <sub>2</sub>	1114.7 $\pm$ 1.8	26.8 $\pm$ 3.1
C <sub>3</sub>	1110.2 $\pm$ 2.7	30.2 $\pm$ 3.4

**Appendix Table A2.4.** Statistical data of SEM and TEM image analyses with n = number of measured valves per culture and expressed as Average  $\pm$  Standard Deviations.

Sample	C <sub>0</sub>	C <sub>1</sub>	C <sub>2</sub>	C <sub>3</sub>
<b>Features size</b>				
Valve length $\mu\text{m}$ (n=15)	19.2 $\pm$ 2.9	19.6 $\pm$ 2	19.5 $\pm$ 2.6	19.4 $\pm$ 3.1
Valves width $\mu\text{m}$ (n=15)	6.9 $\pm$ 0.8	7.1 $\pm$ 0.6	7.1 $\pm$ 0.9	6.97 $\pm$ 1
Valve area $\mu\text{m}^2$ (n=15)	99.1 $\pm$ 12	101.5 $\pm$ 13	100.4 $\pm$ 16	100.3 $\pm$ 15
Mean diameter of areola nm (n=15)	189 $\pm$ 9	182 $\pm$ 8	189 $\pm$ 27	182 $\pm$ 20
Mean diameter of small pore nm (n=15)	70 $\pm$ 9	61 $\pm$ 10	40 $\pm$ 5	35 $\pm$ 4
Width of transapical rib nm (n=15)	190 $\pm$ 38	191 $\pm$ 24	193 $\pm$ 19	188 $\pm$ 23
Width of cross extension nm (n=15)	105 $\pm$ 19	110 $\pm$ 16	108 $\pm$ 26	110 $\pm$ 19
Distance between neighboring areolae within a pore array nm (n=15)	278 $\pm$ 14	272 $\pm$ 15	273 $\pm$ 12	277 $\pm$ 15
Distance between two areolae of two parallel arrays nm (n=15)	346 $\pm$ 24	349 $\pm$ 19	349 $\pm$ 30	347 $\pm$ 18
Mean thickness of porous area nm (n=5)	49 $\pm$ 7	59 $\pm$ 6	71 $\pm$ 5	82 $\pm$ 8
Mean thickness of raphe nm (n=5)	153 $\pm$ 17	175 $\pm$ 15	178 $\pm$ 20	188 $\pm$ 18
Mean thickness of valve nm (n=5)	83 $\pm$ 7	101 $\pm$ 3	108 $\pm$ 2	121 $\pm$ 10

### 2.7.11 Appendix references

- 1 Mirabello, G., Keizer, A., Bomans, P. H., Kovács, A., Dunin-Borkowski, R. E., Sommerdijk, N. A. & Friedrich, H. Understanding the formation mechanism of magnetic mesocrystals with (cryo-) electron microscopy. *Chemistry of Materials* **31**, 7320-7328 (2019).
- 2 Kohl, H. & Reimer, L. *Transmission electron microscopy: physics of image formation*. (Springer, 2008).
- 3 Su, H., Mehdi, B. L., Patterson, J. P., Sommerdijk, N. A., Browning, N. D. & Friedrich, H. Growth kinetics of cobalt carbonate nanoparticles revealed by liquid-phase Scanning transmission electron microscopy. *The Journal of Physical Chemistry C* **123**, 25448-25455 (2019).
- 4 Ianiro, A., Wu, H., van Rijt, M. M., Vena, M. P., Keizer, A. D., Esteves, A. C. C., Tuinier, R., Friedrich, H., Sommerdijk, N. A. & Patterson, J. P. Liquid-liquid phase separation during amphiphilic self-assembly. *Nature chemistry* **11**, 320-328 (2019).

# Chapter 3

## **In situ Manipulation and Micromechanical Characterization of Diatom Frustule Constituents Using Focused Ion Beam Scanning Electron Microscopy**

### **Abstract**

Biocomposite structures are difficult to characterize by bulk approaches due to their morphological complexity and compositional heterogeneity. Therefore, a versatile method is required to assess, for example, the mechanical properties of geometrically simple parts of biocomposites at the relevant length scales. Here, we demonstrate how a combination of Focused Ion Beam Scanning Electron Microscopy (FIB-SEM) and micromanipulators can be used to isolate, transfer, and determine the mechanical properties of frustule constituents of diatom *Thalassiosira pseudonana* (*T.p.*). Specifically, two parts of the diatom frustule, girdle bands and valves, are separated by FIB milling and manipulated using a sharp tungsten tip without compromising their physical or chemical integrity. In situ mechanical studies on isolated girdle bands combined with Finite Element Method (FEM) simulations, enables the quantitative assessment of the Young's modulus of this biosilica;  $E=40.0$  GPa. In addition, the mechanical strength of isolated valves could be measured by transferring and mounting them on top of premilled holes in the sample support. This approach may be extended to any hierarchical biocomposite material, regardless of its chemical composition, to isolate, transfer, and investigate the mechanical properties of selected constituents or specific regions.

### **The results presented in this chapter are based on:**

Soleimani, M., van Breemen, L. C., Maddala, S. P., Joosten, R. R., Wu, H., Schreur-Piet, I., van Benthem, R. A. & Friedrich, H. *In Situ Manipulation and Micromechanical Characterization of Diatom Frustule Constituents Using Focused Ion Beam Scanning Electron Microscopy*. Small Methods **5**, 2100638 (2021).

### 3.1 Introduction

Hybrid materials made from organic and inorganic compounds often possess superior combinations of physical and chemical properties compared to their individual components, which make them attractive for many technological applications<sup>1</sup>. The development of advanced hybrid materials involves many disciplines including materials science and engineering, chemistry and biology<sup>2-5</sup>. In this respect, biocomposites such as bone, teeth, and shells are indispensable elements of living organisms and are an inspirational class of hybrid materials<sup>6,7</sup>. Biocomposites are formed via energy efficient and environmentally benign routes in aqueous environment at ambient temperature. They possess hierarchical ordering resulting in finely tuned properties not yet achievable by synthetic approaches<sup>8-10</sup>. Therefore, being able to accurately measure the properties of distinct components of biocomposites with different characteristics can inspire the fabrication of synthetic hybrids with properties tailored to specific applications<sup>7,11-13</sup>.

As biocomposites often possess structural and compositional heterogeneity, bulk measurements will not lead to a comprehensive determination of their underlying material properties<sup>14,15</sup>. A well-studied biocomposite is nacre which demonstrates outstanding mechanical properties resulting from the stacking of aragonite tiles and organic layers (resembling bricks and mortar)<sup>16</sup>. Not only does its mechanical performance vary with respect to the various loading directions but also different failure mechanisms have been proposed under different loading conditions<sup>17</sup>. It has been suggested that its excellent mechanical performances, such as Young's modulus in the range of 60-70 GPa<sup>18</sup>, depends on several parameters at different length scales, ranging from nano to micrometers<sup>14</sup>. Another, structurally complex biocomposite is the diatom frustule, i.e., the siliceous exoskeletons of unicellular photosynthetic algae, diatoms<sup>19</sup>. Diatoms are distributed throughout most aquatic environments, in an amazing multitude of shapes, and in sizes ranging from 2 to 2000  $\mu\text{m}$  in diameter or length<sup>20</sup>. The diatom frustule, composed of two valves and a number of overlapping girdle bands, possess a species-specific morphology of micro and nanopatterns<sup>21,22</sup>. The current understanding is that girdle bands and valves are different in terms of their structures, functions, and mechanical performance<sup>23-26</sup>. However, the basic mechanical properties such as Young's modulus of the frustule constituents have only been measured independently for a large diatom species<sup>27</sup>.

Mechanical properties of diatoms have been mainly measured by AFM on the frustule of various diatom species<sup>28,29</sup>. However, obtained results rather provide insights into indentation of the frustule's morphology than a quantitative measure of mechanical properties of specific parts, while an independent observation of the indentation action missing. More convincingly, in situ mechanical testing of diatoms have also been conducted in SEM, either on whole frustules<sup>30,31</sup> or on frustule fragments using three-point bending<sup>27</sup>. However, indentation on the entire frustule makes it difficult to distinguish the mechanical responses of the girdle bands from those of the valves. Also, due to the presence of complex hierarchical structures in the valves, a geometrically simplified FEM simulation is not adequate for a precise determination of basic mechanical properties such as the

Young's modulus. Owing to the wide variation of diatom sizes, the mechanical property measurements of the frustule segments in SEM were hitherto limited to large diatoms such as *Coscinodiscus sp.* (~150  $\mu\text{m}$  in diameter). The sample preparation for the SEM measurements of this species required harsh chemical separation of the frustule segments using  $\text{H}_2\text{O}_2$  and  $\text{HCl}$ , which not only resulted in unintentional fracture of the segments<sup>27</sup>, but may also have significantly altered the compositional and mechanical properties of the biosilica<sup>32</sup>.

Above examples demonstrate the importance of developing new techniques to assess the basic mechanical properties of biocomposites at all relevant length scales. This requires precise isolation of different parts of the diatom frustule and measurements on these individual constituents. Electron Microscopy (EM) has been used as an imaging tool to characterize materials at the relevant micro and nanoscales in situ<sup>33-36</sup>. Scanning Electron Microscopy (SEM) may be combined with Focused Ion Beam (FIB) micromachining and micromanipulators, allowing imaging and manipulation of micro and nano-objects in real time<sup>37</sup>. FIB-SEM micromachining is involved in the fabrication and observation of micro and nano-test specimens<sup>38</sup>, and by using a micromanipulator, objects can be picked up, transferred and released from a bulk sample to a particular substrate for further investigation<sup>39,40</sup>. Using a combination of FIB-SEM and micromanipulators, characterization of the mechanical properties of materials on various length scales becomes feasible<sup>41,42</sup>. In situ mechanical testing such as bending, indentation, and compression tests via micromanipulators inside SEM has been one of the attractive approaches for observing the deformation behaviors of micro and nano-scale materials<sup>43-45</sup>. However, to the best of our knowledge there has been no investigation that combined in situ isolation, manipulation, and mechanical characterization of individual constituents of biocomposites such as diatom frustules.

In this chapter, we demonstrate a flexible workflow exploiting FIB-SEM with micromanipulators to isolate, prepare, and characterize selected biosilica segments of diatoms to determine their Young's modulus, on the micrometer scale. As a model and example of biocomposite materials, the diatom frustules of *Thalassiosira pseudonana* (*T.p.*), grown at different salinities, were used.<sup>46</sup> Using our specific sample fabrication, and in situ deformation experiments supported by FEM simulations, the Young's modulus of biosilica diatom frustule constituents, i.e. girdle bands could be quantitatively assessed. The presented methodology may be employed for other in situ characterization of the constituents of hierarchical biocomposites that cannot be accessed by other means.

## 3.2 Results and Discussion

An overview of the entire sample preparation and characterization workflow is shown in Figure 3.1. After deposition of the extracted intact diatom frustules on the SEM sample support, FIB micromachining is used to detach the valves from the girdle bands (Figure 3.1, Step 1). Subsequently either the girdle bands or the valves are transferred to specific locations for in situ deformation experiments (Figure 3.1, Step 2a&2b). Mechanical tests are carried out using a force measurement sensor (FMT-120) attached to a micromanipulator in combination with information from

SEM images to obtain a load-displacement curve (Figure 3.1, Step 3a&3b). Finally, by Finite Element Method (FEM) simulations of the load-displacement curve using all relevant morphological information the Young's modulus of the biocomposite, girdle bands, can be derived (Figure 3.1, Step 4).

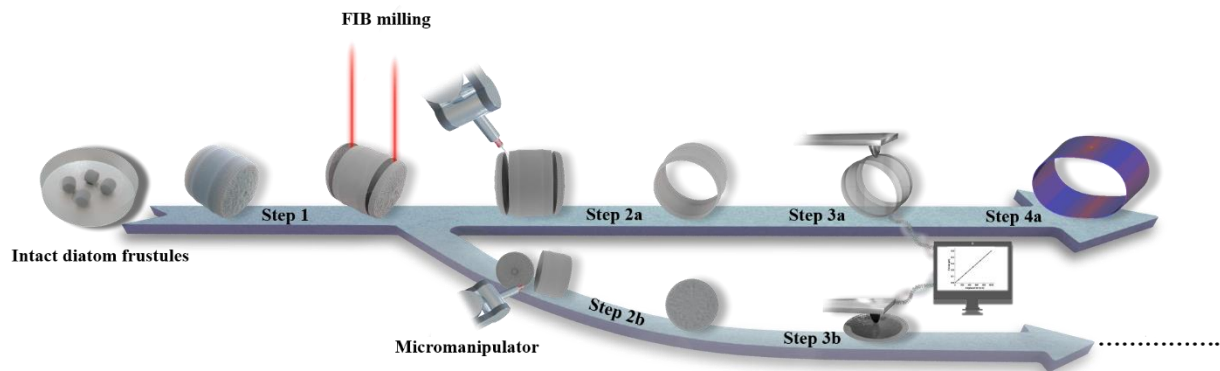


**Figure 3.1.** Scheme of in situ isolation, transfer, and deformation of constituents of diatom frustule. (Step 1) FIB milling on intact diatom frustule; (Step 2a&2b) isolation and transfer of valves and girdle bands; (Step 3a&3b) deformation tests on isolated girdle bands and valves; (Step 4) employing the experimental data for determining the Young's modulus of the girdle bands by FEM simulations.

In the following sections each step of above workflow will be described and discussed, starting with a detailed investigation of the morphological parameters of frustule of *T.p.* in dependence of the growth conditions, including mild extraction of the frustules from living cells, preserving the physical and chemical integrity of the natural biocomposite as best as possible, and deposition on the SEM sample substrate.

### 3.2.1 Morphological parameters of *T.p.*

*T.p.* is one of the smallest and most well-known diatoms. It is of great interest to scientists due to its fully sequenced genome and high adaptability to various environmental conditions, including salinity levels<sup>47-49</sup>. In this study, salinity levels found in nature, namely 28, 36, and 46 PSU (Practical Salinity Unit),<sup>46,50</sup> were employed in the growth medium in order to gain insights into the effect of this factor on the mechanical and morphological parameters of *T.p.* The frustules were extracted from the living cells by washing with ethanol and subsequent drying in a critical point dryer in order to, not only reduce the impact of the extraction process on the natural chemistry and morphology, but also to prevent the collapse of the frustule (more details are provided in the Experimental Section and Appendix Figure A3.1). The dried frustules were then deposited on SEM stubs or TEM grids for morphological analysis. *T.p.* is a centric diatom with a cylinder-shaped cell wall that contains two valves/lids connected by several overlapping girdle bands (Figure 3.2a). As shown in Figure 3.2b, the valve's exterior surface exhibits patterns of ribs known as costae connected by cross-connections, forming areole pores. Within the areole, some small pores called cribrum are located. Unlike the exterior surface, the interior surface of the valves are relatively smooth without ribs and the cribrum pores clearly being visible (Figure 3.2c). Figure 3.2d presents

a girdle band, isolated by ultrasonication, which has porous and nonporous regions. SEM- Energy-Dispersive X-ray Spectroscopy (SEM-EDS) elemental mapping of an intact frustule, from both valve and girdle bands views, shows a homogenous distribution of silicon alongside oxygen and carbon, indicating their uniform distribution throughout the entire diatom frustule (Figure 3.2e-h).

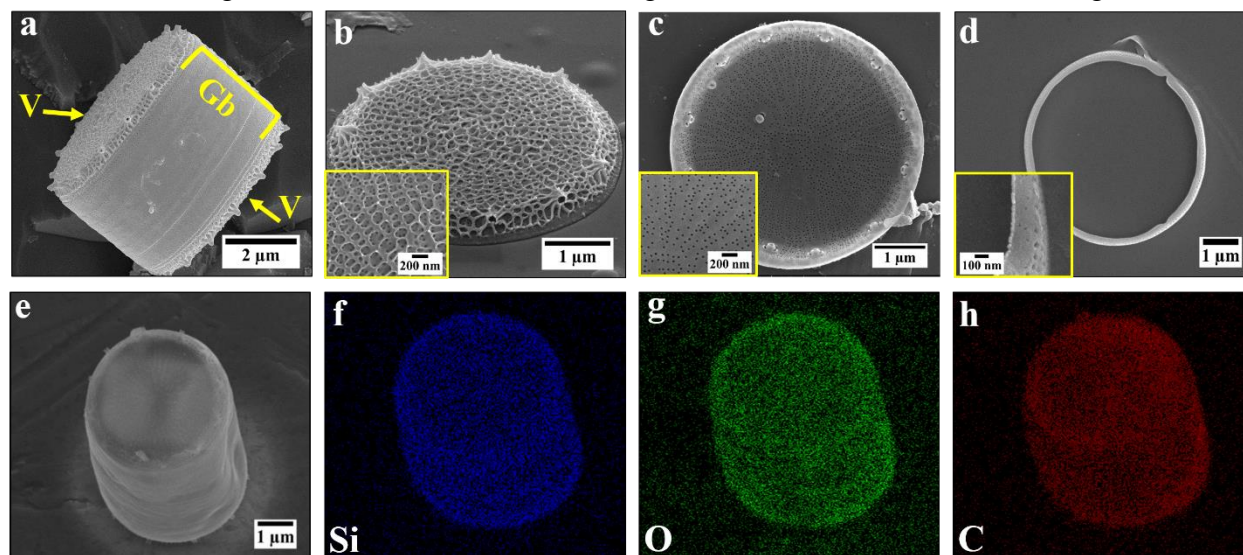


**Figure 3.2.** (a) SEM images of intact mature frustule of *T.p.* (V and Gb referring to valve and girdle bands, respectively); (b) exterior surface of an isolated valve; (c) interior surface of an isolated valve; (d) individual girdle band; Insets in b, c and d show high magnification images.; (e-h) SEM-EDS elemental maps of an entire frustule viewed from the direction of both valve and girdle bands.

To establish whether morphological characteristics such as thickness, pore size, and overall size of the valves and girdle bands of *T.p.* were altered by increasing the salinity levels in the growth medium, TEM and SEM image analyses were conducted. Varying salinity levels did not change the valve diameter and the girdle bands length of the frustule (Appendix Figure A3.2). High magnification SEM images of the interior surface of the valves grown at different salinities show that the cribrum pore size was unchanged when the salinity was increased from 28 to 36 PSU, with the cribrum pore size measuring  $20 \pm 3$  and  $19 \pm 4$  nm in diameter, respectively. At a salinity of 46 PSU the cribrum pore size increased to  $27 \pm 3$  nm (Appendix Figure A3.3&A3.4). The thicknesses of the girdle bands and valves were measured from TEM images<sup>51</sup>, (Appendix Figure A3.5&A3.6). The mean thicknesses of the girdle bands for 28 and 36 PSU were  $26 \pm 5$  and  $25 \pm 5$  nm, respectively, whereas at 46 PSU girdle bands had a thickness of  $21 \pm 4$  nm.

### 3.2.2 Step 1&2: Detaching the valves from girdle bands

The first step in the procedure to determine the mechanical properties of the frustule was to isolate the valves from the girdle bands. Since the thickness of the girdle bands was less than 30 nm and the inside of the cell was empty, resembling a hollow cylinder, the lowest possible ion current (1.5 pA) was employed during the FIB milling procedure to prevent collapsing the structure. Figure 3.3a shows an intact frustule of *T.p.* laying on its girdle bands. By FIB milling, the valves were precisely detached from the girdle bands. Then, one of the detached valves was moved using the



sharp tungsten tip to the right side of the frustule where it was ultimately separated without damaging the girdle bands. The insignificant adhesive force between the detached valve and girdle bands, which may be due to the milling process or electrostatic in nature, was overcome by slightly pushing the valve toward the girdle bands. Finally, after complete separation of the valve via the micromanipulator tip, the valve was removed entirely to eliminate its hindering effect during the deformation tests on the girdle bands (see also Appendix Movie A3.1). As shown in Figure 3.3a this manipulation was entirely performed by push-pull or mechanical manipulation<sup>52</sup>, with a sharp tungsten tip which did not damage the valves or girdle bands.

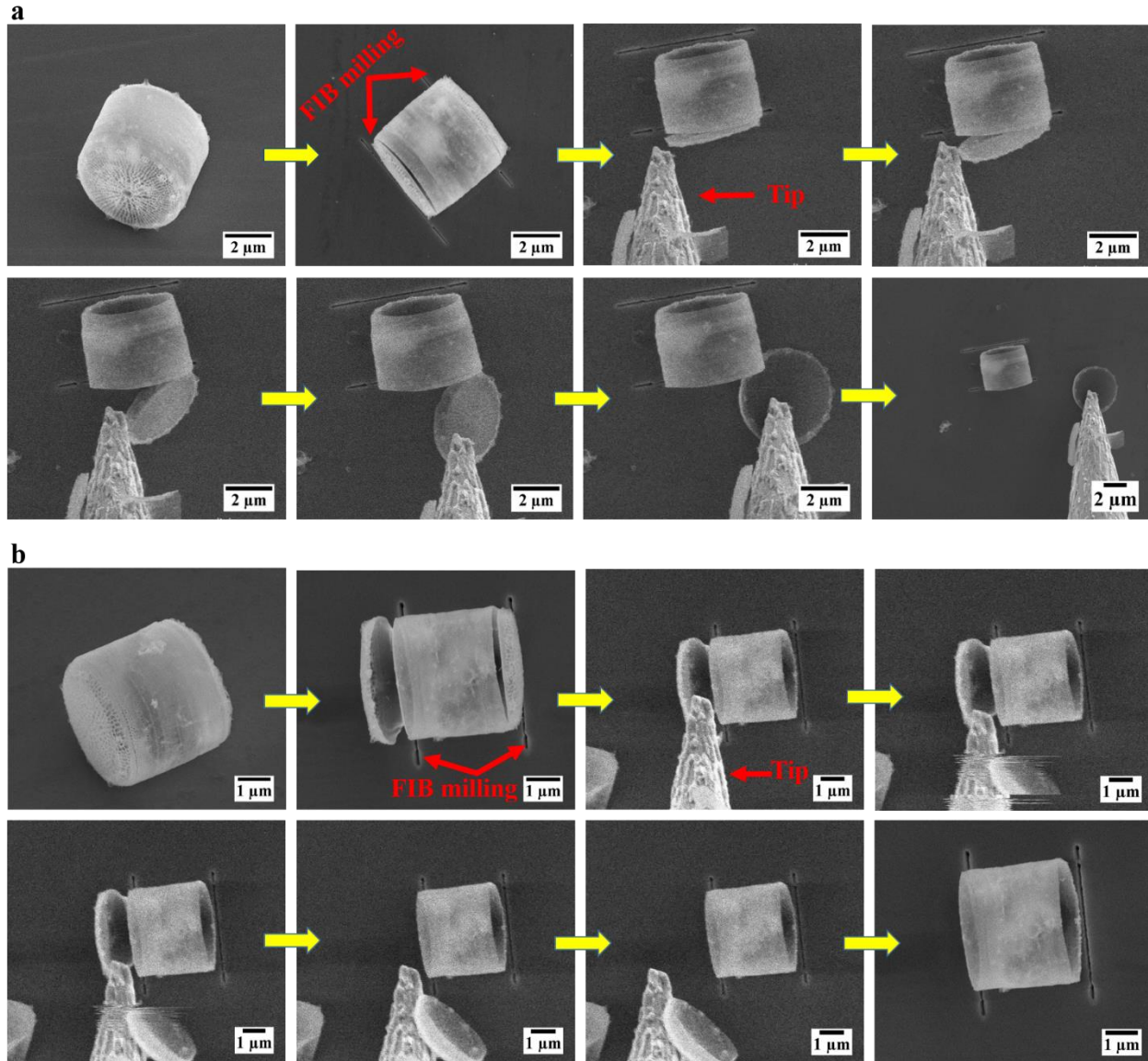


**Figure 3.3.** (a) mechanical manipulation: Intact frustule of *T.p.* positioning on its girdle bands, cutting the valves with FIB milling, from left to right: sequence of mechanical manipulation for removing the valve via a tungsten tip, an isolated girdle bands after complete separation of the valves was obtained; (b) (from left to right) sequence of FIB milling and electrostatic manipulation of an isolated valve from the girdle bands of an intact frustule.

The second method employed to isolate the valves was based on electrostatic manipulation. The detached valves were retained on the silicon wafer by various attractive forces such as van der

Waals<sup>39</sup> and adhesive forces induced by the ion beam during the milling process. The charging of the non-grounded tungsten tip caused by electron beam illumination led to the attraction of the specimen<sup>53</sup>, here the detached valves to the tip. The charged tip was brought into contact with the detached valve. When the attractive forces between the tip and valve (likely van der Waals and electrostatic) were stronger than the aforementioned forces, which held the valve on the substrate, the valve attached to the tip. Figure 3.3b show a series of images of electrostatic manipulation which finally removed the valves and a hollow cylinder-shaped structure was obtained (see also Appendix Movie A3.2). Releasing the electrostatically attached valve from the tip was performed by touching the substrate with the valve and shifting the electron beam irradiation away from the tip. Various parameters such as the electron energy, sample size and shape, roughness of the sample, and distance between the tip and sample are important in electrostatic manipulation inside SEM<sup>54</sup>. It should be noted that it was difficult to selectively choose between one of the two aforementioned manipulations over the other. In general, there may be a link between the type of manipulation and some factors such as the direction between the tip and the valve, which can cause different contact areas, the gap between the detached valve and girdle bands, and contact area between the valve and substrate. Nevertheless, further research should be undertaken to investigate the exact causes which led to electrostatic and mechanical manipulation of the valves.

### 3.2.3 Step 3a: In situ deformation tests on isolated girdle bands

In order to investigate the mechanical behavior of girdle bands in situ deformation tests were performed with a force measurement sensor FMT-120 which was mounted on the micromanipulator. SEM images were continuously acquired throughout the whole process to follow the deformation behavior of the girdle bands. A series of controlled displacement experiments were conducted on the isolated girdle bands of *T.p.* which had been grown at different salinities, 28 and 46 PSU. Throughout the deformation experiments, the force measurement system (FMS) provides force-time data which could be converted to force-displacement information via image analysis of the SEM micrographs. Some images from the deformation tests on isolated girdle bands of *T.p.* grown at different salinities are presented in Figure 3.4a together with representative load-displacement curves. As shown in the SEM images, the girdle bands completely returned to their original shape after retracting the tip, without a significant plastic deformation, suggesting elastic properties of these parts (see also Appendix Movie A3.3). An equal mean maximum force ( $n=3$ ) of  $0.50 \pm 0.02$  and  $0.52 \pm 0.03$   $\mu\text{N}$  were required for about 1050 nm deformation of girdle bands grown at 28 and 46 PSU, respectively. As shown in Figure 3.4b, the aforementioned 20 % difference in thickness due to the different salinity in the growth medium surprisingly did not significantly impact the mechanical behavior of girdle bands. Here it is important to note that it is known that the frustules of *T.p.* grown at 46 PSU is more condensed than 26 PSU<sup>49</sup>. Hence, it could be hypothesized that despite the difference in thickness of the girdle bands at 28 and 46 PSU, the difference in the condensation state of the biosilica might cause close to identical mechanical behaviors. The experimental nonlinearities in the load-displacement curves, as well as the very limited plastic deformation between load-unload curve observed during the first cycle of the experiment (Appendix Figure A3.7) are probably due to rearrangements between individually overlapping girdle bands

(Appendix Figure A3.8) during the deformation tests. Interestingly, no fracture/failure was detected even when the girdle bands were completely compressed and touching the opposing side. The girdle bands showed fully elastic recovery after the tip retraction. To determine whether the organic compounds within the girdle bands contributed to this behavior, the same deformation experiment was performed on a set of thermally treated (450 °C) girdle bands. In this case a noticeable irreversible deformation was observed upon deformation and tip retraction in this sample (Appendix Figure A3.9). While this is a first indication of the role of organics in attaining elasticity of girdle bands, considerably more work will need to be done to determine the effects of various organic compounds such as long-chains polyamines, silaffins, and other macromolecules<sup>22</sup> within the frustules of diatoms on their mechanical performance. It is worth noting that since all of the deformation testes were carried out inside SEM, at high vacuum, the effect of trapped water molecules even if present, cannot noticeably govern the elasticity/plasticity of the girdle bands.

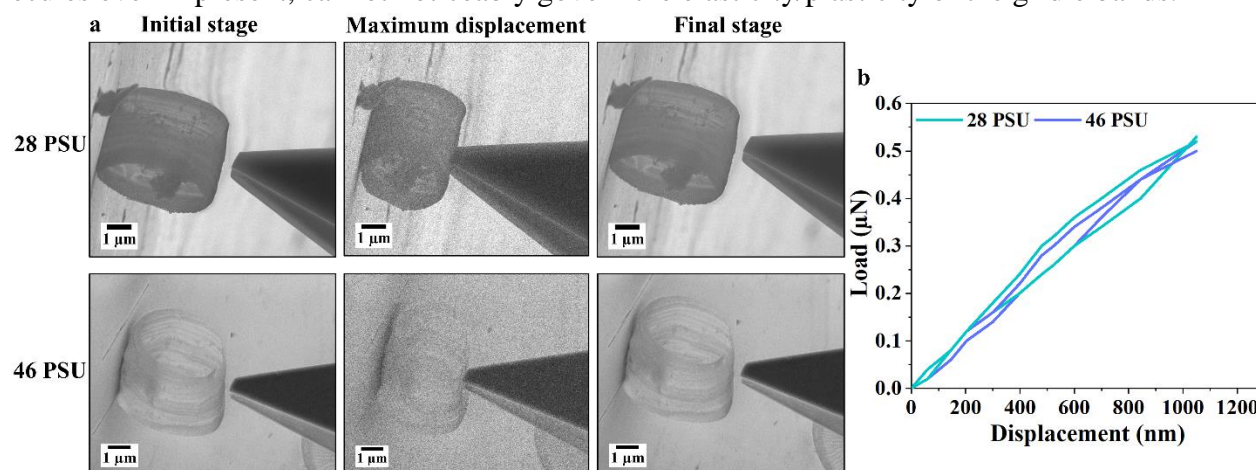


**Figure 3.4.** (a) *In situ* mechanical experiments on isolated girdle bands grown at different salinity (top) 28 PSU; (bottom) 46 PSU. SEM images at different states of the experiment, before, during, and after the deformation tests (poor resolution of images at the maximum displacement is due to the shorter dwell time of imaging during the deformation tests); (b) representative load-displacement curves for 28 PSU (blue) and 46 PSU (green) during the displacement-controlled deformation. For clarity only two of the obtained curves per salinity are shown.

### 3.2.4 Step 4: FEM simulation and deriving the Young's modulus

Based on the experimental results for the required force causing a given displacement and also SEM and TEM image analysis, FEM simulation was employed to determine the intrinsic mechanical properties of girdle bands (grown at 28 PSU), i.e., its Young's modulus. Figure 3.5 exhibits the initial and maximum displacement states of the model and its corresponding elastic load-displacement curve. FEM simulation illustrated that for 0.45 μN force causing 1050 nm displacement, sufficiently close to the obtained experimental value, a Young's modulus  $E$  of 40.0 GPa was determined for our biosilica. This result is comparable to the reported average Young's modulus of biosilica from *Coscinodiscus sp* (36.4 GPa) obtained by three-point bending tests on a large lamella of its frustule inside an SEM<sup>27</sup>.

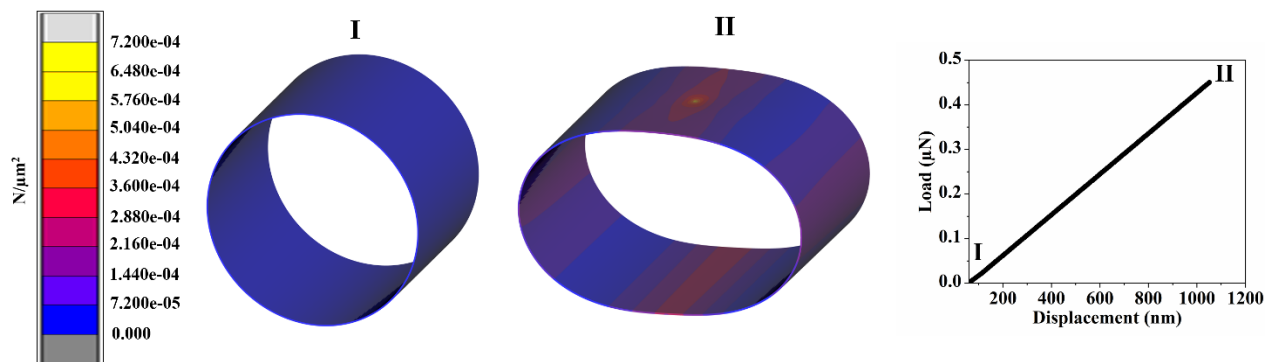


**Figure 3.5.** The images show the situation in the initial undeformed configuration, I, as well as the situation at maximum deformation, II, of the girdle bands as a result of the deformation with the FMT tip. For clarity, the FMT tip is omitted from the images. The colors in the images represent the equivalent Von Mises stress as indicated by the scale bar on the left. The graph on the right-hand side displays the force response in dependence of deformation.

### 3.2.5 Effect of accelerating voltage and deformation cycles on the mechanical behavior of girdle bands

To assess whether and to what extent the mechanical behavior of the girdle bands could be affected by the experimental conditions, in situ deformation experiments were carried out at various accelerating voltages inside the SEM chamber. As can be seen in Figure 3.6a, despite applying various accelerating voltages, from 3 kV (electron dose:  $D=7.5 \times 10^{-7} \text{ C/cm}^2$ ) to 30 kV ( $D=3.2 \times 10^{-6} \text{ C/cm}^2$ ), the girdle bands retained their elasticity. By increasing the accelerating voltage from 3 to 10 kV the amount of applied force for a given displacement remained constant at  $0.50 \pm 0.02 \text{ μN}$ . However, as shown in Figure 3.6b, from 10 to 20 kV there was an enhancement in resistance to deformation ( $0.75 \text{ μN}$  at maximum), indicating increased hardening of the girdle bands by electron irradiation. Further increasing the accelerating voltage to 30 kV resulted in an even more pronounced effect. As shown in the graph, approximately twice the force was required for the same amount of displacement in comparison to 10 kV. These results may be explained by the fact that increasing the energy of the impinging electron inside the EM before and during the mechanical testing can lead to the conversion of less condensed silica structures to more condensed silica networks<sup>55,56</sup>. Since the wall thicknesses of the girdle bands at different acceleration voltages are identical, the observed increase in stiffness is therefore not geometry related. This behavior can only be explained by an increase in the elastic/Young's modulus, which in turn is directly related to its density,<sup>57</sup> i.e. higher density gives a higher modulus. In addition, in order to monitor effects of the number deformation cycles on the mechanical behavior of the girdle bands, a series of deformation test was conducted on one specific set of girdle bands for a given displacement. As shown in Figure 3.6c, the girdle bands kept their elastic behaviors upon deformation and tip retraction without noticeable irreversible deformation throughout various cycles. The maximum forces for a given displacement were measured for 10 consecutive cycles (Figure 3.6d). Interestingly, it can be seen from the data in the graph that the number of deformations did not influence the required force for approximately  $1 \text{ μm}$  displacement of the girdle bands, indicating the independence of the mechanical performance of girdle bands on the number of deformation cycles.



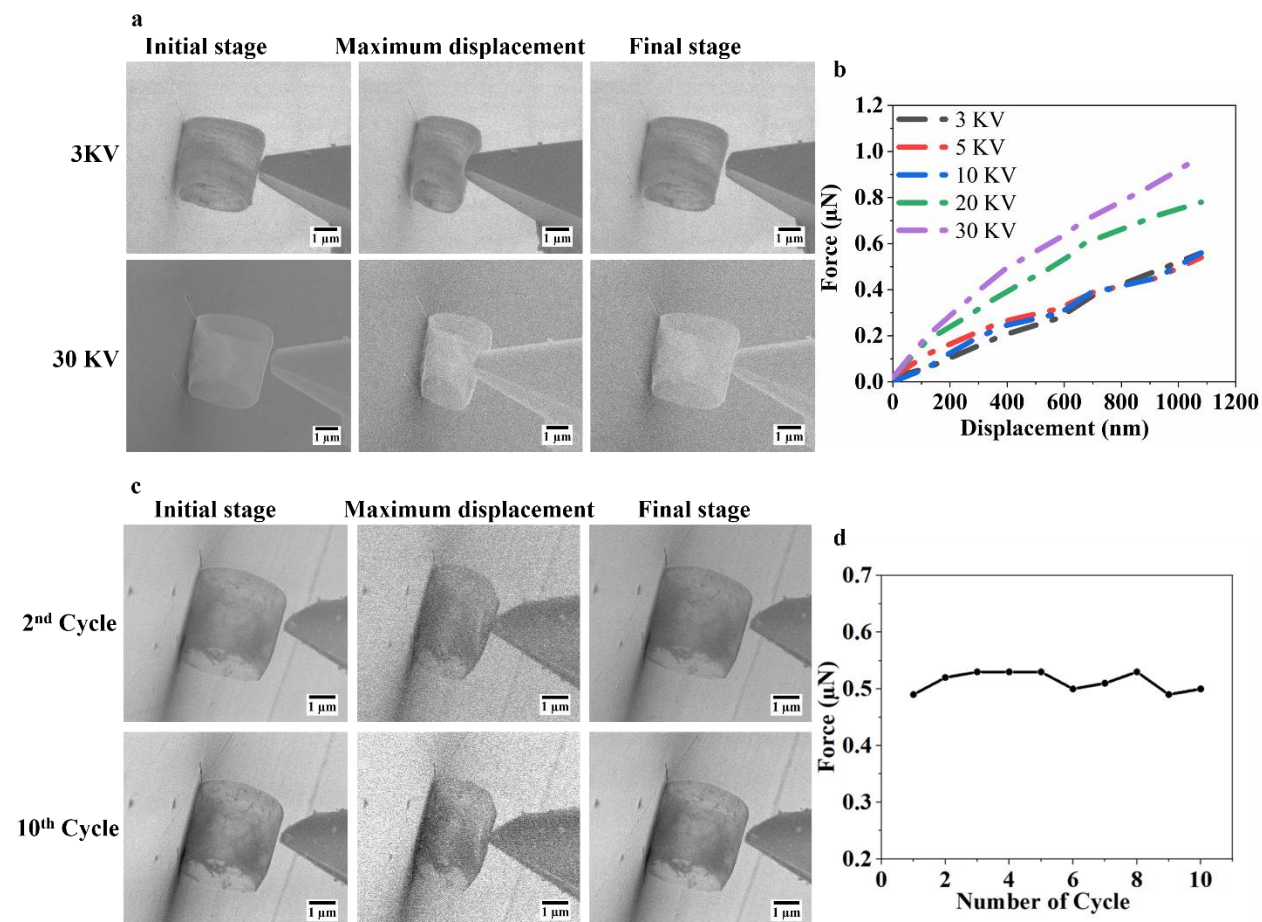


**Figure 3.6.** (a) SEM images of different states of deformation experiments of girdle bands at different applied accelerating voltages; 3 KV; 30 KV; (b) load-displacement curves of an individual set of girdle bands at different accelerating voltages. (c) SEM images of different states of deformation experiments of girdle bands for different cycles; (d) graph showing maximum force measurements in dependence of deformation cycle number of a set of girdle bands.

### 3.2.6 Step 2b&3b: Transferring and in situ deformation on isolate valves

The mechanical properties of the detached valves were also investigated. To this end, holes were drilled in the substrate by FIB milling and the valves were mounted on these holes, thus the effect of the substrate on the mechanical properties of the valves was eliminated. Figure 3.7a presents a sequence of images of transferring and mounting a deposited isolated valve from the substrate to a hole (see also Appendix Movie A3.4). After mounting the valves on their pre-defined holes, deformation experiments were performed by FMT-120 to in situ determine the required force for breaking the valves grown at 28 and 46 PSU. As shown in Figure 3.7b, during the deformation, the fracture took place in the middle of the valve, and the crack propagated through the ribs and areole pores toward the periphery. The obtained mechanical strength of the valves revealed substantial differences for these two salinities. The required force for breaking valves at 28 PSU was  $12.53 \pm 1.43 \mu\text{N}$ . In contrast, valves grown at 46 PSU did not have the same mechanical strength and only  $5.10 \pm 2.04 \mu\text{N}$  was necessary to break them (Figure 3.7c). In order to understand how salinity level regulated the mechanical strength of valves, TEM image analysis was conducted to

measure the thickness of the valves (Appendix Figure A3.6). The mean thickness of the ribs and cross-connections of the whole valves decreased from  $54 \pm 6$  nm to  $19 \pm 8$  nm by increasing the salinity from 28 to 46 PSU. These findings suggest that a higher salinity level in the growth medium led to thinner valves, resulting in less mechanical strength, which is in agreement with the previous study revealing that ribs and cross-connections of the valves have a significant impact on the mechanical properties of frustule of *T.p.*<sup>30</sup> Determination of the Young's modulus of the biosilica in the valves is challenging due to their complex architecture. Potentially techniques like TEM electron tomography can provide a realistic model of complex morphologies at the micro and nano scale for FEM simulations,<sup>58</sup> however, a versatile workflow has not been developed for universal usage of ET data in FEM to date.

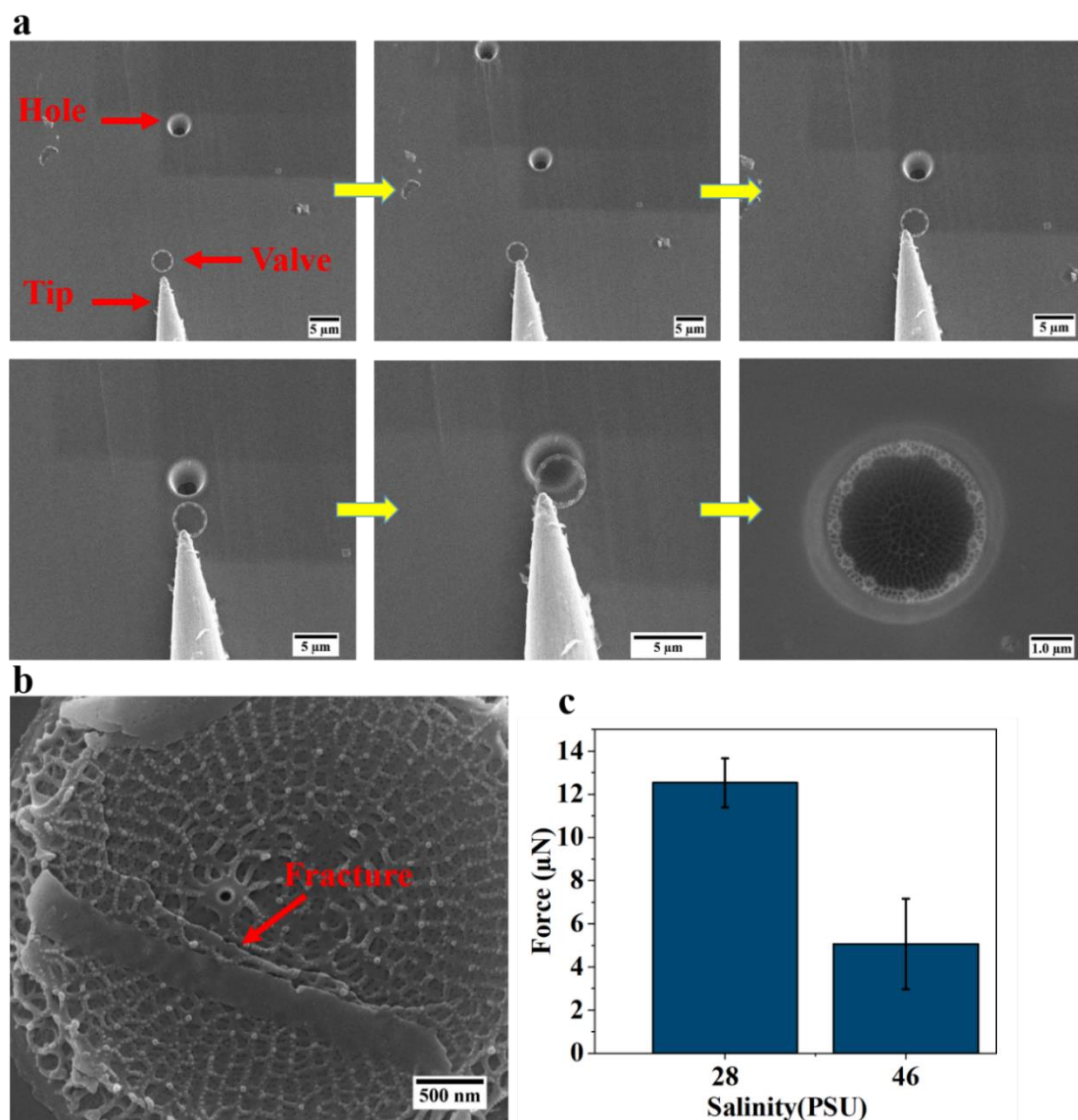


**Figure 3.7.** (a) SEM images of the process of manipulation and transferring of an isolated valve of *T.p.* from the silicon wafer substrate to a prefabricated hole before the in situ deformation tests; (b) SEM image of the fracture in a valve after deformation (the red arrow shows the fracture); (c) bar graphs of required force for breaking the valves grown at salinities 28 and 46 PSU ( $n=5$  valves per culture). Error bars indicate standard deviations.

### 3.3 Conclusions

In summary, a workflow to characterize the mechanical properties of a biocomposite diatom frustule, on the micrometer scale has been developed. The workflow combines FIB micromachining, micromanipulators, and deformation tests with FEM simulations to determine the Young's modulus of biosilica. In situ isolation, transfer, and deformation on different constituents, girdle bands and valves of diatom frustule, *T.p.*, were conducted inside a dual-beam SEM. The effects of salinity levels in the growth medium as well as electron beam damage on the mechanical properties of the frustule could be quantitatively established. The presented in situ sample preparation workflow preserves the delicate components of biocomposites and allows to quantify the mechanical properties of valves and girdle bands individually. Our approach can be extended to other species to accurately measure the mechanical properties of selected constituents of biocomposite materials at different hierarchical levels.

### 3.4 Experimental Section

#### 3.4.1 Diatom culture

*T.p.* (UTEX LB FD2) was obtained from the UTEX Culture Collection of Algae and incubated in artificial seawater supplemented with f/2 medium (ASW-f/2) at different salinity levels termed 28, 36, and 46 practical salinity unit (PSU). These are similar salinities, to which *T.p.* is known to be adaptive, the chemical effects on its frustule are well documented.<sup>46</sup> A climate cabinet (Flohr, Netherlands) with a light/dark cycle of 14 h/10 h at 23 °C and a light intensity of 3000 Lux was employed to grow cell cultures. The cell cultures were shaken daily during the entire experiment to ensure appropriate mixing of the growth medium.

#### 3.4.2 Scanning electron microscopy imaging and Energy-Dispersive x-ray Spectroscopy elemental mapping

For SEM imaging of the intact frustule, a small amount of the critical point dried frustules (Appendix Section A3.6.1) was deposited on a silicon wafer fixed to an SEM stub and sputter-coated with gold of less than 5 nm in thickness using a Quorum Q150T Plus–Turbo molecular pumped sputter coater. Before SEM imaging of the individual valve and girdle bands, the intact frustules were suspended in ethanol using a sonication bath (Branson ultrasonic cleaner, model 1510E-DTH, 42 kHz, USA) for 1 minute to completely split girdle bands from the valves (although this method also often resulted in some broken valves and girdle bands). For EDS elemental mapping, intact frustules were deposited onto a standard aluminum SEM Stub. SEM imaging and EDS elemental mapping were conducted using dual-beam SEM Quanta 3D FEG (Thermo Fisher Scientific, USA), at an acceleration voltage of 5-10 KV. The applied electron dose during the deformation experiments were calculated using following equation:  $D = \frac{I \times t}{S}$  where I is probe current, t is the imaging time and S is the illuminated area.

### 3.4.3 Focused ion beam-scanning electron microscopy and micromanipulator

In order to precisely separate valves and girdle bands from each other, the intact frustules of *T.p.* were deposited on a silicon wafer that was fixed to an aluminum SEM stub. The frustules laying on their girdle bands were selected for isolation of their valves from the girdle bands. The FIB milling process was carried out in a dual-beam SEM Quanta 3D FEG (Thermo Fisher Scientific, USA), equipped with a gallium ion ( $\text{Ga}^+$ ) source operating at an accelerating voltage of 30 kV. Because of the very delicate structure of the frustule of *T.p.*, employing a very low ion beam current (1.5 pA) during a single line scan milling process was critical to prevent structural collapse. Higher currents of the ion beam ( $I \geq 10$  pA) as well as multiple line scans with the current of 1.5 pA, notably damaged the girdle bands as well as valves and led to the structural collapse of the entire frustule. SEM images illustrating the effects of different milling parameters are shown in the Appendix Figure A3.10. One of the crucial aspects of isolating the valves from the girdle bands of *T.p.* was to cut a line between valves and girdle bands, narrow and accurate enough not to cause any significant asymmetry to their overall topology. After cutting the valves from the girdle bands, a micromanipulator (MM3A-EM, Kleindiek Nanotechnik GmbH, Germany) was employed to separate them. The micromanipulator provided a high positional accuracy ( $\sim 10$  nm) for the mechanical movement in three axes inside the SEM chamber. A sharp tungsten tip ( $\sim 150$  nm in radius) attached to the micromanipulator was employed for the manipulation of the valves. After complete isolation of the valve by the tip, the valve was transferred using the tip to another area of the substrate where a hole with a diameter in the range of a valve diameter had been prefabricated by FIB milling.

### 3.4.4 In situ deformation experiments

Mechanical experiments on isolated girdle bands and valves were conducted using a force measurement unit (FMT-120) mounted on the MM3A-EM micromanipulator inside the FIB-SEM chamber. Throughout the deformation experiments, the force measurement system (FMS) provided force-time data which could be converted to force-displacement information via SEM image analysis. To do so, SEM micrographs were acquired continuously throughout the experiment. Then, the displacements were determined by following the positional change of the edge of the girdle bands. Correlated displacements of the girdle bands with various times were determined using a Gatan Digital Micrograph and, subsequently, the corresponding applied force on the girdle bands was noted for each displacement point. The deformation experiments on the girdle bands were carried out in a controlled displacement mode, where the tip was moved toward the girdle bands until the desired deformation was obtained. Furthermore, to monitor the influence of deformation rate on the mechanical properties of girdle bands, a series of experiments were conducted on a set of isolated girdle bands with different loading rates. As seen in the Appendix Figure A3.11, lowering the rate of deformation resulted in a slight decrease in measured load. It should be noted that deformation cycle experiments were carried out in low vacuum mode SEM (LVSEM) at 10 KV with relative humidity of 4.3 %. In addition, the necessary force for breaking the valves was measured via the deformation tests on the isolated valves mounted on prefabricated holes.



### 3.5 References

- 1 Al Zoubi, W., Kamil, M. P., Fatimah, S., Nashrah, N. & Ko, Y. G. Recent advances in hybrid organic-inorganic materials with spatial architecture for state-of-the-art applications. *Progress in Materials Science* **112**, 100663 (2020).
- 2 Yao, H. B., Fang, H. Y., Tan, Z. H., Wu, L. H. & Yu, S. H. Biologically inspired, strong, transparent, and functional layered organic-inorganic hybrid films. *Angewandte Chemie* **122**, 2186-2191 (2010).
- 3 Gibson, R. F. A review of recent research on mechanics of multifunctional composite materials and structures. *Composite Structures* **92**, 2793-2810 (2010).
- 4 Ali, A. & Andriyana, A. Properties of multifunctional composite materials based on nanomaterials: a review. *RSC Advances* **10**, 16390-16403 (2020).
- 5 Kim, Y.-Y., Carloni, J. D., Demarchi, B., Sparks, D., Reid, D. G., Kunitake, M. E., Tang, C. C., Duer, M. J., Freeman, C. L. & Pokroy, B. Tuning hardness in calcite by incorporation of amino acids. *Nature Materials* **15**, 903-910 (2016).
- 6 Arakaki, A., Shimizu, K., Oda, M., Sakamoto, T., Nishimura, T. & Kato, T. Biomineralization-inspired synthesis of functional organic/inorganic hybrid materials: organic molecular control of self-organization of hybrids. *Organic & Biomolecular Chemistry* **13**, 974-989 (2015).
- 7 Luz, G. M. & Mano, J. F. Mineralized structures in nature: examples and inspirations for the design of new composite materials and biomaterials. *Composites Science and Technology* **70**, 1777-1788 (2010).
- 8 Ji, B. & Gao, H. Mechanical properties of nanostructure of biological materials. *Journal of the Mechanics and Physics of Solids* **52**, 1963-1990 (2004).
- 9 Libonati, F. & Buehler, M. J. Advanced structural materials by bioinspiration. *Advanced Engineering Materials* **19**, 1600787 (2017).
- 10 Ghazlan, A., Ngo, T., Tan, P., Xie, Y. M., Tran, P. & Donough, M. Inspiration from Nature's body armours—a review of biological and bioinspired composites. *Composites Part B: Engineering* **205**, 108513 (2021).
- 11 Rim, J. E., Zavattieri, P., Juster, A. & Espinosa, H. D. Dimensional analysis and parametric studies for designing artificial nacre. *Journal of the Mechanical Behavior of Biomedical Materials* **4**, 190-211 (2011).
- 12 Grossman, M., Pivovarov, D., Bouville, F., Dransfeld, C., Masania, K. & Studart, A. R. Hierarchical toughening of nacre-like composites. *Advanced Functional Materials* **29**, 1806800 (2019).
- 13 Munch, E., Launey, M. E., Alsem, D. H., Saiz, E., Tomsia, A. P. & Ritchie, R. O. Tough, bio-inspired hybrid materials. *Science* **322**, 1516-1520 (2008).
- 14 Espinosa, H. D., Rim, J. E., Barthelat, F. & Buehler, M. J. Merger of structure and material in nacre and bone—Perspectives on de novo biomimetic materials. *Progress in Materials Science* **54**, 1059-1100 (2009).
- 15 Ji, B. & Gao, H. Mechanical principles of biological nanocomposites. *Annual Review of Materials Research* **40**, 77-100 (2010).
- 16 Meyers, M. A., Chen, P.-Y., Lin, A. Y.-M. & Seki, Y. Biological materials: structure and mechanical properties. *Progress in Materials Science* **53**, 1-206 (2008).
- 17 Chen, P.-Y., Lin, A., Lin, Y.-S., Seki, Y., Stokes, A., Peyras, J., Olevsky, E., Meyers, M. A. & McKittrick, J. Structure and mechanical properties of selected biological materials. *Journal of the mechanical behavior of biomedical materials* **1**, 208-226 (2008).
- 18 Wang, J., Cheng, Q. & Tang, Z. Layered nanocomposites inspired by the structure and mechanical properties of nacre. *Chemical Society Reviews* **41**, 1111-1129 (2012).
- 19 Hildebrand, M. Diatoms, biomineralization processes, and genomics. *Chemical Reviews* **108**, 4855-4874 (2008).

- 20 Wang, Y., Cai, J., Jiang, Y., Jiang, X. & Zhang, D. Preparation of biosilica structures from frustules of diatoms and their applications: current state and perspectives. *Applied Microbiology and Biotechnology* **97**, 453-460 (2013).
- 21 Soleimani, M., Rutten, L., Maddala, S. P., Wu, H., Eren, E. D., Mezari, B., Schreur-Piet, I., Friedrich, H. & van Benthem, R. A. Modifying the thickness, pore size, and composition of diatom frustule in *Pinnularia* sp. with Al<sup>3+</sup> ions. *Scientific Reports* **10**, 19498 (2020).
- 22 Kröger, N. & Poulsen, N. Diatoms—from cell wall biogenesis to nanotechnology. *Annual Review of Genetics* **42**, 83-107 (2008).
- 23 Wang, Y., Zhang, D., Cai, J., Pan, J., Chen, M., Li, A. & Jiang, Y. Biosilica structures obtained from *Nitzschia*, *Ditylum*, *Skeletonema*, and *Coscinodiscus* diatom by a filtration-aided acid cleaning method. *Applied Microbiology and Biotechnology* **95**, 1165-1178 (2012).
- 24 Goessling, J. W., Su, Y., Maibohm, C., Ellegaard, M. & Kühl, M. Differences in the optical properties of valve and girdle band in a centric diatom. *Journal of the Royal Society Interface Focus* **9**, 20180031 (2019).
- 25 Hamm, C. E., Merkel, R., Springer, O., Jurkojc, P., Maier, C., Pechtel, K. & Smetacek, V. Architecture and material properties of diatom shells provide effective mechanical protection. *Nature* **421**, 841-843 (2003).
- 26 Kumari, E., Görlich, S., Poulsen, N. & Kröger, N. Genetically programmed regioselective immobilization of enzymes in biosilica microparticles. *Advanced Functional Materials* **30**, 2000442 (2020).
- 27 Aitken, Z. H., Luo, S., Reynolds, S. N., Thaulow, C. & Greer, J. R. Microstructure provides insights into evolutionary design and resilience of *Coscinodiscus* sp. frustule. *Proceedings of the National Academy of Sciences* **113**, 2017-2022 (2016).
- 28 Almqvist, N., Delamo, Y., Smith, B., Thomson, N., Bartholdson, Å., Lal, R., Brzezinski, M. & Hansma, P. Micromechanical and structural properties of a pennate diatom investigated by atomic force microscopy. *Journal of Microscopy* **202**, 518-532 (2001).
- 29 Losic, D., Short, K., Mitchell, J. G., Lal, R. & Voelcker, N. H. AFM nanoindentations of diatom biosilica surfaces. *Langmuir* **23**, 5014-5021 (2007).
- 30 Görlich, S., Pawolski, D., Zlotnikov, I. & Kröger, N. Control of biosilica morphology and mechanical performance by the conserved diatom gene *Silicanin-1*. *Communications Biology* **2**, 1-8 (2019).
- 31 Topal, E., Rajendran, H., Zgłobicka, I., Gluch, J., Liao, Z., Clausner, A., Kurzydłowski, K. J. & Zschech, E. Numerical and Experimental Study of the Mechanical Response of Diatom Frustules. *Nanomaterials* **10**, 959 (2020).
- 32 Romann, J., Chauton, M. S., Hanetho, S. M., Vebner, M., Heldal, M., Thaulow, C., Vadstein, O., Tranell, G. & Einarsrud, M.-A. Diatom frustules as a biomaterial: effects of chemical treatment on organic material removal and mechanical properties in cleaned frustules from two *Coscinodiscus* species. *Journal of Porous Materials* **23**, 905-910 (2016).
- 33 Jiang, C., Lu, H., Zhang, H., Shen, Y. & Lu, Y. Recent advances on in situ SEM mechanical and electrical characterization of low-dimensional nanomaterials. *Scanning* **2017**, Article ID 1985149 (2017).
- 34 Wang, M. S., Kaplan-Ashiri, I., Wei, X. L., Rosentsveig, R., Wagner, H. D., Tenne, R. & Peng, L. M. In situ TEM measurements of the mechanical properties and behavior of WS<sub>2</sub> nanotubes. *Nano Research* **1**, 22-31 (2008).
- 35 Shan, Z. In situ TEM investigation of the mechanical behavior of micronanoscaled metal pillars. *Jom* **64**, 1229-1234 (2012).
- 36 Asayesh-Ardakani, H., Yao, W., Yuan, Y., Nie, A., Amine, K., Lu, J. & Shahbazian-Yassar, R. In situ TEM investigation of ZnO nanowires during sodiation and lithiation cycling. *Small Methods* **1**, 1700202 (2017).

- 37 Shi, C., Luu, D. K., Yang, Q., Liu, J., Chen, J., Ru, C., Xie, S., Luo, J., Ge, J. & Sun, Y. Recent advances in nanorobotic manipulation inside scanning electron microscopes. *Microsystems & Nanoengineering* **2**, 1-16 (2016).
- 38 Zhou, X., Li, T., Cui, Y., Fu, Y., Liu, Y. & Zhu, L. In situ focused ion beam scanning electron microscope study of microstructural evolution of single tin particle anode for Li-ion batteries. *ACS Applied Materials & Interfaces* **11**, 1733-1738 (2019).
- 39 Komissarenko, F., Zograf, G., Makarov, S., Petrov, M. & Mukhin, I. Manipulation Technique for Precise Transfer of Single Perovskite Nanoparticles. *Nanomaterials* **10**, 1306 (2020).
- 40 Przybilla, T., Zubiri, B. A., Beltrán, A. M., Butz, B., Machoke, A. G., Inayat, A., Distaso, M., Peukert, W., Schwieger, W. & Spiecker, E. Transfer of Individual Micro-and Nanoparticles for High-Precision 3D Analysis Using 360° Electron Tomography. *Small Methods* **2**, 1700276 (2018).
- 41 Shade, P. A., Groeber, M. A., Schuren, J. C. & Uchic, M. D. Experimental measurement of surface strains and local lattice rotations combined with 3D microstructure reconstruction from deformed polycrystalline ensembles at the micro-scale. *Integrating Materials and Manufacturing Innovation* **2**, 100-113 (2013).
- 42 Antoniou, N., Rykaczewski, K. & Uchic, M. D. In situ FIB-SEM characterization and manipulation methods. *MRS Bulletin* **39**, 347-352 (2014).
- 43 Zang, J., Bao, L., Webb, R. A. & Li, X. Electron beam irradiation stiffens zinc tin oxide nanowires. *Nano letters* **11**, 4885-4889 (2011).
- 44 Romeis, S., Paul, J., Herre, P., de Ligny, D., Schmidt, J. & Peukert, W. Local densification of a single micron sized silica sphere by uniaxial compression. *Scripta Materialia* **108**, 84-87 (2015).
- 45 Yılmaz, M., Wollschläger, N., Esfahani, M. N., Österle, W., Leblebici, Y. & Alaca, B. E. Superplastic behavior of silica nanowires obtained by direct patterning of silsesquioxane-based precursors. *Nanotechnology* **28**, 115302 (2017).
- 46 La Vars, S. M., Johnston, M. R., Hayles, J., Gascooke, J. R., Brown, M. H., Leterme, S. C. & Ellis, A. V. <sup>29</sup>Si {1 H} CP-MAS NMR comparison and ATR-FTIR spectroscopic analysis of the diatoms *Chaetoceros muelleri* and *Thalassiosira pseudonana* grown at different salinities. *Analytical and Bioanalytical Chemistry* **405**, 3359-3365 (2013).
- 47 Sumper, M. & Brunner, E. Silica biomineralisation in diatoms: the model organism *Thalassiosira pseudonana*. *ChemBioChem* **9**, 1187-1194 (2008).
- 48 Armbrust, E. V., Berges, J. A., Bowler, C., Green, B. R., Martinez, D., Putnam, N. H., Zhou, S., Allen, A. E., Apt, K. E. & Bechner, M. The genome of the diatom *Thalassiosira pseudonana*: ecology, evolution, and metabolism. *Science* **306**, 79-86 (2004).
- 49 Johnston, M., Gascooke, J., Ellis, A. & Leterme, S. Diatoms response to salinity changes: investigations using single pulse and cross polarisation magic angle spinning <sup>29</sup>Si NMR spectra. *Analyst* **143**, 4930-4935 (2018).
- 50 Bussard, A., Corre, E., Hubas, C., Duvernois-Berthet, E., Le Corguillé, G., Jourden, L., Couplier, F., Clauquin, P. & Lopez, P. J. Physiological adjustments and transcriptome reprogramming are involved in the acclimation to salinity gradients in diatoms. *Environmental Microbiology* **19**, 909-925 (2017).
- 51 Wu, H., Su, H., Joosten, R. R., Keizer, A. D., van Hazendonk, L. S., Wirix, M. J., Patterson, J. P., Laven, J., de With, G. & Friedrich, H. Mapping and Controlling Liquid Layer Thickness in Liquid-Phase (Scanning) Transmission Electron Microscopy. *Small Methods* **5**, 2001287 (2021).
- 52 Schweizer, P., Dolle, C., Dasler, D., Abellán, G., Hauke, F., Hirsch, A. & Spiecker, E. Mechanical cleaning of graphene using in situ electron microscopy. *Nature communications* **11**, 16024 (2020).
- 53 Denisyuk, A. I., Komissarenko, F. E. & Mukhin, I. S. Electrostatic pick-and-place micro/nanomanipulation under the electron beam. *Microelectronic engineering* **121**, 15-18 (2014).
- 54 Denisyuk, A. I., Krasavin, A. V., Komissarenko, F. E. & Mukhin, I. S. Mechanical, electrostatic, and electromagnetic manipulation of microobjects and nanoobjects in electron microscopes. *Advances in Imaging and Electron Physics* **186**, 101-140 (2014).

- 55 Paul, J., Romeis, S., Tomas, J. & Peukert, W. A review of models for single particle compression and their application to silica microspheres. *Advanced Powder Technology* **25**, 136-153 (2014).
- 56 Mačković, M., Niekiet, F., Wondraczek, L. & Spiecker, E. Direct observation of electron-beam-induced densification and hardening of silica nanoballs by in situ transmission electron microscopy and finite element method simulations. *Acta Materialia* **79**, 363-373 (2014).
- 57 Hu, Y.-J., Zhao, G., Zhang, M., Bin, B., Del Rose, T., Zhao, Q., Zu, Q., Chen, Y., Sun, X. & de Jong, M. Predicting densities and elastic moduli of SiO<sub>2</sub>-based glasses by machine learning. *Npj Computational Materials* **6**, 1-13 (2020).
- 58 Jimbert, P., Iturrondobeitia, M., Fernandez-Martinez, R., Guraya, T. & Ibarretxe, J. in *Advanced Materials Research*. 20-24 (Trans Tech Publ).

### 3.6 Appendix

#### 3.6.1 Sample preparation for scanning electron microscopy and measurement of morphological parameters

In order to harvest the frustules of *Thalassiosira pseudonana* (*T.p.*) grown at different salinities, the living cells were collected from the cultures via centrifugation at 2600 rpm for 5 minutes (Minispin Centrifuge, Eppendorf, Germany). The collected pellet was washed in distilled water and centrifuged at least three times to thoroughly remove the salts and attain a brownish-yellow pellet at the bottom of the centrifuge tube. The pellet was resuspended in an upgraded series of ethanol, from 30 % to anhydrous ethanol, and washed and centrifuged at least 10 times at 2600 rpm in order to remove the intracellular components and obtain off-white frustules. The resultant frustules were suspended again in dehydrated ethanol and dried by a critical point dryer (Leica CPD 300 instrument). Figure A3.1 shows a comparison between air-dried collapsed and critical point dried intact frustules of *T.p.*, indicating the importance of the drying step in preserving the integrity of the frustule. The valves diameter and girdle bands length were measured from scanning electron microscopy (SEM) imaging using the Gatan Digital Micrograph software (Figure A3.2). The mean diameters of cribrum pores were determined through in-house MATLAB scripts as presented in Figure A3.3.

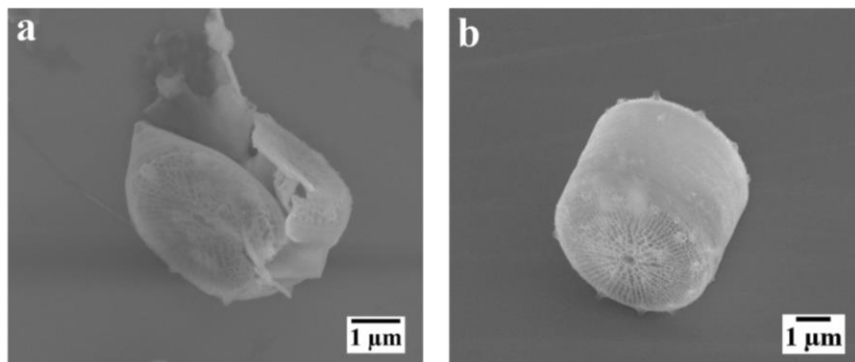


**Figure A3.1.** (a) Air dried collapsed frustule of *T.p.*; (b) Critical point dried intact frustule of *T.p.*

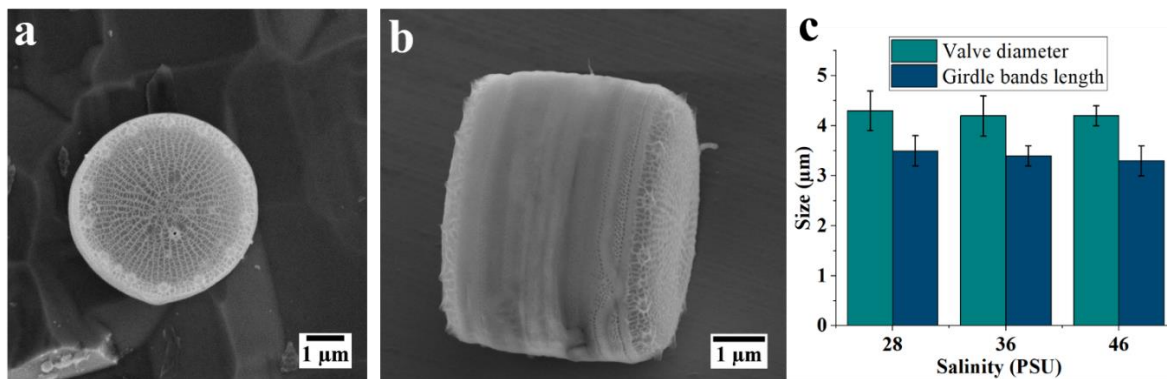


**Figure A3.2.** SEM images of the intact frustules of *T.p.*; (a) valve view; (b) girdle bands view; (c) measured valve diameter and girdle bands length as a function of salinity level in the growth medium acquired from  $n=10$  frustules per culture. Error bars indicate standard deviations.

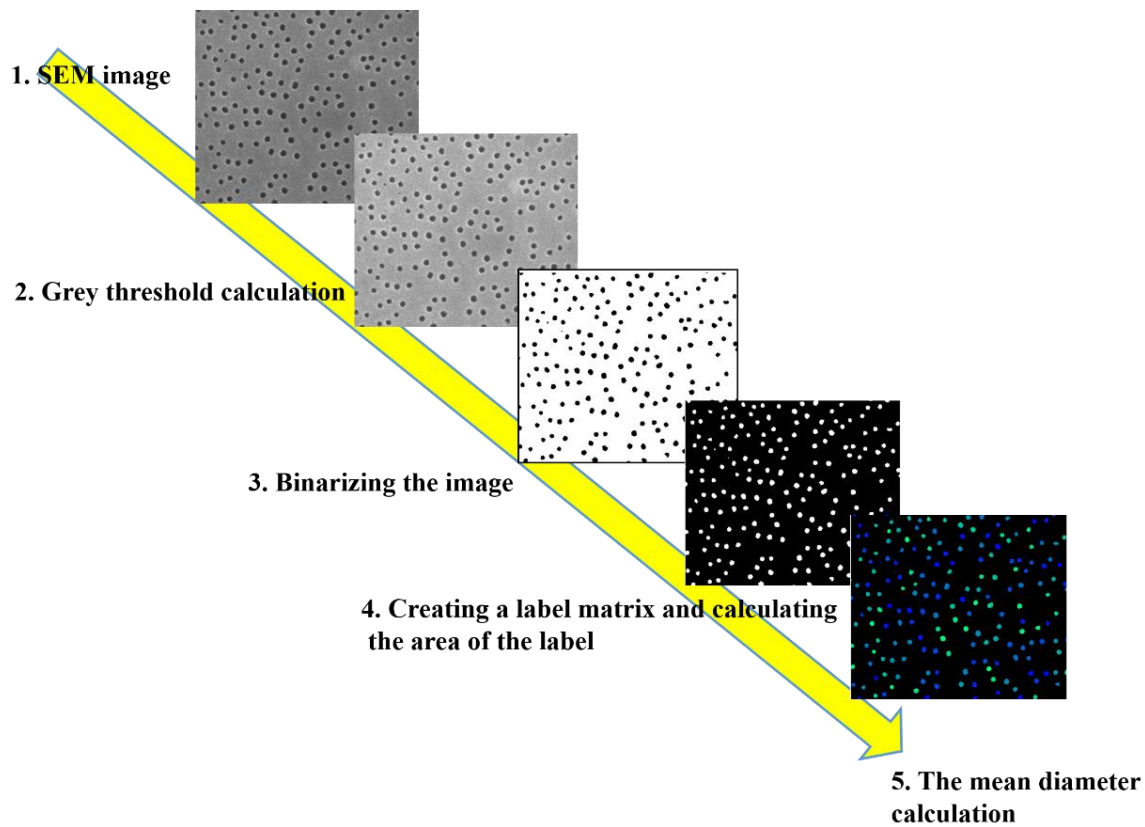


**Figure A3.3.** SEM image analysis process for measuring the mean diameters of cribrum pores via an in-house MATLAB script.

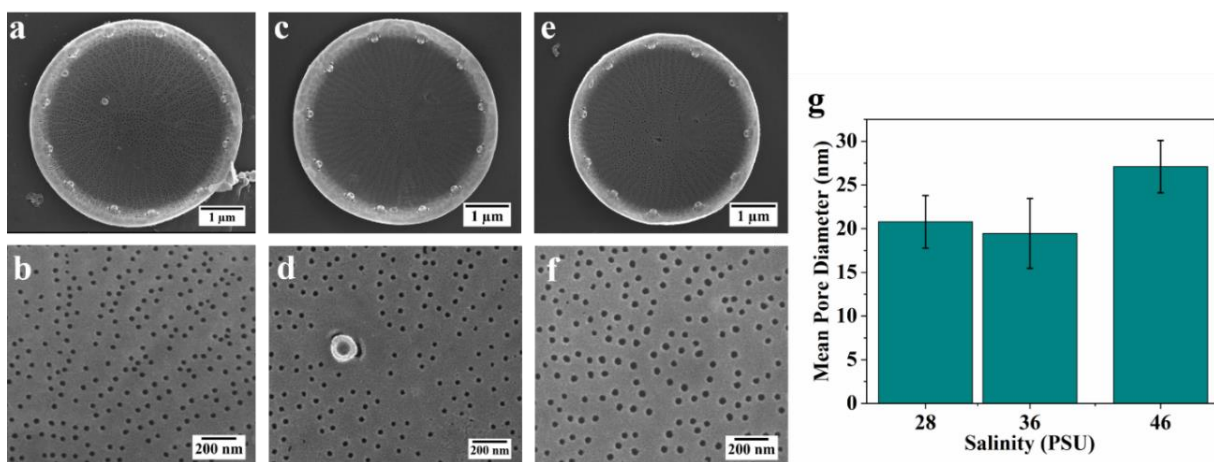


**Figure A3.4.** SEM images of the interior surfaces of isolated valves of *T.p.* grown at different salinities (a,b) 28 PSU; (c,d) 36 PSU; (e,f) 46 PSU; (g) Bar graphs of the measured mean diameter of cribrum pores ( $n=6$  valves per culture). Error bars indicate standard deviations.

### 3.6.2 Thickness measurements

In order to measure the thickness of isolated valves and girdle bands of *T.p.*, transmission electron microscopy (TEM) and associated TEM image analyses were carried out in the following manner. The isolated valves and girdle bands (by bath ultrasonication) were deposited on a continuous carbon grid (CF200-Cu, Electron Microscopy Sciences) and imaged on a Tecnai T20 G2 (Thermo Fisher Scientific, USA) operating at 200 kV and equipped with a LaB<sub>6</sub> filament and a 4k CETA CCD camera. To map the thickness of these constituents of *T.p.* frustule, two TEM images were acquired, one flat field (FFD) TEM image which only contains the unscattered incident electron flux  $I_0$  and one TEM image that records the electron flux  $I_t$  transmitted through the samples. The thickness of valves and girdle bands  $t_D$  can be estimated (Equation (1)) based on Lambert-Beer Law:<sup>1</sup>

$$\frac{I_t}{I_0} = \exp\left(-\left(\frac{t_C}{\Lambda_C} + \frac{t_D}{\Lambda_D}\right)\right) \quad (2)$$

where  $t_C$  is the thickness of the continuous carbon film of the TEM grid, and  $\Lambda_C$  and  $\Lambda_D$  are the elastic mean free paths (EMFP,  $\Lambda$ ) of carbon and silica, respectively. Note that these EMFP values can be found in Table A1, as well as our previous work<sup>2</sup>. All the thickness analysis and EMFP calculations were performed using in-house MATLAB scripts<sup>3</sup>. All scripts were developed in MATLAB version 2018b, <https://nl.mathworks.com/products/matlab.html>. Since it has been revealed previously that the ribs and cross-connections of the valves have a significant impact on the mechanical properties of *T.p.*,<sup>4</sup> the mean thicknesses of the ribs and cross-connections were determined.

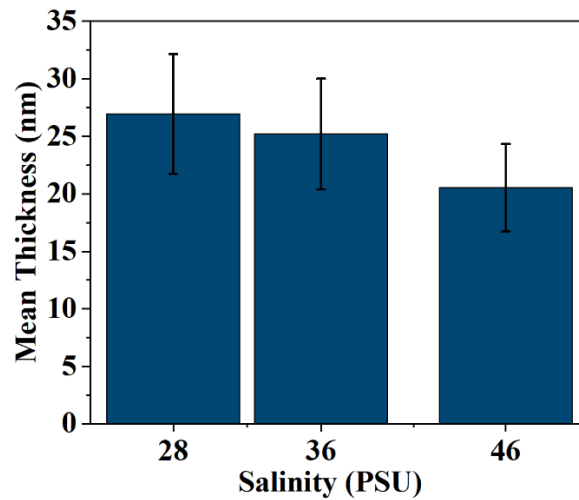


**Figure A3.5.** Bar graphs of thickness measurements of girdle bands grown at different salinities ( $n=5$  girdle bands per culture). Error bars indicate standard deviations.



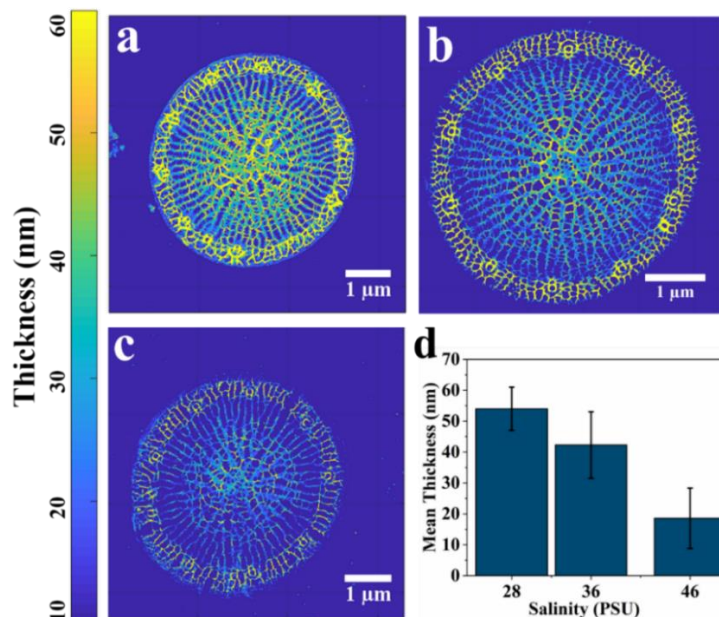


**Figure A3.6.** TEM thickness maps of *T.p.* valves grown at different salinities (a) 28 PSU; (b) 36 PSU; (c) 46 PSU; (d) bar graphs of thickness measurements of ribs and cross-connection of the valves grown at different salinities ( $n=5$  valves pre culture). Error bars indicate standard deviations.

### 3.6.3 Focused ion beam-scanning electron microscopy (FIB-SEM) sample preparation and in situ deformation experimental details

The intact frustules of *T.p.* were located at Eucentric height (10 mm) and tilted to  $52^\circ$  in order to focus the electron beam and the ion beam at the coincidence point. A Pt layer was not used due to the possible alteration to the morphology and mechanical performance of the frustules. Therefore, the milling was conducted at a current of only 1.5 pA with single line scan to preserve the structure of girdle bands and valves (Figure A3.10). As can be seen in the figure A3.10, the valves were completely separated by the FIB milling and can be transferred for further characterization. It is worth noting that one of the challenges of manipulation of the valves was that during manipulation every so often the isolated valves were pumped into the high vacuum in the SEM chamber (data is not shown). The deformation experiments were conducted with a FMT-120 which is an AFM based sensor made of silicon and coated with a piezo-resistive material with the following features; Length: 120 μm, Width: 50 μm, height: 5 μm, Tip radius: < 20 nm, Tip height: > 5 μm, and force resolution of 10 nN. When the FMT tip is brought into contact with the sample, the piezo-resistive material produces an electric signal, which is transformed into a force versus time curve. Calibration was carried out before each deformation measurement by a calibration spring provided by Kleindiek with a spring constant of 9.6 N/m in the following manner. The FMT holder on the manipulator was positioned vertically toward the calibration spring which was attached onto an SEM stub inside the SEM chamber. The very end of the FMT was brought into contact with the very end of spring. Then spring was bent by 1 μm with the FMT. In combination with the spring constant, the force measurement system (FMS) software uses the voltage difference caused by bending the spring to calculate the force. To rule out the possibility of a sharp FMT tip (10 nm



radius originally) penetrating into the test specimens, the FMT tip was flattened by FIB micromachining. Figure A3.12 exhibits the FMT-120 tip and its geometry before and after FIB milling.

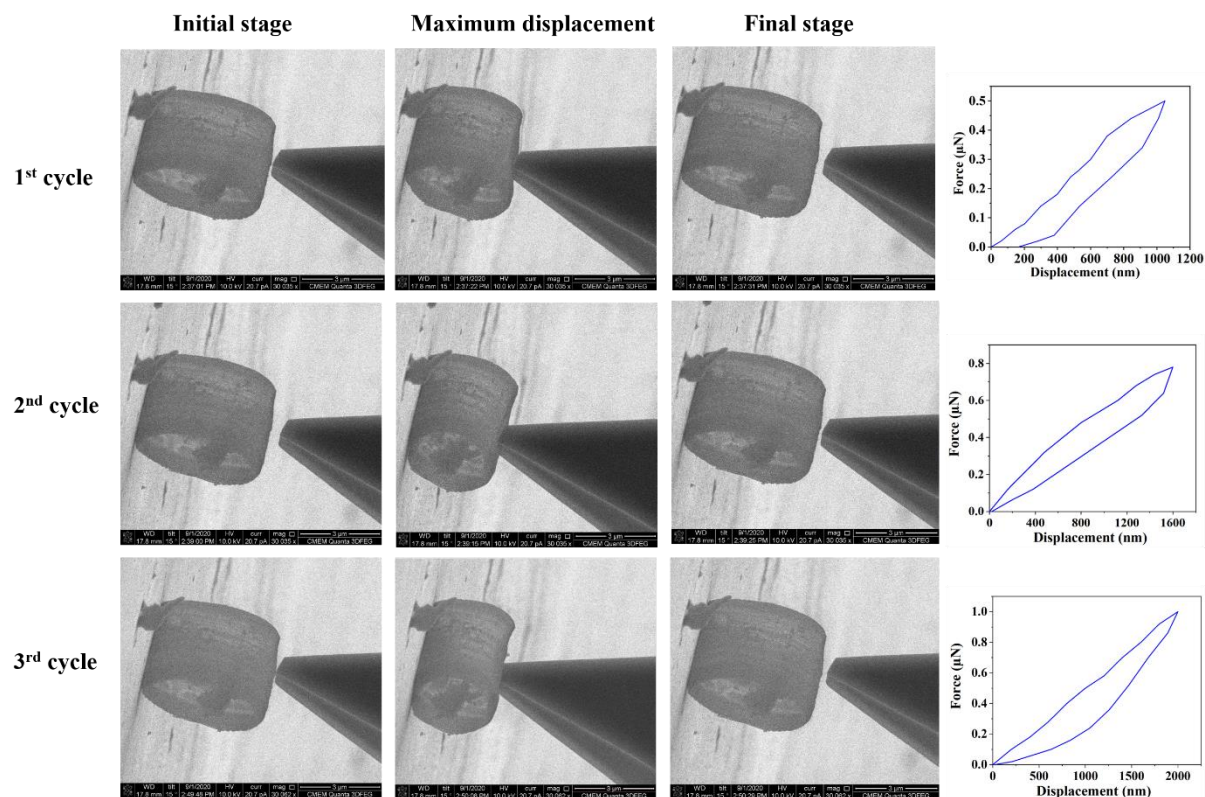


**Figure A3.7.** SEM images of in situ deformation experiments on isolated girdle bands during different cycles with their corresponding force-displacement curves. First cycle shows small irreversible deformations, but no residual displacement was found in the second and third cycle.

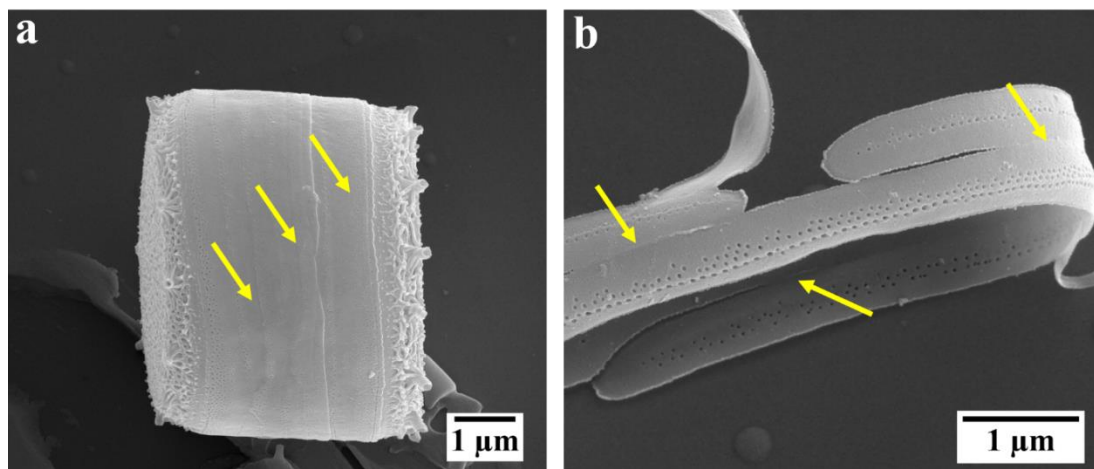


**Figure A3.8.** SEM images of girdle bands of *T.p.*; (a) intact frustule; (b) separated girdle bands (by bath sonicator). The overlapping girdle bands are indicated by yellow arrows.

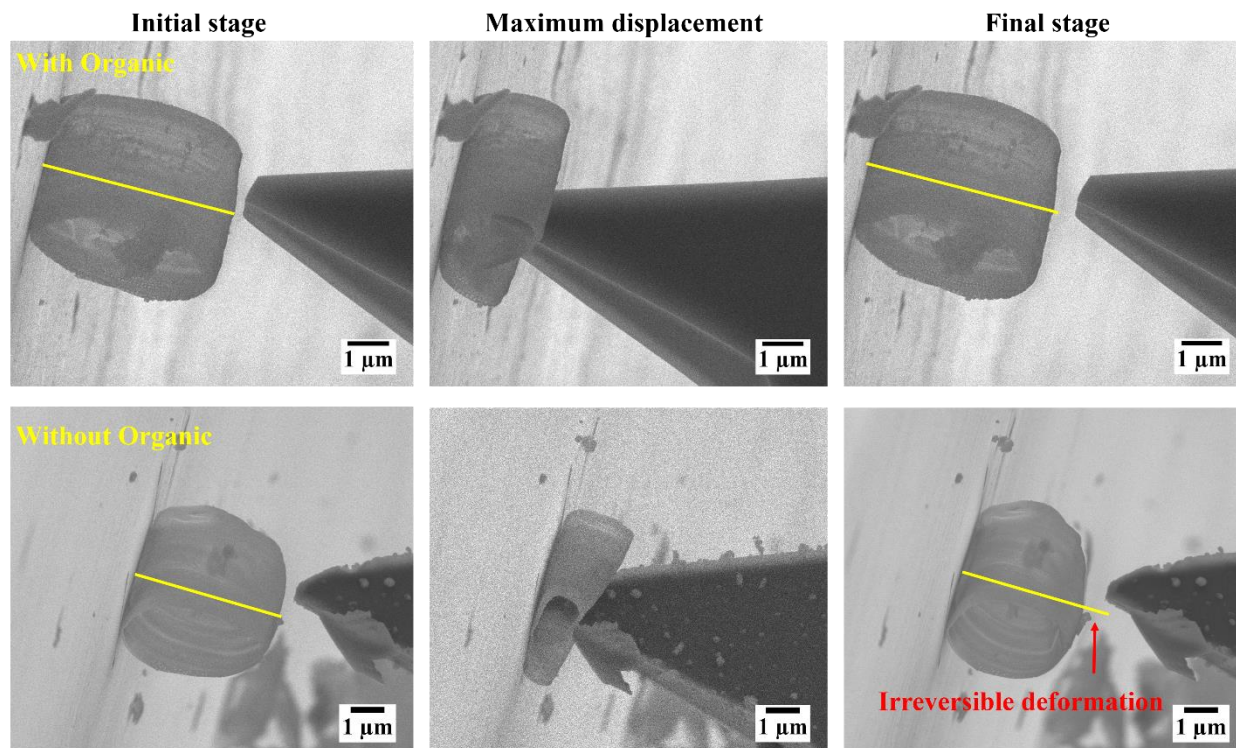


**Figure A3.9.** SEM images of different stages of complete flattening deformation tests on girdle bands; (top) girdle bands with organic compounds show fully elastic behavior; (bottom) thermally treated girdle bands show a significant irreversible deformation after the tip retraction (yellow lines indicate the initial length of the girdle bands).

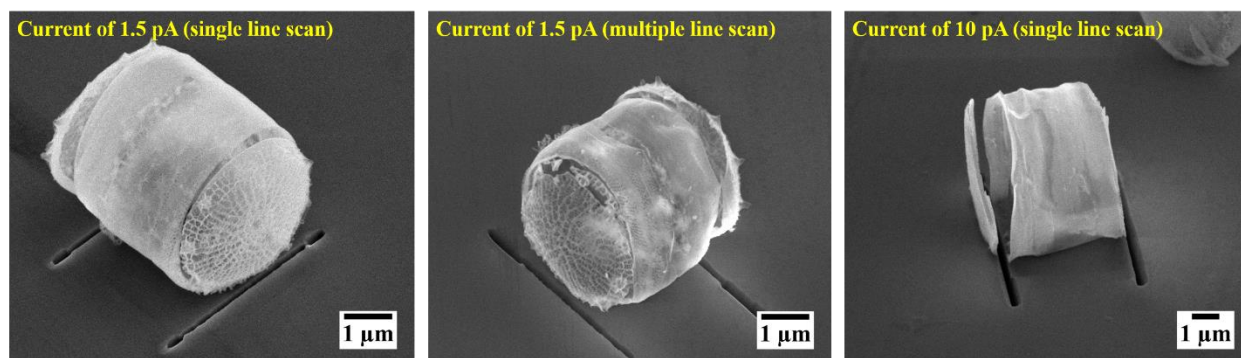


**Figure A3.10.** SEM images of frustule of *T.p.* after FIB milling with different milling parameters.

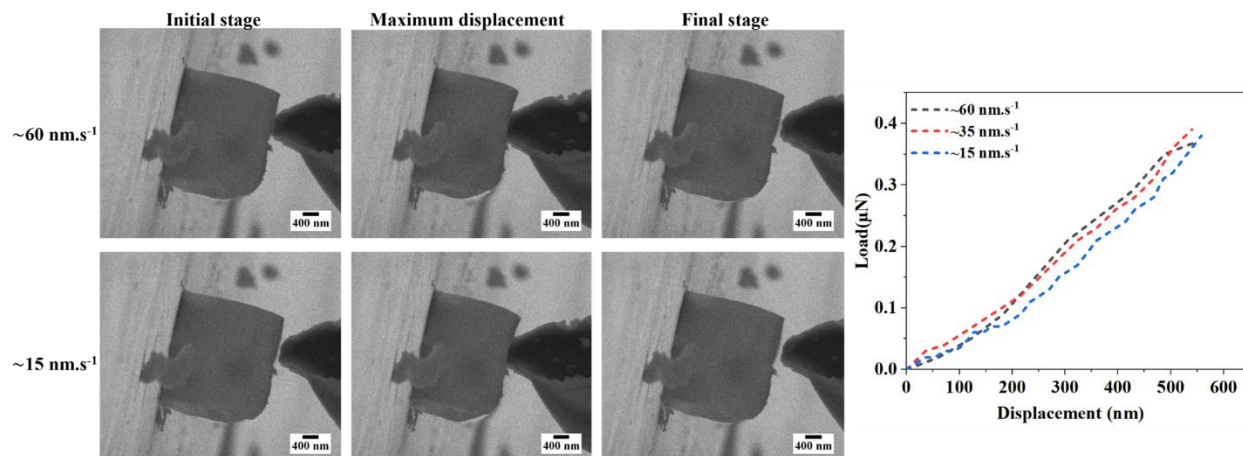


**Figure A3.11.** (left) SEM images of different stages of deformation tests on a set of girdle bands with different loading rates; (right) representative load-displacement curves in correlation with different loading rates, indicating a small decrease in measured load at a decreased rate of deformation.

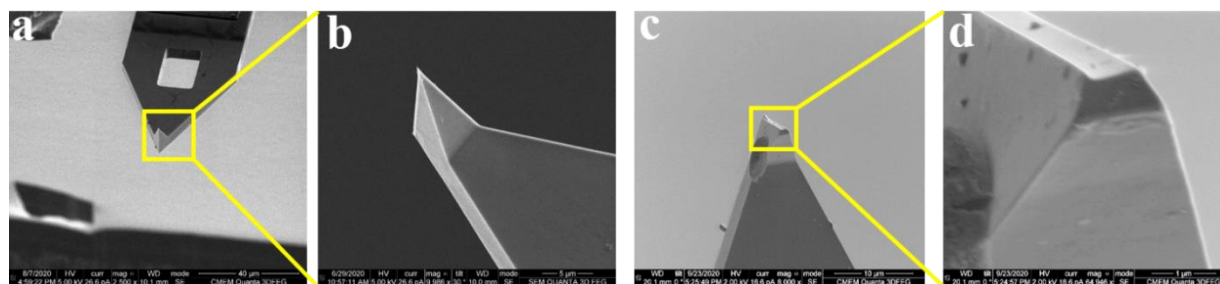


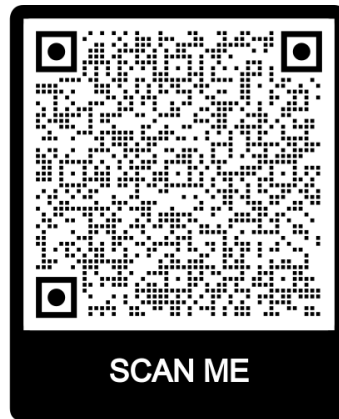
**Figure A3.12.** SEM images of nano indenter (FMT-120) tip. (a,b) before FIB milling; (c,d) after FIB milling.

### 3.6.4 Appendix movies

**Movie A3.1.** In situ mechanical manipulation of an isolated valve.



**Movie A3.2.** In situ electrostatic manipulation of an isolated valve.



**Movie A3.3.** In situ deformation test on isolated girdle bands.



**Movie A3.4.** Mechanical transfer of an isolated valve from the silicon substrate to a prefabricated hole.



**Appendix Table A3.1.** Parameters used in EMFP ( $\Lambda$ ) calculations.

Materials		$M_w$ , g/mol	$\rho$ , g/cm <sup>3</sup>	$\Lambda$ , nm
SiO <sub>2</sub> (amorphous)		60.08	2.00	214.78
Carbon film		12.00	2.10	282.54

### 3.6.5 Appendix References

- 1 Williams, D. B. & Carter, C. B. *Transmission Electron Microscopy: A Textbook for Materials Science*. (Springer, 2009).
- 2 Soleimani, M., Rutten, L., Maddala, S. P., Wu, H., Eren, E. D., Mezari, B., Schreur-Piet, I., Friedrich, H. & van Benthem, R. A. Modifying the thickness, pore size, and composition of diatom frustule in *Pinnularia* sp. with Al<sup>3+</sup> ions. *Scientific Reports* **10**, 19498 (2020).
- 3 Ianiro, A., Wu, H., van Rijt, M. M., Vena, M. P., Keizer, A. D., Esteves, A. C. C., Tuinier, R., Friedrich, H., Sommerdijk, N. A. & Patterson, J. P. Liquid–liquid phase separation during amphiphilic self-assembly. *Nature chemistry* **11**, 320-328 (2019).
- 4 Görlich, S., Pawolski, D., Zlotnikov, I. & Kröger, N. Control of biosilica morphology and mechanical performance by the conserved diatom gene Silicanin-1. *Communications Biology* **2**, 1-8 (2019).



# Chapter 4

## How $\text{Al}^{3+}$ ions in the growth medium affect the frustule Morphology, Chemistry, and Mechanical Properties of Diatom *Thalassiosira pseudonana*

### Abstract

Diatoms are unicellular photosynthetic algae that create a highly ornamented micro and nanostructured biogenic silica exoskeleton known as the frustule. While it is known that during the frustule formation by diatoms, incorporation of  $\text{Al}^{3+}$  into the newly formed silica structure improves its hydrolysis resistance, further effects of this non-essential metal ion are unclear. Here, we investigate the consequences of  $\text{Al}^{3+}$  ion addition on morphological, chemical, and mechanical properties of the frustule of diatom *Thalassiosira pseudonana*. By a combination of spectroscopic and electron microscopic techniques, it is shown that  $\text{Al}^{3+}$  is homogeneously distributed throughout the frustule, within four and six coordination environments, also modifying its morphological parameters and increasing silica condensation. Furthermore, implementation of a versatile approach by combining Focused Ion Beam Scanning Electron Microscopy (FIB-SEM), micromanipulators, electron tomography, and Finite Element Method (FEM) simulations allowed the determination of the Young's modulus of individual frustule constituent's, i.e., girdle bands and valves. A significant impact of  $\text{Al}^{3+}$  on the mechanical properties of the girdle bands is noted. The presented approaches and findings may be employed to study other diatom species and to develop biogenic silica-based materials with tailored properties for industrial applications.

### The results presented in this chapter are based on:

Soleimani, M., Maddala, S.P., van den Broek, S.J., Joosten, R.R., van Hazendonk, L., Wu, H., Liao, W., Mezari, B., Hensen, E., van Breemen, L.C., Friedrich, H., van Bentham, R.A. *How  $\text{Al}^{3+}$  ions in the growth medium affect the frustule Morphology, Chemistry, and Mechanical Properties of Diatom *Thalassiosira pseudonana**. Submitted.

## 4.1 Introduction

Diatoms are unicellular photosynthetic algae, which inhabit most aquatic environments and are well-known due to the fascinating morphology of their siliceous exoskeleton, the frustule<sup>1</sup>. The frustule resembles a petri dish like arrangement and is composed of two valves and several overlapping girdle bands<sup>2</sup>. The frustule formation which takes place in restrained intracellular compartments termed silica deposition vesicles (SDVs) is affected by many biological and chemical factors<sup>3,4</sup>. Besides silicon, in the form of orthosilicic acid, as the essential element for frustule formation, several studies have shown that diatoms can take up several non-essential metal ions, which not only modify the morphological and chemical properties of the frustule but also induce new characteristics<sup>5</sup>. For example, the presence of cadmium ( $\text{Cd}^{2+}$ ) in the growth medium of *Nitzschia palea* alters the morphology of its costa and ribs within the valves<sup>6</sup>, whereas titanium precursors alongside Si induce photocatalytic activity to the frustule of *Thalassiosira weissflogii*<sup>7</sup>. Iron ( $\text{Fe}^{3+}$ ) incorporation into the frustule of *Stephanopyxis turris* results in the association of Iron oxide with its biosilica<sup>8</sup>. Moreover, photoluminescence and electroluminescence are observed as a result of germanium (Ge) incorporation into the frustule of *Craspedostauros sp.* (previously denominated as *Pinnularia sp.*)<sup>9</sup>.

Another non-essential metal ion known to be taken up by diatom species is aluminum ( $\text{Al}^{3+}$ )<sup>10,11</sup>. Alongside its well-documented toxicity to diatoms<sup>12,13</sup>, some beneficial effects due to the presence of  $\text{Al}^{3+}$  in the growth medium of diatoms have been observed as well<sup>14</sup>. More specifically,  $\text{Al}^{3+}$  addition into the growth medium of diatom *Navicula salinarum* has increased its growth rate<sup>15</sup>. Furthermore, the presence of  $\text{Al}^{3+}$  has enhanced iron and phosphorous uptake in diatom *Thalassiosira weissflogii*<sup>16,17</sup>. In addition,  $\text{Al}^{3+}$  incorporation into the frustule of diatoms not only has resulted in catalytic activity in the frustule of *Thalassiosira pseudonana*<sup>18</sup>, but also has led to the modification of the morphological and compositional properties of the frustule of diatom *Craspedostauros sp.*<sup>19</sup>. Most notably,  $\text{Al}^{3+}$  incorporation into the frustules of several diatom species has had remarkable effects on hydrolysis/dissolution resistance<sup>20-22</sup>. The solubility of diatom frustules has been found to decrease by 25 % following the replacement of one out of every 70 Si atoms with  $\text{Al}^{3+}$  in the diatom frustule<sup>23</sup>.

However, despite the aforementioned reports on advantageous aspects of  $\text{Al}^{3+}$  on biological, morphological, and chemical properties of diatom frustules, alongside well-known improvements in mechanical properties and chemical stability of silicate glasses due to incorporation of Al compounds<sup>24</sup>, the effects of  $\text{Al}^{3+}$  on the mechanical properties of diatom frustule have surprisingly not been examined to date. A previous study has established the importance of chemical composition on the mechanical performance of diatom frustules<sup>25</sup>. Also, from both experimental and numerical studies, the critical role of frustule morphology on its mechanical properties has been confirmed<sup>26,27</sup>. Consequently, the question remains unanswered whether there is a link between  $\text{Al}^{3+}$  incorporation and mechanical properties of the diatom frustule in correlation with its morphology and chemical composition.

In this chapter, we aim to shed some new light on the various effects of  $\text{Al}^{3+}$  incorporation in diatom frustules. To this end, the diatom *Thalassiosira pseudonana* (*T.p.*) grown at naturally occurring  $\text{Al}^{3+}$  concentrations is used.  $\text{Al}^{3+}$  distributions and its coordination environment in the frustule, alongside its impact on silica condensation, and morphological variations of the frustule are investigated by a combination of spectroscopic and electron microscopic techniques. Furthermore, a combination of Focused Ion Beam-Scanning Electron Microscopy (FIB-SEM) with in situ micromanipulation and deformation tests together with Finite Element Method (FEM) simulations and electron tomography (ET), allowed to determine the mechanical properties of frustule constituents. This study reveals that *T.p.* not only incorporates  $\text{Al}^{3+}$  into its frustule, impacting its morphology and chemistry, but also that  $\text{Al}^{3+}$  strongly affects the mechanical behavior of the frustule. Understanding the effects of  $\text{Al}^{3+}$  incorporation on morphological, chemical, and mechanical properties of the frustules might have significant implications not only for establishing how various properties of biogenic silica can be tuned by a small amount of non-essential metal ions but also can pave the way to bioinspired silicas with properties designed for technological applications.

## 4.2 Results

### 4.2.1 Overall approach to study the effects of $\text{Al}^{3+}$ incorporation

The first step was to incorporate  $\text{Al}^{3+}$  into the frustule of *T.p.* by co-feeding the diatoms with  $\text{Al}^{3+}$  alongside Si and other essential nutrients, all in the range of their naturally occurring concentrations. Incorporation of  $\text{Al}^{3+}$  into both valves and girdle bands necessitates at least two cell cycle divisions of the mother cell (*Step 1*). Following the incorporation of  $\text{Al}^{3+}$ , morphological and chemical properties of the frustules (obtained by a mild extraction process of organic residuals with ethanol) were investigated by microscopic and spectroscopic techniques (*Step 2*). Intact frustules for mechanical studies were obtained using a critical point dryer (CPD). The frustule constituents, i.e., valves and girdle bands of intact frustules, were precisely separated by a combination of FIB-SEM and micromanipulators (*Step 3*). Subsequently, in situ deformation tests were conducted on isolated girdle bands, in combination with Finite Element Method (FEM) simulations, to determine their Young's modulus (*Step 3a&b*). Alternatively, the isolated valves were transferred and mounted on holes in the sample support using a micromanipulator followed by in situ deformation tests (*Step 4a*). To determine the Young's modulus of the biogenic silica in the valve, Electron Tomography (ET) was conducted to obtain a realistic 3D model of the valve's complex morphol-



ogy (Step 4b). Finally, FEM simulations were carried out with the obtained valve model in combination with the deformation data to determine the Young's modulus of the valve's silica (Step 4c) (Figure 4.1).

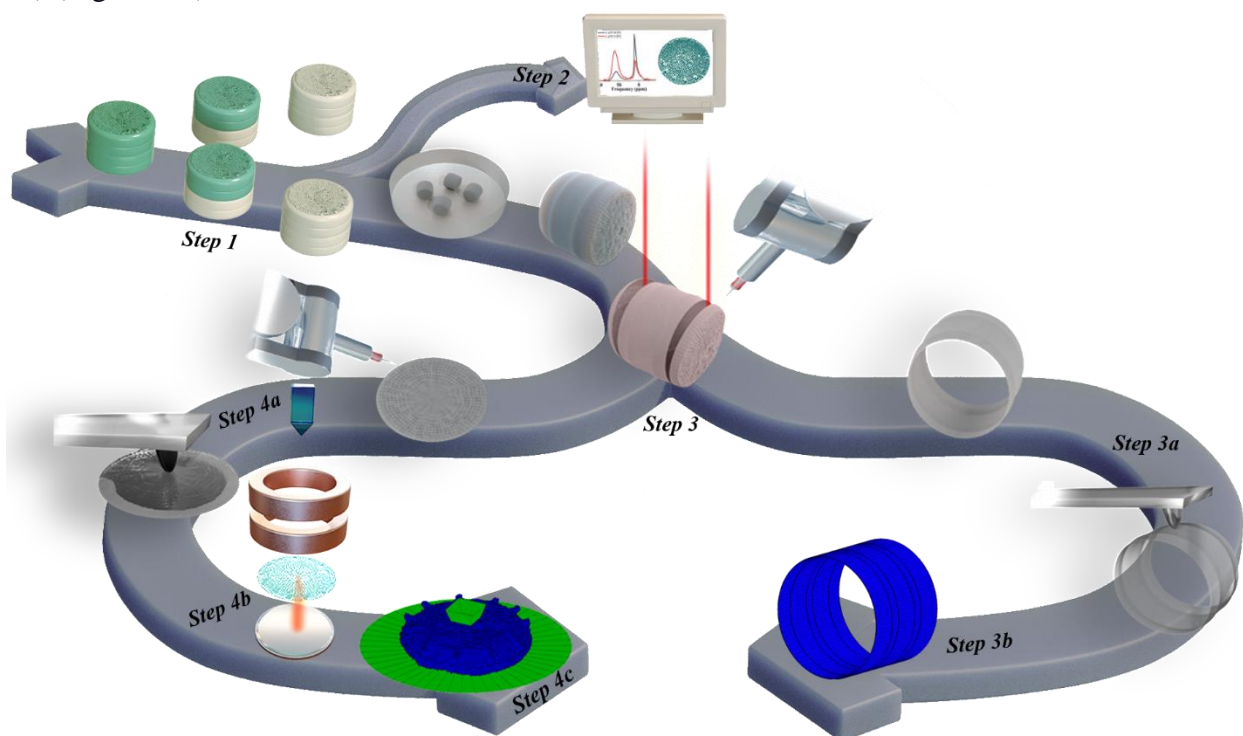


**Figure 4.1.** Schematic illustration of the entire workflow to reveal the effects of  $\text{Al}^{3+}$  on various properties of the frustule of *T.p.* The process begins with co-feeding the diatom cells with  $\text{Al}^{3+}$  and Si where  $\text{Al}^{3+}$  is incorporated into the newly formed valves and girdle bands (Step 1) (note: change of color from green to white indicates  $\text{Al}^{3+}$  incorporation into the newly formed silica); spectroscopic and microscopic techniques allowed to derive fundamental information about the effect of  $\text{Al}^{3+}$  on morphology and chemistry of the frustule (Step 2); following the harvesting of the diatom cell and washing with ethanol, CPD was used to obtain intact frustules; the valves were cut from girdle bands with FIB milling; via micromanipulators valves were completely isolated from girdle bands (Step 3); in situ deformation tests on girdle bands were conducted by a FMT-120 tip to obtain force-distance data for FEM simulations which allowed to determine their young's modules (Step 3a&b); isolated valves were transferred by the micromanipulator and mounted on top of predrilled holes and in situ deformation tests were performed by FMT-120 tip (Step 4a); electron tomography was conducted on the valve (Step 4b); finally, based on the experimental data alongside the acquired 3D model of the valve, the Young's modules of the biosilica of valve was derived by FEM simulations (Step 4c).

#### 4.2.2 Morphological parameters of frustule of *T.p.* and changes due to $\text{Al}^{3+}$ addition

*T.p.* was chosen as model system due to its known genome sequence and extraordinary adaptability to numerous environmental conditions including the presence of  $\text{Al}^{3+}$  in the medium<sup>18,28-31</sup>. Figure 4.2a shows the frustule of *T.p.* which is a cylinder-shaped diatom comprising two valves with a species-specific pattern and a series of overlapping girdle bands between them (see also Appendix Figure A4.1). The exterior surface of the valve possesses the most elaborated structures of the frustule with numerous ribs named costae which are joined by neighboring cross-connections, to form areole pores (Figure 4.2b). Inside the areole pores, some small open pores called cribrum pores can be found<sup>26</sup>. In addition, several tube-shaped structures termed fultoportulae are located

close to the valve circumference, known to be involved in extending linear fibers of chitin<sup>32</sup> (Appendix Figure A4.2). The valve's interior surface is comparatively smooth, lacking ribs and cross-connection while the cribrum pores and fultoportulae can be observed (Figure 4.2c). Figure 4.2d shows an isolated girdle band which has a typical pattern of porous and nonporous regions. In this study,  $\text{Al}^{3+}$  with concentrations of 1  $\mu\text{M}$  and 2  $\mu\text{M}$  were used, which resemble naturally occurring concentrations of  $\text{Al}^{3+}$  in the tropical Angola Basin and the inlet of the Amazon river and the concentration reported in the coastal region, respectively<sup>21,23</sup>. Besides, a control culture without  $\text{Al}^{3+}$  addition referred to 0  $\mu\text{M}$   $\text{Al}^{3+}$  was grown as well.

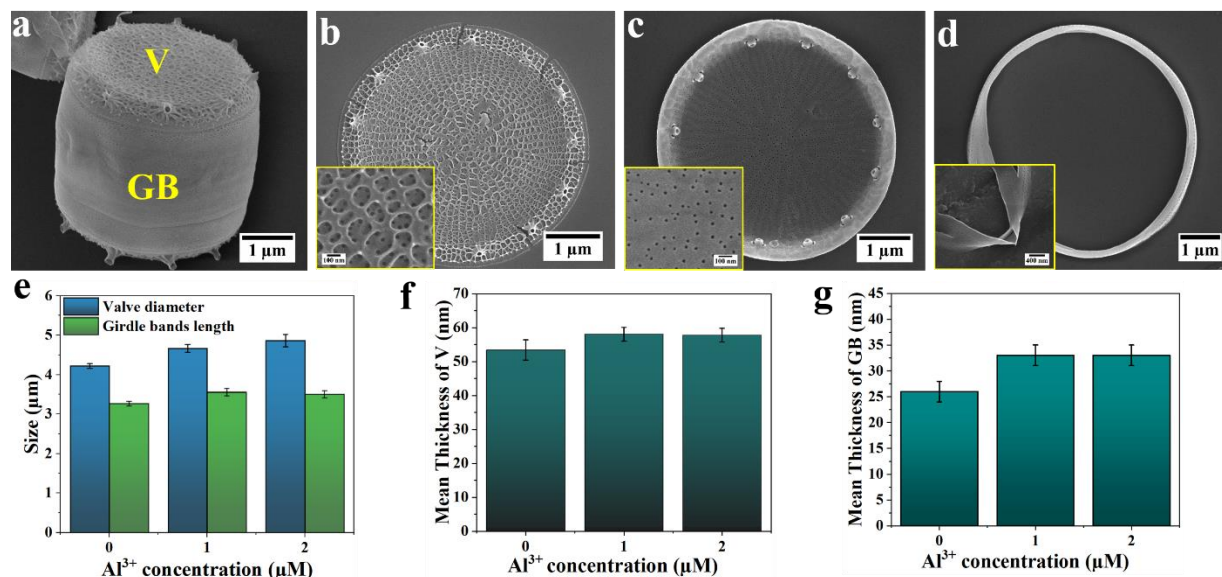


**Figure 4.2.** SEM images of *T.p.* and analysis of morphological parameters of frustules in dependence of  $\text{Al}^{3+}$  concentration in growth medium (a) SEM image of intact frustule of *T.p.*, both valve (V) and girdle bands (GB) are shown; (b) the exterior surface of an isolated valve; (c) the interior surface of an isolated valve (insets in b, c and d show high magnification images); (d) an isolated girdle band; (e) bar graphs of SEM image analysis of valve diameters and girdle band lengths at different  $\text{Al}^{3+}$  concentrations ( $n=10$ ); (f) bar graphs of mean thickness of ribs and cross-connections of valves grown at different  $\text{Al}^{3+}$  concentrations ( $n=5$ ) (obtained by TEM image analysis); (g) bar graphs of mean thickness of girdle bands at different  $\text{Al}^{3+}$  concentrations ( $n=5$ ). Error bars indicate standard error of mean.

It is well established from a variety of studies that morphological parameters play a remarkable role in the mechanical properties of diatom frustules<sup>27,33,34</sup>. Therefore, to understand how the presence of  $\text{Al}^{3+}$  in the growth medium regulates the morphological properties and ultimately the mechanical performance, morphological features such as valves diameters, girdle bands lengths, and their thicknesses were quantified in several SEM and TEM images. By increasing the  $\text{Al}^{3+}$  concentration in the growth medium from 0 to 2  $\mu\text{M}$  some small changes to the morphology of the frustule were observed. For instance, as shown in Figure 4.2e, the valve diameter increased from  $4.2 \pm 0.1$  to  $4.9 \pm 0.2$   $\mu\text{m}$  by increasing the  $\text{Al}^{3+}$  concentration to 2  $\mu\text{M}$ . Also, the length of the girdle bands of the frustule slightly increased from  $3.3 \pm 0.1$  to  $3.5 \pm 0.2$   $\mu\text{m}$ . Moreover, due to the known effect of ribs and cross-connections on the mechanical properties of frustule of *T.p.*<sup>26</sup>, their thicknesses were determined from TEM images, by quantifying the observed mass-thickness contrast using an in-house MATLAB script<sup>35</sup>. As shown in the bar graphs of Figure 4.2f, there was an

insignificant increase in the thickness of the valves grown in the presence of  $\text{Al}^{3+}$ . The mean thickness of ribs and cross-connections of the valves with 0, 1, and 2  $\mu\text{M}$  were  $54\pm3$ ,  $58\pm2$ , and  $58\pm2$  nm, respectively (see also Appendix Figure A4.3). Finally, the mean thickness of isolated girdle bands was also determined by TEM image analysis. As shown in Figure 4.2g the thicknesses of girdle bands grown at 0, 1, and 2  $\mu\text{M}$   $\text{Al}^{3+}$  were  $26\pm2$ ,  $33\pm2$ , and  $33\pm2$  nm, respectively, indicating an about 20 % increase in the thickness due to the presence of  $\text{Al}^{3+}$ .

#### 4.2.3 Assessment of $\text{Al}^{3+}$ distribution and chemical environment within the frustule

In order to ascertain the presence of  $\text{Al}^{3+}$  in the frustule, Energy-Dispersive X-ray Spectroscopy (SEM-EDS) elemental mapping was performed on the sample with 2  $\mu\text{M}$   $\text{Al}^{3+}$ . EDS maps of an isolated valve showed a uniform distribution of aluminum alongside silicon and oxygen demonstrating its homogenous presence throughout the entire valve (Figure 4.3a). As observed for Si and O, the Al signal was stronger at the periphery and center of the valve due to thickness variations. EDS mapping of intact frustules from the girdle bands perspective also revealed the same uniform distribution of Al alongside Si and O (Appendix Figure A4.4).  $\text{Al}^{3+}$  coordination within the frustule was determined using  $^{27}\text{Al}$  solid-state NMR spectroscopy (Figure 4.3b) on frustules produced at 1 and 2  $\mu\text{M}$   $\text{Al}^{3+}$ . The NMR spectra showed two distinct broad peaks at about 55 and 7 ppm, corresponding to 4 and 6 coordinated aluminum species, respectively<sup>10,36</sup>. The broad peaks point towards large structural variability of aluminosilicate species of the frustule. The 4 coordinated aluminum species corresponds to aluminum incorporated within the silica framework<sup>20</sup>, whereas the non-framework aluminum is observed as 6 coordinated. In the frustules produced at 2  $\mu\text{M}$   $\text{Al}^{3+}$  concentration, the relative area of framework aluminum (4 coordinated at about 55 ppm) was greater than the relative area of the non-framework aluminum (6 coordinated observed at about 7 ppm). Whereas in the frustules produced at 1  $\mu\text{M}$   $\text{Al}^{3+}$  concentration the relative area of the framework aluminum was lower than the relative area of the non-framework aluminum. Although the underlying mechanisms are not clear, this result suggest a strong link between aluminum concentration in solution and the nature of aluminum incorporation and this observation agrees with previously published work on the influence of  $\text{Al}^{3+}$  ions on diatom growth under similar conditions<sup>10</sup>. The presence of  $\text{Al}^{3+}$  had a significant effect on the degree of silica condensation in the frustule (Table 1). Single pulse  $^{29}\text{Si}$  NMR revealed the presence of  $\text{Q}^4$  and  $\text{Q}^3$  species. Relative peak positions and relative areas of the spectra were obtained from a fit based on Gaussian distribution functions<sup>37</sup>. In the frustules obtained in the absence of  $\text{Al}^{3+}$ , fully condensed ( $\text{Q}^4$ ) species accounted for 67 % of all Si species, giving a  $\text{Q}^4/\text{Q}^3$  ratio of 2. In contrast, in frustules grown at 2  $\mu\text{M}$   $\text{Al}^{3+}$  concentration the amount of  $\text{Q}^4$  species increased to 75 %, demonstrating that the incorporation of aluminum ions in the frustule substantially increases the degree of condensation of silica to a  $\text{Q}^4/\text{Q}^3$  ratio of 3 (see also Appendix Figure A4.5&A4.6).

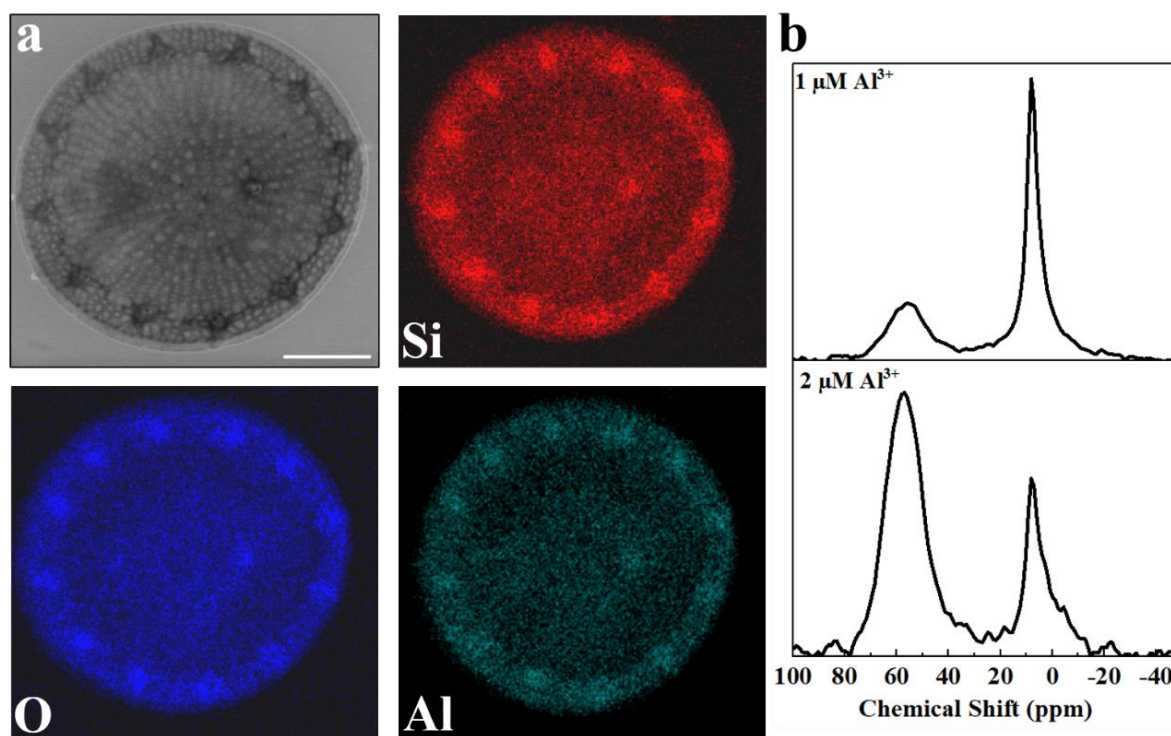


**Figure 4.3.** Macroscopic  $\text{Al}^{3+}$  distribution and its atomic coordination environment in the frustule of *T.p.* (a) SEM image and EDS elemental maps of isolated valve grown in the presence of  $2 \mu\text{M Al}^{3+}$  red=silicon, blue= oxygen, green= aluminum; (b)  $^{27}\text{Al}$  solid-state MAS NMR of diatom *T.p.* grown in the presence of 1 and  $2 \mu\text{M Al}^{3+}$ .

**Table 4.1.** Quantification of peak areas from  $^{29}\text{Si}$  solid-state NMR data of diatom *T.p.* grown at 0 and  $2 \mu\text{M Al}^{3+}$  (SP and CP refer to single pulse and cross polarization MAS NMR spectra respectively). Note: the fittings of SP data gave 95% agreement between the fit and the experimental data, and the fittings of CP data gave 98% agreement. In addition, signal to noise ratios for frustules grown at 0 and  $2 \mu\text{M Al}^{3+}$  were 15.8 and 9.5, respectively.

<i>Thalassiosira pseudonana</i>		$\text{Q}_2$ (%)	$\text{Q}_3$ (%)	$\text{Q}_4$ (%)	$\text{Q}_4/\text{Q}_3$
$0 \mu\text{M Al}^{3+}$	SP	-	33.2	66.7	2.0
	CP	7.8	54.5	37.6	
$2 \mu\text{M Al}^{3+}$	SP	-	24.9	75.0	3.0
	CP	11.1	55.6	33.1	

#### 4.2.4 In situ manipulation, mechanical testing, and FEM simulations to determine the Young's modulus of biosilica in girdle bands

Due to the morphological complexity of the intact frustule of *T.p.*, mechanical deformation of the entire frustule from either valve or girdle band direction may not lead to a meaningful quantitative assessment of its intrinsic mechanical properties e.g. Young's modulus (Appendix Figure A4.7). Therefore, in order to simplify the frustule structure, its morphological basic constituents, i.e. valves and girdle bands, should be isolated from each other prior to mechanical testing. To this

end, SEM-FIB milling was employed to accurately detach valves from girdle bands without damaging the integrity of either structure<sup>35</sup>. As shown in Figure 4.4a, the procedure started with an intact frustule of *T.p.* (obtaining by CPD, see also Appendix Figure A4.8) laying on its girdle bands. Single line scan FIB milling led to the accurate disconnection of the valves from the girdle bands. After FIB milling, the detached valves should be completely isolated from their girdle bands as any residual attachment would likely interfere with the deformation tests on the girdle bands. Thus, as can be seen in Figure 4.4a, the detached valves were transferred by a sharp tungsten probe, leaving the girdle bands fully intact, in a completely mechanical operation without using any adhesive materials (Appendix Movie A4.1). Owing to the possibility to alter the morphology and/or chemical composition of the frustule constituents, SEM compatible glue was deliberately avoided in this procedure. Following the complete detachment of valves from girdle bands, in situ deformation tests were carried out on the isolated girdle bands grown at different  $\text{Al}^{3+}$  concentrations. Several deformation tests by a force sensor (FMT-120 tip) mounted on a micromanipulator were performed through controlled displacement experiments. As can be seen in SEM micrographs, notwithstanding differences in the  $\text{Al}^{3+}$  feed concentrations, girdle bands exhibited a fully elastic behavior upon deformation and tip retraction without any signs of irreversible deformation (Figure 4.4b and Appendix Movie A4.2). However, what stands out in these experiments is that the applied forces for a comparable displacement revealed substantial differences for samples grown in the presence of  $\text{Al}^{3+}$ . Figure 4.4c shows that for about 1050 nm displacement the applied force for girdle bands grown at 2  $\mu\text{M}$   $\text{Al}^{3+}$  ( $1.60 \pm 0.08$   $\mu\text{N}$ ) is almost three times higher than the force required for girdle bands grown in the absence of  $\text{Al}^{3+}$  addition ( $0.52 \pm 0.02$   $\mu\text{N}$ ). As shown in Figure 4c there are some nonlinearities in the force-displacement curves of the samples, which were likely caused by internal rearrangements between overlapping girdle bands (Appendix Figure A4.1). In order to obtain an intrinsic mechanical property of biosilica in the girdle bands, i.e., the Young's modulus, FEM simulations were carried out based on the obtained experimental values. Figure 4.4d exhibits the initial status and maximum deformation of the model of the girdle bands, and a comparison of its corresponding force-displacement curve with girdle bands grown without  $\text{Al}^{3+}$  addition. As can be seen in Figure 4.4d there is excellent agreement between the experimental and simulation results in the lower region of the curves. The slight deviations at higher displacements can be due to slight buckling of the girdle bands during their deformation. Based on our experimental force-displacement data as well as considering the thickness and length variations of the girdle bands, the obtained Young's modulus of this biosilica grown at 0 and 2  $\mu\text{M}$   $\text{Al}^{3+}$  were 40 and 90 GPa, respectively. These results indicate a massive increase in the Young's modulus of the girdle bands due to the presence of  $\text{Al}^{3+}$  in the growth medium.



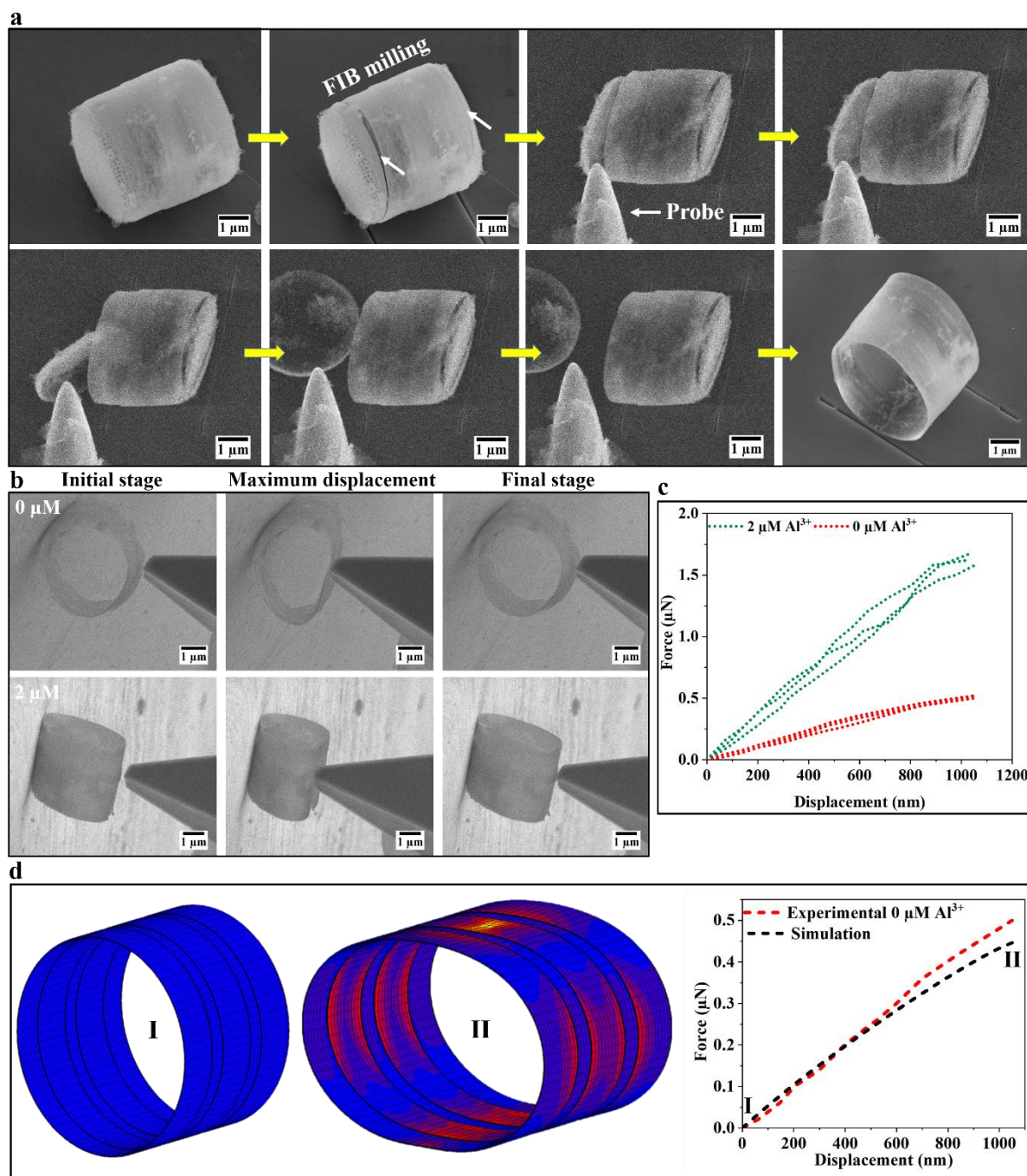


**Figure 4.4.** Effect of  $\text{Al}^{3+}$  on Young's modulus of the isolated girdle bands determined by a combination of mechanical manipulation, in situ deformation test, and FEM simulations. (a) SEM images of the process of isolation of valves from girdle bands of intact frustule of *T.p.* from left to right: an intact frustule of *T.p.* (obtained by CPD) laying on its girdle bands, separation of the valves from girdle bands by using line scan FIB milling followed by a sequence of mechanical manipulations by a sharp tungsten probe leading to isolation of intact girdle bands (resembling a hollow open-ended cylinder) (b) SEM images of different stages of in situ deformation experiments by FMT-120 tip on isolated girdle bands grown at different  $\text{Al}^{3+}$  concentrations; (c) three representative force-displacement curves each of girdle bands grown at 0 and 2  $\mu\text{M}$   $\text{Al}^{3+}$ ; (d) FEM model showing the initial undeformed state and at the maximum deformation state. The colors in the images represent the occurring Von Mises stresses. A comparison of force-displacement curves for the experimental and simulation results is shown on the right side.

#### 4.2.5 Determining the Young's modulus of biosilica in valves by in situ manipulation, mechanical testing, electron tomography, and FEM simulations

To assess whether and how  $\text{Al}^{3+}$  may modify the mechanical performance of the valves, mechanical testing on the valves, fully detached from the girdle bands, was also conducted. In this case, the relatively flat geometry represents an additional challenge, (Appendix Figure A4.9), as precautions have to be taken to avoid effects of the underlying substrate, throughout its deformation, on the determination of the valves mechanical properties. To this end, several holes with the slightly smaller diameter than the valves were drilled in the substrate by FIB milling. Subsequently, the isolated valves were transferred and mounted on these holes through mechanical manipulation. As shown in Figure 4.5a, this manipulation was performed with a tungsten probe, and resulted repeatedly in successful mounting of isolated valves exactly on top of the holes (see for example Appendix Movie A4.3). Following this step, deformation tests were conducted to obtain force-displacement curves for valves grown at 0 and 2  $\mu\text{M}$   $\text{Al}^{3+}$  concentrations. Figure 4.5b shows the valve at different stages of deformation testing, confirming an elastic behavior of the valve as well (Appendix Movie A4.4). A controlled displacement deformation test was performed for approximately 350 nm on each valve (about half of the required displacement to fracture the valves). As shown in Figure 4.5b, valves grown at 0 and 2  $\mu\text{M}$   $\text{Al}^{3+}$  exhibited rather comparable force-displacement curves. Due to the minimal morphological changes to valves by  $\text{Al}^{3+}$  addition, these results infer comparable mechanical properties of biosilica in the valves. For a more quantitative determination of the Young's modulus, however, owing to the complex morphology of the valve, using a simplified model in FEM will not allow sufficient accuracy. Therefore, electron tomography (ET) on an isolated valve (obtained by bath sonication) was conducted to acquire a realistic 3D geometry of its complex morphology which can ultimately be employed for FEM simulations. Figure 4.5c presents the workflow of ET, starting with acquisition of the TEM tilt-series followed by alignment and reconstruction of a 3D intensity map. Finally, segmentation and visualization of the reconstructed 3D intensity map was performed in Avizo software (Appendix Movie A4.5). The obtained 3D model (surface triangulation) of the valve was employed as input for FEM simulations in combination with the experimental force-displacement results to determine the Young's modulus. Figure 4.5d shows the maximum displacement state of the model during the simulations and the best fit comparison of their corresponding force-displacement curves with the experimental data. Based on this result, the determined Young's modulus of biosilica in the valves grown at both 0 and 2  $\mu\text{M}$   $\text{Al}^{3+}$  was 16.8 GPa, indicating a noticeably lower modulus in comparison to the girdle bands.

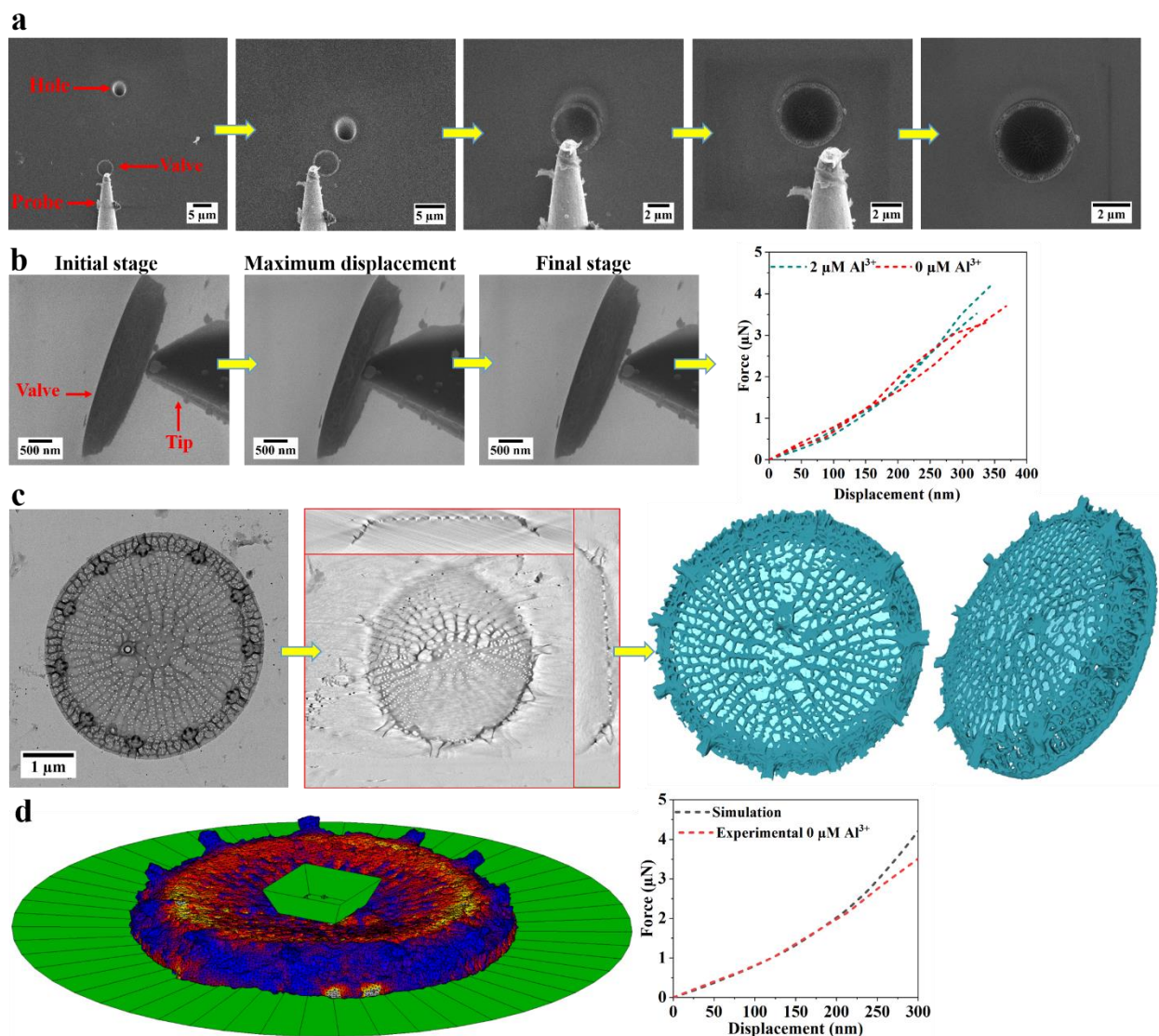


**Figure 4.5. Determining the effect of  $\text{Al}^{3+}$  on the Young's modulus of biosilica in isolated valves by combining mechanical manipulation, in situ deformation, ET, and FEM simulations.** (a) SEM images of the sequence of transferring an isolated valve to a prefabricated hole on the substrate by a tungsten probe; (b) left: SEM images of different stages of in situ deformation experiments on a valve mounted on holes, right: representative force-distance curves of isolated valves grown at 0 and 2  $\mu\text{M}$   $\text{Al}^{3+}$ ; (c) from left to right: TEM image of a valve of *T.p.*, slices through electron tomogram of the valve, and top and side view of segmented valve visualized by surface triangulation; (d) FEM simulation snap shot of the valve model at the maximum deformation stage. The colors in the image represents the equivalent Von Mises stresses. The right graphs exhibit a comparison of force-displacement curves between the experimental and simulation results.

### 4.3 Discussion

The results of this study reveal the effects of  $\text{Al}^{3+}$  ions in the growth medium on the morphological, chemical, and mechanical properties of frustule of diatom *T.p.*  $\text{Al}^{3+}$  incorporation leads to an enhancement in the silica crosslinking ( $\sim 30\%$  increase) and slight modifications of the morphology of the frustule. Consistent with previous studies, these findings further support the link between  $\text{Al}^{3+}$  incorporation and morphological changes of the frustule<sup>38</sup>. Furthermore, SEM-EDS elemental



mapping and  $^{27}\text{Al}$  NMR solid-state demonstrate the homogenous distribution of  $\text{Al}^{3+}$  and its incorporation within the silica network of the frustule, respectively. It is known that four coordinated Al species are integrated within the silica structure of the frustule<sup>10</sup>. Hence, it could be hypothesized that the presence of these Al species within the frustule is due to  $\text{Al}^{3+}$  uptake and internalization by diatom cells prior to cell wall formation inside the SDVs rather than simple deposition on the surface of the frustule.

Previously reported values of Young's modulus for different diatom frustules vary from 0.347 GPa to 300 GPa<sup>34,39-41</sup>, likely depending on diatom species, chemical treatment, and more notably the location of indentation on the frustule. Furthermore, several studies have shown that valves are different than girdle bands in term of their morphological parameters<sup>42,43</sup>, light harvesting<sup>44</sup>, and more importantly their mechanical performance<sup>45,46</sup>. In accordance with these investigations, our results demonstrate that the silica in girdle bands has a different Young's modulus than the silica in valves but also, these silicas seem to be differently affected by  $\text{Al}^{3+}$  incorporation. Interestingly, in situ deformation tests on the  $\text{Al}^{3+}$  incorporated girdle bands showed a significant enhancement in the required force for a given displacement and consequently an increase in their Young's modulus (90 GPa) in comparison to the Al-free girdle bands (40 GPa). In contrast, despite the presence of  $\text{Al}^{3+}$  in the silica of the valve its mechanical properties seems unaltered, showing a Young's modulus of 16.8 GPa. It is now well established that girdle bands and valves are formed within different types of SDVs at different growth stages<sup>47</sup>. The valves are formed by diatom cells during cell division whereas girdle bands are constructed during cell expansion during the interphase<sup>3</sup>. Besides, it has been hypothesized that certain conditions such as limitations in iron in the growth medium may lead to increase the duration of the frustule formation, resulting in enhanced silica content of constituents of the frustules with improved mechanical performance<sup>48</sup>. Furthermore, it has been shown that the presence of  $\text{Al}^{3+}$  in the growth medium of diatoms can decrease their growth rate and increase the thickness of the frustule<sup>38</sup>. Accordingly, a likely overall explanation for enhanced mechanical performance of the girdle bands in the presence of  $\text{Al}^{3+}$  can be due to a decreasing rate of formation during the cell expansion during the interphase which not only causes the morphological changes in the girdle bands but as shown here can lead to strengthening of the overlapping girdle bands as well. Alternatively, as it has already been confirmed that the addition of Al compounds into silicate glasses leads to increasing their crosslinking density and subsequently their Young's modulus<sup>24</sup>. The observed increased crosslinking density of silica in the frustule can mainly be stemming from girdle bands rather than valves which is ultimately manifested in their exceptionally high Young's modulus. However, further research should be undertaken to investigate the effect of  $\text{Al}^{3+}$  on crosslinking of biosilica within valves and girdle bands individually.

Various methods have been introduced to modify the chemical and morphological properties of diatom frustules for technological applications<sup>5,49</sup>. For instance, post modification of frustules after their harvesting<sup>50,51</sup> and genetic manipulations of living diatoms<sup>52,53</sup> have been conducted to achieve the desired micro- and nanostructures in the frustule. Despite the fact that the pore size

and thickness of the frustules, can be well-controlled, the post-modification technique either requires large diatom frustules such as *Coscinodiscus sp* and *Thalassiosira eccentrica* for atomic layer deposition<sup>50</sup> or harsh chemical treatment using HF to control the pore size of frustules<sup>51</sup>. Moreover, genetic manipulation necessitates knowledge of the genome sequence of diatom which is only available for a few diatom species<sup>28,54</sup>. Therefore, a more flexible approach has been studied where by alteration of the growth medium condition, due to the flexibility of the frustule formation, its morphological and chemical properties can be tuned. For example, the presence of various non-essential metal ions in the medium<sup>55,56</sup>, salinity<sup>4,57</sup>, and temperature<sup>58,59</sup> have been employed to modify the frustules' composition and morphology. In accordance with these studies, our finding here not only show that morphological properties of diatom frustule can be modified in the presence of  $\text{Al}^{3+}$  but also can lead to an enhancement in the mechanical properties of rather 'unpopular' constituents of the frustule, i.e., girdle bands. As previously suggested, due to their remarkable flexibility and low thickness, the girdle bands can be of great importance for possible industrial applications such as force actuator, sensor, and filters in microfluidic systems<sup>60</sup>. The combination of findings in this study provides unprecedented support for the conceptual idea that the morphological characteristics of the diatom frustule can be modified by controlled growth conditions as well as the intrinsic mechanical properties of selected constituents can be improved.

## 4.4 Materials and Methods

### 4.4.1 Diatom culture and $\text{Al}^{3+}$ addition

*Thalassiosira pseudonana* (UTEX LB FD2) was received from UTEX Culture Collection of Algae and maintained in artificial seawater medium supplemented with f/2 medium (ASW-f/2) at the following conditions: at 23 °C with 14 h light/10 h dark cycle, and light intensity of 3000 Lux. Synchronization of the culture was performed prior to  $\text{Al}^{3+}$  addition. To this end, about 1ml of a stock culture was used to incubate a starter culture in ASW-f/2. After a week, living cells were gently collected under sterile conditions by centrifugation at 2500 rpm for 3 minutes and maintained in a silicon-free medium (a medium containing all of the ASW-f/2 chemicals except for silicon) to obtain a relatively synchronized starter culture. Typically, after 24 hours, 30 ml of ASW-f/2 medium and desired  $\text{Al}^{3+}$  concentration (in the form of dissolved aluminum chloride) was inoculated in culture flasks with 0.5 ml of the synchronized starter culture. Accordingly, the new biogenic silica cell wall formation in the diatom takes place while  $\text{Al}^{3+}$  is present in the medium and can be taken up and incorporated into the frustule. It is worth noting that due to the wide variation and unknown Al species in growth medium conditions, we simply used term  $\text{Al}^{3+}$  throughout this thesis.

### 4.4.2 Sample preparation and characterization with Scanning electron microscopy imaging and Energy-Dispersive X-ray Spectroscopy elemental mapping

Extraction of various internal and external organic compounds in the frustule is necessary before any morphological characterization. Therefore, after harvesting the diatom cells from the cultures using centrifugation at 2600 rpm for 5 minutes (Minispin Centrifuge, Eppendorf, Germany), a

brownish-yellow pellet at the bottom of the centrifuge tube was obtained. The resultant pellet was washed and centrifuged with Milli Q water at least 3 times to completely remove the salts and unreacted precursors. Subsequently, the obtained pellets were washed in ethanol in combination with centrifugation several times. Then the resultant pellets were suspended in anhydrous ethanol and dried by a critical point dryer (Leica CPD 300 instrument) to obtain intact frustule of *T.p.* In order to split the valves from the girdle bands, the suspended frustules were centrifuged at 14,500 rpm three times followed by sonication in a bath sonicator (Branson ultrasonic cleaner, model 1510E-DTH, 42 kHz, USA) for 1 minute (it should be noted that this procedure usually led to isolated cracked valves and girdle bands). Before the SEM imaging of the intact frustule or its constituents, a sputter-coater (Quorum Q150T Plus–Turbo molecular pumped sputter coater) with a gold target was employed to coat the samples with less than 5 nm in thickness. For EDS elemental mapping, an adequate amount of the sample was placed onto a standard copper TEM grid covered by a 10 nm continuous carbon film and inserted into an in-house made TEM grid sample holder for SEM. SEM imaging and EDS mapping were conducted inside a dual-beam SEM Quanta 3D FEG (Thermo Fisher Scientific, USA), operating at an acceleration voltage of 5 and 10 kV, respectively.

#### 4.4.3 Focused Ion Beam-Scanning Electron Microscopy and micromanipulator

The separation of valves and girdle bands from an intact frustule of *T.p.* was an essential step in the workflow to obtain their intrinsic mechanical properties individually. Hence, the intact frustules of *T.p.* obtained by critical point dryer were placed on a silicon wafer substrate that was fixed by silver paste to a standard SEM stub. The boundaries between the valves and girdle bands of the frustules were precisely cut by single line scans (20–40 nm width) using FIB milling. Because of its high spatial resolution of a few nanometers, FIB milling led to well preserved isolated valves and girdle bands. The FIB milling process was conducted in a dual-beam SEM Quanta 3D FEG (Thermo Fisher Scientific, USA), equipped with a gallium ion ( $\text{Ga}^+$ ) source operating at optimum conditions of an accelerating voltage of 30 kV and a beam current of 1.5 pA. These milling parameters were important to prevent the structural collapse of the frustule as previously reported in detail<sup>35</sup>. Following the detachment of the valves from the girdle bands by FIB milling, a micromanipulator (MM3A-EM, Kleindiek Nanotechnik GmbH, Germany) with positional accuracy of about 10 nm and freedom of movement in three axes was used to completely separate them. For the manipulation of the valves, tungsten probe with the radius of approximately 150 nm mounted on the micromanipulator was employed. Subsequently, the isolated valves were transferred through mechanical manipulation by the tungsten probe to an area of the substrate where several holes with diameters comparable to the valve diameters had been pre-milled by FIB milling at an accelerating voltage of 30 kV and current of 1 nA. The valves were mounted on the holes with the probe without using any SEM-compatible glue.

#### 4.4.4 Mechanical testing on isolated valves and girdle bands

In situ deformation tests were performed on isolated girdle bands as well as isolated valves mounted on the predefined holes. Force measurement sensor FMT-120, an AFM-based sensor with

the resolution of 10 nN, (Kleindiek Nanotechnik GmbH, Germany) mounted on the micromanipulator was employed to measure the applied force on the specimens. Throughout the in situ experiments, FMT-120 provided force-time data which in correlation with image analysis of SEM micrographs could be converted to force-displacement curves. To this end, SEM images were acquired continually during the measurements. Then, in order to determine the displacement, Gatan digital micrograph software was used to follow the edge of the samples or the small particles attached to the FMT-120 tip throughout the mechanical testing. Finally, the corresponding applied force on the girdle bands/valves was determined for each displacement stage.

#### 4.4.5 TEM thickness measurements and electron tomography

Samples of valves and girdle bands of *T.p.* (isolated by bath sonication) were prepared by depositing 10  $\mu$ l of their suspensions on a 200-mesh standard TEM grid covered by carbon films. A Tecnai T20 G2 microscope (Thermo Fisher Scientific, USA) operated at 200 kV, equipped with a LaB<sub>6</sub> filament and a 4k CETA CMOS camera was employed for TEM image acquisition. Thickness quantification of valves and girdle bands were performed based on mass-thickness contrast considerations with an in-house MATLAB script (see detailed information of procedure in Appendix page 3). For electron tomography of the valve a tilt series was acquired by tilting the sample from  $-73$  to  $73^\circ$ , at  $2^\circ$  increments and acquiring an image at each tilt step. Tilt-series alignment and 3D reconstruction were performed in IMOD<sup>61</sup>. Alignment was performed through manual tracking of gold fiducial positions across all slices in the tilt-series, followed by model fitting and minimization of the residuals. The tomogram was reconstructed using the Simultaneous Iterative Reconstructive Technique (SIRT) with 20 iterations. The TEM images of the tilt-series had a pixel size of 1.337 nm and were binned by a factor 2 prior to reconstruction of the final tomogram. The reconstruction was segmented and visualized using Avizo software (AvizoFire 9.2, Thermo Fisher Scientific). It is worth noting that cribrum pores were not included in the obtained 3D reconstruction of the valve.

#### 4.4.6 <sup>29</sup>Si and <sup>27</sup>Al solid state NMR details

Measurements were performed on an Oxford magnet of a static magnetic field at 9.4 T (operating frequency for <sup>1</sup>H and <sup>29</sup>Si at 400.1 and 79.5 MHz, respectively) equipped with a Bruker NEO spectrometer. The <sup>1</sup>H and <sup>29</sup>Si chemical shifts were referenced to tetramethylsilane at 0 ppm. All samples were packed into either a 6 mm (o. d.) PENCIL rotor with two Teflon restrictors or a 1.6 mm (o. d.) PENCIL rotor and measured with Varian 6 mm or 1.6 mm HXY probe heads. Nitrogen gas was used to spin the rotor. For <sup>29</sup>Si MAS NMR measurement of diatom samples, the temperature was regulated at 15 °C during measurement to avoid further silica condensation. For <sup>29</sup>Si MAS NMR spectra, the magic-angle spinning (MAS) rate was set to 4 kHz. Due to the low sample quantity, the <sup>29</sup>Si T<sub>1</sub> relaxation time constant was not determined, and a time constant of 3000 s was chosen as the recycle delay based on previous observations of similar samples for semi-quantitative comparison<sup>62</sup>. High-power proton decoupling was applied using the two-pulse phase modulation (TPPM)<sup>63</sup> scheme with a flip angle of 15 degree and a <sup>1</sup>H r.f. at ca. 62.5 kHz during signal

acquisition. Typically, between 260 and 380 transients were averaged to obtain spectra with acceptable signal-to-noise ratios. For spectra processing, 250 Hz of apodization was applied. SSNake<sup>64</sup> software was used to afford spectra fitting result. For 1D  $^1\text{H}$  MAS NMR spectra, the MAS rate was set to 25 kHz.  $^1\text{H}$   $T_1$  relaxation time constants were measured using saturation-recovery experiment, and the recycle delay was set to 5 times of  $^1\text{H}$   $T_1$ .  $^{27}\text{Al}$  MAS NMR spectra were recorded using an 11.7 Tesla Bruker DMX500 NMR spectrometer, operating at 132 MHz for  $^{27}\text{Al}$ . The spectra were recorded with a spinning rate of 25 kHz and a single excitation pulse length of 1  $\mu\text{s}$  with a 1 s repetition time. The reference signal for the  $^{27}\text{Al}$  chemical shift was a saturated solution of  $\text{Al}(\text{NO}_3)_3$ .

#### 4.4.7 FEM Simulations of the valve and girdle band

Finite element method (FEM) simulations were conducted using the commercial software package MSC.Marc in order to determine the intrinsic material properties of biogenic silica in both the valve and girdle band, i.e. their Young's modulus. The mesh of the valve was generated based on the surface mesh that was experimentally obtained by electron tomography and consisted out of approximately 230 000 second order tetrahedral elements. During the conversion from surface mesh towards a volume mesh some of the fine microstructural details had to be removed in order to reduce the complexity of the numerical model. The indenter itself was modeled as an impenetrable surface with an infinite stiffness. The bottom of the valve was placed in close contact with a circular impenetrable surface which acts as the floor of the sample holder. In the center of this surface a hole was placed in order to resemble the deformation tests inside the SEM. Three equidistant nodes which were placed in close contact with the bottom surface were constrained in all three directions in order to prevent all rigid body modes of the valve, including all rotations. Finally, a load case was specified which describes the z-displacement of the indenter identical to the deformation test as performed inside the SEM. For the entire girdle bands the assumption was made that it consists out of five individual perfectly cylindrical girdle bands with an overlap of 30 % between individual bands as previously inferred<sup>65</sup>. The uniform thickness of each band was set at the experimentally obtained values. In total, the model consists out of 16 000 second order hexahedral elements. The bottom of the girdle band was fixed in the  $x$ - $y$ -plane in order to represent the surface of the sample support and the indenter was replaced by a point displacement in the  $z$ -direction in order to reduce complexity of the model. Due to the relatively low geometrical stiffness of the entire structure this was a valid choice and it has been compared to numerical results obtained in our previous study in which the actual indenter was included<sup>35</sup>.

#### 4.5 Reference

- 1 Hildebrand, M. Diatoms, biomineralization processes, and genomics. *Chemical Reviews* **108**, 4855-4874 (2008).
- 2 Luís, A. T., Hlúbiková, D., Vaché, V., Choquet, P., Hoffmann, L. & Ector, L. Atomic force microscopy (AFM) application to diatom study: review and perspectives. *Journal of Applied Phycology* **29**, 2989-3001 (2017).
- 3 Kröger, N. & Poulsen, N. Diatoms—from cell wall biogenesis to nanotechnology. *Annual Review of Genetics* **42**, 83-107 (2008).

- 4 Vrieling, E. G., Sun, Q., Tian, M., Kooyman, P. J., Gieskes, W. W., van Santen, R. A. & Sommerdijk, N. A. Salinity-dependent diatom biosilicification implies an important role of external ionic strength. *Proceedings of the National Academy of Sciences* **104**, 10441-10446 (2007).
- 5 Su, Y., Lundholm, N. & Ellegaard, M. Effects of abiotic factors on the nanostructure of diatom frustules—ranges and variability. *Applied Microbiology and Biotechnology* **102**, 5889-5899 (2018).
- 6 Heredia, A., Figueira, E., Rodrigues, C. T., Rodríguez-Galván, A., Basiuk, V. A., Vrieling, E. G. & Almeida, S. F. Cd<sup>2+</sup> affects the growth, hierarchical structure and peptide composition of the biosilica of the freshwater diatom *Nitzschia palea* (Kützinger) W. Smith. *Phycological Research* **60**, 229-240 (2012).
- 7 Lang, Y., del Monte, F., Rodriguez, B. J., Dockery, P., Finn, D. P. & Pandit, A. Integration of TiO<sub>2</sub> into the diatom *Thalassiosira weissflogii* during frustule synthesis. *Scientific Reports* **3**, 1-11 (2013).
- 8 Kaden, J., Brückner, S. I., Machill, S., Krafft, C., Pöpl, A. & Brunner, E. Iron incorporation in biosilica of the marine diatom *Stephanopyxis turris*: dispersed or clustered? *Biometals* **30**, 71-82 (2017).
- 9 Jeffries, C., Solanki, R., Rangineni, Y., Wang, W., Chang, C. h. & Rorrer, G. L. Electroluminescence and photoluminescence from nanostructured diatom frustules containing metabolically inserted germanium. *Advanced Materials* **20**, 2633-2637 (2008).
- 10 Machill, S., Köhler, L., Ueberlein, S., Hedrich, R., Kunaschk, M., Paasch, S., Schulze, R. & Brunner, E. Analytical studies on the incorporation of aluminium in the cell walls of the marine diatom *Stephanopyxis turris*. *BioMetals* **26**, 141-150 (2013).
- 11 Liu, Q., Zhou, L., Liu, F., Fortin, C., Tan, Y., Huang, L. & Campbell, P. G. Uptake and subcellular distribution of aluminum in a marine diatom. *Ecotoxicology and Environmental Safety* **169**, 85-92 (2019).
- 12 Gillmore, M. L., Golding, L. A., Angel, B. M., Adams, M. S. & Jolley, D. F. Toxicity of dissolved and precipitated aluminium to marine diatoms. *Aquatic Toxicology* **174**, 82-91 (2016).
- 13 Xie, J., Bai, X., Lavoie, M., Lu, H., Fan, X., Pan, X., Fu, Z. & Qian, H. Analysis of the proteome of the marine diatom *Phaeodactylum tricornutum* exposed to aluminum providing insights into aluminum toxicity mechanisms. *Environmental Science & Technology* **49**, 11182-11190 (2015).
- 14 Zhou, L., Tan, Y., Huang, L., Fortin, C. & Campbell, P. G. Aluminum effects on marine phytoplankton: implications for a revised Iron Hypothesis (Iron–Aluminum Hypothesis). *Biogeochemistry* **139**, 123-137 (2018).
- 15 Vrieling, E., Poort, L., Beelen, T. & Gieskes, W. Growth and silica content of the diatoms *Thalassiosira weissflogii* and *Navicula salinarum* at different salinities and enrichments with aluminium. *European Journal of Phycology* **34**, 307-316 (1999).
- 16 Santana-Casiano, J. M., González-Dávila, M., Laglera, L. M., Pérez-Peña, J., Brand, L. & Millero, F. J. The influence of zinc, aluminum and cadmium on the uptake kinetics of iron by algae. *Marine Chemistry* **59**, 95-111 (1997).
- 17 Zhou, L., Tan, Y., Huang, L. & Wang, W.-X. Enhanced utilization of organic phosphorus in a marine diatom *Thalassiosira weissflogii*: A possible mechanism for aluminum effect under P limitation. *Journal of Experimental Marine Biology and Ecology* **478**, 77-85 (2016).
- 18 Köhler, L., Machill, S., Werner, A., Selzer, C., Kaskel, S. & Brunner, E. Are diatoms “green” aluminosilicate synthesis microreactors for future catalyst production? *Molecules* **22**, 2232 (2017).
- 19 Soleimani, M., Rutten, L., Maddala, S. P., Wu, H., Eren, E. D., Mezari, B., Schreur-Piet, I., Friedrich, H. & van Benthem, R. A. Modifying the thickness, pore size, and composition of diatom frustule in *Pinnularia* sp. with Al<sup>3+</sup> ions. *Scientific Reports* **10**, 19498 (2020).
- 20 Liu, D., Yuan, P., Tian, Q., Liu, H., Deng, L., Song, Y., Zhou, J., Losic, D., Zhou, J. & Song, H. Lake sedimentary biogenic silica from diatoms constitutes a significant global sink for aluminium. *Nature Communications* **10**, 1-7 (2019).

- 21 Koning, E., Gehlen, M., Flank, A.-M., Calas, G. & Epping, E. Rapid post-mortem incorporation of aluminum in diatom frustules: Evidence from chemical and structural analyses. *Marine Chemistry* **106**, 208-222 (2007).
- 22 Van Cappellen, P., Dixit, S. & van Beusekom, J. Biogenic silica dissolution in the oceans: Reconciling experimental and field-based dissolution rates. *Global Biogeochemical Cycles* **16**, 23-21-23-10 (2002).
- 23 Dixit, S., Van Cappellen, P. & van Bennekom, A. J. Processes controlling solubility of biogenic silica and pore water build-up of silicic acid in marine sediments. *Marine Chemistry* **73**, 333-352 (2001).
- 24 Xiang, Y., Du, J., Smedskjaer, M. M. & Mauro, J. C. Structure and properties of sodium aluminosilicate glasses from molecular dynamics simulations. *The Journal of Chemical Physics* **139**, 044507 (2013).
- 25 Romann, J., Chauton, M. S., Hanetho, S. M., Vebner, M., Heldal, M., Thaulow, C., Vadstein, O., Tranell, G. & Einarsrud, M.-A. Diatom frustules as a biomaterial: effects of chemical treatment on organic material removal and mechanical properties in cleaned frustules from two *Coscinodiscus* species. *Journal of Porous Materials* **23**, 905-910 (2016).
- 26 Görlich, S., Pawolski, D., Zlotnikov, I. & Kröger, N. Control of biosilica morphology and mechanical performance by the conserved diatom gene Silicanin-1. *Communications Biology* **2**, 1-8 (2019).
- 27 Gutiérrez, A., Guney, M. G., Fedder, G. K. & Dávila, L. P. The role of hierarchical design and morphology in the mechanical response of diatom-inspired structures via simulation. *Biomaterials Science* **6**, 146-153 (2018).
- 28 Armbrust, E. V., Berges, J. A., Bowler, C., Green, B. R., Martinez, D., Putnam, N. H., Zhou, S., Allen, A. E., Apt, K. E. & Bechner, M. The genome of the diatom *Thalassiosira pseudonana*: ecology, evolution, and metabolism. *Science* **306**, 79-86 (2004).
- 29 Sumper, M. & Brunner, E. Silica biomineralisation in diatoms: the model organism *Thalassiosira pseudonana*. *ChemBioChem* **9**, 1187-1194 (2008).
- 30 Berges, J. A., Varela, D. E. & Harrison, P. J. Effects of temperature on growth rate, cell composition and nitrogen metabolism in the marine diatom *Thalassiosira pseudonana* (Bacillariophyceae). *Marine Ecology Progress Series* **225**, 139-146 (2002).
- 31 Johnston, M., Gascooke, J., Ellis, A. & Leterme, S. Diatoms response to salinity changes: investigations using single pulse and cross polarisation magic angle spinning  $^{29}\text{Si}$  NMR spectra. *Analyst* **143**, 4930-4935 (2018).
- 32 Hildebrand, M., Kim, S., Shi, D., Scott, K. & Subramaniam, S. 3D imaging of diatoms with ion-abrasion scanning electron microscopy. *Journal of Structural Biology* **166**, 316-328 (2009).
- 33 Gutiérrez, A., Gordon, R. & Dávila, L. P. Deformation modes and structural response of diatom frustules. *J. Mater. Sci. Eng. Adv. Technol* **15**, 105-134 (2017).
- 34 Aitken, Z. H., Luo, S., Reynolds, S. N., Thaulow, C. & Greer, J. R. Microstructure provides insights into evolutionary design and resilience of *Coscinodiscus* sp. frustule. *Proceedings of the National Academy of Sciences* **113**, 2017-2022 (2016).
- 35 Soleimani, M., van Breemen, L. C., Maddala, S. P., Joosten, R. R., Wu, H., Schreur-Piet, I., van Benthem, R. A. & Friedrich, H. In Situ Manipulation and Micromechanical Characterization of Diatom Frustule Constituents Using Focused Ion Beam Scanning Electron Microscopy. *Small Methods* **5**, 2100638 (2021).
- 36 Abraham, A., Lee, S.-H., Shin, C.-H., Hong, S. B., Prins, R. & van Bokhoven, J. A. Influence of framework silicon to aluminium ratio on aluminium coordination and distribution in zeolite Beta investigated by  $^{27}\text{Al}$  MAS and  $^{27}\text{Al}$  MQ MAS NMR. *Physical Chemistry Chemical Physics* **6**, 3031-3036 (2004).
- 37 Mahler, J. & Sebal, A. Deconvolution of  $^{29}\text{Si}$  magic-angle spinning nuclear magnetic resonance spectra of silicate glasses revisited—some critical comments. *Solid State Nuclear Magnetic Resonance* **5**, 63-78 (1995).

- 38 Soleimani, M., Rutten, L., Maddala, S. P., Wu, H., Eren, E. D., Mezari, B., Schreur-Piet, I., Friedrich, H. & van Benthem, R. A. Modifying the thickness, pore size, and composition of diatom frustule in *Pinnularia* sp. with Al<sup>3+</sup> ions. *Scientific Reports* **10**, 19498 (2020).
- 39 Almqvist, N., Delamo, Y., Smith, B., Thomson, N., Bartholdson, Å., Lal, R., Brzezinski, M. & Hansma, P. Micromechanical and structural properties of a pennate diatom investigated by atomic force microscopy. *Journal of Microscopy* **202**, 518-532 (2001).
- 40 Subhash, G., Yao, S., Bellinger, B. & Gretz, M. Investigation of mechanical properties of diatom frustules using nanoindentation. *Journal of Nanoscience and Nanotechnology* **5**, 50-56 (2005).
- 41 Losic, D., Short, K., Mitchell, J. G., Lal, R. & Voelcker, N. H. AFM nanoindentations of diatom biosilica surfaces. *Langmuir* **23**, 5014-5021 (2007).
- 42 Zgłobicka, I., Gluch, J., Liao, Z., Werner, S., Guttman, P., Li, Q., Bazarnik, P., Plocinski, T., Witkowski, A. & Kurzydłowski, K. J. Insight into diatom frustule structures using various imaging techniques. *Scientific Reports* **11**, 1-10 (2021).
- 43 Kumari, E., Görlich, S., Poulsen, N. & Kröger, N. Genetically programmed regioselective immobilization of enzymes in biosilica microparticles. *Advanced Functional Materials* **30**, 2000442 (2020).
- 44 Goessling, J. W., Su, Y., Maibohm, C., Ellegaard, M. & Köhl, M. Differences in the optical properties of valve and girdle band in a centric diatom. *Journal of the Royal Society Interface Focus* **9**, 20180031 (2019).
- 45 Wang, Y., Zhang, D., Cai, J., Pan, J., Chen, M., Li, A. & Jiang, Y. Biosilica structures obtained from *Nitzschia*, *Ditylum*, *Skeletonema*, and *Coscinodiscus* diatom by a filtration-aided acid cleaning method. *Applied Microbiology and Biotechnology* **95**, 1165-1178 (2012).
- 46 Hamm, C. E., Merkel, R., Springer, O., Jurkojc, P., Maier, C., Pecht, K. & Smetacek, V. Architecture and material properties of diatom shells provide effective mechanical protection. *Nature* **421**, 841-843 (2003).
- 47 Heintze, C., Formanek, P., Pohl, D., Hauptstein, J., Rellinghaus, B. & Kröger, N. An intimate view into the silica deposition vesicles of diatoms. *BMC Materials* **2**, 1-15 (2020).
- 48 Wilken, S., Hoffmann, B., Hersch, N., Kirchgessner, N., Dieluweit, S., Rubner, W., Hoffmann, L. J., Merkel, R. & Peeken, I. Diatom frustules show increased mechanical strength and altered valve morphology under iron limitation. *Limnology and Oceanography* **56**, 1399-1410 (2011).
- 49 Zhang, D., Wang, Y., Cai, J., Pan, J., Jiang, X. & Jiang, Y. Bio-manufacturing technology based on diatom micro-and nanostructure. *Chinese Science Bulletin* **57**, 3836-3849 (2012).
- 50 Losic, D., Triani, G., Evans, P. J., Atanacio, A., Mitchell, J. G. & Voelcker, N. H. Controlled pore structure modification of diatoms by atomic layer deposition of TiO<sub>2</sub>. *Journal of Materials Chemistry* **16**, 4029-4034 (2006).
- 51 Zhang, D., Wang, Y., Zhang, W., Pan, J. & Cai, J. Enlargement of diatom frustules pores by hydrofluoric acid etching at room temperature. *Journal of Materials Science* **46**, 5665-5671 (2011).
- 52 Hildebrand, M. Prospects of manipulating diatom silica nanostructure. *Journal of Nanoscience and Nanotechnology* **5**, 146-157 (2005).
- 53 De Tommasi, E., Gielis, J. & Rogato, A. Diatom frustule morphogenesis and function: a multidisciplinary survey. *Marine Genomics* **35**, 1-18 (2017).
- 54 Kroth, P. G., Bones, A. M., Daboussi, F., Ferrante, M. I., Jaubert, M., Kolot, M., Nymark, M., Bártulos, C. R., Ritter, A. & Russo, M. T. Genome editing in diatoms: achievements and goals. *Plant Cell Reports* **37**, 1401-1408 (2018).
- 55 Basharina, T. N., Danilovtseva, E. N., Zelinskiy, S. N., Klimenkov, I. V., Likhoshway, Y. V. & Annenkov, V. V. The effect of titanium, zirconium and tin on the growth of diatom *Synedra acus* and morphology of its silica valves. *Silicon* **4**, 239-249 (2012).
- 56 Falasco, E., Bona, F., Badino, G., Hoffmann, L. & Ector, L. Diatom teratological forms and environmental alterations: a review. *Hydrobiologia* **623**, 1-35 (2009).
- 57 Trobajo, R., Rovira, L., Mann, D. G. & Cox, E. J. Effects of salinity on growth and on valve morphology of five estuarine diatoms. *Phycological Research* **59**, 83-90 (2011).



- 58 Hansen, L. R., í Soylu, S., Kotaki, Y., Moestrup, Ø. & Lundholm, N. Toxin production and temperature-induced morphological variation of the diatom *Pseudo-nitzschia seriata* from the Arctic. *Harmful Algae* **10**, 689-696 (2011).
- 59 Jung, S. W., Youn, S. J., Shin, H. H., Yun, S. M., Ki, J.-S. & Lee, J. H. Effect of temperature on changes in size and morphology of the marine diatom, *Ditylum brightwellii* (West) Grunow (Bacillariophyceae). *Estuarine, Coastal and Shelf Science* **135**, 128-136 (2013).
- 60 Wang, Y., Cai, J., Jiang, Y., Jiang, X. & Zhang, D. Preparation of biosilica structures from frustules of diatoms and their applications: current state and perspectives. *Applied Microbiology and Biotechnology* **97**, 453-460 (2013).
- 61 Kremer, J. R., Mastronarde, D. N. & McIntosh, J. R. Computer visualization of three-dimensional image data using IMOD. *Journal of Structural Biology* **116**, 71-76 (1996).
- 62 Maddala, S. P., Liao, W.-C., Joosten, R. R., Soleimani, M., Tuinier, R., Friedrich, H. & van Benthem, R. A. Chain length of bioinspired polyamines affects size and condensation of monodisperse silica particles. *Communications Chemistry* **4**, 1-11 (2021).
- 63 Bennett, A. E., Rienstra, C. M., Auger, M., Lakshmi, K. & Griffin, R. G. Heteronuclear decoupling in rotating solids. *The Journal of chemical physics* **103**, 6951-6958 (1995).
- 64 Van Meerten, S., Franssen, W. & Kentgens, A. ssNake: A cross-platform open-source NMR data processing and fitting application. *Journal of Magnetic Resonance* **301**, 56-66 (2019).
- 65 Hildebrand, M., York, E., Kelz, J. I., Davis, A. K., Frigeri, L. G., Allison, D. P. & Doktycz, M. J. Nanoscale control of silica morphology and three-dimensional structure during diatom cell wall formation. *Journal of Materials Research* **21**, 2689-2698 (2006).

## 4.6 Appendix

### 4.6.1 Appendix figures and experimental details

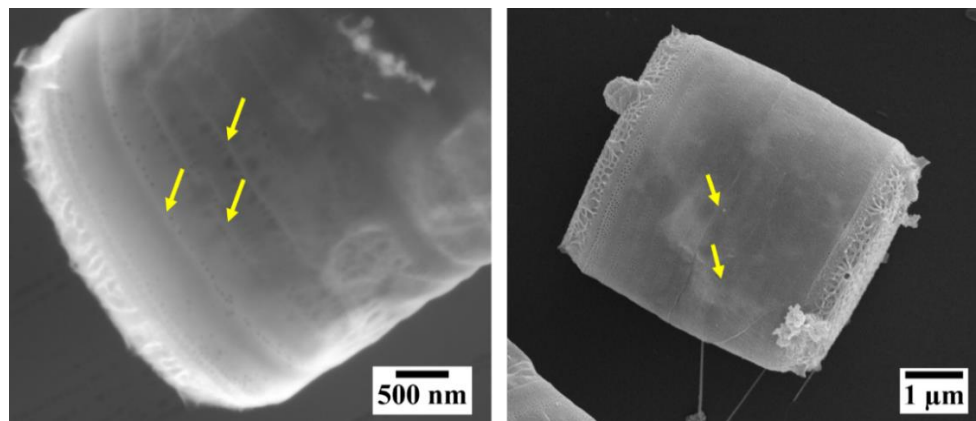


**Figure A4.1** SEM images of girdle bands view where the overlapping between the girdle bands are indicated.

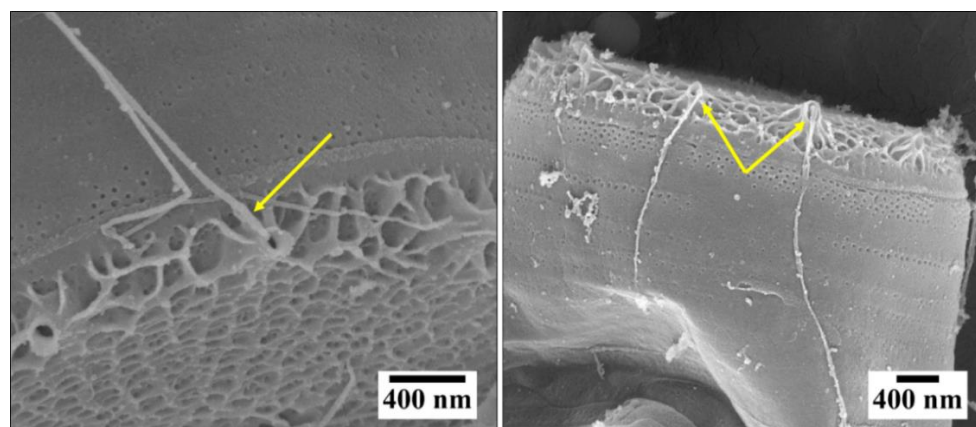


**Figure A4.2** SEM images of fultoportulae structures and linear fibers extending from them indicated by yellow arrows.

#### Thickness measurements

Due to the known effect of ribs and cross-connections on the mechanical properties of *T.p.*<sup>1,2</sup> their mean thicknesses were measured using TEM image analysis by an in-house MATLAB script. Appendix Figure A4.3 shows the image-processing procedures. First, a thickness map of the whole valve was calculated using a previously reported method<sup>2-4</sup> based on Lambert-Beer type absorption contrast. Note that the thickness of the thin carbon TEM support film was also taken into consideration and was subtracted in the calculation. Second, a binary mask of the valve regions containing ribs and cross-connections was created by manual thresholding. After removing small objects using MATLAB built-in function *Bwareaopen*, the total area of the ribs and cross-connection in the valve can be determined. Third, by multiplying the thickness map of the whole valve (Step 2) with the binary mask of ribs and cross-connections (Step 3) the thickness map of the ribs and cross-

connections was obtained. From this map the mean thickness of ribs and cross-connections in an isolated valve of *T.p.* and the corresponding standard error were determined.

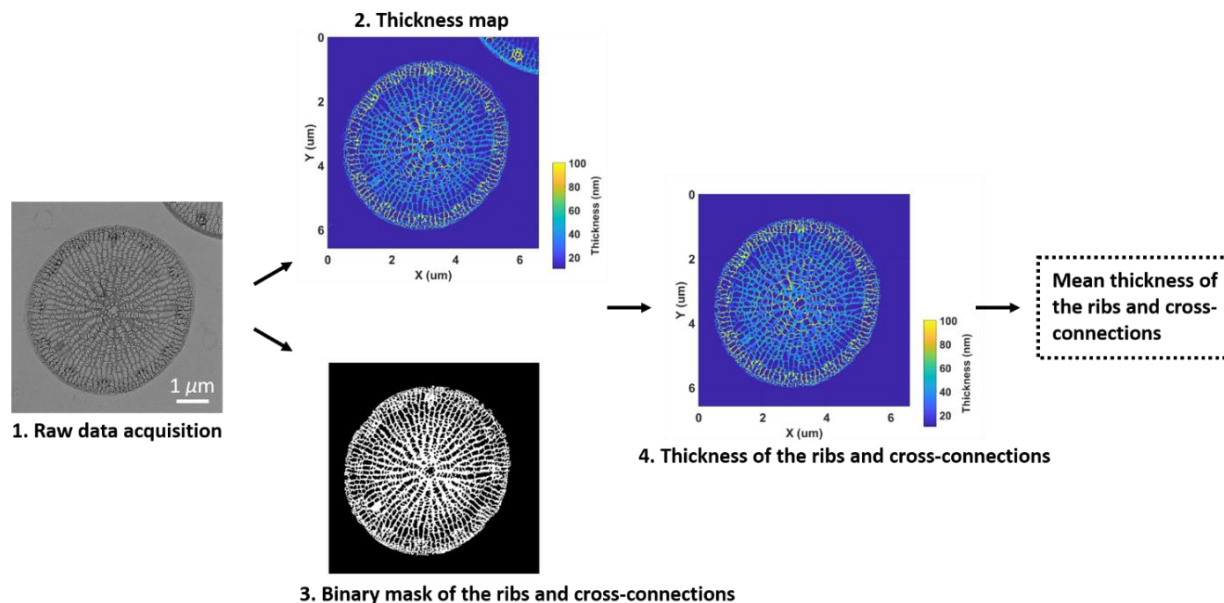


**Figure A4.3** Schematics of TEM image-processing procedure for measuring the mean thickness of the ribs and cross-connection of valve of *T.p.*

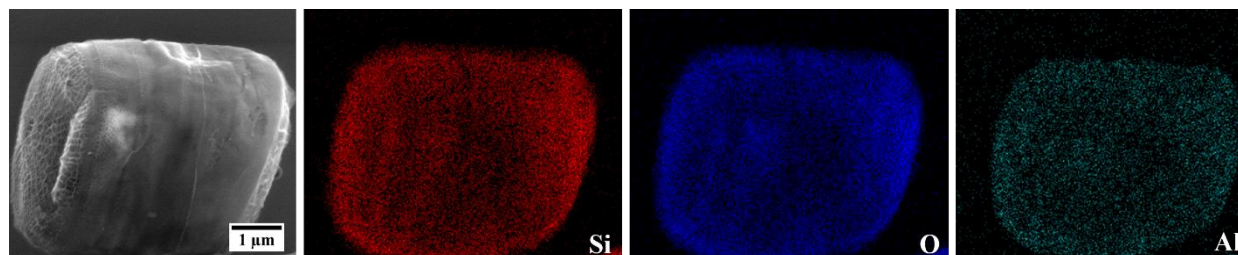


**Figure A4.4** SEM-EDS elemental maps from girdle band view of frustule of *T.p.* grown at  $2 \mu\text{M Al}^{3+}$  (scale bar= $2 \mu\text{m}$ ).

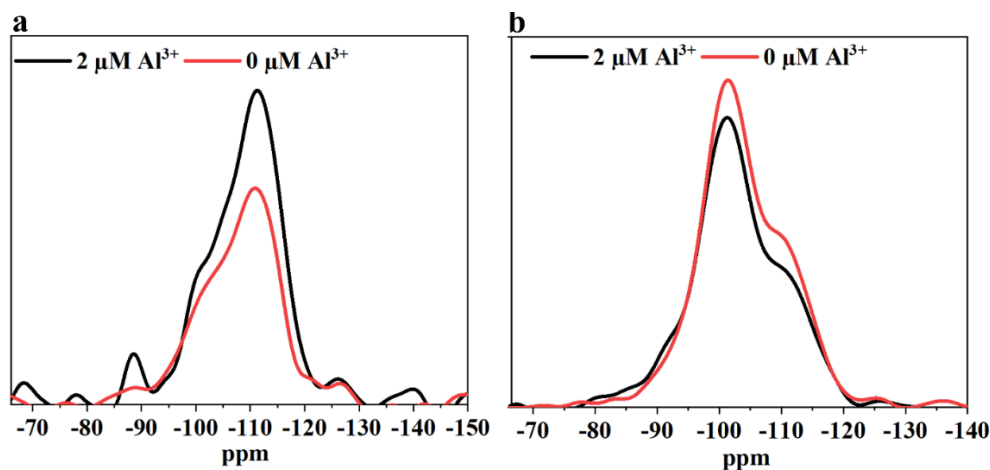


**Figure A4.5**  $^{29}\text{Si}$  solid state NMR spectra of *T.p.* grown at 0 and  $2 \mu\text{M Al}^{3+}$ . (a) Single pulse; (b) cross polarization MAS NMR spectra.

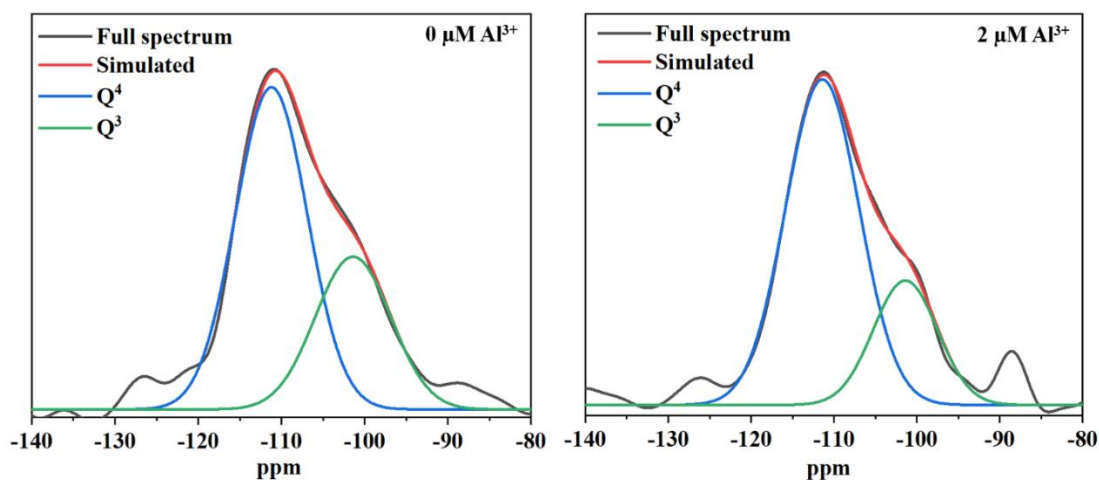


**Figure A4.6.** Decomposition of  $^{29}\text{Si}$  solid state NMR spectra of *T.p.* grown at 0 and  $2\ \mu\text{M}\ \text{Al}^{3+}$ .

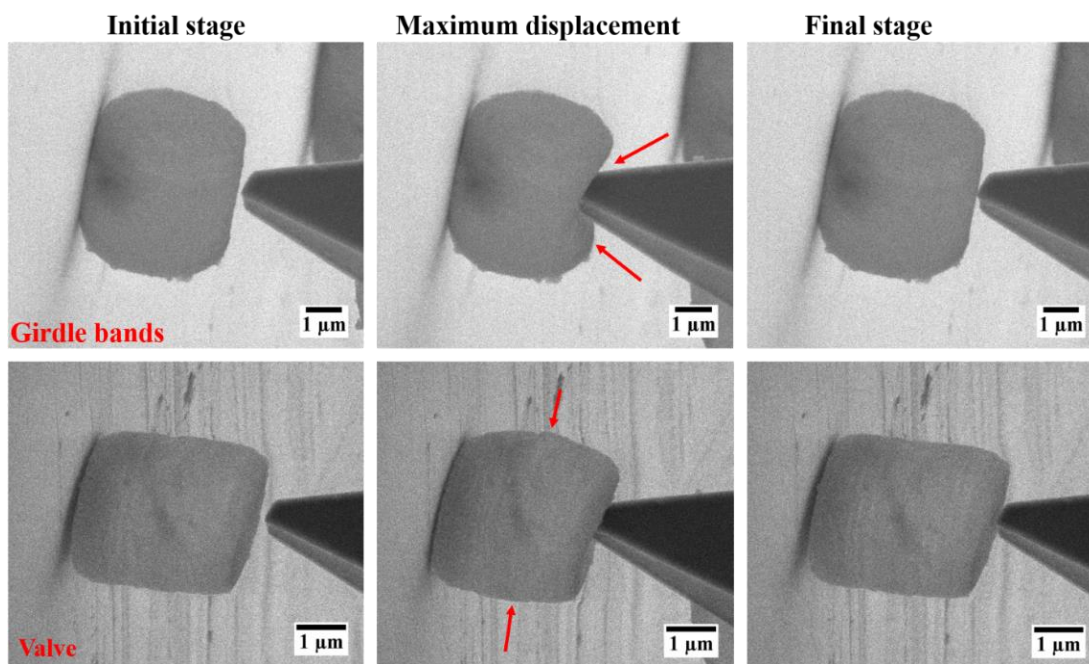


**Figure A4.7** In situ deformation test on intact frustule of *T.p.* (top) on girdle bands direction; (bottom) on the valve direction. In both cause an elastic behavior is observed and frustules retain their initial structures. The red arrows indicate the bulking and bulging behaviors of the intact frustule during the deformation tests respectively.

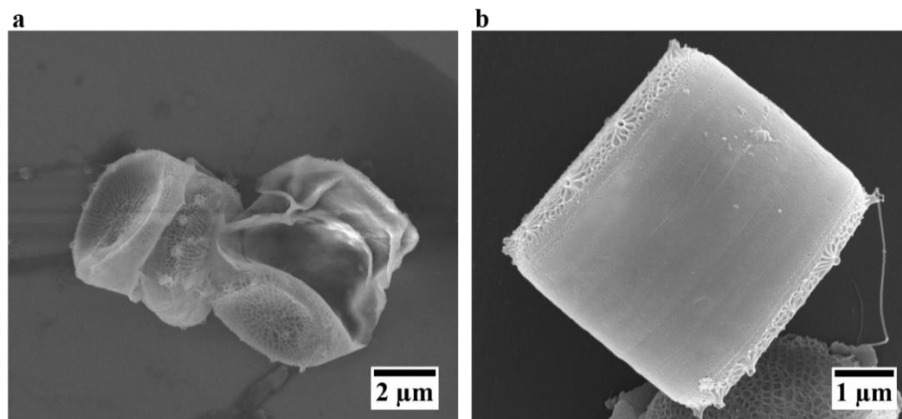


**Figure A4.8** Comparison of different drying procedures (a) Air dried collapsed frustule of *T.p.*; (b) Critical point dried intact frustule of *T.p.*

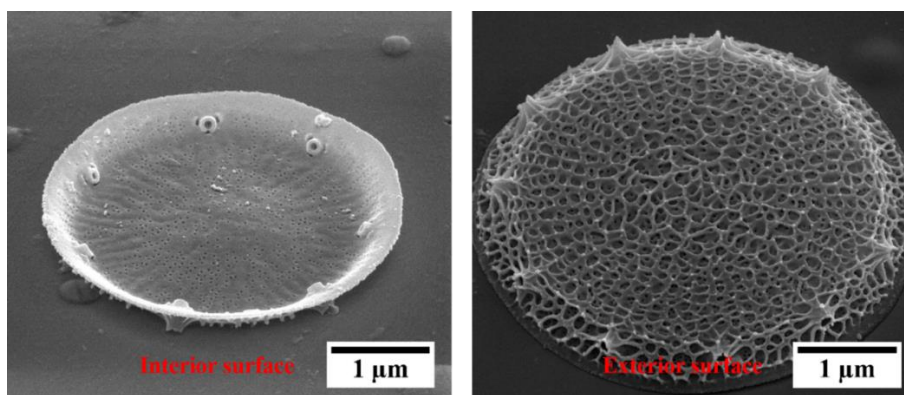
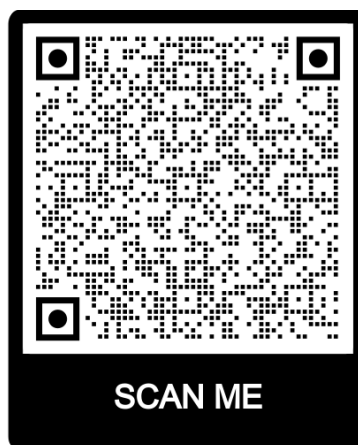


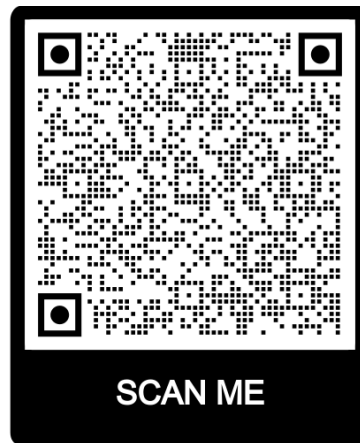
**Figure A4.9** SEM images of interior and exterior surface of isolated valves of *T.p.* resembling a plate-like structure. It was impossible to conduct any mechanical testing on this structure unless transferring and mounding the valve on a pre-milled hole in the substrate, otherwise, the effect of substrate cannot be ignored.

## 4.6.2 Appendix Movies

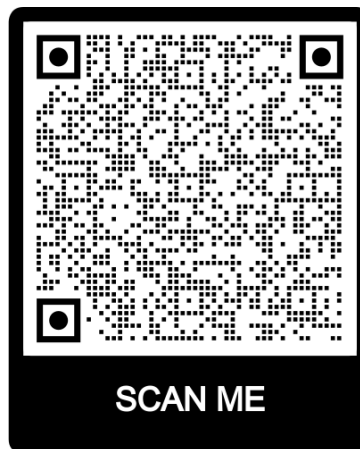
**Movie A4.1:** In situ mechanical manipulation of valves.



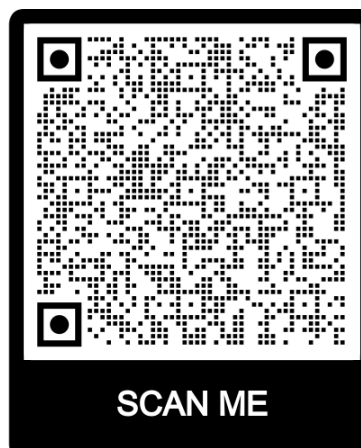
**Movie A4.2:** In situ deformation test on isolated girdle bands.



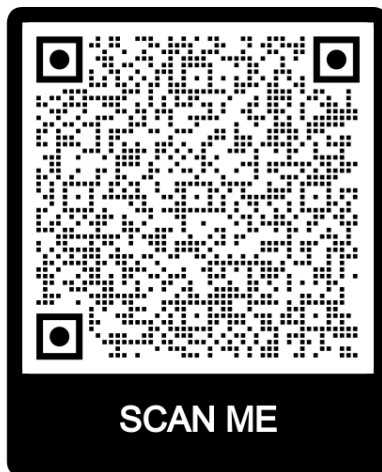
**Movie A4.3:** In situ transferring and mounting the isolated valves on the holes.



**Movie A4.4:** In situ deformation test on an isolated valve.



**Movie A4.5:** ET and 3D model of the valve.



#### 4.6.3 Appendix references

- 1 Görlich, S., Pawolski, D., Zlotnikov, I. & Kröger, N. Control of biosilica morphology and mechanical performance by the conserved diatom gene Silicanin-1. *Communications Biology* **2**, 1-8 (2019).
- 2 Soleimani, M., van Breemen, L. C., Maddala, S. P., Joosten, R. R., Wu, H., Schreur-Piet, I., van Benthem, R. A. & Friedrich, H. In Situ Manipulation and Micromechanical Characterization of Diatom Frustule Constituents Using Focused Ion Beam Scanning Electron Microscopy. *Small Methods*, 2100638 (2021).
- 3 Wu, H., Su, H., Joosten, R. R., Keizer, A. D., van Hazendonk, L. S., Wirix, M. J., Patterson, J. P., Laven, J., de With, G. & Friedrich, H. Mapping and Controlling Liquid Layer Thickness in Liquid-Phase (Scanning) Transmission Electron Microscopy. *Small Methods* **5**, 2001287 (2021).
- 4 Ianiro, A., Wu, H., van Rijt, M. M., Vena, M. P., Keizer, A. D., Esteves, A. C. C., Tuinier, R., Friedrich, H., Sommerdijk, N. A. & Patterson, J. P. Liquid-liquid phase separation during amphiphilic self-assembly. *Nature chemistry* **11**, 320-328 (2019).



# Chapter 5

## Investigating the Morphology and Mechanics of Biogenic Hierarchical Materials at and below Micrometer Scale

### Abstract

Investigating and understanding the intrinsic material properties of biogenic materials, which have evolved over millions of years into admirable structures with difficult to mimic hierarchical levels, holds the potential of replacing trial and error-based materials optimization in our efforts to make synthetic materials of similarly advanced complexity and properties. An excellent example is biogenic silica which is found in the exoskeleton of unicellular photosynthetic algae termed diatoms. Due to the complex micro and nanostructures found in their exoskeleton, determining the intrinsic mechanical properties of biosilica in diatoms has only partly been accomplished. Here, a general method is presented in which a combination of in situ deformation test inside an SEM with a realistic 3D model of the frustule of diatom *Craspedostauros sp.* (*C.sp.*) obtained by electron tomography, alongside Finite Element Method (FEM) simulations, enables quantification of the Young's modulus ( $E=2.4$  GPa) of this biogenic hierarchical silica. The presented workflow can be readily extended to other diatom species, biominerals or even synthetic hierarchical materials.

### The results presented in this chapter are based on:

Soleimani, M., van den Broek, S.J., Joosten, R.R., van Hazendonk, L., Maddala, S.P., van Breemen, L.C., van Benthem, R.A. and Friedrich, H. *Investigating the Morphology and Mechanics of Biogenic Hierarchical Materials at and below Micrometer Scale.*

Submitted.



## 5.1 Introduction

Biocomposites such as shell, bone, and teeth have been an inspirational class of materials for designing new synthetic materials with tunable and advanced properties through biomimetic and bioinspired approaches<sup>1-5</sup>. The hierarchical morphology of such materials imparts extraordinary mechanical properties, achievable neither by their individual constituents nor any synthetic counterparts<sup>6,7</sup>. Thus, our ability to measure the intrinsic material properties of such complex biomaterials is an indispensable first step towards overcoming trial and error-based materials optimization in our synthetic efforts to design them with similarly advanced property levels for desired applications<sup>8,9</sup>. One such hierarchical biocomposite is the siliceous exoskeleton of diatoms, the frustule, consisting of two valves and several overlapping girdle bands<sup>10,11</sup>. Diatoms are unicellular photosynthetic algae that live in aquatic and terrestrial environments with a size range from 2 to 2000  $\mu\text{m}$ <sup>12</sup>. The frustule with species-specific morphology<sup>13</sup> is a composite or hybrid material owing to the presence of various organic macromolecules such as silaffines and long-chain polyamines within its hydrated amorphous biogenic silica structure<sup>14,15</sup>. The current understanding is that these hybrid organic-inorganic structures, i.e. the frustule, act as mechanical protection against diatom predators<sup>16,17</sup>.

In recent years, researchers have shown an increased interest in the mechanical properties of frustules of a variety of diatom species by using several experimental techniques. For instance, mechanical properties of diatoms *Coscinodiscus sp* and *Navicula pilliculosa* have been measured by AFM at different regions of their frustules, confirming the key role of sub-micron morphological characteristics<sup>18,19</sup>. Conventional nanoindentation in combination with simulations studies has been performed on large diatoms such as *Coscinodiscus sp* and *Synedra sp.*, suggesting that the Young's modulus and hardness of biosilica is species-specific<sup>20</sup>. Furthermore, in situ mechanical testing such as indentation on the whole diatom frustule or bending test on frustule's fragments have been performed inside SEM to determine contact stiffness and Young's modulus, respectively<sup>21,22</sup>. Besides these experimental studies, several simulations also have been conducted on simplified frustule models to obtain their mechanical properties<sup>23-25</sup>. For most of these computational studies SEM images of the frustules have been employed as initial data and the 3D models have been built based on them. Despite bringing new insights on the correlation between morphological and mechanical properties of the frustule, the simplified models used in these studies pose a limit.

An appealing approach to overcome the limitations of above approaches is to use current 3D imaging methods, i.e. tomography techniques<sup>26-29</sup>, to obtain a realistic 3D model of the frustule. Surprisingly, only one 3D frustule structure of a large diatom *Didymosphenia geminata* (about 90  $\mu\text{m}$  in length) has so far been acquired by nano X-ray computed tomography<sup>30,31</sup>. Subsequently, the obtained model has been used for FEM simulations in correlation with experimental results from in situ microindentation on the frustule to derive its mechanical properties<sup>32</sup>. Owing to the small size of most diatoms (about 60 % of diatoms have a size range of 5-100  $\mu\text{m}$ )<sup>33</sup> nano X-ray computed tomography can only be suited for characterizing few species and nanostructured features

of most diatom frustules may not be identified due to the low spatial resolution (down to 400 nm)<sup>34</sup>. An alternative approach that provides nanometer resolution is Electron Tomography (ET)<sup>35-37</sup> which may serve as versatile technique to obtain realistic 3D morphologies of small diatom frustules with sufficiently high resolution.

In recent years, there has been an increasing interest in ET investigations on different aspects of internal structures of diatom cells. For instance, by using cryo-ET, structure and spatial segregation of photosystem II complexes in thylakoid membranes of diatom *Phaeodactylum tricornutum* as well as photosystems II and I in the thylakoid membrane of diatom *Thalassiosira pseudonana* have been elucidated, respectively<sup>38,39</sup>. Furthermore, cryo-ET has been used to reveal the silicification process of diatom *Chaetoceros tenuissimu*, leading to a new observation regarding this process, where silicification is controlled by the cell machinery outside of the silica deposition vesicles (SDVs)<sup>40</sup>. However, to the best of our knowledge, no previous study has investigated diatom frustules by ET in the context of understanding the intrinsic mechanical properties of biosilica.

In this chapter, we present a general approach to quantify the Young's modulus of hierarchical biosilica on the example of diatom *Craspedostauros sp.* (*C.sp.*) at and below micrometer length scale by a combination of in situ mechanical testing inside SEM with a 3D model obtained from ET alongside FEM simulations. In addition, in situ manipulation of the valves is conducted, repositioning them in the best possible orientation for in situ mechanical deformation testing. The presented methodology enables the quantitative mechanical characterization of complex 3D morphologies for instance as found in hierarchical biocomposites.

## 5.2 Results and discussion

### 5.2.1 Morphology and chemical composition of the frustule of diatom *C.sp.*

*C.sp.* is a raphid pennate marine diatom. It has an imperfect rectangular prism shape, consisting of two valves and a number of girdle bands that connect them. Figure 5.1a shows an intact frustule of *C.sp.* laying on its girdle bands where the valve face can be clearly seen. The valve comprises the most intricate structure of the frustule with various features such as a thick structure in the middle called central nodule, raphe ribs which are elongated throughout the valve, and several porous and nonporous regions. As shown in Figure 5.1c, within the porous region there are several well-organized arrays of pores known as areolae (about 200 nm in diameter in a slight gradient, larger near the central nodule and smaller near the edge) which are connected by transapical ribs. Unlike the valves, the morphology of the girdle bands (not shown) is much simpler and comprises some porous and non-porous regions without a specific arrangement. In order to determine the chemical composition of the frustule, SEM-EDS elemental mapping was performed on the intact frustule which is shown in Figure 5.1a. As can be seen in Figure 5.1d-f a homogenous distribution of silicon, oxygen and carbon are observed throughout the frustule. (Differences in signal intensity can be attributed to differences in local frustule thickness and not concentration variations.) Signals of Si and O are notably more pronounced than C within the frustule specifically in the central

nodule and raphe. (The strong C signal in the middle of the frustule is due to some residue of internal organelles being left behind on account of the mild washing procedure).

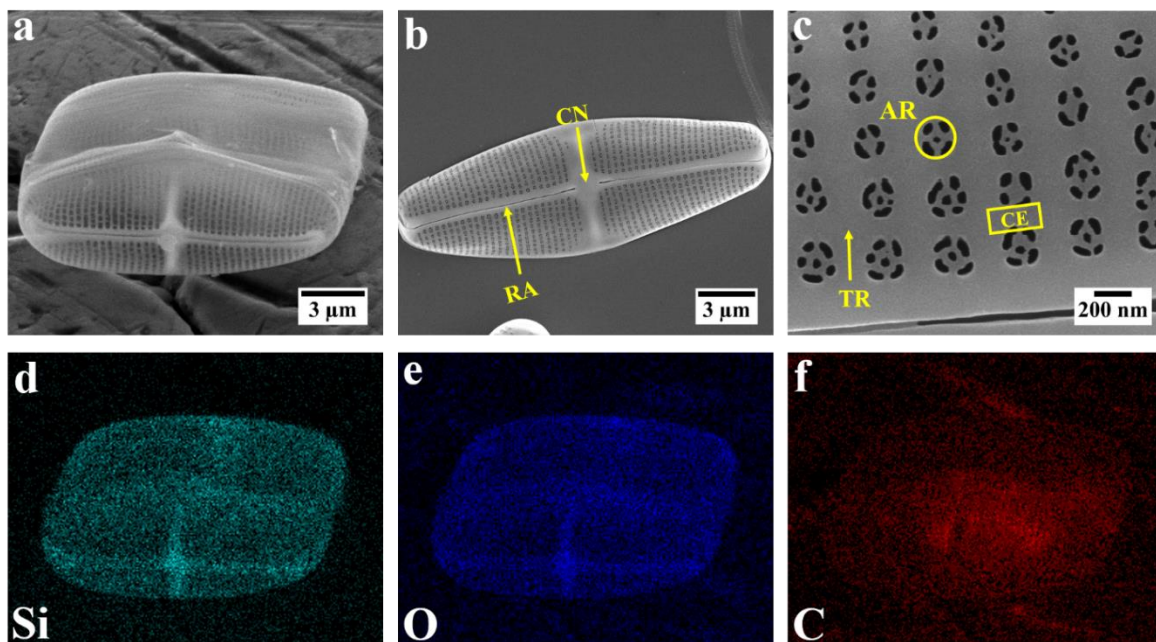


**Figure 5.1.** (a-c) SEM images of frustule of *C.sp.* (a) intact frustule of *C.sp.*; (b) isolated valve deposited on its convex orientation (RA= raphe; CN= central nodule); (c) porous area of the valve (TR= transapical rib; CE= cross extension; AR= areola); (d-f) EDS elemental mapping of the intact frustule; green=silicon, blue= oxygen, red= carbon.

### 5.2.2 Positioning of the frustule for in situ mechanical testing

The first step in the procedure to measure the mechanical properties of the frustule of *C.sp.* was to establish the best possible positioning of the frustule prior to the mechanical testing. There were multiple options: First, conducting in situ mechanical probing on an intact frustule of *C.sp.* either on its valve or on its girdle bands, with different positioning. After deposition of several intact frustules on the SEM sample support, we found that in individual cases the frustule can stand up, on its valve or girdle band, as well as lay down, on its girdle bands (Figure 5.2a-d). However, as expected due to their shape anisotropy, most of the frustules were lying down on their girdle bands. Attempted deformation tests with an indenter tip in the middle of a valve with the frustule standing up led to the movement of the entire frustule rather than deformation owing to the curved structure of the valve (Figure 5.2a). In addition, performing this experiment on the girdle bands regardless of their positioning, led to the penetration of the tip into the frustule (Figure 5.2b,c). Most importantly, the size of the intact frustule makes it challenging if not impossible to perform STEM-ET experiments. Therefore, in a somewhat simplified version, an isolated valve was chosen for such an experiment. Nonetheless, after deposition of separated valves and girdle bands on the sample support, most of the valves were laying down flat on the support (Figure 5.2d,e). In this position, due to the small distance between the curved part of the valve and the substrate, the potential effect of substrate on the acquired force-distance data, in case of touch down, is unknown. In addition, the applied force by the FMT-120 tip in this position is acting relatively locally, rather

than deforming most of the structure of the valve. Thus, the only meaningful position was found where the valve was standing up on one side (Figure 5.2f). In this orientation, the valve could be deformed with minimal effects of the substrate.

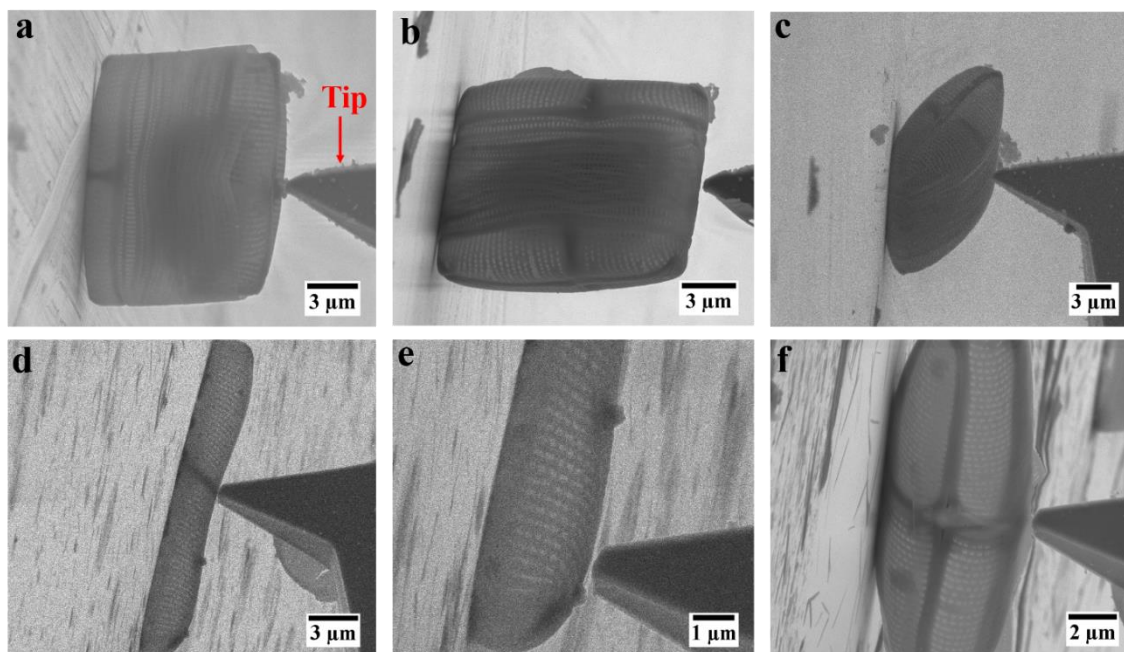


**Figure 5.2.** SEM images of different orientations of intact frustule and isolated valves of *C.sp.* for in situ deformation tests. (a) Intact frustule standing upright; (b) Intact frustule standing on girdle bands; (c) Intact frustule laying on the girdle bands; (d,e) deformation test at different locations of an isolated valve laying flat; (f) deformation test on isolated valve standing on its side.

However, the likelihood of finding this orientation after random liquid mediated deposition was low. Therefore, after deposition of the valve on the substrate, repositioning was needed prior to mechanical testing. To this end, a sharp tungsten tip mounted on the micromanipulator was employed to reposition valves to stand up on their sides. Figure 5.3a-f present a sequence of the mechanical repositioning of an isolated valve requiring lifting, moving, and longitudinally rotating it to stand up on its side. This manipulation was conducted through mechanical manipulation alone without using any adhesive due to the possible alteration to the chemical and mechanical properties of the valves (Appendix Movie A5.1). In recent years this type of in situ manipulation of small objects inside SEM has received attention due to its flexibility to clean the surface of 2D samples and transfer submicron specimens with high positional accuracy<sup>41,42</sup>. Similarly, here, we showed that mechanical manipulation can be used to reposition the specimens in which mechanical testing can certainly be carried out in a meaningful way.



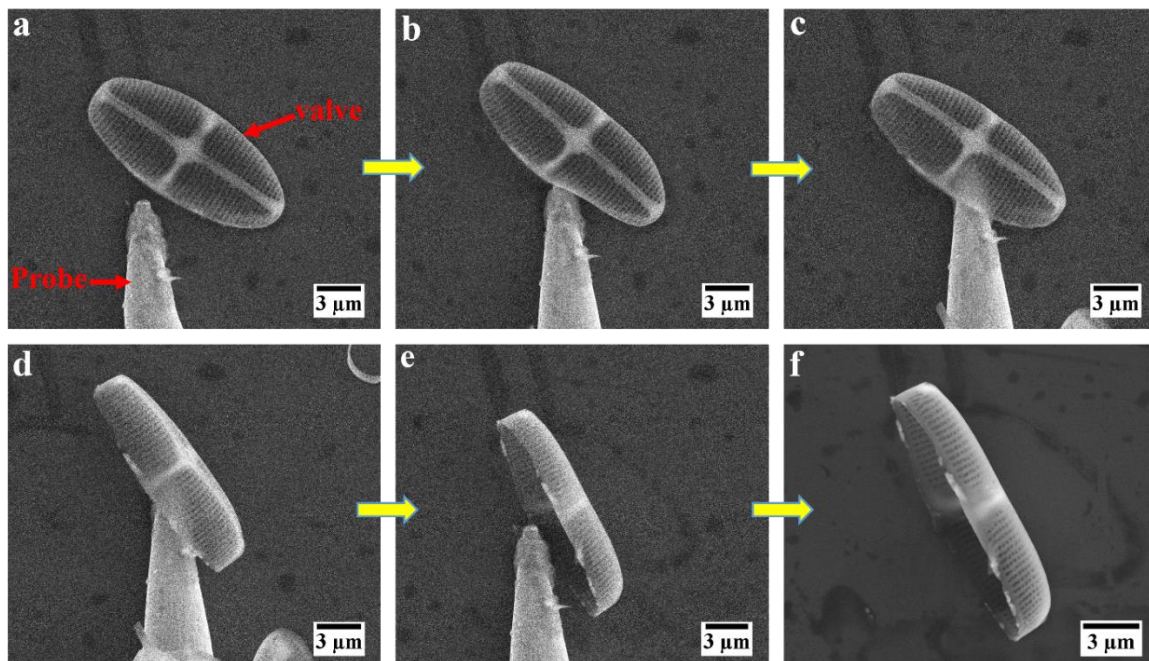


**Figure 5.3.** (a-f) SEM image sequence acquired during repositioning of an isolated valve from its flat orientation to standing on its side.

### 5.2.3 In situ deformation experiment, STEM electron tomography and FEM simulations

To quantify the mechanical properties of the valve, a series of in situ indenter tip deformation tests were carried out with a force measurement sensor FMT-120. The FMT-120 tip was mounted on a micromanipulator for moving it into the valves to obtain force-time data which in correlation with the SEM images acquired constantly throughout the experiment translate into a force-displacement curve. Figure 5.4a shows different stages of a valve during this indenter deformation experiment. As can be seen, the valve exhibited a fully elastic behavior upon deformation and tip retraction without noticeable irreversible deformation (Appendix Movie A5.2). In accordance with previous studies this elastic behavior has already been observed for other diatom species such as *Thalassiosira pseudonana* and *T. punctigera*<sup>16,43</sup>. Figure 5.4b presents the load-displacement curves of such experiments for three different valves of *C.sp.* measured up to a displacement of approximately 1100 nm. After the first cycle of deformation test, the displacement was increased to approximately 2500 nm, leading to fracture of the valve. It can be seen in Figure 5.4c that fracture took place in the middle of the valve under the region where force was applied by the FMT-120 tip. The cracks propagated along the central nodule and extended through the areola and transcostal ribs.

Based on the experimental load-displacement data alone it is not possible to determine the intrinsic mechanical properties such as Young's modulus of the biosilica of the valve because of its complex morphology. Therefore, ET was necessary to obtain a realistic model of the valve for detailed FEM simulations. ET was performed in microprobe STEM mode over an angular range from  $-63^{\circ}$  to

63° at 2° increments (Figure 5.4d). Details of alignment, reconstruction, segmentation and visualization (surface meshing compatible with FEM) are provided in the materials and methods section. In Figure 5.4d, a STEM image, a numerical cross-section through the reconstruction and a 3D surface view of the valve containing all essential features (valve raphe, central nodule, and areole) are shown. For simplicity, the small pores within the areola were not included in the surface mesh (Appendix Movie A5.3). The obtained mesh surface as well as the experimental load-displacement data were utilized in the FEM simulations to determine the Young's modulus of the biosilica constituting the valve. Figure 5.4e shows the undeformed and the deformed model in FEM alongside the comparison between the experimental and simulation load-displacement curves in the low regime of the curves. As shown in Figure 5.4e the experimental results match the numerical data. Based on these findings, a Young's modulus of 2.4 GPa was determined for this biosilica. In accordance with the present results, previous studies have suggested that Young's modulus of diatom biosilica can be varied from 0.347 to 300 GPa<sup>18,44</sup>. Despite the fact that the obtained value here is significantly lower than the reported average Young's modulus of fused silica<sup>45</sup>, it must be noted that the frustule is a biocomposite and therefore exhibits considerable variation in mechanical properties compared to fused silica. These results provide further support for the hypothesis that the mechanical properties of diatom frustules are also species-specific in addition to their morphological features<sup>20</sup>.

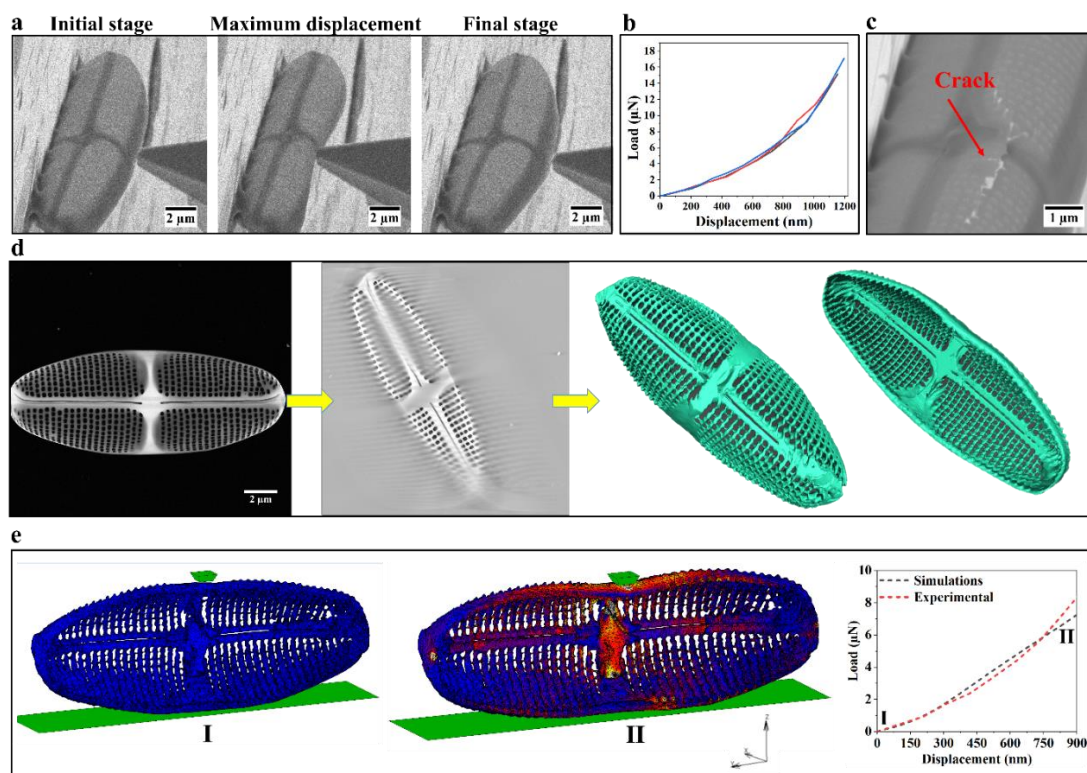


**Figure 5.4.** Overall workflow to quantify Young's modulus of biosilica in the valve. (a) SEM images of an isolated valve at different stages during the in situ deformation test; (b) load-displacement curves for three valves; (c) crack formed by deformation of the valve; (d) from left to right STEM image of the valve, a slice of the reconstructed 3D intensity map of the valve, and 3D surface views of the valve; (e) initial undeformed and final deformed stages of the realistic valve model in FEM simulations and a comparison between experimental and simulated load-displacement curves.

### 5.3 Conclusions

A versatile approach by a combination of in situ deformation, electron tomography, and FEM simulations was developed to determine the mechanical properties of the diatom frustule. The micromechanical performance of the valves of diatom *C.sp.* was studied by in situ deformation tests inside an SEM. STEM-ET was carried out to obtain a realistic 3D model of the complex valve morphology including all essential features. Based on the obtained load-displacement data as well as the 3D surface mesh of the valve, FEM simulation led to determine Young's modulus of this biosilica. The presented workflow can be readily extended to other diatom species, biominerals or even synthetic hierarchical materials.

### 5.4 Materials and Methods

#### 5.4.1 Diatom culture

*Craspedostauros sp.* (UTEX B679) was obtained from the UTEX Culture Collection of Algae. The cells of *C.sp.* were cultivated in artificial seawater supplemented with f/2 medium in a climate cabinet (Flohr, Netherlands) under the following parameters: day/night cycle of 14/10 h, constant temperature of 23°C, and a light intensity of 3000 Lux. In order to assure proper mixing of the growth medium, the cell culture flasks were shaken manually once per day during the entire experiment.

#### 5.4.2 Sample preparation for SEM imaging and mechanical testing

The living cells were collected by centrifugation at 2600 rpm for 5 minutes (Minispin Centrifuge, Eppendorf, Germany). Then, the pellet was suspended in Mill-Q water and washed at least three times together with centrifugation to completely remove the salt and unreacted chemicals. The brownish-yellow pellet at the bottom centrifuge tube was dispersed in Ethanol. After at least 10 times washing with ethanol an off-white pellet was obtained which was suspended in anhydrous ethanol. The resultant suspension was dried by a critical point dryer (Leica CPD 300 instrument) to obtain intact diatom frustules. This mild extraction process is intended to avoid any chemical or physical changes to the biosilica frustules (air drying of entire frustule often led their structural collapse). In order to separate the valves from the girdle bands, the suspension was centrifuged at a speed of 14000 rpm and then sonicated by using a bath sonicator at room temperature (Bransonic ultrasonic cleaner, model 1510E-DTH, 42 kHz, USA)) for about 5 minutes.

#### 5.4.3 Scanning Electron Microscopy and Energy Dispersive X-ray Spectroscopy

For SEM imaging and EDS elemental mapping of the intact frustule of *C.sp.*, a tiny amount of the critical point dried white pellet was deposited on a standard aluminium SEM stub. These experiments were conducted using a SEM Quanta 3D FEG instrument Equipped with EDAX EDS detector (Thermo Fisher Scientific, USA), at an acceleration voltage of 10 kV.



#### 5.4.4 Mechanical manipulation and in situ deformation tests

To investigate the mechanical properties of isolated valves, 50  $\mu\text{l}$  of the obtained suspension of the bath sonicated pellet (which separates valves from girdle bands and avoids structural collapse upon drying) was dropped on a silicon wafer attached to the SEM stub followed by drying in air. A micromanipulator (MM3A-EM, Kleindiek Nanotechnik GmbH, Germany) was used to reposition the valves (if necessary). The micromanipulator is also known for having high positional accuracy of about 10 nm for the mechanical movement in three axes inside the SEM chamber<sup>46</sup>. For manipulation of the valves, a tungsten probe was used with approximately 150 nm in radius mounted on the micromanipulator. Also, in situ deformation tests were conducted inside the SEM chamber using a highly sensitive (10 nN resolution) AFM-based force measurement sensor referred to FMT-120 tip (Kleindiek Nanotechnik GmbH, Germany) which was mounted on the micromanipulator. Throughout the deformation testing, force-time data are provided by the force measurement system (FMS) which in correlation with SEM images can be transformed into force-displacement data<sup>47</sup>.

#### 5.4.5 Scanning Transmission Electron Microscopy (STEM) tomography and segmentation

STEM imaging was carried out on the cryoTITAN (Thermo Fisher Scientific, previously FEI), equipped with a field emission gun (FEG) and a high angle annular dark field (HAADF) STEM detector (Fishione, USA). The microscope was operated at 300 kV acceleration voltage at an extraction voltage of 4500 V in microprobe STEM mode at a nominal magnification of 6.600 $\times$  with frame time of 40 s, dwell time of 2  $\mu\text{s}$ , and camera length of 1.150 m. The tomographic tilt-series was acquired over an angular range from -63 to 63 degrees, at 2 degree increments. The raw data was aligned and reconstructed using IMOD<sup>48</sup>. Alignment was performed through manual tracking of fiducial gold markers throughout the entire tilt-series, followed by model fitting and minimization of the residuals. Subsequently, by using the Simultaneous Iterative Reconstructive Technique (SIRT) with 20 iterations the tomogram was reconstructed. To segment and visualize the reconstruction Avizo software (Avizo Fire 9.2, Thermo Fisher Scientific) was employed resulting in a surface mesh. It should be noted that for simplicity, small pores within the areola are not included in the segmentation.

#### 5.4.6 FEM simulations

Finite element method (FEM) simulations were conducted using the commercial software package MSC.Marc in order to determine the intrinsic material properties of the biosilica of *C.sp.*, i.e. its Young's modulus. The mesh of the valve was generated based on the surface mesh that was experimentally obtained by tomography and consists out of approximately 450,000 second order tetrahedral elements. The electron material properties were assumed to be linearly elastic. The indenter was modeled as an impenetrable surface with an infinite stiffness. The valve was fixed in all three directions at one single bottom node in order to prevent rigid body modes and was at this same node supported by an impenetrable surface which acts as the sample support. To prevent rotations of the diatom in the x-y-plane and y-z-plane two nodes, each located at the outer apexes of the valve, were constrained with respect to each other and to prevent rotations in the x-z-plane

one single node just below the indenter is constrained. Finally, a load case was specified which describes the z-displacement of the indenter identical to the compression experiment as performed inside the SEM.

## 5.5 References

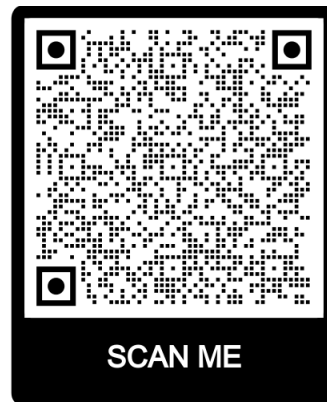
- 1 Arakaki, A., Shimizu, K., Oda, M., Sakamoto, T., Nishimura, T. & Kato, T. Biomimetalization-inspired synthesis of functional organic/inorganic hybrid materials: organic molecular control of self-organization of hybrids. *Organic & Biomolecular Chemistry* **13**, 974-989 (2015).
- 2 Luz, G. M. & Mano, J. F. Mineralized structures in nature: examples and inspirations for the design of new composite materials and biomaterials. *Composites Science and Technology* **70**, 1777-1788 (2010).
- 3 Libonati, F. & Buehler, M. J. Advanced structural materials by bioinspiration. *Advanced Engineering Materials* **19**, 1600787 (2017).
- 4 Espinosa, H. D., Rim, J. E., Barthelat, F. & Buehler, M. J. Merger of structure and material in nacre and bone—Perspectives on de novo biomimetic materials. *Progress in Materials Science* **54**, 1059-1100 (2009).
- 5 Thula, T. T., Rodriguez, D. E., Lee, M. H., Pendi, L., Podschun, J. & Gower, L. B. In vitro mineralization of dense collagen substrates: a biomimetic approach toward the development of bone-graft materials. *Acta Biomaterialia* **7**, 3158-3169 (2011).
- 6 Ji, B. & Gao, H. Mechanical properties of nanostructure of biological materials. *Journal of the Mechanics and Physics of Solids* **52**, 1963-1990 (2004).
- 7 Ji, B. & Gao, H. Mechanical principles of biological nanocomposites. *Annual Review of Materials Research* **40**, 77-100 (2010).
- 8 Grossman, M., Pivovarov, D., Bouville, F., Dransfeld, C., Masania, K. & Studart, A. R. Hierarchical toughening of nacre-like composites. *Advanced Functional Materials* **29**, 1806800 (2019).
- 9 Rim, J. E., Zavattieri, P., Juster, A. & Espinosa, H. D. Dimensional analysis and parametric studies for designing artificial nacre. *Journal of the Mechanical Behavior of Biomedical Materials* **4**, 190-211 (2011).
- 10 Soleimani, M., Rutten, L., Maddala, S. P., Wu, H., Eren, E. D., Mezari, B., Schreur-Piet, I., Friedrich, H. & van Benthem, R. A. Modifying the thickness, pore size, and composition of diatom frustule in *Pinnularia* sp. with Al<sup>3+</sup> ions. *Scientific Reports* **10**, 19498 (2020).
- 11 Hildebrand, M. Diatoms, biomineralization processes, and genomics. *Chemical Reviews* **108**, 4855-4874 (2008).
- 12 Wang, Y., Cai, J., Jiang, Y., Jiang, X. & Zhang, D. Preparation of biosilica structures from frustules of diatoms and their applications: current state and perspectives. *Applied Microbiology and Biotechnology* **97**, 453-460 (2013).
- 13 De Stefano, L., Lamberti, A., Rotiroli, L. & De Stefano, M. Interfacing the nanostructured biosilica microshells of the marine diatom *Coscinodiscus wailesii* with biological matter. *Acta Biomaterialia* **4**, 126-130 (2008).
- 14 Kröger, N. & Poulsen, N. Diatoms—from cell wall biogenesis to nanotechnology. *Annual Review of Genetics* **42**, 83-107 (2008).
- 15 Abdelhamid, M. A. & Pack, S. P. Biomimetic and bioinspired silicifications: Recent advances for biomaterial design and applications. *Acta Biomaterialia* **120**, 38-56 (2021).
- 16 Hamm, C. E., Merkel, R., Springer, O., Jurkojc, P., Maier, C., Prechtel, K. & Smetacek, V. Architecture and material properties of diatom shells provide effective mechanical protection. *Nature* **421**, 841-843 (2003).
- 17 Pančić, M., Torres, R. R., Almeda, R. & Kiørboe, T. Silicified cell walls as a defensive trait in diatoms. *Proceedings of the Royal Society B* **286**, 20190184 (2019).

- 18 Losic, D., Short, K., Mitchell, J. G., Lal, R. & Voelcker, N. H. AFM nanoindentations of diatom biosilica surfaces. *Langmuir* **23**, 5014-5021 (2007).
- 19 Almqvist, N., Delamo, Y., Smith, B., Thomson, N., Bartholdson, Å., Lal, R., Brzezinski, M. & Hansma, P. Micromechanical and structural properties of a pennate diatom investigated by atomic force microscopy. *Journal of Microscopy* **202**, 518-532 (2001).
- 20 Moreno, M. D., Ma, K., Schoenung, J. & Dávila, L. P. An integrated approach for probing the structure and mechanical properties of diatoms: Toward engineered nanotemplates. *Acta biomaterialia* **25**, 313-324 (2015).
- 21 Aitken, Z. H., Luo, S., Reynolds, S. N., Thaulow, C. & Greer, J. R. Microstructure provides insights into evolutionary design and resilience of *Coscinodiscus* sp. frustule. *Proceedings of the National Academy of Sciences* **113**, 2017-2022 (2016).
- 22 Görlich, S., Pawolski, D., Zlotnikov, I. & Kröger, N. Control of biosilica morphology and mechanical performance by the conserved diatom gene Silicanin-1. *Communications Biology* **2**, 1-8 (2019).
- 23 Lu, J., Sun, C. & Wang, Q. J. Mechanical simulation of a diatom frustule structure. *Journal of Bionic Engineering* **12**, 98-108 (2015).
- 24 Gutiérrez, A., Gordon, R. & Dávila, L. P. Deformation modes and structural response of diatom frustules. *J. Mater. Sci. Eng. Adv. Technol* **15**, 105-134 (2017).
- 25 Gutiérrez, A., Guney, M. G., Fedder, G. K. & Dávila, L. P. The role of hierarchical design and morphology in the mechanical response of diatom-inspired structures via simulation. *Biomaterials Science* **6**, 146-153 (2018).
- 26 Möbus, G. & Inkson, B. J. Nanoscale tomography in materials science. *Materials Today* **10**, 18-25 (2007).
- 27 Lu, X., Bertei, A., Finegan, D. P., Tan, C., Daemi, S. R., Weaving, J. S., O'Regan, K. B., Heenan, T. M., Hinds, G. & Kendrick, E. 3D microstructure design of lithium-ion battery electrodes assisted by X-ray nano-computed tomography and modelling. *Nature Communications* **11**, 2079 (2020).
- 28 Saghi, Z. & Midgley, P. A. Electron tomography in the (S) TEM: from nanoscale morphological analysis to 3D atomic imaging. *Annual Review of Materials Research* **42**, 59-79 (2012).
- 29 Fijneman, A. J., Goudzwaard, M., Keizer, A. D., Bomans, P. H., Gebäck, T., Palmlöf, M., Persson, M., Höglblom, J., de With, G. & Friedrich, H. Local quantification of mesoporous silica microspheres using multiscale electron tomography and lattice Boltzmann simulations. *Microporous and Mesoporous Materials* **302**, 110243 (2020).
- 30 Zglobicka, I., Li, Q., Gluch, J., Płocińska, M., Noga, T., Dobosz, R., Szoszkiewicz, R., Witkowski, A., Zschech, E. & Kurzydłowski, K. J. Visualization of the internal structure of *Didymosphenia geminata* frustules using nano X-ray tomography. *Scientific Reports* **7**, 1-7 (2017).
- 31 Zglobicka, I., Chmielewska, A., Topal, E., Kutukova, K., Gluch, J., Krüger, P., Kilroy, C., Swieszkowski, W., Kurzydłowski, K. J. & Zschech, E. 3D diatom-designed and selective laser melting (SLM) manufactured metallic structures. *Scientific Reports* **9**, 1-9 (2019).
- 32 Topal, E., Rajendran, H., Zglobicka, I., Gluch, J., Liao, Z., Clausner, A., Kurzydłowski, K. J. & Zschech, E. Numerical and experimental study of the mechanical response of diatom frustules. *Nanomaterials* **10**, 959 (2020).
- 33 Zhang, D., Wang, Y., Cai, J., Pan, J., Jiang, X. & Jiang, Y. Bio-manufacturing technology based on diatom micro-and nanostructure. *Chinese Science Bulletin* **57**, 3836-3849 (2012).
- 34 Kampschulte, M., Langheinrich, A. C., Sender, J., Litzlbauer, H. D., Althöhn, U., Schwab, J. D., Alejandro-Lafont, E., Martels, G. & Krombach, G. A. Nano-Computed Tomography: Technique and Applications. *roefo* **188**, 146-154, doi:10.1055/s-0041-106541 (2016).
- 35 Friedrich, H., De Jongh, P. E., Verkleij, A. J. & De Jong, K. P. Electron tomography for heterogeneous catalysts and related nanostructured materials. *Chemical reviews* **109**, 1613-1629 (2009).
- 36 Neumüller, J. Electron tomography—a tool for ultrastructural 3D visualization in cell biology and histology. *Wiener Medizinische Wochenschrift* **168**, 322-329 (2018).

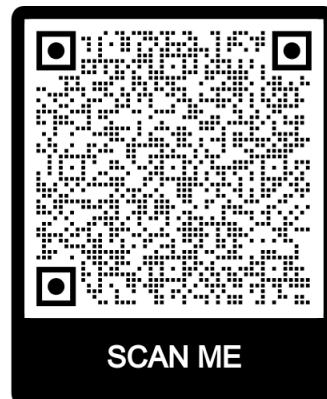
- 37 Evans, J. E. & Friedrich, H. Advanced tomography techniques for inorganic, organic, and biological materials. *MRS Bulletin* **41**, 516-521 (2016).
- 38 Levitan, O., Chen, M., Kuang, X., Cheong, K. Y., Jiang, J., Banal, M., Nambiar, N., Gorbunov, M. Y., Ludtke, S. J. & Falkowski, P. G. Structural and functional analyses of photosystem II in the marine diatom *Phaeodactylum tricornutum*. *Proceedings of the National Academy of Sciences* **116**, 17316-17322 (2019).
- 39 Arshad, R., Calvaruso, C., Boekema, E. J., Büchel, C. & Kouřil, R. Revealing the architecture of the photosynthetic apparatus in the diatom *Thalassiosira pseudonana*. *Plant physiology* **186**, 2124-2136 (2021).
- 40 Mayzel, B., Aram, L., Varsano, N., Wolf, S. G. & Gal, A. Structural evidence for extracellular silica formation by diatoms. *Nature Communications* **12**, 4639 (2021).
- 41 Schweizer, P., Dolle, C., Dasler, D., Abellán, G., Hauke, F., Hirsch, A. & Spiecker, E. Mechanical cleaning of graphene using in situ electron microscopy. *Nature communications* **11**, 16024 (2020).
- 42 Shi, C., Luu, D. K., Yang, Q., Liu, J., Chen, J., Ru, C., Xie, S., Luo, J., Ge, J. & Sun, Y. Recent advances in nanorobotic manipulation inside scanning electron microscopes. *Microsystems & Nanoengineering* **2**, 1-16 (2016).
- 43 Soleimani, M., van Breemen, L. C., Maddala, S. P., Joosten, R. R., Wu, H., Schreur-Piet, I., van Benthem, R. A. & Friedrich, H. In Situ Manipulation and Micromechanical Characterization of Diatom Frustule Constituents Using Focused Ion Beam Scanning Electron Microscopy. *Small Methods* **5**, 2100638 (2021).
- 44 Subhash, G., Yao, S., Bellinger, B. & Gretz, M. Investigation of mechanical properties of diatom frustules using nanoindentation. *Journal of Nanoscience and Nanotechnology* **5**, 50-56 (2005).
- 45 Dahmani, F., Lambropoulos, J., Schmid, A., Burns, S. & Pratt, C. Nanoindentation technique for measuring residual stress field around a laser-induced crack in fused silica. *Journal of Materials Science* **33**, 4677-4685 (1998).
- 46 Komissarenko, F., Zograf, G., Makarov, S., Petrov, M. & Mukhin, I. Manipulation Technique for Precise Transfer of Single Perovskite Nanoparticles. *Nanomaterials* **10**, 1306 (2020).
- 47 Wang, C., Peng, Q., Wu, J., He, X., Tong, L., Luo, Q., Li, J., Moody, S., Liu, H. & Wang, R. Mechanical characteristics of individual multi-layer graphene-oxide sheets under direct tensile loading. *Carbon* **80**, 279-289 (2014).
- 48 Kremer, J. R., Mastronarde, D. N. & McIntosh, J. R. Computer visualization of three-dimensional image data using IMOD. *Journal of Structural Biology* **116**, 71-76 (1996).

## 5.6 Appendix Movies

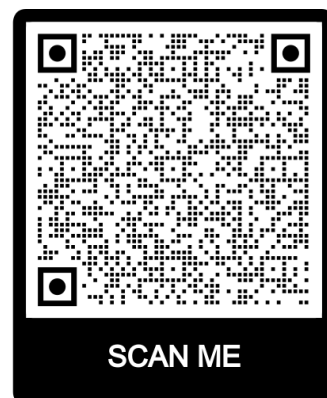
**Movie A5.1:** In situ mechanical manipulation of an isolated valve of *C.sp.*



**Movie A5.2:** In situ deformation test on an isolated valve of *C.sp.*



**Movie A5.3:** ET and 3D model of a valve of *C.sp.*



# Chapter 6

## **In situ Fabrication, Manipulation, and Mechanical Characterization of Free-Standing Silica Thin Films Using Focused Ion Beam Scanning Electron Microscopy**

### **Abstract**

Determination of mechanical properties of (silica) thin films is important for the development of new applications. However, a versatile approach for small-scale sample fabrication and in situ mechanical testing of these materials is currently lacking which can overcome the existing difficulties in conventional testing approaches. Here we show that by combining Focused Ion Beam Scanning Electron Microscopy (FIB-SEM) with micromanipulators free-standing silica beams of the desired dimensions can be fabricated. Using in situ bending tests on such beams inside the SEM and Finite Element Method simulations, the Young's modulus of thin-film silica and the effects of Ga ion beam radiation on Young's Modulus are determined. Furthermore, the effects of controlled relative humidity on the mechanical behavior of silica beams is investigated. The demonstrated FIB-SEM approach can be extended to other materials and preparation conditions to measure, model, and optimize mechanical properties of thin films for a wide range of (coating) applications.

### **The results presented in this chapter are based on:**

Soleimani M, Maddala SP, Wismans M, Liao WC, van Breemen LC, van Benthem RA, Friedrich H. *In Situ Fabrication, Manipulation, and Mechanical Characterization of Free-Standing Silica Thin Films Using Focused Ion Beam Scanning Electron Microscopy*. Advanced Materials Interfaces. 2102201 (2022).

## 6.1 Introduction

The use of silica-based materials, such as porous micro and nanoparticles, thin films, nanotubes and nanowires is ubiquitous throughout many application fields, including catalysis, biomedical, sensing, or chromatography<sup>1-6</sup>. Among them, silica thin films have received great attention for sensing and antireflective coatings applications<sup>6-9</sup>. The design and fabrication of such materials specifically for those applications requires accurate characterization of properties at all relevant length scales. For instance, it is well-established that the mechanical properties of materials such as thin films at micro and nanoscale are different from their bulk counterparts<sup>10-13</sup>. However, experimental determination of the mechanical properties of micro and nanoscale thin films, including silica, remains an extremely challenging task<sup>10,14</sup>. Amongst available approaches, nanoindentation is most commonly used for measuring small scale silica thin films<sup>15-17</sup>. It requires simple specimen preparation and is comparatively easy to perform while the Young's modulus and hardness of the thin film materials are measurable<sup>18,19</sup>. Nevertheless, several limitations still exist related to the effect of the substrate, particularly relevant for films thinner than a micrometer, such as an indentation maximum of only about 10 % of the depth, as well as the lack of in situ observation during deformation, which all restrict general applicability of conventional nanoindentation<sup>20-22</sup>. Taken together, above limitations point to the need for a more versatile approach that eliminates substrate effects, i.e. by realizing free-standing silica films/beams in the appropriate respective length scales. Subsequently, performing mechanical testing via indentation in real-time with high resolution force and displacement information becoming available would enable the monitoring of the specimen deformation behavior and concurrent phenomena in great detail.

Currently available top down procedures for fabricating micro and nano-objects with well-defined patterns and structure<sup>23,24</sup>, may be employed to obtain free standing silica films and beams<sup>25</sup>. In addition, recent progress in in situ electron microscopy (EM)<sup>26-28</sup>, has enabled real time monitoring of deformation behavior and characterization of the fundamental mechanical properties of the silica specimen<sup>29,30</sup>. Lastly, robotics manipulation can be applied for handling and manipulation of micro and nanoscale objects with high positional accuracy<sup>31,32</sup>. This technique can be employed to transfer and manipulate the thin film specimen into a mechanical testing device<sup>33</sup>. Nevertheless, the aforementioned techniques cannot easily be integrated into one single versatile workflow to perform in situ sample fabrication, handling/transfer, and characterization of silica beams. Several processing steps are involved in the top down nanofabrication stages which usually require strong chemical etchants and multiple masks, and thus limit their integration<sup>34</sup>.

To overcome these limitations, Scanning Electron Microscopy (SEM) can be combined with Focused Ion Beam (FIB) micromachining and nano/micromanipulation, addressing all abovementioned experimental requirements for fabrication, transfer, and characterization of small scale samples in real time.<sup>35</sup> More specifically, FIB micromachining with its milling capabilities and high spatial resolution of a few nanometers can accurately fabricate specimens,<sup>36</sup> while micromanipulators are involved in handling, picking up, and assembly of submicron objects.<sup>37,38</sup> With the help of gas precursor decomposition and deposition using an electron or ion beam, the specimen can



also be fixed to the substrate of interest inside the FIB-SEM.<sup>39</sup> Furthermore, the mechanical properties of a wide range of materials have been measured by various in situ testing geometries, such as deformation,<sup>30</sup> uniaxial buckling,<sup>40</sup> tensile,<sup>41</sup> indentation,<sup>42</sup> and compression tests<sup>43</sup> all within SEM. An example of in situ manipulation and fabrication of specimens and conducting mechanical testing within FIB-SEM has been shown on micropillars and isolated nanowires.<sup>44</sup> Specifically, nanoporous gold micropillars have been fabricated by FIB micromachining while by a combination of micromanipulator and electron-beam induced Pt-organic deposition the nanowires have been isolated, transferred, and glued to a testing device. Finally, in situ tensile and microcompression tests were conducted to measure the mechanical properties of nanowires and micropillars, respectively. However, to the best of our knowledge, there has been no detailed investigation on the combination of in situ fabrication, manipulation, and mechanical testing of thin-film materials exclusively inside FIB-SEM.

To date, for thin films, free-standing samples with desired size and geometry have been fabricated by FIB milling. Subsequently, the specimen has been transferred by micromanipulators with the help of adhesive materials to a mechanical testing device inside the TEM holder. Finally, in situ tensile tests on electron transparent dog-bone shaped specimens have been conducted inside TEM.<sup>45</sup> In general, alongside several advantages of in situ mechanical testing via TEM such as being able to monitor the mechanical processes of various materials close to atomic resolution,<sup>46-48</sup> determining the effects of grain boundaries,<sup>49</sup> crystal structure<sup>50</sup> and orientation<sup>51</sup> on the mechanical characteristics of different specimens, this approach is restricted due to requiring an electron transparent thin film specimen, the need to transfer the sample into the testing device,<sup>33</sup> and suffers from a noticeable effect of high energy electron irradiation on the mechanical properties of the specimens, particularly observed for silica-based structures.<sup>52,53</sup> Therefore, a streamlined and versatile approach to fabricate, manipulate, and test the mechanical properties of thin film specimens *in situ* in a single instrument (inside FIB-SEM) can be appealing to address the above limitations.

In this chapter, we demonstrate such a workflow exploiting FIB-SEM with micromanipulators to fabricate, manipulate, and characterize the mechanical properties of free-standing silica thin films in situ. Mechanical delamination combined with FIB micromachining and micromanipulation is employed to fabricate (sub)micron sized silica beams from homogenous thin film inside an SEM. Manipulation of objects is performed by a sharp tungsten probe without the need for adhesives. In situ bending tests on double clamped silica beams of different width in combination with Finite Element Method simulations enabled us to quantify the Young's modulus of silica thin films and the effects of Ga ion beam irradiation. This streamlined in situ workflow reduces the number of necessary fabrication, transfer, and characterization steps and enables mechanical testing of a wide range of nano/micro thin film samples inside FIB-SEM. Moreover, due to low acceleration voltage (<10 kV) in this approach, electron beam damage effects on the mechanical properties of silica structures are known to be insignificant.<sup>54</sup>

## 6.2 Results and discussion

A schematic illustration of the entire sample fabrication, manipulation, and bending test workflow inside a FIB-SEM is shown in Figure 6.1. For our silica thin films, the process starts by spin coating of pre-oligomerized silica precursor (TEOS) on the surface of a silicon wafer resulting in a thin film of desired thickness (Step1). Subsequently, the thin film is delaminated from the substrate using a carbon tape. The carbon tape is subsequently placed on another silicon wafer comprising several trenches engraved by prior FIB milling (Step 2). The carbon tape is removed by thermal treatment (at 450 °C), upon which the remaining silica film either completely covers the pre-milled trenches or could be detached from the substrate and could be transferred to the trenches by a tungsten probe mounted on a micromanipulator (Step 3). These silica thin films were cut to size via FIB milling to produce silica beams with different lateral dimensions, followed by removal of the neighboring cut-out fragments using a tungsten probe. The fabricated silica beams were “clamped” on both ends by electron beam induced Pt deposition, to avoid movement during the mechanical testing (Step 4). Finally, in situ bending tests were conducted on the beams using the tip of a force measurement unit (FMT-120) attached to a micromanipulator in combination with SEM image analysis to acquire force-distance curves (Step 5).

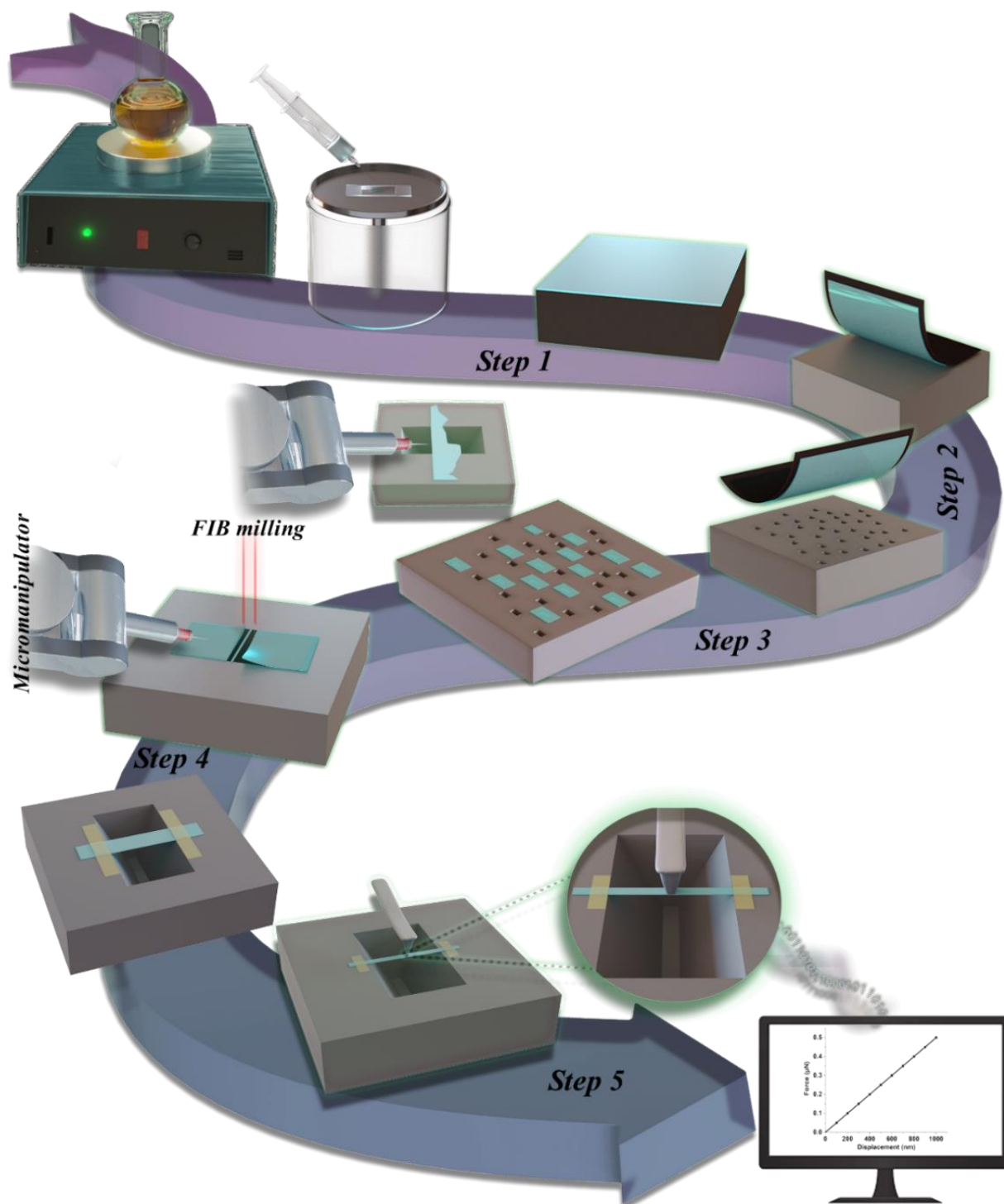


**Figure 6.1.** Schematic illustration of the in situ fabrication, manipulation, and mechanical testing workflow of free standing silica beams. (Step 1) Flat thin film formation by spin coating of the precursor solution on a silicon wafer; (Step 2) delamination of silica thin film from spin coating substrate and covering the as pre-patterned trenches by carbon tape with attached silica thin film; (Step 3) carbon tape removal and mechanical manipulation of the film fragments; (Step 4) combination of FIB milling and manipulation of the film fragments followed by Pt deposition to “clamp” both sides of the beam; (Step 5) in situ bending tests by FMT-120 tip in combination with SEM image analysis allowing to obtain a force-distance curve.

In the following sections, detailed descriptions of each step of this workflow will be provided, including an investigation of the chemical properties and composition of the silica thin films.

### 6.2.1 Thin film formation and delamination to obtain free standing silica films

The first step in this workflow involves preparation of silica thin films of uniform thickness. To this end, an adequate amount of the silica stock solution was deposited on a silicon wafer and then spin coated to form thin film at the desired film thickness (Appendix Figure A6.1, and Experimental section for details). We observed that films having a thicknesses of less than 300 nm were largely crack free. Mechanical properties of silica beams were measured on film fragments with uniform thickness. To assess the film only, thus avoiding effects of the substrate, the as-prepared silica thin films were delaminated from the substrate using adhesive carbon tape. Due to the reasonable weak van der Waals interactions between the silica film and the substrate this step can also be performed by the Scotch tape method (resembling the mechanical exfoliation of 2D materials)<sup>55</sup>. Then, the tape containing fragments of silica film (approximately half of the entire film) was deposited on a silicon wafer, which had already been pre-patterned with arrays of grooves/trenches by FIB milling. (The width and length of the trenches were between 10 to 20  $\mu\text{m}$  to enable mechanical testing with an FMT-120 tip). Subsequently, the tape was removed by calcination at 450  $^{\circ}\text{C}$ . At this temperature carbon tape can be removed completely without reaching the glass-transition temperature of silica<sup>56</sup>. Figure 6.2a shows SEM images of FIB trenches which have been fully covered by the silica film after tape removal (the dark areas of the trenches underneath of the silica films are likely due to a locally lower secondary electron yield). Moreover, randomly distributed silica film fragments were observed all over the silicon wafer which could easily be manipulated (Figure 6.2b). As shown in Figure 6.2c, a fragment of silica film is easily transferred and mounted on top of a trench using a sharp tungsten probe mounted on a micromanipulator. The micromanipulator could also be conveniently used to clean the surfaces of interest of any debris/ashes resulting from the previous handlings (Appendix Figure A6.2 & Movie A6.1).

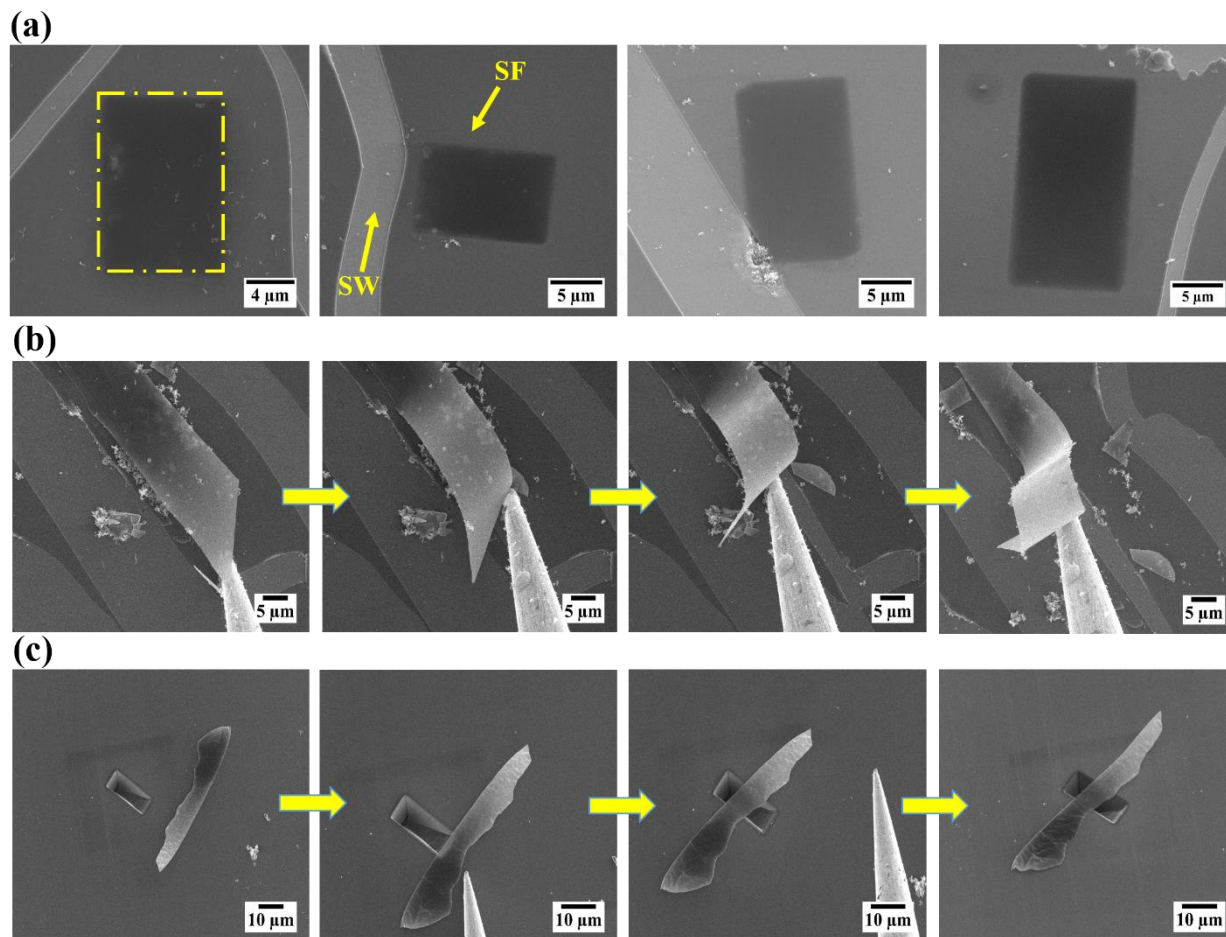


**Figure 6.2.** (a) SEM images of FIB trenches in a silicon wafer (SW) which have been fully covered by the silica film (SF); (b) SEM images of mechanical manipulation of a silica film fragment by a tungsten probe; (c) sequence of SEM images of mechanically moving a silica film fragment over a FIB trench.

### 6.2.2 Chemical analysis of silica thin films

To identify the chemical properties and composition of the silica thin films, SEM-EDS elemental mapping was conducted after delamination and IR analysis after removal of the carbon tape by thermal treatment. As shown in Figure 6.3a, the EDS elemental map demonstrated a homogeneous distribution of Si alongside O in silica thin films without any organic/inorganic impurities being detectable. The IR spectrum exhibits several well resolved peaks in the range of 800-1300  $\text{cm}^{-1}$  (Figure 6.3b). The peaks at 802 and 1064  $\text{cm}^{-1}$  are assigned to the symmetric and asymmetric stretching vibrations of the Si–O–Si bonds, respectively, while the band at 952  $\text{cm}^{-1}$  is attributed to the stretching vibration of the free silanol (Si–OH) bond<sup>57,58</sup>. Furthermore, quantitative  $^{29}\text{Si}$  solid state magic angle spinning ( $^{29}\text{Si}$ -MAS) NMR was performed on finely ground silica powders obtained by calcination of silica thin film precursor at 450 °C. As shown in Figure 6.3c,  $^{29}\text{Si}$  NMR spectrum showed  $Q^4$ ,  $Q^3$  and  $Q^2$  peaks at -109, -101 and -91 ppm, respectively<sup>59</sup>. The spectrum was fitted based on Gaussian distribution function to obtain the relative peak positions and relative areas<sup>60</sup>. 71 % of the silica was composed of fully condensed  $Q^4$  species and the overall  $Q^4/Q^3$  ratio

was 2.75, indicating a typically high-condensation degree of the silica, as expected after the high-temperature treatment to remove the carbon tape.

(a)

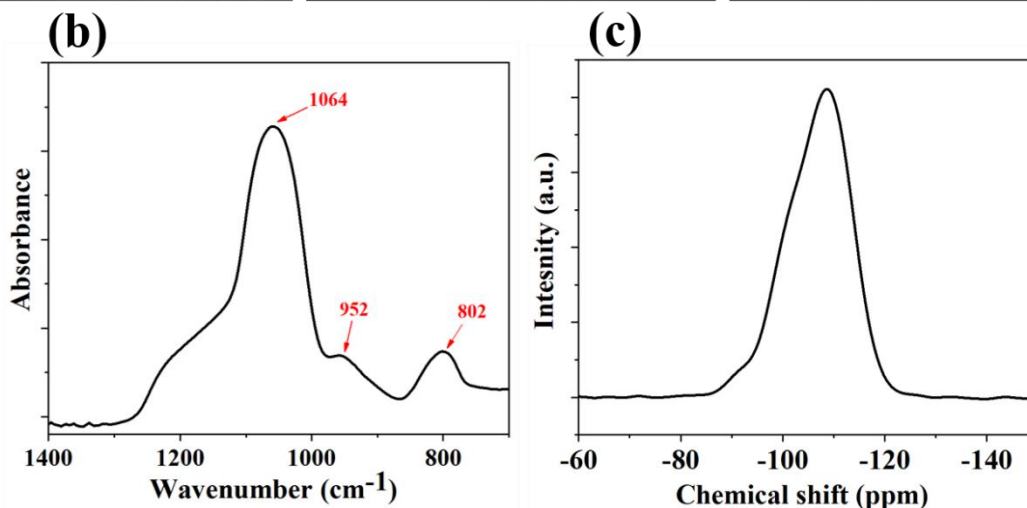
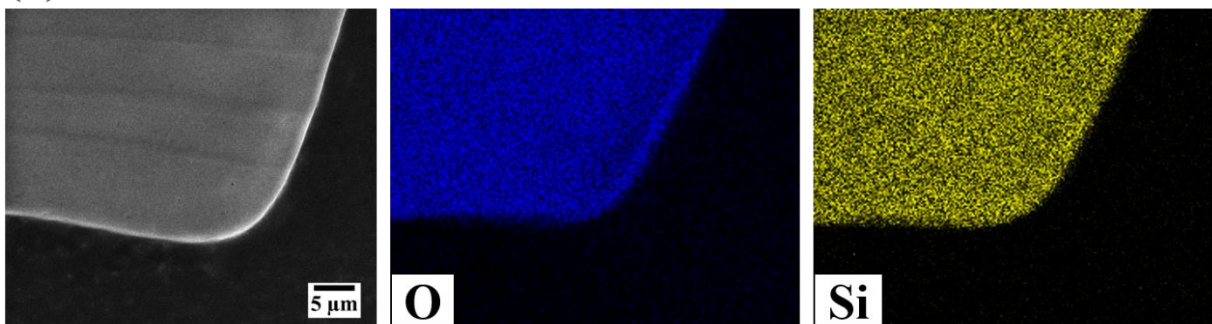


**Figure 6.3.** (a) SEM-EDS elemental maps of a fragment of silica film attached to the carbon tape with oxygen map (blue) and silicon map (yellow); (b) IR spectrum of the silica film; (c) Quantitative  $^{29}\text{Si}$ -MAS NMR spectrum of the silica film precursor after thermal treatment at 450 °C.

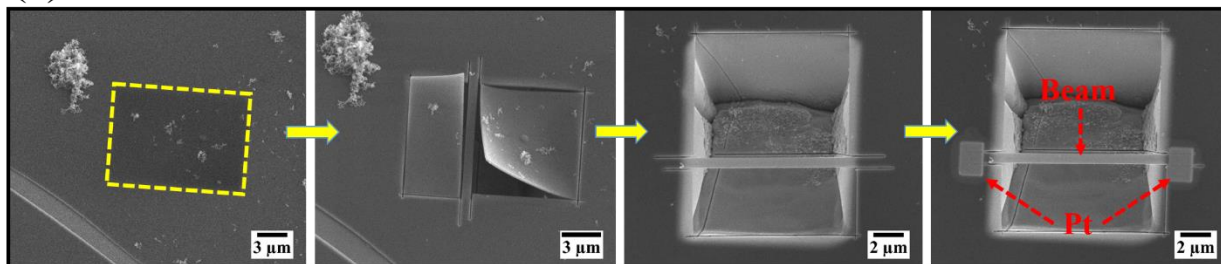
### 6.2.3 Thin beam fabrication and manipulation

After placing the silica film over the FIB trenches, either by direct deposition of delaminated films or mechanical transfer of a film fragment by the tungsten probe, FIB milling was performed to fabricate silica beams with desired dimensions. To this end, two adjacent rectangular cuts were made leaving the intended beam in the middle, spanning the trench. Figure 6.4a presents a sequence of SEM images of the entire beam fabrication process starting from a trench covered by the silica film and ending with a double “clamped” silica beam. To minimize the effect of the Ga ions, the silica beams were cut by the lowest possible ion beam current (1.5 pA) resulting in extremely narrow cut lines (20–40 nm) on each side of the beam. After FIB milling the silica beams were still surrounded on both sides by rectangular cut-off fragments of the films which could be easily removed via mechanical manipulation<sup>61</sup> (Figure 6.4b, see also Appendix Movie A6.2). As shown in the SEM images (Figure 6.4b), this mechanical manipulation led to obtaining a free-standing silica thin beam spanning the middle of the trench. Finally, both sides of the beam were “clamped” by electron beam induced Pt deposition. This “clamping” was done as close as possible



to the trench edges in order to precisely fix the suspended length of the silica beams and exclude effects of movement or sliding between the beam and the substrate. A major advantage of combining FIB line cutting and mechanical manipulation is avoidance of high ion beam currents which may cause significant changes to the specimen's properties. In addition, transferring the specimen into the testing device, which is one of the main challenges of mechanical testing of thin films and low dimensional materials<sup>33,62,63</sup>, is not needed by fabrication and characterization of the specimen exclusively inside the FIB-SEM.

(a)



(b)

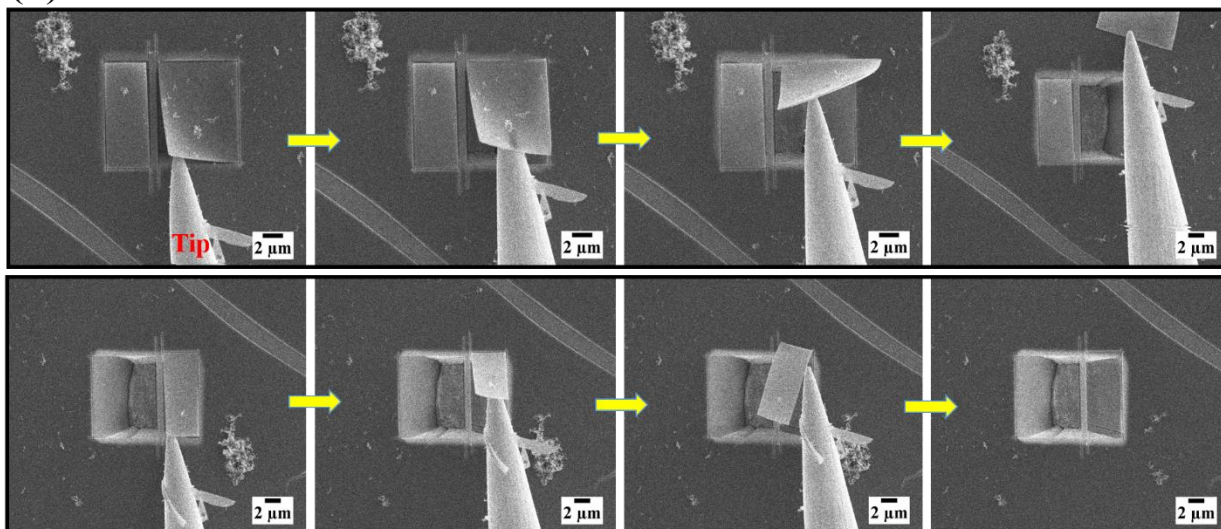


**Figure 6.4.** (a) From left to right SEM images of a FIB trench covered by a silica thin film, FIB cutting of free standing silica beam and removal of surrounding film fragments, and electron beam induced Pt deposition to “clamp” both sides of the silica beam; (b) SEM snapshots during removal of the two rectangular FIB cut film fragments on the sides of the silica beam, using a tungsten probe.

#### 6.2.4 In situ mechanical testing of “clamped” silica beams

To analyze the mechanical properties of fabricated silica beams, in situ bending tests were carried out with a force measurement sensor (FMT-120) mounted on a micromanipulator. During the bending tests SEM images were constantly acquired to follow the deformation behavior of the beams. Several experiments were performed on each fabricated beam with controlled displacements (see Experimental section for details). Figure 6.5a presents a series of SEM images during a load-unload cycle of a silica beam with a maximum displacement of about 1  $\mu\text{m}$ . From the SEM images it can be observed that the silica beam returned to its original position after retracting the tip without noticeable irreversible deformation (see also Appendix Movie A6.3). In contrast to



earlier findings, where superplastic deformation was observed for silica nanowires,<sup>29</sup> in our case no evidence of plasticity was noticed, possibly due to the larger size of the silica beams in this study. In Figure 6.5b the linear elastic regime in the low deformation region of the force-distance curves for such silica beams is shown. Consequently, based on the measured force-distance data, the width, length, and thickness of the silica beam, the Young's modulus can be determined using equation 1<sup>64</sup>:

$$E = \frac{FL^3}{192uI} \quad (1)$$

where  $I$  is the moment of inertia calculated by  $I = \frac{wh^3}{12}$ ,  $w$  is the width,  $h$  is the silica beam thickness, and  $F$ ,  $u$ , and  $L$  representing the applied force, displacement, and suspended length of the clamped silica beam, respectively. With above equation the Young's modulus of a beam (length=10.3  $\mu\text{m}$ , width=350 $\pm$ 21 nm, thickness=200 nm) was calculated to 66 $\pm$ 3 GPa. Furthermore, the force for fracture of the silica beams in dependence of their widths (with thickness of 190 $\pm$ 10 nm) was measured. As can be seen in Figure 6.5c, the required force for fracture expectedly increased with increasing beam width. Nevertheless, as shown in the graph there is a linear regime where force to fracture scaled with beam width (660–2500 nm) and a nonlinear regime where higher forces were required for beams narrower than 500 nm. SEM images also show that the fracture took place in the middle of the beam (Figure 6.5c inset). Despite the limited number of beams measured in these experiments, the observed deviation from linearity in force to fracture for small beam widths is interesting and deserves a more detailed investigation. To rule out possible effects of the position of the FMT-120 tip on such deviation, precautions had to be taken. Therefore, prior to the bending tests, we ensured that the tip landing position was always close to the middle of the fabricated beams as the bending test in the midspan of the beam is necessary to determine the Young's modulus by equation 1. In the following sections, the effects of Ga ion beam irritation and relative humidity are investigated in detail while other factors including the tip landing position may also affect the mechanical measurements on the silica beams.

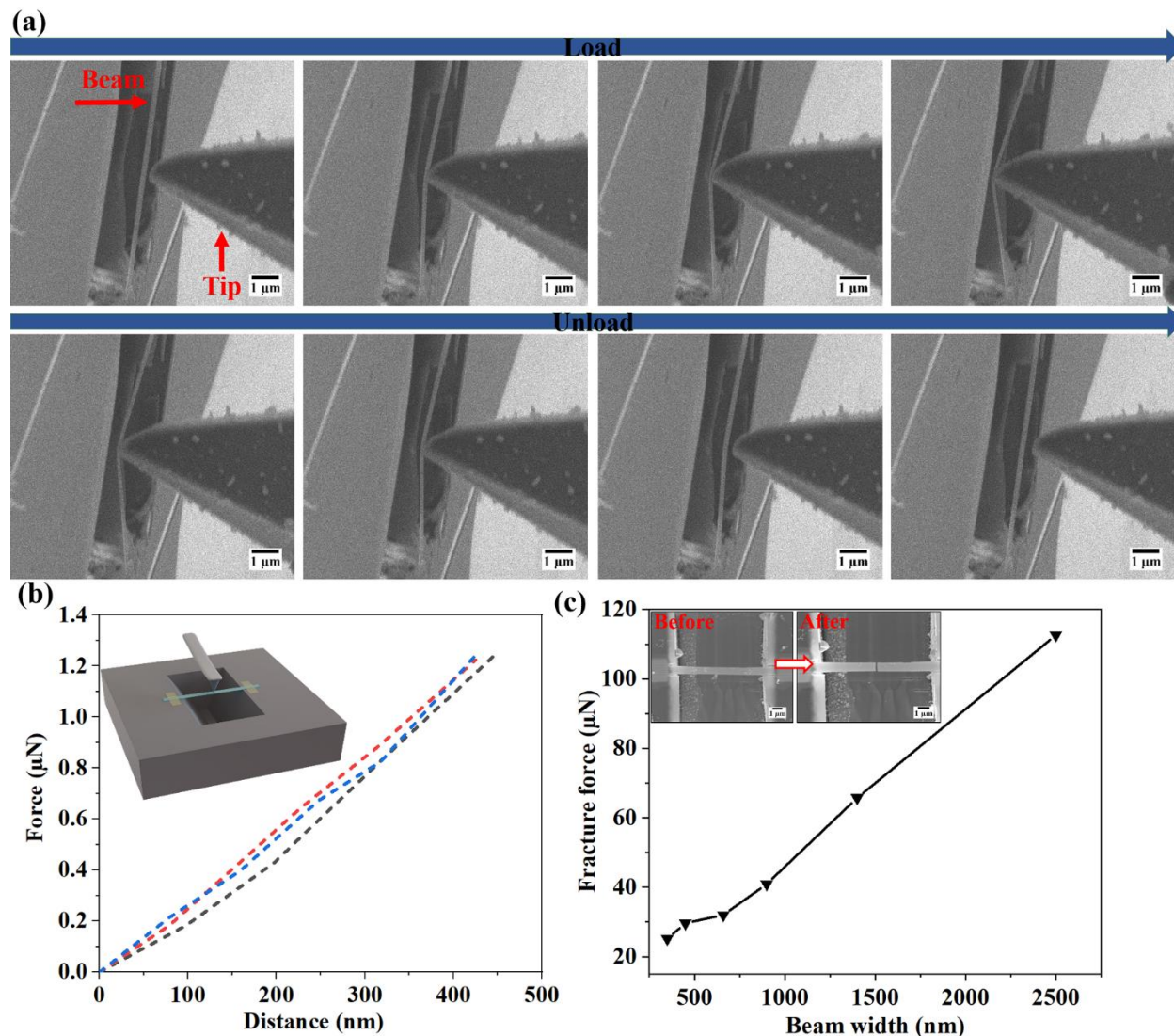


**Figure 6.5.** (a) SEM snapshots of in situ bending test on a clamped silica beam during load-unload cycle; (b) measured force-distance curves within the linear region for three silica beams having identical dimensions; (c) graph showing maximum forces to fracture plotted against the beam widths.

### 6.2.5 Effects of Ga ion irradiation on the mechanical properties of silica beams

Fabrication of micro and nanostructures via FIB milling or cutting is commonly conducted using Ga ions. This process is accompanied by several inevitable side effects for instance residual stresses, surface damage, and ion implantation that may result in different altered morphological, chemical and mechanical properties of the specimen<sup>65-69</sup>. In addition, a higher image intensity can be observed at the edges of prepared beams indicating changes in secondary electron yield likely caused by Ga ion implantation or silica densification (Appendix Figure A6.3). Hence, to obtain detailed insights into the effects of Ga ions on the mechanical properties of silica beams, the FIB cutting parameters were fixed, beams of different width prepared, and their Young's modulus measured and compared. Figure 6.6a-e shows prepared silica beams with their widths in the range from  $250 \pm 15$  nm to  $1400 \pm 48$  nm, and Figure 6.6f shows their respective Young's modulus ( $E$ ),

determined from the linear region of the corresponding force-distance curves. While the beam with a narrow width of  $250 \pm 15$  nm exhibited a high Young's modulus ( $73 \pm 3$  GPa), at wider width of  $1400 \pm 48$  nm a much lower value ( $42 \pm 1$  GPa) was obtained. These results clearly indicate a significant effect of the FIB cutting on the mechanical properties of beams as narrow beams were more severely affected. This can be explained by the fact that Ga ions can lead to a densification of the silica networks in thin films<sup>45</sup>, thus increasing the Young's modulus of the silica beam. To establish the spatial range of the Ga ion beam irradiation effects on the Young's modulus of silica thin beams, Finite element method (FEM) simulation was conducted (see also Appendix Figure A6.4, and Experimental section for the details) based on a model of an unaffected silica mid-section, combined with an affected section on each side, referred to as "silica plus" (Figure 6.6g). The effective modulus is shown in Figure 6.6h for the "silica plus layer" ( $w_+$ ) as a function of the total width of the beam and the modulus of the "silica plus" layer (see also Appendix Figure A6.5). The modulus increased for an increasing modulus of the silica plus layer ( $w_+$ ) and an increasing width. The optimally fitted combination of width and modulus for the silica plus layer equaled 100 nm and 75 GPa respectively (Appendix Figure A6.6 & A6.7). According to these data, we can indeed infer that the high Young's modulus observed for narrow beams is due to the Ga ion beam irradiation and that these effects become insignificant for beams wider than 450 nm. It can thus be suggested that the obtained Young's modulus of wider beams better represents the native value for the silica film in this study which is lower than the Young's modulus of bulk fused silica<sup>70</sup>. These findings suggest that in general the noticeable effect of Ga ion beam should be taken into account when considering the fabrication and mechanical testing of thin films on length scales below 500 nm inside FIB-SEM.

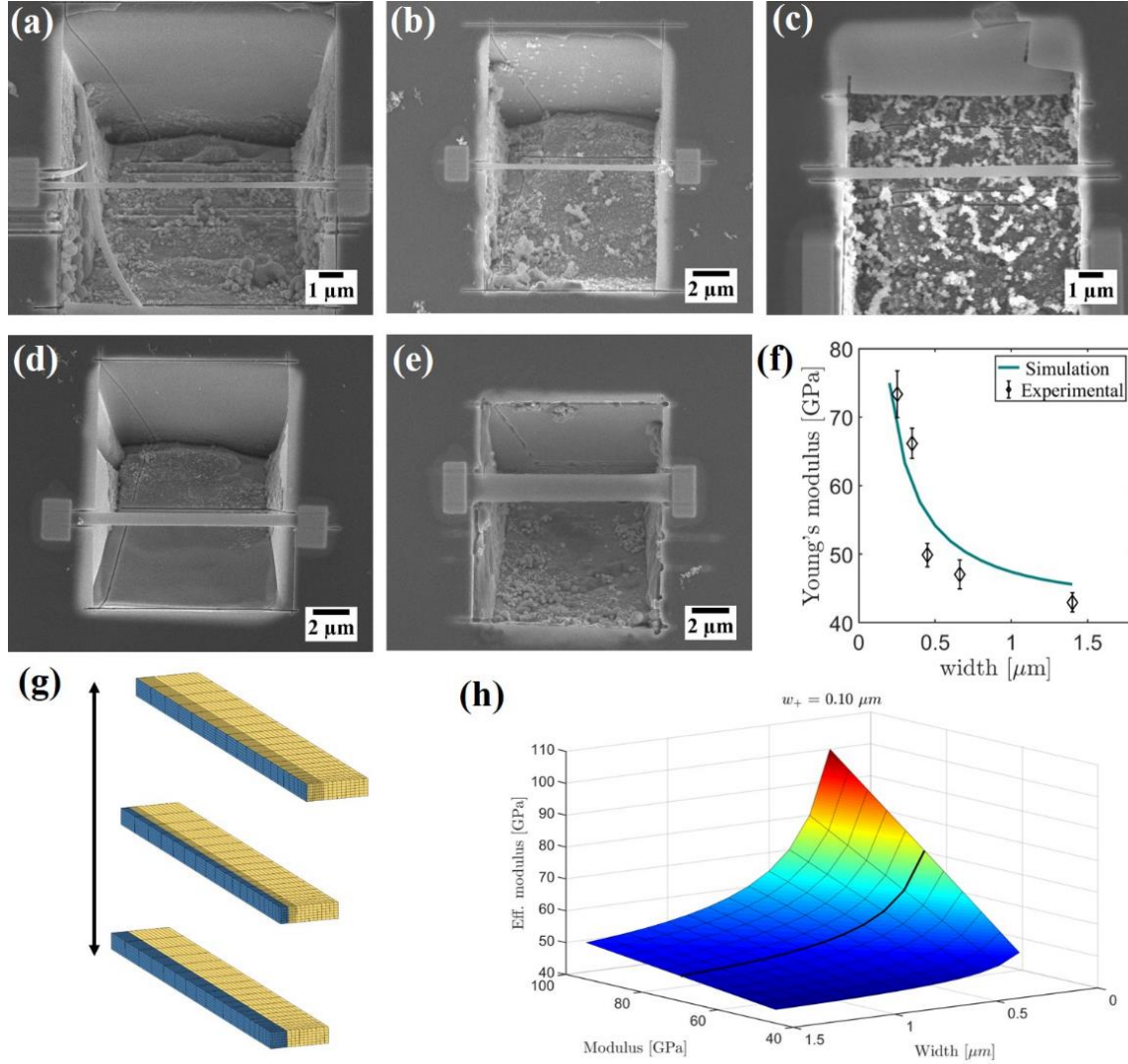


**Figure 6.6.** (a-e) SEM images of clamped silica beams with different widths; (f) Young's modulus of the silica beams plotted against their widths; (g) simulations performed with a range of widths of the silica plus layer, (the yellow elements indicate the bulk silica in the center of the beam and the blue elements indicate the silica plus at each side); (h) a typical effective modulus computed using the analytical solution for  $0.1 \mu\text{m}$  width of silica plus layer ( $w_+$ ) as a function of total width of the beam and the modulus of the affected "silica plus" layer (the best fitting result of a modulus of 75 GPa is shown with the solid black line).

### 6.2.6 Effects of relative humidity on the mechanical behavior of silica beams

Because of the high vacuum inside the EM chamber/column, the effect of environmental parameters such as relative humidity on the mechanical performance of the thin films including silica is unknown at submicron scales. Interestingly, by varying the pressure and temperature inside the SEM chamber using low vacuum mode, the relative humidity (RH) can be adjusted in situ. Hence, to determine how relative humidity influences the mechanical behavior of the silica beams, a series of bending tests were performed on a fabricated silica beam at different RH values; ranging from 0 to 61 %. Figure 6.7a shows the final states of silica beams after bending at RH values of 0, 19, 45, 56, and 61 %. As shown in Figure 6.7a the beam returned to its original position after bending

and tip retraction which accompanied a plastic deformation through a series of experiments (Appendix Figure A6.8). The maximum force for a given displacement was measured at different RH values (Figure 6.7b). It can be seen from the data in the graph that the RH values in this experiment did not significantly change the required force ( $9.7 \pm 0.8 \mu\text{N}$ ) for a roughly 800 nm displacement. However, there was a clear increase in residual beam distortion/elongation as the RH value increased from 19 % to 61 % RH (Figure 6.7a). To rule out possible effects of the number of consecutive bending tests on one beam, a series of experiments was also conducted on a beam at high vacuum mode for 5 consecutive cycles. However, no notable change in the residual beam size and shape was observed (Appendix Figure A6.9). This finding suggests that humidity inside the SEM chamber induced plasticity in silica beams which was absent at high vacuum condition for a beam with similar dimensions. Nevertheless, these results at low (4.3 %) to moderate (61 %) relative humidity do not conclusively demonstrate the effect of relative humidity on plasticity of silica beams and further research should be undertaken to investigate the effect of elevated relative humidity on the intrinsic mechanical properties of silica-based structures particularly silica thin films. To our knowledge, the research on the effect of relative humidity on the mechanical properties of materials inside SEM has been mainly conducted on biological samples<sup>71,72</sup>. The experimental work presented here provides one of the first investigations into how to conduct in situ mechanical tests on a fabricated small scale specimen under controlled relative humidity inside the SEM chamber.

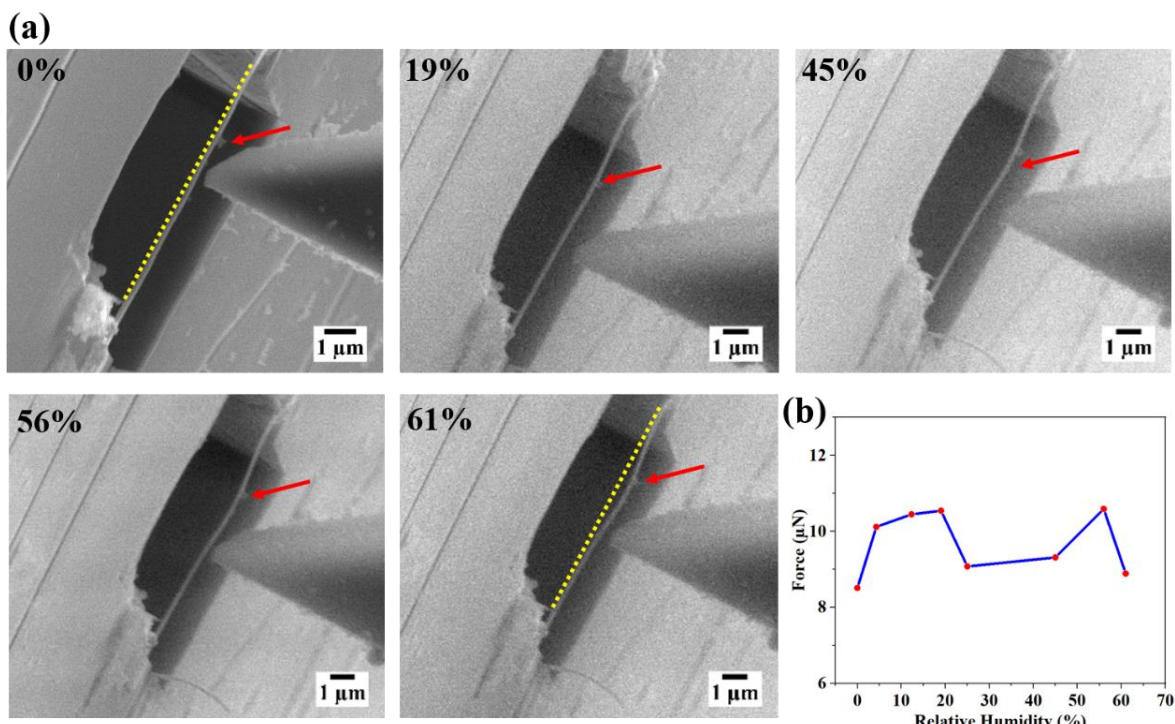


**Figure 6.7.** (a) SEM images of residual deformations of silica beams after bending tests and tip retraction at different RH values, yellow dash lines indicate the initial shape of the silica beam, red arrows indicate the changes in the beam shape at different RH values after the bending test; (b) Plot of maximum force for about 800 nm displacement of the beam in correlation with relative humidity.



### 6.3 Conclusions

A versatile workflow to fabricate and manipulate silica thin films as well as to characterize their mechanical properties inside FIB-SEM has been developed. The workflow combines FIB micromachining, micromanipulators, and in situ bending tests to determine the Young's modulus of silica beams of different widths. The combination of FIB milling and micromanipulation offers a flexible approach for small-scale specimen fabrication with target-specific size. The Young's modulus of silica beams was found to vary inversely with the beam widths. FEM simulation confirmed that this is due to increased Ga ion beam effects on silica beams of narrower widths. Also, preliminary experiments on the effect of controlled relative humidity on the mechanical behavior of a silica beam show that the silica beam has plastic behavior at high relative humidity. Our flexible workflow can be extended to other thin-film materials to accurately fabricate specimens in small-scales and characterize their mechanical properties in real-time.

### 6.4 Experimental Section

#### 6.4.1 Preparation of silica stock solution of pre-oligomerized tetraethoxysilane and thin film

Tetraethyl orthosilicate (TEOS), acetic acid, and 2-propanol were purchased from Sigma Aldrich and used without further purification. To prepare pre oligomerized silica stock solution, a mixture of 58.5g of TEOS in 159g 2-propanol was stirred at RT for about 1 hours. Then, 53.6 g water and 5.9 g acetic acid were added to the above solution. After 24 hours, the mixture was diluted with 2-propanol to the desired concentration. To lower the pH value of the resulting mixture to 1.5, concentrated nitric acid was used. As a typical experiment for thin film formation, approximately 100  $\mu$ l of diluted stock solution was placed on a silicon wafer as a substrate and spun at 3000 rpm for 2 minutes using the spin coater Laurell Model WS-650SX-6NPP/LITE. The prepared film was then dried at room temperature.

#### 6.4.2 Energy-Dispersive x-ray Spectroscopy and $^{29}\text{Si}$ Solid State NMR

For EDS elemental mapping, the silica film was peeled off from the silicon wafer substrate by the carbon tape. Then, the carbon tape contained silica film fragments was deposited onto a standard aluminum SEM Stub. SEM imaging and EDS elemental mapping of the film fragments was carried out by dual-beam SEM Quanta 3D FEG (Thermo Fisher Scientific, USA), at an acceleration voltage of 5 KV. Solid state magic angle spinning (MAS) NMR measurements were performed on an Oxford magnet of a static magnetic field at 9.4 T (operating frequency for  $^1\text{H}$  and  $^{29}\text{Si}$  at 400.1 MHz and 79.5 MHz, respectively) equipped with a Bruker NEO spectrometer. The static magnetic field was externally referenced to tetramethylsilane (TMS) at 0 ppm for  $^{29}\text{Si}$  chemical shift. The sample was packed into 6 mm (o. d.) PENCIL rotor with two Teflon restrictors and measured with Varian 6 mm HXY probe head. Nitrogen gas was used to spin the rotor, and the MAS rate was set to 4 kHz.  $^{29}\text{Si}$  T1 relaxation time constant was determined using saturation-recovery experiment, and the recycle delay of 1D  $^{29}\text{Si}$ -MAS NMR was set to 5 times of  $^{29}\text{Si}$  T1. No proton decoupling

was applied during signal acquisition. For spectra processing 50 Hz of apodization was applied. SSNake software<sup>73</sup> was used to afford spectra fitting result.

#### **6.4.3 Delamination and covering trenches by silica thin films**

To prepare free standing silica thin films, the following steps were taken: First, 20 trenches (length: 10-20  $\mu\text{m}$ ; width: 10-12  $\mu\text{m}$ ; depth: 4  $\mu\text{m}$ ) on a silicon wafer were engraved by using a dual-beam SEM Quanta 3D FEG (Thermo Fisher Scientific, USA), equipped with a gallium ion ( $\text{Ga}^+$ ) source operational at the accelerating voltage of 30 kV and current of 5 nA. Second, as prepared film on the different substrate was peeled off by a carbon tape which led to attaching the silica film to the tape. Subsequently the tape was placed on the silicon wafer which contains the pre patterned trenches. Finally, the tape was removed by thermal treatment in an oven under room pressure at a rate of 10  $^{\circ}\text{C}.\text{min}^{-1}$  up to 160  $^{\circ}\text{C}$  and incubated for 1 h at 160  $^{\circ}\text{C}$ , additionally calcined at the rate of 10  $^{\circ}\text{C}.\text{min}^{-1}$  to 450  $^{\circ}\text{C}$ , the sample temperature was maintained for 2 h at 450  $^{\circ}\text{C}$ .

#### **6.4.4 Focused ion beam-scanning electron microscopy and micromanipulator**

After carbon tape removal and covering the trenches by the silica film fragments, the silica beams with desired width and length could be fabricated by FIB milling process which was carried out inside the aforementioned FIB-SEM. Employing a very low ion beam current (1.5 pA) during the milling process was important to minimize the morphological and mechanical damage to the film. After cutting the silica film with the desirable width and length, a micromanipulator (MM3A-EM, Kleindiek Nanotechnik GmbH, Germany) was employed to remove the adjoining films fragments which can hamper the mechanical testing. The micromanipulator provided a high positional accuracy of about 10 nm for the mechanical movement in three axes inside the SEM chamber. A tungsten probe (150-200 nm radius) attached to the micromanipulator was employed for the manipulation of the film fragments. After carbon tape removal by thermal treatment, often clean silica films over the trenches which did not require further cleaning steps were obtained. In some cases trenches were either covered or surrounded by carbon ash residues which can hamper the reproducibility of beam fabrication or block the electron beam during the bending tests. Therefore, in order to eliminate these issues, the residues were removed by the tungsten probe through mechanical manipulation as shown in Figure A6.2. Here we note that only crack/damage free sections of the silica films covering the trenches were selected for beam fabrication.

#### **6.4.5 In situ mechanical testing**

In situ bending tests on the as-fabricated beams were carried out by a force measurement sensor FMT-120 tip (Kleindiek Nanotechnik GmbH, Germany) mounted on the micromanipulator inside the SEM chamber. FMT-120 is a highly sensitive AFM-based sensor made of silicon and coated with piezoresistive materials with a force resolution of 10 nN. During the bending tests, force-time data are provided by the force measurement system (FMS) which finally could be transformed to force-displacement data by SEM image analysis. To this end, throughout the bending tests, SEM images were taken constantly. Then, the displacements were determined by tracking the positional



change of the tip or the small particles attached to the tip using a Gatan Digital Micrograph. Finally, the resultant applied force on the beam was noted for each displacement point.

#### 6.4.6 Finite Element Method (FEM) simulations

The bending test is simulated using the finite element software MSC.Marc<sup>®</sup>. A linear elastic material model is used. Only a quarter of the beam is modelled due to symmetry (Appendix Figure A6.4). The mesh consists out of quadratic elements using full integration, 6 elements are used along the thickness. A displacement is applied on the symmetry line of the x direction and the reaction forces are computed. The length of the line load is consisted with the size of the indenter which equals 750 nm. The end of the beam is fixed in all direction. The model consists out of two phases: bulk silica and a layer of silica plus with an increased Young's modulus. The layer of silica plus is the layer which may be affected by the Ga-ion beam. The modulus of the bulk silica is set on 40 GPa. The modulus of silica plus is varied between 50 GPa and 100 GPa. A Poisson ratio of 0.2 is used for both phases. During the simulations, the width of the silica plus layer is varied between 12.5 nm and 200 nm. The length and thickness of the beam remain constant, 10.5  $\mu\text{m}$  and 190 nm respectively. Simulations are conducted for a range of width of the beam, width of the silica plus layer and its modulus. The results and the comparison to the experimental results are shown in appendix Figure A6.6. The elements colored blue indicates the silica plus layer while the red elements are the bulk silica. These simulations are based on the assumption that the Ga ion beam affected the entire thickness of the beam.

#### 6.4.7 In situ mechanical testing under controlled relative humidity

In order to carry out the bending test on a fabricated silica beam at controlled relative humidity (RH), a series of experiments was conducted at low vacuum mode. In this experiment, the pressure was kept constant at 1 mbar and the relative humidity was controlled by adjusting the temperature from 20 to -20°C. It should be noted that the first cycle of this experiment was performed at high vacuum mode and room temperature. Subsequently, by changing the SEM configuration from high vacuum to low vacuum mode, the RH was regulated from 4.3 to 61 % by adjusting the temperature of the Peltier stage. In addition, since the conventional sample holder of the Peltier stage is not compatible with our micromanipulator and FMT-120 tip, a house-made sample holder was built for this experiment (Appendix Figure A6.10).

### 6.5 Reference

- 1 Manzano, M. & Vallet-Regí, M. Mesoporous silica nanoparticles for drug delivery. *Advanced Functional Materials* **30**, 1902634 (2020).
- 2 Patel, A. C., Li, S., Wang, C., Zhang, W. & Wei, Y. Electrospinning of porous silica nanofibers containing silver nanoparticles for catalytic applications. *Chemistry of Materials* **19**, 1231-1238 (2007).
- 3 Yang, X., Tang, H., Cao, K., Song, H., Sheng, W. & Wu, Q. Templated-assisted one-dimensional silica nanotubes: synthesis and applications. *Journal of Materials Chemistry* **21**, 6122-6135 (2011).
- 4 Kaushik, A., Kumar, R., Huey, E., Bhansali, S., Nair, N. & Nair, M. Silica nanowires: Growth, integration, and sensing applications. *Microchimica Acta* **181**, 1759-1780 (2014).

- 5 Liu, Z., Quan, K., Li, H., Chen, J., Guan, M. & Qiu, H. Preparation of Silica-Based Superficially Porous Silica and its Application in Enantiomer Separations: a Review. *Journal of Analysis and Testing* **5**, 242–257 (2021).
- 6 Lei, Q., Guo, J., Nouredine, A., Wang, A., Wuttke, S., Brinker, C. J. & Zhu, W. Sol–Gel-Based Advanced Porous Silica Materials for Biomedical Applications. *Advanced Functional Materials* **30**, 1909539 (2020).
- 7 Bautista, M. & Morales, A. Silica antireflective films on glass produced by the sol–gel method. *Solar Energy Materials and Solar Cells* **80**, 217–225 (2003).
- 8 Biswas, P., Chiavaioli, F., Jana, S., Basumallick, N., Trono, C., Giannetti, A., Tombelli, S., Mallick, A., Baldini, F. & Bandyopadhyay, S. Design, fabrication and characterisation of silica-titania thin film coated over coupled long period fibre gratings: Towards bio-sensing applications. *Sensors and Actuators B: Chemical* **253**, 418–427 (2017).
- 9 Lari, N., Ahangarani, S. & Shanaghi, A. Preparation of nanostructure silica antireflective coatings by using sol–gel method. *Optik* **126**, 5363–5367 (2015).
- 10 Hemker, K. J. & Sharpe Jr, W. N. Microscale characterization of mechanical properties. *Annu. Rev. Mater. Res.* **37**, 93–126 (2007).
- 11 Arzt, E. Size effects in materials due to microstructural and dimensional constraints: a comparative review. *Acta Materialia* **46**, 5611–5626 (1998).
- 12 Namazu, T., Isono, Y. & Tanaka, T. Evaluation of size effect on mechanical properties of single crystal silicon by nanoscale bending test using AFM. *Journal of Microelectromechanical systems* **9**, 450–459 (2000).
- 13 Haque, M. & Saif, M. Deformation mechanisms in free-standing nanoscale thin films: A quantitative in situ transmission electron microscope study. *Proceedings of the National Academy of Sciences* **101**, 6335–6340 (2004).
- 14 Chen, J., Shi, J., Wang, Y., Sun, J., Han, J., Sun, K. & Fang, L. Nanoindentation and deformation behaviors of silicon covered with amorphous SiO<sub>2</sub>: a molecular dynamic study. *RSC Advances* **8**, 12597–12607 (2018).
- 15 Shimizu, W. & Murakami, Y. Microporous silica thin films with low refractive indices and high Young's modulus. *ACS Applied Materials & Interfaces* **2**, 3128–3133 (2010).
- 16 Chemin, N., Klotz, M., Rouessac, V., Ayral, A. & Barthel, E. Mechanical properties of mesoporous silica thin films: Effect of the surfactant removal processes. *Thin Solid Films* **495**, 210–213 (2006).
- 17 Jauffrès, D., Yacou, C., Verdier, M., Dendievel, R. & Ayral, A. Mechanical properties of hierarchical porous silica thin films: Experimental characterization by nanoindentation and Finite Element modeling. *Microporous and Mesoporous Materials* **140**, 120–129 (2011).
- 18 Chen, S., Liu, L. & Wang, T. Investigation of the mechanical properties of thin films by nanoindentation, considering the effects of thickness and different coating–substrate combinations. *Surface and Coatings Technology* **191**, 25–32 (2005).
- 19 Bhushan, B. & Li, X. Nanomechanical characterisation of solid surfaces and thin films. *International Materials Reviews* **48**, 125–164 (2003).
- 20 Han, S. M., Saha, R. & Nix, W. D. Determining hardness of thin films in elastically mismatched film-on-substrate systems using nanoindentation. *Acta Materialia* **54**, 1571–1581 (2006).
- 21 Saha, R. & Nix, W. D. Effects of the substrate on the determination of thin film mechanical properties by nanoindentation. *Acta Materialia* **50**, 23–38 (2002).
- 22 Ma, Z., Zhou, Y., Long, S. & Lu, C. On the intrinsic hardness of a metallic film/substrate system: Indentation size and substrate effects. *International Journal of Plasticity* **34**, 1–11 (2012).
- 23 Cui, Z. *Nanofabrication: Principles, Capabilities and Limit*, Springer, Boston, MA, USA. 211 (2008).
- 24 Fang, F., Zhang, X., Gao, W., Guo, Y., Byrne, G. & Hansen, H. N. Nanomanufacturing—Perspective and Applications. *CIRP Annals* **66**, 683–705 (2017).
- 25 Sundararajan, S. & Bhushan, B. Development of AFM-based techniques to measure mechanical properties of nanoscale structures. *Sensors and actuators A: Physical* **101**, 338–351 (2002).

- 26 Li, X., Sun, M., Shan, C., Chen, Q. & Wei, X. Mechanical properties of 2D materials studied by in situ microscopy techniques. *Advanced Materials Interfaces* **5**, 1701246 (2018).
- 27 Kang, W., Merrill, M. & Wheeler, J. M. In situ thermomechanical testing methods for micro/nano-scale materials. *Nanoscale* **9**, 2666-2688 (2017).
- 28 Jiang, C., Lu, H., Zhang, H., Shen, Y. & Lu, Y. Recent advances on in situ SEM mechanical and electrical characterization of low-dimensional nanomaterials. *Scanning*, Article ID 1985149 (2017).
- 29 Yılmaz, M., Wollschläger, N., Esfahani, M. N., Österle, W., Leblebici, Y. & Alaca, B. E. Superplastic behavior of silica nanowires obtained by direct patterning of silsesquioxane-based precursors. *Nanotechnology* **28**, 115302 (2017).
- 30 Romeis, S., Paul, J., Herre, P., Hanisch, M., Taylor, R. N. K., Schmidt, J. & Peukert, W. In situ deformation and breakage of silica particles inside a SEM. *Procedia Engineering* **102**, 201-210 (2015).
- 31 Fukuda, T., Nakajima, M., Ahmad, M. R., Shen, Y., Nogawa, K. & Kojima, M. in *10th IEEE International Conference on Nanotechnology*. 111-114 (IEEE).
- 32 Fukuda, T., Arai, F. & Nakajima, M. *Micro-nanorobotic manipulation systems and their applications*. (Springer Science & Business Media, 2013).
- 33 Liebig, J., Göken, M., Richter, G., Mačković, M., Przybilla, T., Spiecker, E., Pierron, O. & Merle, B. A flexible method for the preparation of thin film samples for in situ TEM characterization combining shadow-FIB milling and electron-beam-assisted etching. *Ultramicroscopy* **171**, 82-88 (2016).
- 34 Gates, B. D., Xu, Q., Stewart, M., Ryan, D., Willson, C. G. & Whitesides, G. M. New approaches to nanofabrication: molding, printing, and other techniques. *Chemical Reviews* **105**, 1171-1196 (2005).
- 35 Shi, C., Luu, D. K., Yang, Q., Liu, J., Chen, J., Ru, C., Xie, S., Luo, J., Ge, J. & Sun, Y. Recent advances in nanorobotic manipulation inside scanning electron microscopes. *Microsystems & Nanoengineering* **2**, 1-16 (2016).
- 36 Tseng, A. A. Recent developments in nanofabrication using focused ion beams. *Small* **1**, 924-939 (2005).
- 37 Ampem-Lassen, E., Simpson, D., Gibson, B., Trpkovski, S., Hossain, F., Huntington, S., Ganesan, K., Hollenberg, L. & Prawer, S. Nano-manipulation of diamond-based single photon sources. *Optics Express* **17**, 11287-11293 (2009).
- 38 Mazerolle, S., Breguet, J.-M., Steinecker, A., Agnus, J., Perez, R. & Michler, J. Nanomanipulation in a scanning electron microscope. *Journal of Materials Processing Technology* **167**, 371-382 (2005).
- 39 Reyntjens, S. & Puers, R. Focused ion beam induced deposition: fabrication of three-dimensional microstructures and Young's modulus of the deposited material. *Journal of Micromechanics and Microengineering* **10**, 181 (2000).
- 40 Zang, J., Bao, L., Webb, R. A. & Li, X. Electron beam irradiation stiffens zinc tin oxide nanowires. *Nano letters* **11**, 4885-4889 (2011).
- 41 Cao, K., Feng, S., Han, Y., Gao, L., Ly, T. H., Xu, Z. & Lu, Y. Elastic straining of free-standing monolayer graphene. *Nature communications* **11**, 1-7 (2020).
- 42 Ghisleni, R., Rzepiejewska-Malyska, K., Philippe, L., Schwaller, P. & Michler, J. In situ SEM indentation experiments: Instruments, methodology, and applications. *Microscopy Research and Technique* **72**, 242-249 (2009).
- 43 Romeis, S., Paul, J., Ziener, M. & Peukert, W. A novel apparatus for in situ compression of submicron structures and particles in a high resolution SEM. *Review of Scientific Instruments* **83**, 095105 (2012).
- 44 Gianola, D. S., Sedlmayr, A., Mönig, R., Volkert, C. A., Major, R. C., Cyrankowski, E., Asif, S., Warren, O. L. & Kraft, O. In situ nanomechanical testing in focused ion beam and scanning electron microscopes. *Review of Scientific Instruments* **82**, 063901 (2011).

- 45 Mačković, M., Przybilla, T., Dieker, C., Herre, P., Romeis, S., Stara, H., Schrenker, N., Peukert, W. & Spiecker, E. A novel approach for preparation and in situ tensile testing of silica glass membranes in the transmission electron microscope. *Frontiers in Materials* **4**, 10 (2017).
- 46 Wang, B., Zhang, Z., Cui, J., Jiang, N., Lyu, J., Chen, G., Wang, J., Liu, Z., Yu, J. & Lin, C. In situ TEM study of interaction between dislocations and a single nanotwin under nanoindentation. *ACS Applied Materials & Interfaces* **9**, 29451-29456 (2017).
- 47 Tedstone, A. A., Lewis, D. J., Hao, R., Mao, S.-M., Bellon, P., Averbach, R. S., Warrens, C. P., West, K. R., Howard, P. & Gaemers, S. Mechanical properties of molybdenum disulfide and the effect of doping: an in situ TEM study. *ACS Applied Materials & Interfaces* **7**, 20829-20834 (2015).
- 48 Sun, J., Xu, F. & Sun, L.-T. In situ investigation of the mechanical properties of nanomaterials by transmission electron microscopy. *Acta Mechanica Sinica* **28**, 1513-1527 (2012).
- 49 De Hosson, J. T., Soer, W. A., Minor, A. M., Shan, Z., Stach, E. A., Asif, S. S. & Warren, O. L. In situ TEM nanoindentation and dislocation-grain boundary interactions: a tribute to David Brandon. *Journal of Materials Science* **41**, 7704-7719 (2006).
- 50 Lahouij, I., Vacher, B. & Dassenoy, F. Direct observation by in situ transmission electron microscopy of the behaviour of IF-MoS<sub>2</sub> nanoparticles during sliding tests: influence of the crystal structure. *Lubrication Science* **26**, 163-173 (2014).
- 51 Liu, Z., Yuan, X., Wang, S., Liu, S., Tan, H. H. & Jagadish, C. Nanomechanical behavior of single taper-free GaAs nanowires unravelled by in-situ TEM mechanical testing and molecular dynamics simulation. *Materials Science and Engineering: A* **806**, 140866 (2021).
- 52 Mačković, M., Niekietel, F., Wondraczek, L. & Spiecker, E. Direct observation of electron-beam-induced densification and hardening of silica nanoballs by in situ transmission electron microscopy and finite element method simulations. *Acta Materialia* **79**, 363-373 (2014).
- 53 Zheng, K., Wang, C., Cheng, Y.-Q., Yue, Y., Han, X., Zhang, Z., Shan, Z., Mao, S. X., Ye, M. & Yin, Y. Electron-beam-assisted superplastic shaping of nanoscale amorphous silica. *Nature Communications* **1**, 24 (2010).
- 54 Soleimani, M., van Breemen, L. C., Maddala, S. P., Joosten, R. R., Wu, H., Schreur-Piet, I., van Benthem, R. A. & Friedrich, H. In Situ Manipulation and Micromechanical Characterization of Diatom Frustule Constituents Using Focused Ion Beam Scanning Electron Microscopy. *Small Methods* **5**, 2100638 (2021).
- 55 Gao, E., Lin, S.-Z., Qin, Z., Buehler, M. J., Feng, X.-Q. & Xu, Z. Mechanical exfoliation of two-dimensional materials. *Journal of the Mechanics and Physics of Solids* **115**, 248-262 (2018).
- 56 Ojovan, M. I. Viscosity and glass transition in amorphous oxides. *Advances in Condensed Matter Physics*, 1-24 (Article ID 817829) (2008).
- 57 Portaccio, M., Della Ventura, B., Mita, D., Manolova, N., Stoilova, O., Rashkov, I. & Lepore, M. FT-IR microscopy characterization of sol-gel layers prior and after glucose oxidase immobilization for biosensing applications. *Journal of sol-gel Science and Technology* **57**, 204-211 (2011).
- 58 Chen, X., Jiang, J., Yan, F., Tian, S. & Li, K. A novel low temperature vapor phase hydrolysis method for the production of nano-structured silica materials using silicon tetrachloride. *RSC Advances* **4**, 8703-8710 (2014).
- 59 Huh, S., Wiench, J. W., Yoo, J.-C., Pruski, M. & Lin, V. S.-Y. Organic functionalization and morphology control of mesoporous silicas via a co-condensation synthesis method. *Chemistry of Materials* **15**, 4247-4256 (2003).
- 60 Mahler, J. & Sebald, A. Deconvolution of <sup>29</sup>Si magic-angle spinning nuclear magnetic resonance spectra of silicate glasses revisited—some critical comments. *Solid State Nuclear Magnetic Resonance* **5**, 63-78 (1995).
- 61 Schweizer, P., Dolle, C., Dasler, D., Abellán, G., Hauke, F., Hirsch, A. & Spiecker, E. Mechanical cleaning of graphene using in situ electron microscopy. *Nature Communications* **11**, 1743 (2020).
- 62 Hosseinian, E. & Pierron, O. N. Quantitative in situ TEM tensile fatigue testing on nanocrystalline metallic ultrathin films. *Nanoscale* **5**, 12532-12541 (2013).

- 63 Kobler, A., Kashiwar, A., Hahn, H. & Kübel, C. Combination of in situ straining and ACOM TEM: A novel method for analysis of plastic deformation of nanocrystalline metals. *Ultramicroscopy* **128**, 68-81 (2013).
- 64 Li, H., Yue, Y., Han, X. & Li, X. Plastic deformation enabled energy dissipation in a bionanowire structured armor. *Nano letters* **14**, 2578-2583 (2014).
- 65 Li, P., Chen, S., Dai, H., Yang, Z., Chen, Z., Wang, Y., Chen, Y., Shan, W., Peng, W. & Duan, H. Recent advances in focused ion beam nanofabrication for nanostructures and devices: fundamentals and applications. *Nanoscale* **13**, 1529-1565 (2020).
- 66 Samayoa, M., Haque, M. & Cohen, P. Focused ion beam irradiation effects on nanoscale freestanding thin films. *Journal of Micromechanics and Microengineering* **18**, 095005 (2008).
- 67 Liu, J., Niu, R., Gu, J., Cabral, M., Song, M. & Liao, X. Effect of ion irradiation introduced by focused ion-beam milling on the mechanical behaviour of sub-micron-sized samples. *Scientific Reports* **10**, 10324 (2020).
- 68 Kim, S., Park, M. J., Balsara, N. P., Liu, G. & Minor, A. M. Minimization of focused ion beam damage in nanostructured polymer thin films. *Ultramicroscopy* **111**, 191-199 (2011).
- 69 Velez, N. R., Allen, F. I., Jones, M. A., Donohue, J., Li, W., Pister, K., Govindjee, S., Meyers, G. F. & Minor, A. M. Nanomechanical testing of freestanding polymer films: in situ tensile testing and T g measurement. *Journal of Materials Research* **36**, 2456–2464 (2021).
- 70 Dahmani, F., Lambropoulos, J., Schmid, A., Burns, S. & Pratt, C. Nanoindentation technique for measuring residual stress field around a laser-induced crack in fused silica. *Journal of Materials Science* **33**, 4677-4685 (1998).
- 71 Shen, Y., Nakajima, M., Ahmad, M. R., Kojima, S., Homma, M. & Fukuda, T. Effect of ambient humidity on the strength of the adhesion force of single yeast cell inside environmental-SEM. *Ultramicroscopy* **111**, 1176-1183 (2011).
- 72 Shen, Y., Nakajima, M., Yang, Z., Tajima, H., Najdovski, Z., Homma, M. & Fukuda, T. Single cell stiffness measurement at various humidity conditions by nanomanipulation of a nano-needle. *Nanotechnology* **24**, 145703 (2013).
- 73 Van Meerten, S., Franssen, W. & Kentgens, A. ssNake: A cross-platform open-source NMR data processing and fitting application. *Journal of Magnetic Resonance* **301**, 56-66 (2019).

## 6.6 Appendix

### 6.6.1 Free standing silica film formation

Among various techniques for thin film formation, spin coating was chosen due to being relatively easy to perform and well established<sup>1</sup>. Figure A6.1a-d, show the process of thin-film delamination of spin coated silica film from the silicon wafer by carbon tape. It has been established the thickness of the thin film can be adjusted by changing parameters such as rotational speed of the spin coater, spinning time, and fume exhaust<sup>2</sup>. In the present study, by varying the rotational speed of the spin coater from 500 to 5000 rpm at constant spinning time of two minutes, silica films with various thickness were obtained (Figure A6.1e-h). Decreasing the rotational speed of the spin coater resulted in thicker films that contained many cracks (Figure A6.1i,j) mostly noticeable in films with a thickness of more than 300 nm. Accordingly, for beam fabrication we prepared only crack-free silica film with less than 300 nm in thickness. It is worth noting that at the edge of the silicon wafer, the thickness of the film was greater than the middle part due to edge-bead effect<sup>3</sup>. In the substrate with size of about 1 cm<sup>2</sup> there was approximately 10 % increase in the thickness of the film at the edges. Due to this difference in the thickness of the film at the edge of the substrate as well as a random distribution of the film fragments on top and around the trenches after carbon tape removal, obtaining many trenches covered by identical film thickness was challenging.

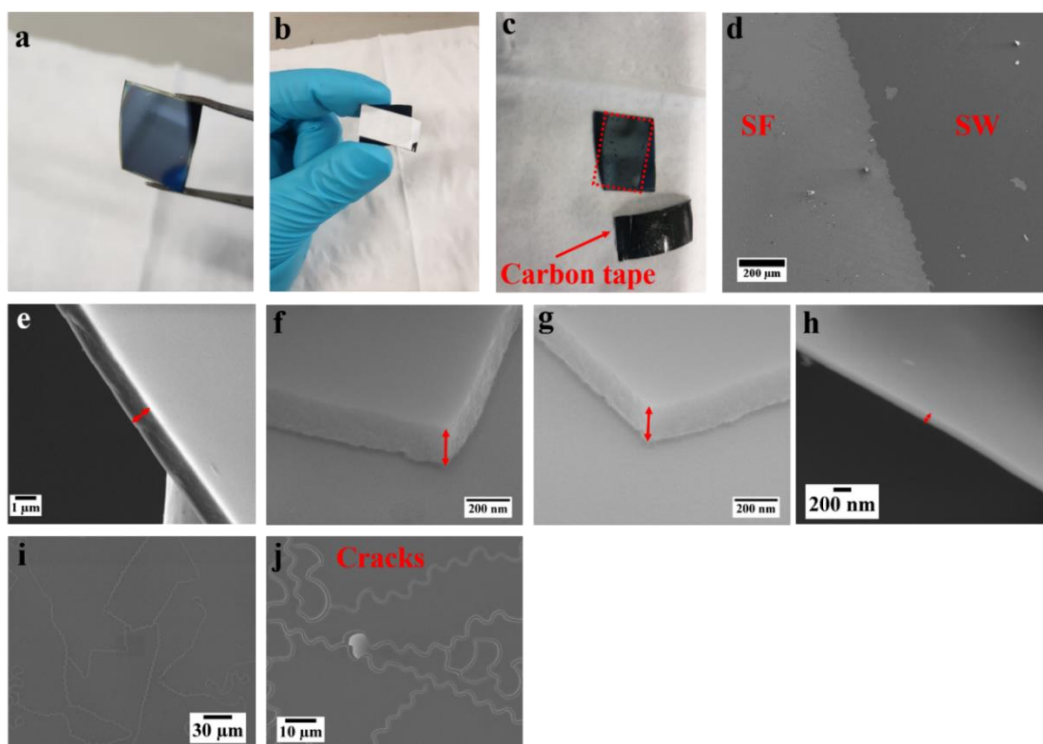


**Figure A6.1.** (a-c) photographs of deposited silica film on silicon wafer and silica film delamination from the silicon wafer by carbon tape; (d) SEM image of the boundary between the silica film (SF) and silicon wafer (SW) after delamination by carbon tape; (e-h) cross-section view SEM images of silica films with different thickness; (i,j) SEM images of cracks in the silica film with thickness greater than 300 nm.

### 6.6.2 Mechanical cleaning

Recently, an in situ mechanical cleaning procedure has been introduced for removal of contamination from the surface of graphene inside an EM<sup>4</sup>. In this method, using a micromanipulator and a sharp metallic tip contaminations could be completely removed without damage to a single layer of graphene. Similarly, in our study, due to the several handling steps prior to silica beam fabrication, the surface of the silica film was contaminated. After thermal treatment of carbon tape, the silica film was covered/surrounded by carbon ash and debris preventing further characterization (Figure A6.2). However, owing to the weak interactions between these contaminants and the silica film, mechanical manipulation via a sharp tungsten probe was performed to completely sweep them away from the area of interest. As shown in Figure A6.2, by moving the probe over the surface of silica film on a trench or its surrounding, the probe removed the contaminating ash without damaging the film underneath

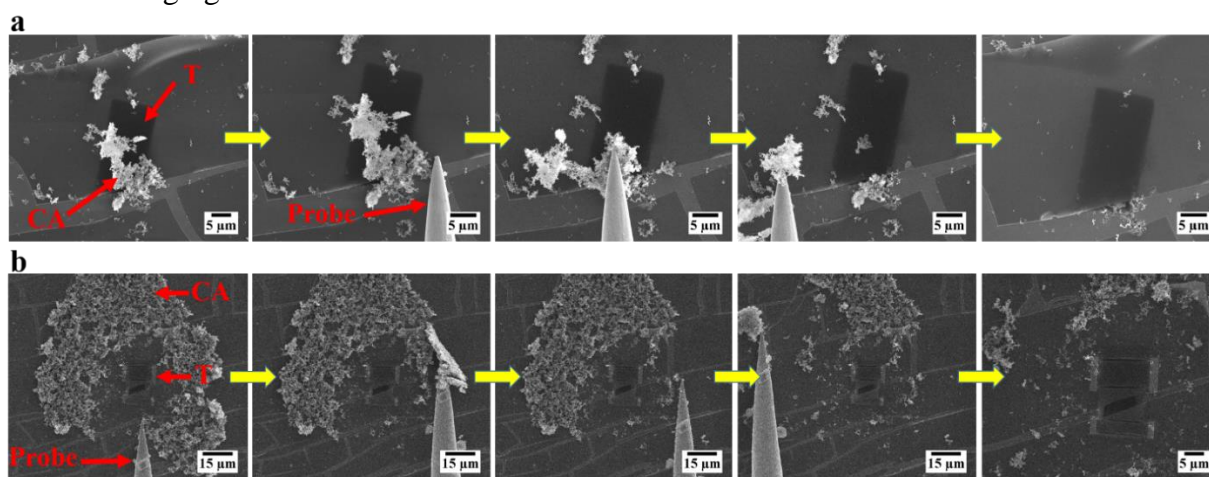


**Figure A6.2.** (a,b) Sequence of SEM images of mechanical cleaning by a tungsten probe for carbon ashes removal and obtaining trenches covered by the silica films (T=trench and CA=carbon ash).

### 6.6.3 Effect of Ga ion beam and Finite Element Method (FEM) simulations

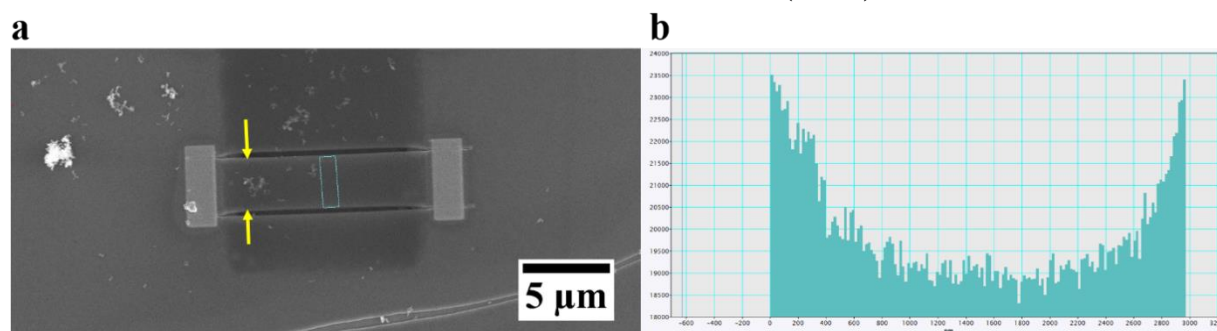


**Figure A6.3.** (a) SEM image of a silica beam (yellow arrows indicate that the edges of the beam are brighter (due to increased secondary electron yield likely caused by Ga ion implantation or silica densification)); (b) intensity profile across the width of the beam, demonstrating a higher SE intensity at the edges of the beam.

In order to get some insights into the effect of Ga ion beam irradiation on the mechanical properties of silica beams, FEM simulations were performed with the following details. Figure A6.4 shows



the geometry and the applied boundary conditions of the FEM simulation. Simulations were conducted for a range of beam widths. For each beam width, the width of the silica plus layer and its modulus was changed as schematically shown in Figure A6.5. A displacement was applied on the geometry and the reaction forces were computed for a range of beam widths, the width of the silica plus layer and its Young's modulus. From the computed displacement and forces, the effective modulus was computed and compared to the experimental results, see Figure A6.6 & A6.7.

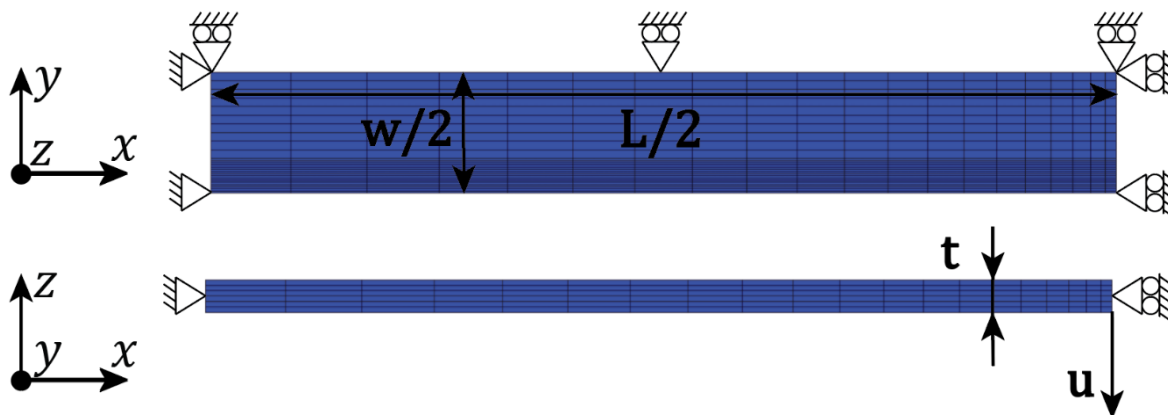
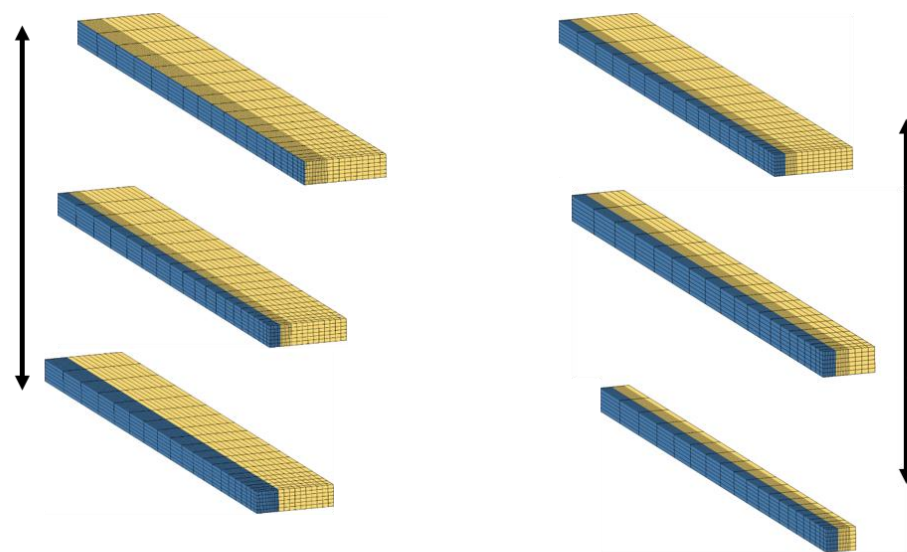


**Figure A6.4.** Top and side view of the geometry and the applied boundary conditions. ( $w$ ,  $L$ ,  $t$ , and  $u$  represent width, length, thickness, and displacement respectively).



Change in width of the silica+ layer

Change in width of the beam

**Figure A6.5.** Simulations performed with a range of width of the silica plus layer (left) and a range of width of the beam (right). The yellow elements correspond to bulk silica and the blue elements correspond to silica plus.

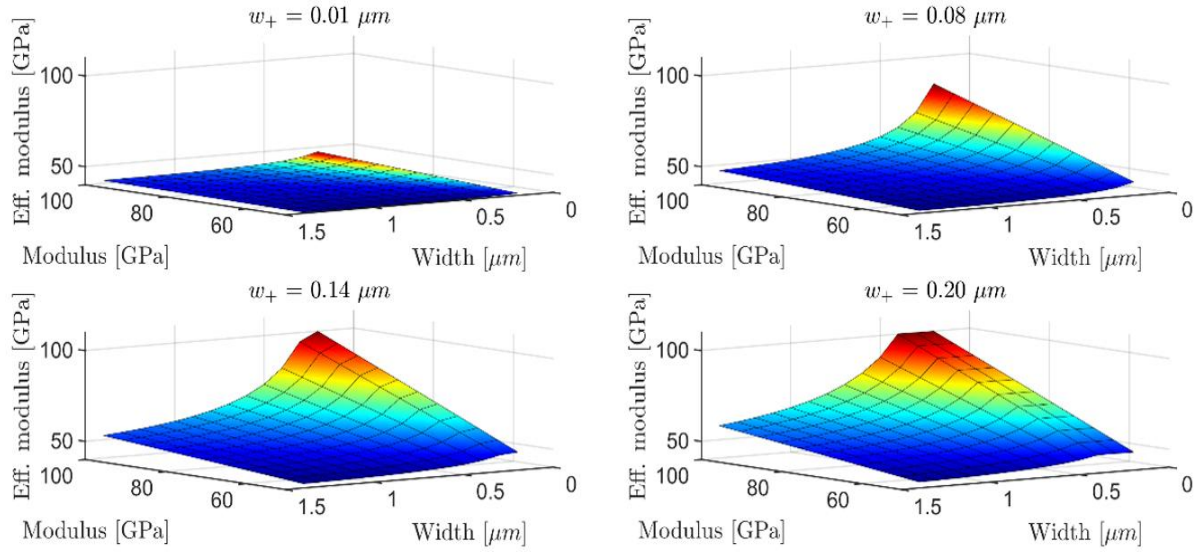


**Figure A6.6.** Effective modulus computed using the analytical solution for four different widths of silica plus layer as a function of width of the beam and the modulus of the silica plus layer.

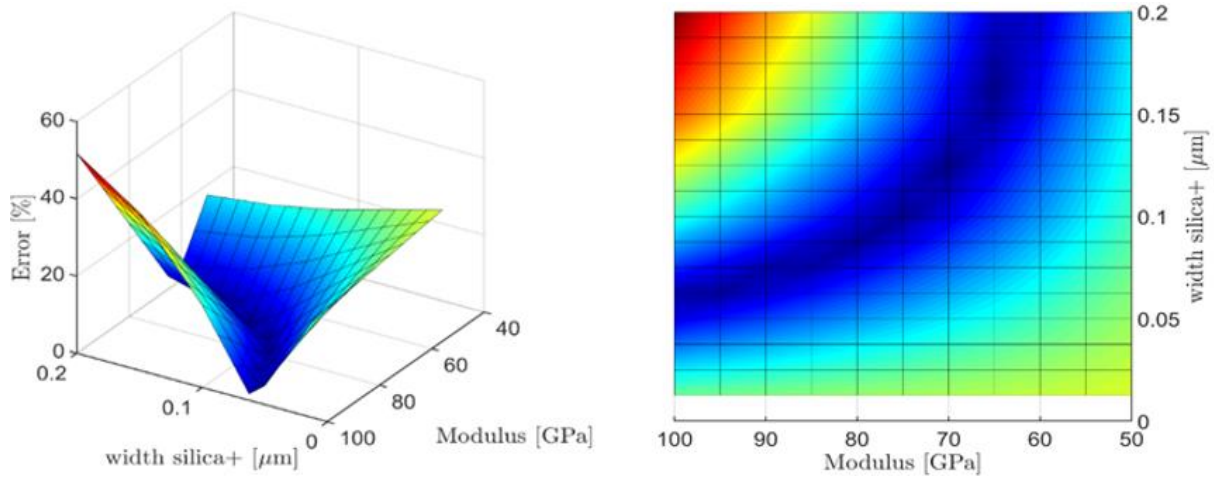


**Figure A6.7.** Computed absolute error with respect to modulus and width of the silica plus layer.

#### 6.6.4 Comparing bending tests at high vacuum and under relative humidity conditions

In situ bending tests at different relative humidity conditions by varying the temperature of Peltier stage from 20 °C to -20 °C at constant pressure of 1 mbar.

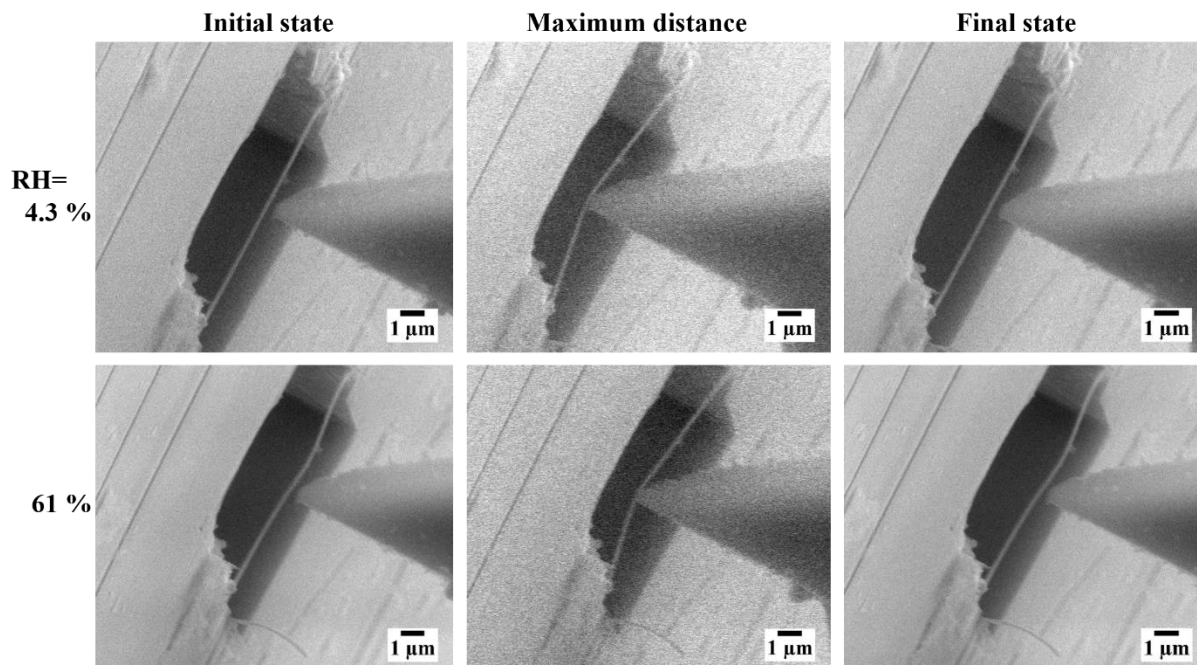


**Figure A6.8.** SEM images of initial, maximum distance, and final state of a double clamp silica beam at the lowest (4.3 %,  $T=16$  °C) and highest (61 %,  $T=-20$  °C) relative humidity.

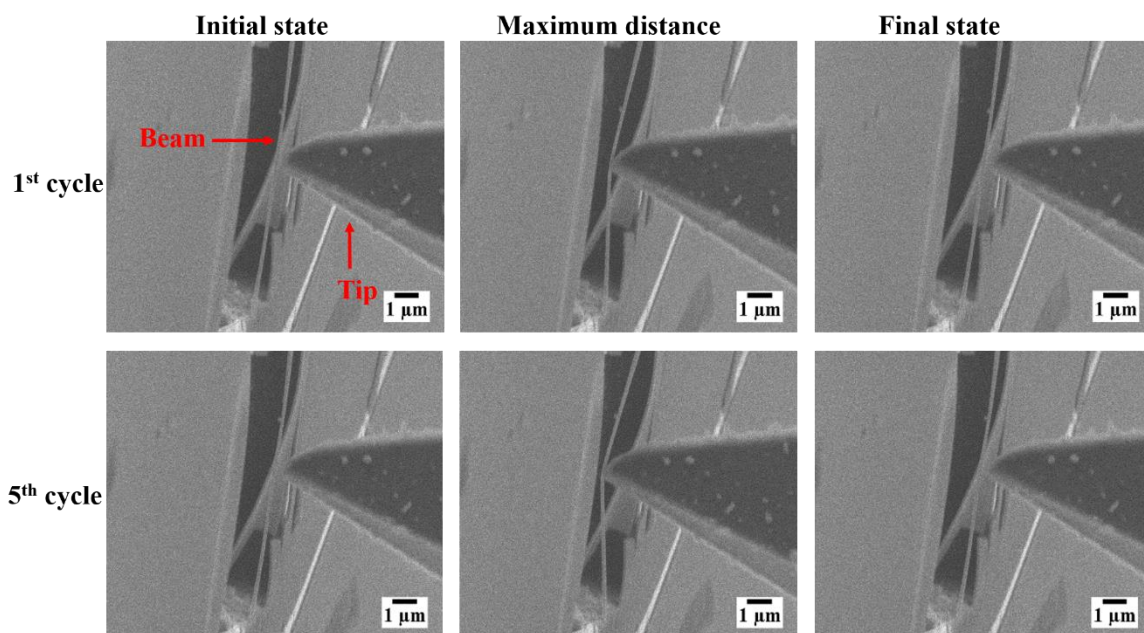


**Figure A6.9.** SEM images of initial, maximum distance (for different distances), and final state of a bending test on double clamp silica beam at high vacuum mode for the first and fifth cycle.

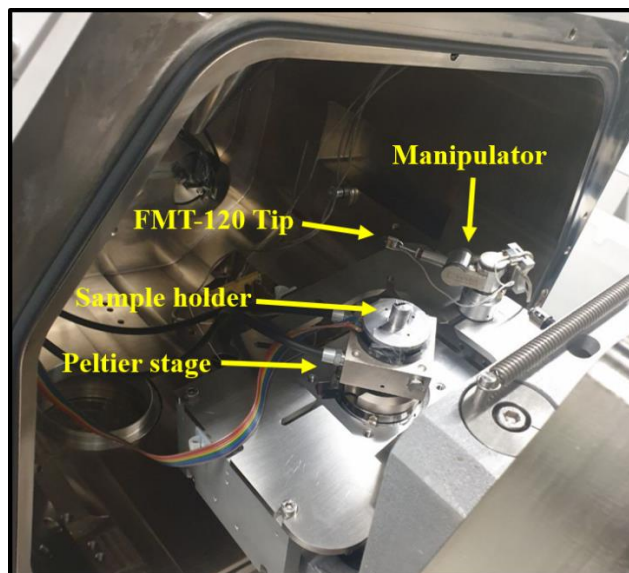


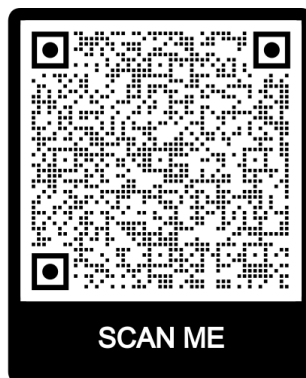
**Figure A6.10.** A photograph of inside of the SEM chamber showing the accessories for performing a bending test on the fabricated silica beams under relative humidity condition.

### 6.6.5 Appendix Movies

**Movie A6.1:** In situ mechanical cleaning of surface of the film.



**Movie A6.2:** In situ mechanical manipulation of film fragments.



**Movie A6.3:** In situ bending test on a double clamped silica beam.



#### 6.6.6 Appendix references

- 1 Mustafa, H. A. M. & Jameel, D. A. Modeling and the main stages of spin coating process: A review. *Journal of Applied Science and Technology Trends* **2**, 91-95 (2021).
- 2 Tyona, M. A theoritical study on spin coating technique. *Advances in materials Research* **2**, 195 (2013).
- 3 Yan, Y., Zhou, P., Zhang, S.-X., Guo, X.-G. & Guo, D.-M. Effect of substrate curvature on thickness distribution of polydimethylsiloxane thin film in spin coating process. *Chinese Physics B* **27**, 068104 (2018).
- 4 Schweizer, P., Dolle, C., Dasler, D., Abellán, G., Hauke, F., Hirsch, A. & Spiecker, E. Mechanical cleaning of graphene using in situ electron microscopy. *Nature Communications* **11**, 1743 (2020).

# Chapter 7

## 7.1 Summary

This thesis set out to unravel the links between morphology, chemistry, and mechanics of biogenic silica of diatom frustules and their growth conditions, focusing mainly on the effects of  $\text{Al}^{3+}$  ions and salinity. To this end, it was also essential to develop new experimental approaches that provide new insights and a new understanding of the properties of biogenic silica that ultimately can be adapted and used in a wide range of applications. In order to monitor the morphological and chemical properties of diatom frustules, several spectroscopic and microscopic techniques were employed. We observed that  $\text{Al}^{3+}$  not only was homogenously incorporated into the diatom frustules but also led to an increased silica crosslinking density as well as modifying frustule morphological parameters. Furthermore, a combination of advanced electron microscopy techniques such as focused ion beam (FIB), electron tomography, in situ manipulation, and mechanical testing were utilized to determine the mechanical properties of diatom frustule as well as synthetic silica thin films. It was found that  $\text{Al}^{3+}$  and salinity modify the mechanical properties of frustule constituents differently. The findings of this thesis are briefly summarized in the following paragraphs.

In chapter 2, frustule formation in diatom *Craspedostauros sp.*<sup>1</sup>, including changes to overall morphology, silica thickness, and composition, in the presence of  $\text{Al}^{3+}$  ions at different concentrations, was investigated. Our results showed that in the presence of  $\text{Al}^{3+}$  the total silica uptake from the growth medium increased, although a decrease in the growth rate was observed. This led to a higher inorganic content per diatom resulting in a decreased pore diameter and a thicker frustule as evidenced by electron microscopy. Furthermore,  $^{27}\text{Al}$  solid-state NMR, FIB-SEM, and EDS results confirmed that  $\text{Al}^{3+}$  was incorporated into the frustule during the silicification process, thus, improving hydrolysis resistance.

In order to determine the mechanical properties of a diatom frustule and ultimately reveal the influence of the growth medium conditions on these properties, a streamlined analysis workflow was developed in chapter 3. By a combination of FIB-SEM and micromanipulators, frustule constituents, i.e., valves and girdle bands of the diatom *Thalassiosira pseudonana*, were isolated from each other so that their mechanical properties could be investigated individually. To be specific, the

---

<sup>1</sup> Previously referred to as *Pinnularia sp.*



girdle bands and valves were separated by FIB milling and manipulated using a sharp tungsten tip without compromising their physical or chemical integrity. In situ mechanical studies on isolated girdle bands combined with Finite Element Method (FEM) simulations, enabled the quantitative assessment of Young's modulus of this biosilica;  $E=40.0$  GPa. In addition, the mechanical strength of isolated valves was measured by transferring and mounting them on top of pre-milled holes in the sample support. Above methodology was used to study the effects of salinity in the growth medium. While there was no noticeable difference in mechanical properties of girdle bands, a significant decrease of the force to fracture of the valve were observed by increasing the salinity level from 28 to 46 PSU.

Following the development of our versatile approach to study the mechanical properties of diatom frustule constituents at micrometer length scale, the influence of  $Al^{3+}$  on these properties was investigated in chapter 4. Diatom *Thalassiosira pseudonana* was again used as a model system to study the effects of this non-essential metal ion on morphological, chemical, and mechanical properties of the frustule. By a combination of spectroscopic and electron microscopic techniques, it was shown that  $Al^{3+}$  was homogeneously distributed throughout the frustule, within four and six coordinated environments, modifying its morphological parameters, and increasing silica condensation. Furthermore, combining the developed analysis workflow with TEM electron tomography, and FEM simulations allowed the determination of the Young's modulus of this biosilica in the individual frustule constituent's i.e. girdle bands and valves. The results indicated an increase in the silica crosslinking ( $Q^4/Q^3$  ratio from 2.0 to 3.0), enhancement in thickness of girdle bands (from  $26\pm2$  to  $33\pm2$  nm) and a noticeable increase in the Young's modulus of the girdle bands (from 40 to 90 GPa) by  $Al^{3+}$  incorporation. As it was previously observed that thickening of the frustule is an effective defense strategy against predators, comparatively it may be hypothesized that by increasing the thickness of the girdle bands as well as silica condensation of the frustule in the presence of  $Al^{3+}$ , this diatom species can obtain superior mechanical protection against possible predators.

In Chapter 5, as another proof of concept for the developed workflow, the mechanical properties of a different diatom species, the pennate *Craspedostauros sp.*, were studied on a factor of 5 larger length scale. In addition, in situ mechanical manipulation of isolated valves on the sample support was shown which can be used to reposition the complex valve structures for in situ mechanical testings. Furthermore, a combination of in situ deformation tests inside an SEM with a 3D model of frustule of diatom *Craspedostauros sp.* (*C.sp.*) obtained by STEM electron tomography, alongside FEM simulations enabled quantitative determination of Young's modulus of this complex biogenic silica structure:  $E=2.4$  GPa. Taken together, the results of chapter 3, 4, and 5 suggest that there is a correlation between diatom species and the Young's modulus of their frustule, i.e., the intrinsic mechanical properties are species-specific. In addition, due to their morphological differences, the Young's modulus of different constituents of a diatom frustule, girdle bands and valves, differ from each other.



In the final experimental Chapter 6, the developed methodology was extended to synthetic silica thin films as a model example, determining their mechanical properties. To this end, free-standing silica beams of the desired dimensions were fabricated by combining FIB-SEM with micromanipulators. Using in situ bending tests on such beams inside the SEM and Finite Element Method simulations, the Young's modulus of synthetic thin-film silica and the effects of Ga ion beam radiation were determined. Furthermore, the effects of controlled relative humidity on the mechanical behavior of silica beams were investigated, demonstrating that plastic deformation of the silica beams occur at high relative humidity. Although, unfortunately, outside the scope of this thesis, the developed FIB-SEM approach can be readily extended to determine the effect of  $\text{Al}^{3+}$  on mechanical properties of synthetic silica which can be compared with the obtained results in biogenic silica of diatoms.

This versatile method holds several advantages compared to the conventional sample preparation and testing techniques. For instance, fabrication, handling/transfer, and characterization of silica beams are conducted within a single instrument (FIB-SEM) without compromising their chemical and physical properties. On the contrary, top-down nanofabrication techniques which involve various steps requiring strong chemical etchants and multiple masks may change the native chemical properties of specimens<sup>1</sup>. In addition, conducting mechanical testing inside an SEM, rule out the possible effect of high energy electron irradiation on the mechanical properties of the specimens, which particularly is observed for silica-based structures inside TEM<sup>2</sup>.

## 7.2 Outlook

Biocomposite materials provide great insight into how nature has been able to optimize multiple functional properties by combining relatively simple components e.g., brittle materials with organic molecules. The development of mesoscale characterization techniques has provided unique opportunities not only to advance our understanding of the properties and behavior of these materials but also to utilize the obtained knowledge in the fabrication of man-made materials with improved properties<sup>3</sup>. In this aspect, biogenic silica in diatom frustules has been an inspiring topic for a variety of scientific disciplines to reveal its formation as well as its chemical and morphological properties. A wide range of tools has been used to characterize diatom growth and frustule formation at the different length scales. These techniques have provided new insights into the biological process within the cell, silica condensation inside the SDV, the structural properties of the frustule, etc.<sup>4-7</sup>. The obtained knowledge from these aspects of diatom may offer new routes for fabrication of bioinspired/biomimetic silica with tailored structural and materials properties. However, there is abundant room for further progress to answer many key questions regarding the frustule formation, modification, and its functional properties.

For instance, despite the fact that there is no clear explanation for why diatom frustules possess highly ordered micro and nanostructures, it has been suggested that the frustule holds several essential functions such as mechanical protection and light-harvesting<sup>8,9</sup>. Likewise, even though the frustule formation is known to be flexible in correlation with the growth medium environment<sup>10</sup>,

it is still unknown why morphological parameters are altered by the presence of non-essential metal ions or changing the salinity level. Similarly, in the present study, we showed that morphological, chemical, and mechanical properties of diatom frustule are modified by altering their growth medium condition. However, there are still many key questions unanswered about how and why these modifications took place within the cells. What are the role of  $\text{Al}^{3+}$  or salinity in silica formation within the SDVs? How do diatoms adjust their cell functions in correlation with environmental changes? Answering these and other question may pave the way for materials scientists to exploit the biogenic silica of diatom frustule as well as bioinspired silica-based materials with tunable morphological, chemical, and mechanical characteristics.

In chapter 2, by increasing the  $\text{Al}^{3+}$  concentration in the medium the thickness increased and the pore size of the frustule decreased. It is unclear whether  $\text{Al}^{3+}$  is changing these parameters by interacting with macromolecules such as long-chain polyamines, silaffines, and other macromolecules in the SDV during the frustule formation or physiological processes in diatom cells have been disrupted by this metal ion. In order to address the former question, a biomimetic approach is needed to investigate the interaction between  $\text{Al}^{3+}$  and the mentioned macromolecules in the presence of  $\text{Si}(\text{OH})_4$ . It has already been observed that in a bioinspired approach the silica particle size can easily be controlled by changing the size of the polyamine in the reaction vessel<sup>11</sup>. Similarly, this process can be monitored while  $\text{Al}^{3+}$  is also present in the medium to determine whether  $\text{Al}^{3+}$  can modify the silica particle size and morphology.

Additionally, in chapter 2, several high contrast spherical particles were observed within the cell which contained large amounts of Al, P, and O. It is known that the formation of aluminophosphates granules is a detoxification mechanism in many living organisms including diatoms<sup>12</sup>. However, further research is needed not only to investigate how these particles are formed but also to determine their structural and chemical properties. In situ nanosurgery within an SEM with the help of FIB milling and micromanipulator<sup>13,14</sup> can shed some new light on the structural and chemical properties of these particles (Figure 7.1a,b). Figure 7.1 shows a preliminary nanosurgery experiment where the internal structure of diatom *C.sp.* grown in the presence of  $2\ \mu\text{M}\ \text{Al}^{3+}$  can be seen. Prior to the nanosurgery, a nanofork was made by FIB milling (Figure 7.1c). After exposing the particles within the cell during the slice and view process by FIB milling, the nanofork mounted on the micromanipulator was used to extract one of the particles (Figure 7.1d,e). The idea is to mount the obtained fragment/the particle (Figure 7.1f) on a TEM grid. Then electron tomography and Raman spectroscopy can be employed to reveal the fine details of the internal structures and chemical properties of such particles, respectively. This would be a fruitful area for further work which, unfortunately, was also beyond the scope of this thesis.

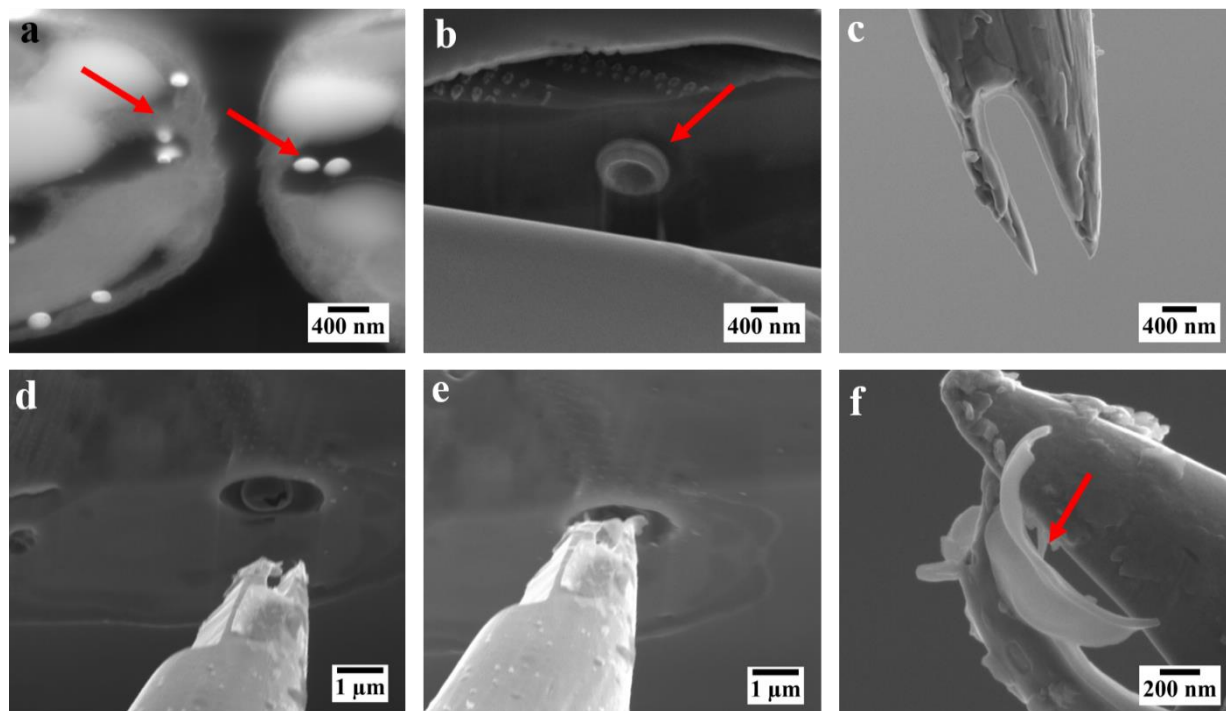


**Figure 7.1.** SEM images of internal structure of diatom *C.sp.* and a preliminary “nanosurgery” process. (a) BSE image of the inside of the cell (the red arrows indicate the spherical particles); (b) SE image showing a spherical particle within the cell; (c) nanofork made by FIB milling of a tungsten probe; (d-f) sequence of images of nanosurgery process, leading to obtain a fragment of a particle attached to the nanofork.

In this thesis the incorporation of  $\text{Al}^{3+}$  into the silica frameworks in the frustule of *T.p.* was shown, leading to increasing the silica condensation as well as a significant enhancement in the mechanical performance of the girdle bands. However, it is still unclear how  $\text{Al}^{3+}$  is distributed at nanometer length scales and what the impact of  $\text{Al}^{3+}$  can be on the local silica condensation. In order to address these topics, a new technique is needed to pinpoint the distribution of  $\text{Al}^{3+}$  at nanometer length scales and also monitor the degree of silica condensation at different locations of the diatom frustule. To this end, Photo-Induced Force Microscopy (PiFM) may be employed to shed some new lights on these aspects. PiFM is a scanning probe microscopy technique that combines atomic force microscopy (AFM) with a tunable infrared laser (IR) to simultaneously generate 3D topographic data as well as chemical imaging of the sample. This technique can provide a lateral spatial resolution of below 10 nm and a probing depth of about 30 nm. In PiFM, specific wavelength and fingerprint-like absorption characteristics of molecules are used<sup>15,16</sup>. Therefore, the position of the peaks in PiFM spectra corresponds to those in FTIR absorption spectra. It is known due to the shorter Si-O bond in comparison to Al-O and higher mass of Si compared to Al, the presence of  $\text{Al}^{3+}$  within the silica frameworks leads to redshift in the Si-O-Si vibration range in IR spectroscopy<sup>17</sup>. Thus, the presence of  $\text{Al}^{3+}$  within silica networks of the frustule at nanometer length scales can certainly be detected in PiFM as well. In addition, as it has been shown via IR spectroscopy the degree of silica condensation in diatom frustule can be estimated<sup>18</sup>, PiFM can be a superior

tool with its high spatial resolution to determine the condensation of silica within different locations of the frustule which may lead to revealing another level of complexity in the hierarchical ordering of biogenic silica.

Extending beyond biogenic silica in the last experimental chapter of this thesis, silica thin films were investigated as a model example of synthetic silica. However, in order to compare the properties of biogenic and synthetic silica, it is essential to fabricate synthetic materials with similar composition and morphology as those found in diatom frustules. For instance, biomimetic/bioinspired methods can be employed to synthetic silica structures with comparable morphological features. In this aspect, we conducted a preliminary experiment where hollow silica tubes with similar structures found in the girdle bands of diatom *T.p.* were fabricated. As can be seen in Figure 7.2a, silica tubes are hollow and their diameter can be controlled by the diameter of sacrificial templates. Alongside their diameter, the composition of such structures can easily be modified by the initial precursors. Figure 7.2b shows SEM-EDS elemental mapping of silica tubes with Si:Al ratio of 100:1, where Al is homogenously distributed alongside Si and O. Despite the fact that the surface of these structures are extremely rough and their thicknesses are higher than what was observed in the girdle bands of *T.p.*, these data are an initial step toward achieving silica structures with similar features and properties as found in diatom frustules. Alongside the formation of such materials, their mechanical properties and effect of  $\text{Al}^{3+}$  for sure is an interesting topic to discover. Similar to other small-scale materials studied in this thesis, a micromanipulator can be used to isolate a fragment silica tube (Figure 7.2c). Subsequently, FIB micromachining can be employed to fabricate tubes with desired dimensions for in situ mechanical testing.

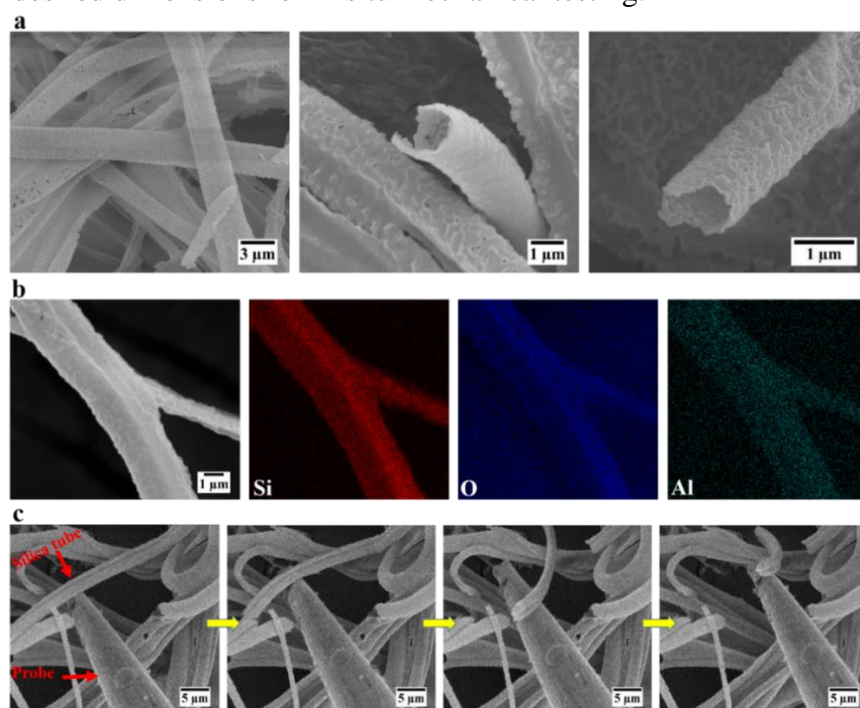


**Figure 7.2.** (a) SEM images of fabricated hollow silica tubes; (b) EDS elemental mapping of hollow silica tubes incorporated with  $\text{Al}^{3+}$ ; (c) SEM images of a sequence of manipulation of a silica tube by a tungsten probe. This procedure is essential for preparation of the specimen for mechanical testing.

To achieve the goals of this thesis, it was essential to develop and implement streamlined workflows by a combination of FIB-SEM and micromanipulators to accurately measure the mechanical properties of diatom frustules as well as silica thin films. The challenges related to the sample preparation without compromising their chemical and physical properties, handling/transferring the specimens, in situ observation of specimen behavior upon deformation, and conducting real-time mechanical testing on micro-scale specimen<sup>19,20</sup> were completely addressed in our approach. This method showed its capability to simplify complicated geometries, e.g. diatom frustule, fabricate micro and nanoscale objects such as silica thin beams, manipulate micrometer specimens with high positional accuracy, e.g. valves and silica film fragments, and more importantly characterize the mechanical properties of small-scale materials, e.g. valve, girdle bands, and silica beams, in their native states all within a dual-beam system. Obviously, due to the flexibility of our method, it can easily be extended to fabricate and manipulate small-scale biominerals, 3D architected materials, composites, polymeric materials, and synthetic hierarchical materials and measure their mechanical properties in real time. In addition, scale-specific mechanical properties (size effects) which are known to be important parameters in designing the mechanical properties of materials, can be revealed by such an in situ procedure. Obtaining fundamental understandings and insights of the size effects will provide a great opportunity for developing small-scale devices and materials for a variety of applications ranging from electronics to medicine<sup>19,21-23</sup>. For instance, recently via in situ deformation experiments within an SEM, we showed that calcium phosphate (CaP) ceramics which on the macro-scale are known to be brittle, exhibited fully elastic behavior due to its nanofiber structures, indicating its application as flexible tissue scaffold in regenerative medicines<sup>24</sup>.

### 7.3 References

- 1 Gates, B. D., Xu, Q., Stewart, M., Ryan, D., Willson, C. G. & Whitesides, G. M. New approaches to nanofabrication: molding, printing, and other techniques. *Chemical Reviews* **105**, 1171-1196 (2005).
- 2 Zheng, K., Wang, C., Cheng, Y.-Q., Yue, Y., Han, X., Zhang, Z., Shan, Z., Mao, S. X., Ye, M. & Yin, Y. Electron-beam-assisted superplastic shaping of nanoscale amorphous silica. *Nature Communications* **1**, 1-8 (2010).
- 3 Chen, P.-Y., Lin, A., Lin, Y.-S., Seki, Y., Stokes, A., Peyras, J., Olevsky, E., Meyers, M. A. & McKittrick, J. Structure and mechanical properties of selected biological materials. *Journal of the mechanical behavior of biomedical materials* **1**, 208-226 (2008).
- 4 Gröger, C., Sumper, M. & Brunner, E. Silicon uptake and metabolism of the marine diatom *Thalassiosira pseudonana*: solid-state <sup>29</sup>Si NMR and fluorescence microscopic studies. *Journal of Structural Biology* **161**, 55-63 (2008).
- 5 Mayzel, B., Aram, L., Varsano, N., Wolf, S. G. & Gal, A. Structural evidence for extracellular silica formation by diatoms. *Nature communications* **12**, 1-8 (2021).
- 6 Zgłobicka, I., Gluch, J., Liao, Z., Werner, S., Guttman, P., Li, Q., Bazarnik, P., Plocinski, T., Witkowski, A. & Kurzydowski, K. J. Insight into diatom frustule structures using various imaging techniques. *Scientific Reports* **11**, 1-10 (2021).
- 7 Kumar, S., Rechav, K., Kaplan-Ashiri, I. & Gal, A. Imaging and quantifying homeostatic levels of intracellular silicon in diatoms. *Science Advances* **6**, eaaz7554 (2020).

- 8 Ellegaard, M., Lenau, T., Lundholm, N., Maibohm, C., Friis, S. M. M., Rottwitt, K. & Su, Y. The fascinating diatom frustule—can it play a role for attenuation of UV radiation? *Journal of Applied Phycology* **28**, 3295-3306 (2016).
- 9 Hamm, C. E., Merkel, R., Springer, O., Jurkojc, P., Maier, C., Prechtel, K. & Smetacek, V. Architecture and material properties of diatom shells provide effective mechanical protection. *Nature* **421**, 841-843 (2003).
- 10 Su, Y., Lundholm, N. & Ellegaard, M. Effects of abiotic factors on the nanostructure of diatom frustules—ranges and variability. *Applied Microbiology and Biotechnology* **102**, 5889-5899 (2018).
- 11 Maddala, S. P., Liao, W.-C., Joosten, R. R., Soleimani, M., Tuinier, R., Friedrich, H. & van Benthem, R. A. Chain length of bioinspired polyamines affects size and condensation of monodisperse silica particles. *Communications Chemistry* **4**, 1-11 (2021).
- 12 Liu, Q., Zhou, L., Liu, F., Fortin, C., Tan, Y., Huang, L. & Campbell, P. G. Uptake and subcellular distribution of aluminum in a marine diatom. *Ecotoxicology and Environmental Safety* **169**, 85-92 (2019).
- 13 Chen, B. K., Anchel, D., Gong, Z., Cotton, R., Li, R., Sun, Y. & Bazett-Jones, D. P. Nano-Dissection and Sequencing of DNA at Single Sub-Nuclear Structures. *Small* **10**, 3267-3274 (2014).
- 14 Fukuda, T., Nakajima, M., Ahmad, M. R., Shen, Y., Nogawa, K. & Kojima, M. in *10th IEEE International Conference on Nanotechnology*. 111-114 (IEEE).
- 15 Jahng, J., Kwon, H. & Lee, E. S. Photo-induced force microscopy by using quartz tuning-fork sensor. *Sensors* **19**, 1530 (2019).
- 16 Otter, L. M., Förster, M. W., Belousova, E., O'Reilly, P., Nowak, D., Park, S., Clark, S., Foley, S. F. & Jacob, D. E. Nanoscale Chemical Imaging by Photo-Induced Force Microscopy: Technical Aspects and Application to the Geosciences. *Geostandards and Geoanalytical Research* **45**, 5-27 (2021).
- 17 Fu, D., Park, K., Delen, G., Attila, Ö., Meirer, F., Nowak, D., Park, S., Schmidt, J. E. & Weckhuysen, B. M. Nanoscale infrared imaging of zeolites using photoinduced force microscopy. *Chemical Communications* **53**, 13012-13014 (2017).
- 18 Alipour, L., Hamamoto, M., Nakashima, S., Harui, R., Furiki, M. & Oku, O. Infrared microspectroscopy of bionanomaterials (diatoms) with careful evaluation of void effects. *Applied Spectroscopy* **70**, 427-442 (2016).
- 19 Hemker, K. J. & Sharpe Jr, W. N. Microscale characterization of mechanical properties. *Annu. Rev. Mater. Res.* **37**, 93-126 (2007).
- 20 Liebig, J., Göken, M., Richter, G., Mačković, M., Przybilla, T., Spiecker, E., Pierron, O. & Merle, B. A flexible method for the preparation of thin film samples for in situ TEM characterization combining shadow-FIB milling and electron-beam-assisted etching. *Ultramicroscopy* **171**, 82-88 (2016).
- 21 Zhu, T., Bushby, A. & Dunstan, D. Materials mechanical size effects: a review. *Materials Technology* **23**, 193-209 (2008).
- 22 Stanimirović, Z., Stanimirović, I. & Takanata, K. Mechanical properties of MEMS materials. *Micro Electronic and Mechanical Systems*, 165-176 (2009).
- 23 Wang, W., Liao, S., Zhu, Y., Liu, M., Zhao, Q. & Fu, Y. Recent applications of nanomaterials in prosthodontics. *Journal of Nanomaterials* **2015** (2015).
- 24 Zhang, Y., Li, J., Soleimani, M., Giacomini, F., Friedrich, H., Truckenmüller, R. & Habibovic, P. Biodegradable Elastic Sponge from Nanofibrous Biphasic Calcium Phosphate Ceramic as an Advanced Material for Regenerative Medicine. *Advanced Functional Materials* **31**, 2102911 (2021).

## List of publications

1. **Soleimani M**, Maddala SP, Wismans M, Liao WC, van Breemen LC, van Benthem RA, Friedrich H. *In Situ Fabrication, Manipulation, and Mechanical Characterization of Free-Standing Silica Thin Films Using Focused Ion Beam Scanning Electron Microscopy*. Advanced Materials Interfaces. 2102201 (2022).
2. **Soleimani, M.**, van Breemen, L. C., Maddala, S. P., Joosten, R. R., Wu, H., Schreur-Piet, I., van Benthem, R. A. & Friedrich, H. *In Situ Manipulation and Micromechanical Characterization of Diatom Frustule Constituents Using Focused Ion Beam Scanning Electron Microscopy*. Small Methods **5**, 2100638 (2021).
3. **Soleimani, M.**, Rutten, L., Maddala, S. P., Wu, H., Eren, E. D., Mezari, B., Schreur-Piet, I., Friedrich, H. & van Benthem, R. A. *Modifying the thickness, pore size, and composition of diatom frustule in Craspedostauros sp. with  $Al^{3+}$  ions*. Scientific Reports **10**, 19498 (2020).
4. **Soleimani, M.**, van den Broek, S.J., Joosten, R.R., van Hazendonk, L., Maddala, S.P., van Breemen, L.C., van Benthem, R.A. & Friedrich, H. *Investigating the Morphology and Mechanics of Biogenic Hierarchical Materials at and below Micrometer Scale*. Submitted.
5. **Soleimani, M.**, Maddala, S.P., van den Broek, S.J., Joosten, R.R., Wu, H., Liao, W., Mezari, B., Hensen, E., van Breemen, L.C., Friedrich, H. & van Benthem, R.A. *How  $Al^{3+}$  ions in the growth medium affect the frustule Morphology, Chemistry, and Mechanical Properties of Diatom Thalassiosira pseudonana*. Submitted.

## Publications outside the scope of this thesis

1. Zhang, Y., Li, J., **Soleimani, M.**, Giacomini, F., Friedrich, H., Truckenmüller, R. & Habibovic, P. *Biodegradable Elastic Sponge from Nanofibrous Biphasic Calcium Phosphate Ceramic as an Advanced Material for Regenerative Medicine*. Advanced Functional Materials **31**, 2102911 (2021).
2. Maddala, S. P., Liao, W.-C., Joosten, R. R., **Soleimani, M.**, Tuinier, R., Friedrich, H. & van Benthem, R. A. *Chain length of bioinspired polyamines affects size and condensation of monodisperse silica particles*. Communications Chemistry **4**, 160 (2021).



3. Majumdar, S., Zhang, H., **Soleimani, M.**, Van Benthem, R. A., Heuts, J. P. & Sijbesma, R. P. *Phosphate Triester Dynamic Covalent Networks*. ACS Macro Letters **9**, 1753-1758 (2020).
4. Maddala, S.P., **Soleimani, M.**, Friedrich, H. & van Benthem, R. A. *Bioinspired One-Pot synthesis of Silica Particles from 10 to 1100 nm*. To be submitted.
5. Maddala, S. P., van Eck, E., Vena, R P., van Poll, Joosten, R. R., **Soleimani, M.**, Friedrich, H. & van Benthem, R. A. *Polyamine-Phosphate assisted Biomimetic synthesis of silica particles*. To be submitted.

## Curriculum vitae

Mohammad Soleimani was born on November 3<sup>rd</sup> 1990 in Ilam province, Iran. After finishing his high school studies in experimental sciences in 2009 at Rajaee School in Ilam, he studied pure chemistry at Ilam University (2009-2013). Following his graduation, he moved to Tehran University, Iran, where he obtained his MSc degree in nano chemistry-nano science and technology in 2015. During his MSc graduation project, he worked on the fabrication and characterizing of bi-metallic Metal-Organic Frameworks (MOFs) for catalysis applications. In January 2018 he moved to the Netherlands to join the laboratory of Materials and Interface Chemistry at the Eindhoven University of technology as a Ph.D. student under the supervision of prof. Nico Sommerdijk and dr. Heiner Friedrich. Since, August 2019, he continued his Ph.D. project titled “Exploring the Morphology, Chemistry, and Mechanics of Biogenic Silica in Diatoms” under the supervision of prof. Rolf van Benthem and dr. Heiner Friedrich at the laboratory of Physical Chemistry (SPC).

# Acknowledgements

Sometimes I think to myself how lucky I am, to be here and work with some of the best scientists in the world. I could have not imagined accomplishing such a thesis and fulfilling the requirements for being awarded a Ph.D. at TU/e. My project went through a few phases, from learning how to deal with a living organism, becoming a doctoral orphan, changing my promotor, to developing and designing a new way of measuring the properties of small-scale objects inside SEM. Many brilliant people helped me during my journey and I owe them a lot. Without their help, I could not finalize even half of what is written in this thesis.

*Rolf*, thank you very much for guiding me and accepting me as your Ph.D. student. We had many fruitful meetings together and I can say that I thrived by our constructive discussions about each step of the project. You are an excellent scientist and I am honored to work with you.

*Heiner*, thank you so much for supervising me in such a way to be curious about everything. Honestly, you are not the easiest person to work with, but you are the best one. During our meetings and discussions, you always look at hidden angles of the work and came out with new ideas when I was stuck. I think after four years, I am a much better scientist and writer mainly because of your high level of standards.

*Sai*, I cannot thank you enough for being such an incredible friend and colleague. You helped me greatly and I will not forget your valuable support during my Ph.D. project. We traveled a lot together and I really enjoyed accompanying you. Sometimes it was difficult to convince you about scientific topics particular related to our projects but meanwhile, it was inspiring and tempting to reach a common point with you.

*Remco*, you kindly adopted the SMG refugees to your group. You helped and supported several doctoral orphans to finalize their projects. Thank you very much for giving me the opportunity to work in SPC as well.

*My former SMG colleagues;*

*Mark*, thank you for being such a good officemate. You locked me in several time (of course unintentionally) and always complained: why I am so quiet as if I am not here! Deniz, my brother, I already miss you and our conversation about politics. You were wonderful and you were always a problem solver. *Bernette*, thank you very much for reading my thesis and correcting many small details that I could not see. *Machi*, thank you for your help during these years and also for accepting my offer to be my paranymph. *Mohammad. M*, it was truly comforting when I realized that there is an Iranian fellow in the group before I joined SMG. Thank you for your advice and support. *Luco*, I was lucky to have such a hardworking MSc student. Thank you for helping me with one of the difficult parts of the project. *Hanglong*, my friend, thank you for contributing to my works, you are brilliant. *Laura*, thank you for helping me with Avizo and the reconstruction of tomography data. *Anne* and *Pauline* thank you for your support with TEM, microtome, and light microscope. *Rick*, you are really good at what you are doing. Many thanks for contributing to my works. *Ingeborg*, I cannot thank you enough for supporting me in the last four years. You trained me how to work with FIB-SEM which had a significant role in my project. *Imanda*, you were the

first person from SMG that I got acquainted with. I was really happy to read your first email for an interview. Thank you for organizing the group and helping us.

*My SPC colleagues;*

*Catarina*, thank you for your comments during FAMs on my work and also sorry for not being the most organized person in the labs. *Bert*, you are an amazing scientist, it was a great pleasure knowing you. *Mark, Lisette, Siyu, Eva, Stijn, Joeri, Stefan, Max, Dixil, Tommaso, Jiankang, Jeroen, and Ton*, it was a pleasure to meet you and work with you in SPC. *Luuk*, thank you for being my paranymp during the defense ceremony. *Pleunie*, thank you for taking care of everything in SPC. A big thanks to my collaborators in the Department of Biomedical and Mechanical Engineering, *Lambert, Martijn*, and *Sten* for their valuable contributions to my thesis. Also, I would like to thank *Brahim* for his sincere support with NMR measurements. My thesis contains several high-resolution graphical images which I think help the readers to get a clear gist about the chapters, these images are made by collaboration with my friend *Siyamak Parsa*. I deeply appreciate your assistance, *Siyamak*. I would also like to thank *Igor Zlotnikov* for his help and attempts to conduct the mechanical studies in his lab, *Assaf Gal* for his feedback on the FIB slice and view process, *Lydia Köhler* and *Susanne Machill* for their instructions and support with cultivating diatoms, and *Wei-Chih Liao*, for his contributions with NMR experiments.

I would like to express my gratitude to the committee members; prof. *Stephen Weiner*, prof. *Eike Brunner*, prof. *Patrick Anderson*, and prof. *Emiel Hensen* for their positive feedback and constructive comments on my thesis and for taking part in the defense ceremony. Also, I would like to thank prof. *Fausto Gallucci* for chairing the ceremony.